

Thermo-mechanical properties and cracking during solidification of thin slab cast steel

Maria Begoña Santillana

Title: Thermo-mechanical properties and cracking during solidification of thin slab
cast steel
Author: M. B. Santillana
ISBN/EAN: 978-90-805661-9-4
Copyright: Tata Steel Nederland Technology B.V.

All rights reserved. No part of the material protected by this copyright notice may be reproduced or utilised in any form or by any means, without written permission from the publisher.

Thermo-mechanical properties and cracking during solidification of thin slab cast steel

Proefschrift

ter verkrijging van de graad van doctor
aan de Technische Universiteit Delft,
op gezag van de Rector Magnificus prof. ir. K.C.A.M. Luyben,
voorzitter van het College voor Promoties,
in het openbaar te verdedigen op donderdag 4 juli 2013 om 10:00 uur

door

Maria Begoña SANTILLANA
Ingenieur in Metaalkunde
Universidad Tecnológica Nacional, Argentina
geboren te San Nicolás, Argentina.

Dit proefschrift is goedgekeurd door de promotoren:

Prof. dr. R. Boom

Prof. dr. D. G. Eskin

Samenstelling promotiecommissie:

Rector Magnificus

Prof.dr. R. Boom

Prof.dr. D.G. Eskin

Prof. dr. B.G. Thomas

Prof. dr. K.C. Mills

Prof. ir. L. Katgerman

Dr. ing. U. Prahl

Dr. A. Burghardt

Prof.dr.ir. J. Sietsma

voorzitter

Technische Universiteit Delft, promotor

Brunel University (UK), promotor

University of Illinois at Urbana-Champaign (USA)

Imperial College, London (UK)

Technische Universiteit Delft

RWTH Aachen (Duitsland)

Tata Steel R&D, IJmuiden

Technische Universiteit Delft (reserveid)

Keywords: continuous casting, steel, solidification, hot tearing, cracking, mechanical properties

This research was sponsored by Tata Steel Research & Development and carried out as part of the programme of the Materials innovation institute M2i under the project number M41.5.08320

To Emiel and Max who gave me my favourite title- "Mama"

Hay hombres que de su ciencia
Tienen la cabeza llena;
Hay sabios de todas menas,
Mas digo sin ser muy ducho -
Es mejor que aprender mucho
El aprender cosas buenas.

José Hernandez, La vuelta del Martin Fierro, Capitulo XXXII, verso 3

There are some men who have their heads full with the things they know
wise men come in all sizes, but I don't need much sense to say:
better is than learning a lot of things, to learn things that are good.

José Hernandez, The return of Martin Fierro, Chapter XXXII, verse 3

Table of contents

Chapter 1

Introduction	1
1.1 Scope of this study.....	1
1.2 Outline of the thesis	2
References.....	5

Chapter 2

Fundamentals of solidification, hot tearing and alloying elements in continuously cast steel	7
2.1 The continuous casting process.....	7
2.2 History of continuous casting	9
2.3 Solidification theory.....	11
2.3.1 Constitutional undercooling ^[1,8]	12
2.4 Hot tearing theory	13
2.4.1 Hot tearing definition	16
2.5 Hot tearing Criteria.....	18
2.5.1 Non-mechanical criteria.....	18
Feurer's criterion	18
Clyne and Davies' criterion	19
Katgerman's criterion	19
2.5.2 Mechanical criteria	19
Stress-based criteria	19
Strain-based criteria	20
Novikov's criterion	20
Magnin's criterion.	20
Won's criterion ^[12]	20
Critical strain-rate criteria.....	21
Prokhorov's criterion.....	21
Braccini's criterion	21
RDG criterion (Rappaz-Drezet-Gremaud).....	21
2.6 The effect of alloying elements and non-metallic particles in steel.....	22
2.6.1 Fe-Mn-S system.....	23
2.6.2 The critical Mn/S ratio.....	25
2.6.3 Mn/S ratio and brittle temp range	26
2.6.4 Sulphur-rich non-metallic particles.....	27
2.6.5 Titanium nitrides precipitation during solidification.....	28
2.6.6 The combined effect of solutes in grain growth.....	29
2.7 The pursuit for understanding of hot tearing during continuous casting.....	32
References.....	33

Chapter 3

Analysis of solidification path and phase diagrams of commercial steel grades	37
3.1 Problem background and statistical analysis	37
3.2 Phase composition and solidification path analysis – Phase diagram assessment	41
3.2.1 Equilibrium phase diagrams	41
3.2.2 Non-equilibrium Scheil calculations	43
3.2.3 Thermal analysis for equilibrium phase diagram validation	45
3.2.4 Differential Thermal Analysis and Differential Scanning Calorimetry.....	50
LCAK Sample study	51
Heating cycles	51
Cooling cycles	53
HSLA samples study	55
Heating cycles	55
Cooling cycles	56
3.3 Peritectic phase transition	57
3.3.1 Carbon equivalent formulae	59
3.3.2 Peritectic range	61
3.3.3 Peritectic equivalent “Ep” in QuickSeg model	63
3.3.4 Thermo-Calc	65
3.4 Concentric Solidification Technique	66
3.4.1 Experimental data collection.....	67
3.4.2 Results evaluation	67
3.4.3 Non-metallic inclusions in the Concentric Solidification samples	69
LCAK steel	69
LR-HSLA steel	71
HSLA steel	74
3.4.4 EPMA analysis in the Concentric Solidification samples.....	77
3.4.5 Growth restriction in the Concentric Solidification samples.....	79
3.5 Concluding remarks: what additional studies are required for further hot cracking assessment of steels	81
References.....	82

Chapter 4

Thermo-mechanical behaviour of commercial steel grades for thin slab continuous casting	85
4.1 Hot tensile test of commercial steel grades at different temperatures.....	85
4.1.1 Introduction	85
4.1.2 Testing methodology	87
4.1.3 Results and Discussion	89
LCAK.....	90
HSLA.....	92
LR-HSLA.....	94
4.1.4 Characteristic temperatures	96
Zero strength temperature.....	96
Zero ductility temperature	97
4.1.5 Constitutive equations	97
4.2 Fractographic analysis on the hot tensile test samples.....	100
4.2.1 LCAK.....	101
ZST sample.....	101
1440°C samples	102

MDT samples	103
4.2.2 LR-HSLA.....	104
ZST sample.....	104
MDT samples	105
4.2.3 HSLA.....	105
ZST sample.....	106
MDT sample.....	106
4.2.4 Non-metallic inclusions in the hot tensile test samples	106
LCAK steel	107
LR-HSLA steel	109
HSLA steel	110
4.3 Thermo-mechanical behaviour and hot tearing susceptibility.	112
References.....	114

Chapter 5

Effect of chemical composition on microstructure of commercial steel grades	117
5.1 Introduction	117
5.2 Microstructural study of as-cast samples.....	119
5.2.1 Effect of fluid flow on dendrites growth	120
5.2.2 Outer equiaxed “chill” zone in continuous casting of steels.....	122
5.3 Measurement of primary dendrite spacing	124
5.4 Phase field modelling	125
5.4.1 Introduction to the phase field	125
5.4.2 Multiphase-field model and MICRESS® software.....	126
5.4.3 Boundary conditions.....	127
5.4.4 Nucleation model.....	129
5.5 Simulations of commercial steel grades	130
5.5.1 Quantitative evaluation of simulated microstructure.....	135
5.5.2 Evaluation of the hot-cracking susceptibility using the Rappaz criterion	138
5.5.3 Precipitation of carbo-nitride particles.....	140
5.6 Influence of microstructure on hot tearing susceptibility	144
References.....	145

Chapter 6

Physical modelling of cracking during continuous casting solidification	149
6.1 Introduction	149
6.2 Mould cracking simulator (MCS)	149
6.2.1 Description of the original mould simulator	149
6.2.2 Development of the Mould cracking simulator ^[3]	151
The submerged split-chill tensile test (SSCT) ^[4,5]	151
SSCT Experimental procedure ^[5]	151
Design and development of the hot cracking rig	152
6.2.3 First experiments in the MCS with Al- 2%Cu	153
6.2.4 A priori cold test procedure for steel	155
6.2.5 MCS steel experiments	156
6.2.6 Fractography of the MCS steel samples.....	159
6.3 Assessment of the physical modelling results	163
References.....	164

Chapter 7

Discussion and conclusions	165
7.1 Results analysis and hot tearing susceptibility.....	165
7.2 Conclusions	168
References.....	169
Summary.....	171
Samenvatting	173
List of Publications	175
Acknowledgments	177
Curriculum Vitae.....	179

Chapter 1

Introduction

1.1 Scope of this study

Nowadays a vast majority of the steel produced worldwide is via the continuous casting process route because this is the most low-cost, efficient and high quality method to mass produce metal products in a variety of sizes and shapes. Most of the continuous casters are the initial manufacturing step of a product which is very close to the final shape, reducing the need for further finishing. During continuous casting the liquid steel is solidified under controlled conditions of heat extraction to a semi-finished product that can subsequently be processed until final shape is reached.

The Tata Steel group established in 1907, is among the top ten global steel companies and one of the world's most geographically-diversified steel producers, with operations in 26 countries, the IJmuiden Steel Works is Tata Steel's largest and most cost-efficient steel making facility in Europe, where all the steel produced is continuously cast.

However, there is no perfect process and cracking during solidification of continuously cast steel slabs has been one of the main problems in casting for many years ^[1].

In literature many terms are used for the phenomenon of crack formation at temperatures close to the solidus temperature, e.g. hot tearing, hot shortness, hot cracking or solidification cracking. Regardless of the name, hot tears represent a failure that occurs during casting in the regions of a solidifying slab that are at temperatures between solidus (T_S) and liquidus (T_L) and are subjected to simultaneously acting tensile and compressive stresses ^[2-4].

This research originates from the industrial demand for defect-free high-speed casting of steels and this thesis focuses on the thermo-mechanical behaviour of steel grades in relation to the solidification conditions in the continuous casting mould. A main topic in this study is to determine the thermo-mechanical properties relevant for hot tearing of carbon steels under different solidification conditions and casting configurations. This is motivated by the continuous trend towards improving casting productivity by increasing casting speed in combination with higher quality demands. The assessment of these thermo-mechanical properties is also needed for the development of new steel grades to understand the combination of various properties.

Thermo-mechanical properties are inherent to each steel composition and are poorly known at temperatures in the solidification range. Only few publications are available where these properties are actually measured ^[5-8]. Therefore it is important for the improvement of the performance of continuous casters, to determine these properties more precisely.

The development of a hot tearing criterion for continuous casting of steels will enable process optimization to eliminate or reduce cracking during solidification, ultimately avoiding shell breakouts. In addition, obtained results of the thermo-mechanical properties of carbon steels will be applied to validate and improve computer simulations of continuous casting of steel.

The importance of this study for Tata Steel Group can be seen in better understanding of what is happening in the solidifying shell inside and immediately beneath the mould during continuous casting, particularly for decreasing or eliminating the hot cracking. The success of this study helps to further increase casting speeds with confidence in a more reliable and stable process and to develop new steel grades based on now well-known thermo-mechanical behaviour during solidification.

1.2 Outline of the thesis

Low carbon steel is not expected to be sensitive to hot tearing, but in the Direct Sheet Plant (DSP) caster from Tata Steel in IJmuiden, The Netherlands, a low carbon aluminium killed (LCAK) steel grade has a high risk of breakouts due to cracking during solidification. On the other hand, a high strength low alloyed (HSLA) steel grade, a micro-alloyed steel with extra additions of vanadium, nitrogen and niobium, has a very low breakout occurrence in the DSP caster. However, a similar steel grade, a low-range HSLA (LR-HSLA), with the same concentration of niobium but a lower concentration of vanadium and nitrogen, is also very sensitive to breakouts (see *Table 1.1* for the chemical composition of these steel grades).

Due to the challenging here mentioned reasons, it was for me simple to choose these three steel grades for this PhD study.

Table 1.1. Chemical composition of three steel grades considered in this thesis.

Grade	LCAK	LR-HSLA	HSLA
C (wt%)	0.045	0.045	0.045
Mn (wt%)	0.22	0.8	0.8
S (wt%)	0.005	0.005	0.005
V (wt%)	-	0.04	0.13
Nb (wt%)	-	0.013	0.013
N (ppm) max.	50	100	150
Liquidus temperature (°C)	1532	1528	1528
Solidus temperature(°C)	1513	1507	1505
Hot tearing susceptibility	Highest	High	Low

To provide a theoretical background for this thesis, the continuous casting process, the fundamentals of solidification, and the basics of hot tearing including a general knowledge overview of the role of the alloying elements during solidification are explained in Chapter 2.

Although the steel grades considered in this study are not extremely different in chemical composition, there is a big effect on hot tearing behaviour under continuous casting conditions. Several of those features and the effect of chemical composition are evaluated in Chapter 3. A phase diagram assessment for phase composition and solidification path analysis in equilibrium and under Scheil conditions is described in this chapter. Further, the different steel grades are analysed with differential thermal analysis (DTA), performed at Seteram Laboratories, France; to identify the main phase transformations that occur during solidification. As part of the thermal analysis, an evaluation of the steel grades with the method of concentric solidification technique^[9,10] has been completed, the tests were carried out in the University of Wollongong, Australia and the results analysis and metallographic studies was done by myself at Tata Steel IJmuiden Technology Centre. The concentric solidification technique is an experimental technique developed to enable high-resolution in-situ observation at elevated temperatures of phase transitions, including the peritectic transformation. Moreover, the non-metallic particles found at the surfaces of samples after testing with concentric solidification technique^[10] and the manganese-sulphur ratio within the samples has brought new insight to the analysed steels.

In Chapter 4 stresses and strains in the steel shell are examined giving relevant data on finding the macroscopic mechanism of steel cracking susceptibility at different temperatures. Therefore, hot tensile tests (HTT)^[6-8] were performed by Dr. Hanao and Dr. Mizukami at Sumitomo Metal Industries Corporate Labs, Japan; at different temperatures in the solidification range at high volume fractions of solid; because only the raw data was provided to myself, it was my task to perform the extensive data analysis and calculations. This was followed by the analysis of the structure of the fracture and of different precipitates positioned on the fracture surface, which I performed together with MSc. Sabri Sengo at Tata Steel IJmuiden Technology Centre. The determined constitutive equations and relationships I did develop can be further used in computer simulations. Additional to this mechanical study, the fracture surfaces of post mortem samples following hot tensile testing I investigated with scanning electron microscopy (SEM), which provided an invaluable insight into the fracture mechanism adding a better understanding with respect to the behaviour of these steel grades during solidification.

Segregating elements in steel can influence the hot tearing susceptibility as they can widen the brittle temperature range (ΔT_B), displacing its lower limit to lower temperatures^[8,11-13]. The focus on the microstructure features related to the non-metallic particles found at the fracture surfaces of the samples after hot tensile testing is therefore very important. These particles I thoroughly investigated with SEM and energy-dispersive X-ray spectroscopy (EDX) at Tata Steel IJmuiden Technology Centre.

This study also highlights the effect of the chemical composition on the microstructure that may affect the hot tearing sensitivity. Moreover, from the microstructural examination of the

steel slabs, two unexpected features were observed, the absence of an outer equiaxed zone, commonly called “chill zone” and the presence of “bent dendrites”. All these features I investigated in Chapter 5. In addition, microstructure simulations with phase-field for the three steel grades are explored and evaluated by myself, including their microstructural differences and hot tearing susceptibility due to the effects of vanadium, nitrogen and titanium in the dendritic structure formed during the first stages of solidification under continuous casting conditions. The phase field calculations here reported have been done in collaboration with Dr. B. Böttger in RWTH- ACCESS, Germany as part of the M2i-Tata Steel-ACCESS Valorisation project “Thermodynamic calculations and MICRESS® simulations of microstructure evolution during continuous casting of technical steel grades”.

State-of-the-art technology includes tensile testing equipment that can operate at or close to solidification temperatures of steel. However, this equipment cannot simulate actual thermo-mechanical conditions occurring during the continuous casting process. Mould simulator testing equipment has been developed to mimic continuous casting conditions^[14], merely to study mould flux behaviour, but this equipment lacks the feature to assess the mechanical properties of the solidifying shell. The development of the so-called Mould Cracking Simulator as a unique facility to combine these features is explained in Chapter 6. This Mould Cracking Simulator is developed for physical modelling of hot tearing during continuous casting, thus the data acquired and fractographic analysis during the first tests, including metallographic studies of the cracks and dendritic structures of the solidified shells produced during testing are also included in this chapter. During the first stages of this PhD research, I came with the idea to develop a test to assess the strength of the steel shell during solidification, the modification of the Mould Simulator was a direct and natural choice for me considering that this device was already available at Tata Steel IJmuiden Technology Centre. Mr. Marcel Cruijff assisted me with the design of the Mould Cracking Simulator.

In the final Chapter 7, I discuss the empirical findings from this study that provide a new understanding of hot tearing during solidification under continuous casting conditions.

References

1. Suzuki, M., Suzuki, M., and Nakada, M., *Perspectives of research on high-speed conventional slab continuous casting of carbon steels*, ISIJ International, 41 (7), 2001, 670-682.
2. Brimacombe, J. K. and Sorimachi, K., *Crack formation in the continuous casting of steel*, Metallurgical and Materials Transactions B, 8 (2), 1977, 489-505.
3. Li, C., *Thermal-mechanical model of solidifying steel shell behavior and its applications in high speed continuous casting of billets*, PhD, University of Illinois at Urbana-Champaign, USA, 2004.
4. Thomas B.G., *Continuous Casting Consortium*, 2006,
5. Lankford, W. T., *Some considerations of strength and ductility in the continuous-casting process*, Metallurgical and Materials Transactions B, 3 (6), 1972, 1331-1357.
6. Mizukami, H., Hiraki, S., Kawamoto, M., and Watanabe, T., *Tensile strength of carbon steel during and after solidification*, Tetsu to Hagane, 84 (11), 1-11-1998, 763-768.
7. Mizukami, H., Yamanaka, A., and Watanabe, T., *High temperature deformation behavior of peritectic carbon steel during solidification*, ISIJ International, 42 (9), 2002, 964-973.
8. Nakagawa, T., Umeda, T., Murata, J., Kamimura, Y., and Niwa, N., *Deformation Behavior during Solidification of Steels*, ISIJ International, 35 (6), 1995, 723-729.
9. Phelan, D., Reid, M., and Dippenaar, R., *Kinetics of the peritectic reaction in an Fe-C alloy*, Materials Science & Engineering A, 477 (1-2), 2008, 226-232.
10. Reid, M., Phelan, D., and Dippenaar, R., *Concentric solidification for high temperature laser scanning confocal microscopy*, ISIJ International, 44 (3), 2004, 565-572.
11. Chojecki, A., Telejko, I., and Bogacz, T., *Influence of chemical composition on the hot tearing formation of cast steel*, Theoretical and Applied Fracture Mechanics, 27 , 1997, 99-105.
12. Hansson K., *On the hot crack formation during solidification of iron-base alloys*, PhD, Royal Institute of Technology, 2001.
13. Pierer, R., Bernhard, C., and Chimani, C., *A contribution to hot tearing in the continuous casting process*, La Revue de Metallurgie, 2 , 2007, 72-83.
14. *Simulator for solidification in continuous casting mold*, ISIJ International, 25 (1985), 1985, 352-352.

Chapter 2

Fundamentals of solidification, hot tearing and alloying elements in continuously cast steel

Nowadays 95% of the steel produced worldwide is continuously cast. Solidification is a phase transformation changing liquid into a solid, more manageable phase. For metallic alloys the solidification involves the formation of crystals with a preferred growth direction, where most of the casting processes results in a dendritic (from the Greek dendron, tree-like) morphology. From a thermodynamic point of view, solidification requires a heat flux from the system to the surroundings and the relative thermodynamic stability of the phases present. Heat transfer plays a very important role in the formation of the solidification structure, including microsegregation of solute alloying elements. During solidification, three regions are present, the liquid, the liquid plus solid (the so-called mushy zone), and the solid region. "The mushy zone is the region where all of the microstructural characteristics are determined" ^[1] and it largely influences the strength of the material during processing. Hot tears are separations which might form during casting, when the temperatures of sub-areas of the material are between solidus (T_S) and liquidus (T_L) and are subject of simultaneously acting tensile stresses ^[2]. Hot tearing however, is an example of material failure and is still one of the major problems in casting technology. Commercial alloys include several alloying elements, that during solidification will segregate interdendritically at the grain boundaries. As a result, the solidification temperature of this film is much lower than the solidus calculated from the initial composition of the alloy. Therefore, segregating elements in the alloys can influence the hot tearing susceptibility.

2.1 The continuous casting process

The principle of the continuous casting process ^[3] for steel is based on pouring liquid steel into a water cooled copper mould which is also open at the bottom. The process starts with a temporary bottom which is attached to a dummy bar. During start casting this dummy bar is pulled through the strand guidance and cut from the solidified steel at the end of the caster. Heat transfer to the water cooled copper immediately solidifies the liquid steel and a solid skin is formed which increases in thickness down the length of the mould. The mould is oscillated sinusoidally at a frequency which provides negative strip i.e. the mould moves downward faster than the solidifying skin for a percentage of the oscillation cycle. Mould powder is added to the free surface of the liquid steel not only to provide thermal and chemical insulation from the environment, but also as lubricant in the interface between the solidifying shell and the mould.

As soon as the solidified shell is sufficiently thick to contain the liquid steel, the strand leaves the mould and is further cooled by water sprays of the secondary cooling system. The reason why the copper mould is not continued for further solidification is that because of the shell cooling and contracting, the mould becomes less efficient in heat transfer due to the “air gap” formation between the copper wall and the outer side of the solidified shell. It is therefore, more efficient to use direct water spraying from high pressure nozzles. However, the hot solidified skin cannot withstand the pressure arising from the liquid steel within the solidified shell and, if not constrained, would bulge outwards. Therefore, it is necessary to support the continuously solidifying shell by rollers. *Figure 2.1* shows the schematic of the process.

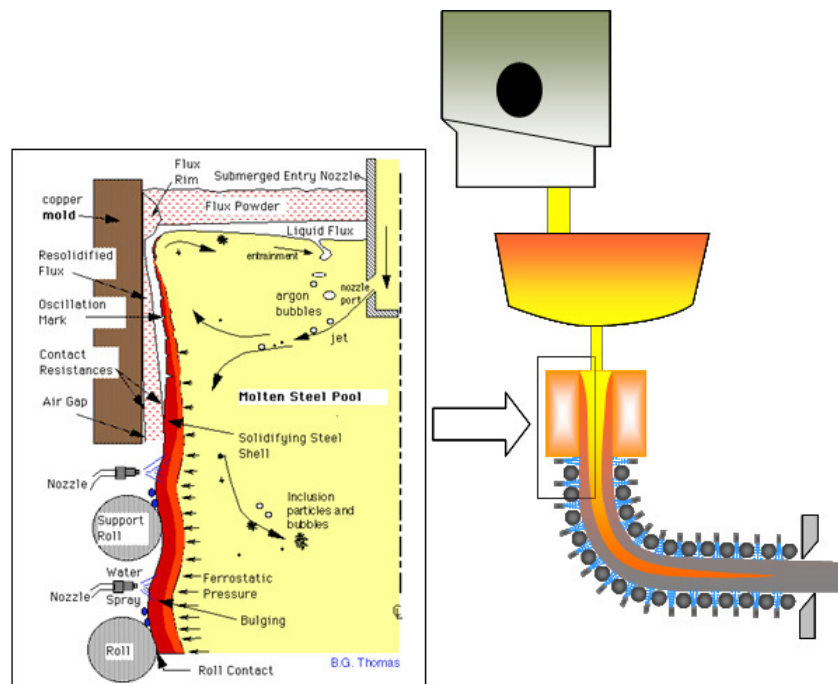


Figure 2.1. Schematic overview of the continuous casting process, left-hand side from ref. [4].

In steady state the solidifying shell is withdrawn from the mould at a constant velocity commonly named “casting speed” by withdrawal rolls further down in the machine. The strand becomes completely solid after passing several meters down the machine. The position depends on the maximum design casting speed, cooling conditions and product thickness. After the strand leaves the machine, it is cut either with a torch that travels at the same speed as the strand, or with a pendulum shear.

In the course of continuous casting development, several caster types have been realized, with significant differences in design height (*Figure 2.2*), including the vertical variant with the option to rotate around its axis. Some of these types, though, were constrained in caster productivity either due to limited support length (i.e., vertical type) or due to casting speed being limited by high mould friction (i.e., horizontal type). Besides, there are characteristic differences with respect to product quality as well. [3,5]

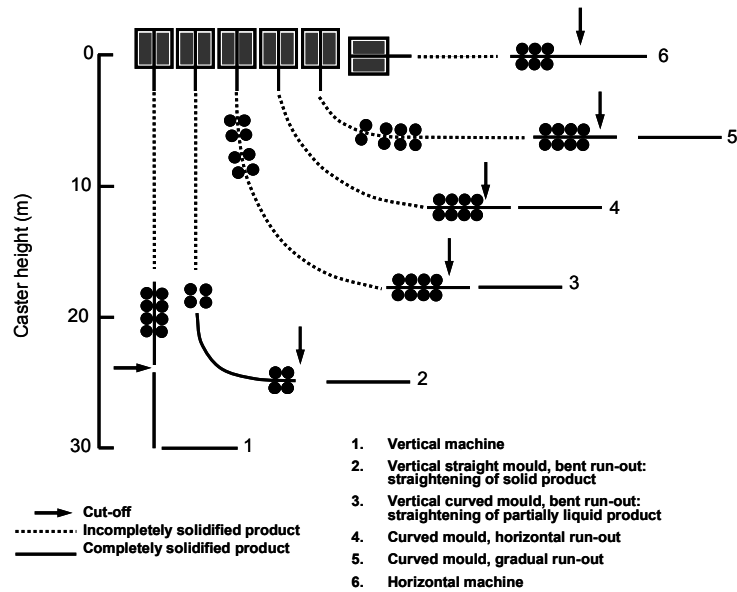


Figure 2.2. Caster designs [5].

2.2 History of continuous casting

Continuous casting (CC) of steel, as an industrialized method of solidification processing, has a relatively short history of less than 70 years. In fact, the CC ratio for the world steel industry, now approaching 95% of crude steel output, attained a mere 4% in 1970 (Figure 2.3)^[6] During the rather lengthy incubation, i.e., before the 1950's, important development stimuli came from the nonferrous industry, which had applied CC processes already—in particular, by the travelling mould principle—using casting wheels and/or belts to overcome mould friction.

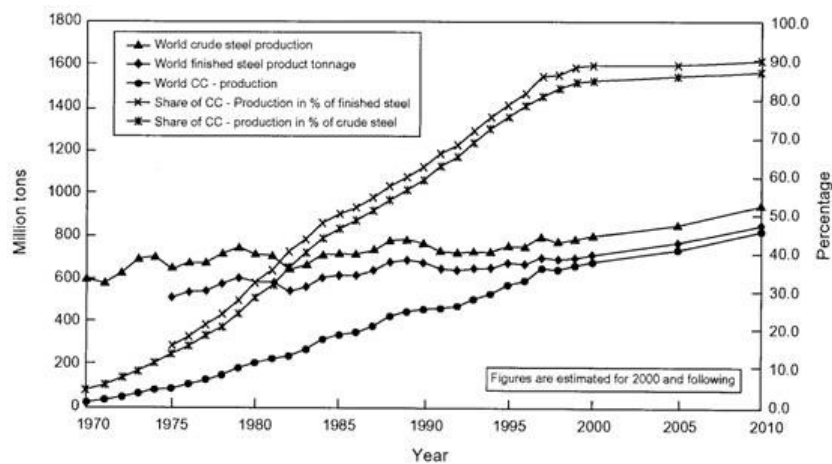


Figure 2.3. World steel production from 1970 up to 2010 [6]

The most spectacular of early CC attempts has been the direct strip casting effort by Sir Henry Bessemer in 1856. After successful blowing experiments in a melting crucible to produce liquid steel, he then disposed of it in his double-roller apparatus, which he used to cast thin strip for brass powder (“artist’s gold”) manufacture. However, he did not pursue this technology further on^[3,5], even when he did patent it.

The very first apparatus resembling a conventional CC machine is due to Benjamin Atha of the Atha & Illingworth Co. in Harrison (N.J.), USA, a tool steelmaker in the mid 1880's. Independently, the German inventor and steel industry consultant R. M. Daelen patented in 1889 a similar (not actually used) apparatus with shear cutting on the fly. This was indicative of the often-encountered phenomenon that identical solutions to a given task may surface simultaneously at different locations when circumstances have matured^[3,5].

For steel casting, considerable problems occurred due to sticking of the solidified shell to the water cooled mould; and the relative motion between the metal being cast and the mould wall was therefore required. It was not until 1933 when Siegfried Junghans developed and patented his mould oscillation system that laid the foundations for the large scale application of the process of continuous casting of steel.

After the 2nd World War the first semi-industrial pilot plants were built. One of the first machines constructed was a vertical caster installed in 1946 in Great Britain^[3,5].

To reduce the number of intermediate production steps or combine them in a continuous line, thus reducing material losses, energy consumption and the required manpower, a series of near-net-shape machines are nowadays well established. Thin slab casting is one of these technologies that have been successful for some decades.

Thin slab casting technology started commercial operation in the late 80's of the last century. Today, more than 60 installations are operating world wide. The quality of the products has improved dramatically, allowing a significant part of the steel products to be produced through this technology.

Tata Steel took its share in this development by introducing the Direct Sheet Plant (DSP) in IJmuiden in the year 2000. The facility focuses on the production of thin-gauged material through one single casting strand and a (semi-) endless rolling process, *Figure 2.4*.

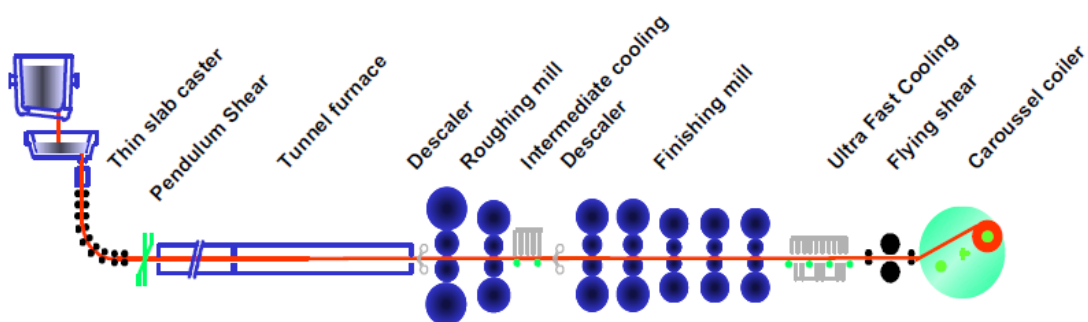


Figure 2.4. Layout of Tata Steel Direct Sheet Plant in IJmuiden, The Netherlands^[7].

The caster has a 90 mm thick funnel shaped mould and is equipped with liquid core reduction allowing a slab thickness of 70 mm. To reach casting speeds up to an actual maximum of 6 m/min, the steel is fed into the mould with a specially designed Submerged Entry Nozzle and an adjustable multiple pole Electro-Magnetic Brake is installed^[7].

2.3 Solidification theory

According to solidification theory ^[1], solid nuclei appear firstly in the liquid or close to the mould wall. To further grow those nuclei need to extract heat of their formation (latent heat) and have a thermally undercooled zone around. Conduction is the most favourable manner of heat extraction, via a close attachment to the mould or slag film.

Thus those just formed crystals of the preferred orientation opposite to the main heat flow direction advance rapidly, leading to the formation of the columnar zone. These solid crystals have a preferred growth direction, which encourage dendrite (tree-like) morphologies.

During the growth of the columnar zone, three regions can be distinguished, the liquid, liquid plus solid (so-called mushy zone), and the solid region (*Figure 2.5*). The mushy zone is the region where all of the microstructural characteristics are decided.

New dendrite trunks, crystallographically related to the initial primary dendrite, after branching can form new grains with different growing direction than the original dendrite (see *Figure 2.5*).

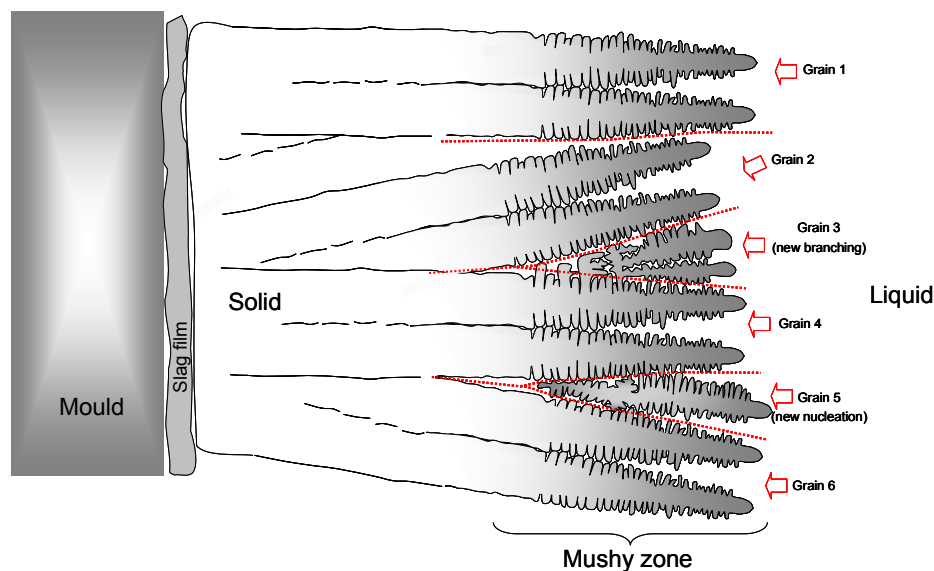


Figure 2.5. Schematic view of a dendrite growing and branching. In dashed-red the hypothetical grain boundaries are marked.

The transition from columnar to equiaxed (CET: columnar-equiaxed transition) growth occurs when one or more of the following assumptions for nuclei take place:

- Beyond a certain stage in the development of the columnar dendrites, branches become detached and can grow independently.
- Due to increased undercooling, new nuclei are formed in the liquid, particularly for high alloyed steels at the centre of the product.
- Non-metallic inclusions can act as nuclei as well and form new grains ahead of the columnar grains.

The new equiaxed dendrite structure, whilst growing in the melt, forms a barrier ahead of the columnar zone, stopping the growth of this zone. However, there is an effect of temperature, segregating elements and alloy composition in the CET.

These dendrites tend to have an equiaxed shape because their latent heat is extracted radially through the undercooled melt.

2.3.1 Constitutional undercooling ^[1,8]

During solidification of alloys, there is a substantial change in the concentration ahead of the solid/liquid interface (red square-dotted line in *Figure 2.6*). A solute-rich layer is formed in front of a growing interface, in which liquid composition is a maximum C_L^* at the interface and decreases with increasing distance from the interface. With the aid of the phase diagram (blue dashed lines in *Figure 2.6*), the equilibrium liquidus temperature of the liquid as a function of distance from the interface is plotted in the green full line in *Figure 2.6*.

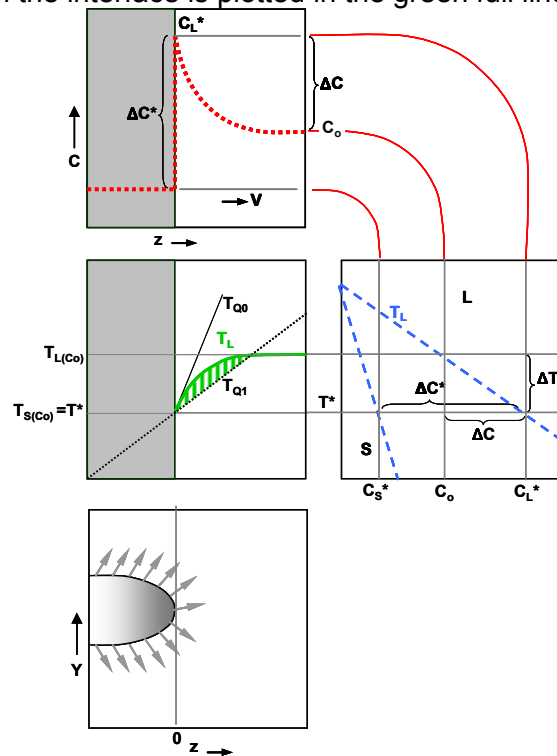


Figure 2.6. Solute distribution at the dendrite tip ^[1,8].

The equilibrium liquidus temperature increases with distance from the interface because the lower the solute content, the higher the liquidus temperature (in this particular case of the phase diagram). The actual temperature in the liquid phase is superimposed on the same graph (T_{Q0} & T_{Q1}). Since equilibrium is assumed at the solid-liquid interface, this curve must pass through T^* ($=T_{L(C_o)}$) at the interface $z=0$, but otherwise its shape is dictated by heat flow.

T_{Q0} in combination with T_L (green full line), shows a condition where the interface is exactly at the equilibrium liquidus temperature and where every point in front of the interface is at a temperature above liquidus. This represents the condition necessary for stable plane front

solidification. If any instability causes a protuberance to form on the flat interface, it will find itself in a superheated environment and will melt back.

On the other hand, T_{Q1} in combination with T_L represents an unstable case; here, liquid immediately in front of the interface is at actual temperature (T_{Q1}) that is below its equilibrium liquidus temperature. It is, therefore, undercooled. Constitutional undercooling indicates that the undercooling arises from a change in composition and not from temperature.

According with the constitutional undercooling theory, this result in instability of the plane front since any protuberance forming on the interface would find itself in undercooled liquid and therefore would not disappear. In other words, the constitutional undercooling theory deals with the question which state, solid or liquid, is thermodynamically stable in front of an initially plane front interface. If liquid, the interface is assumed to remain plane; if solid, the interface is assume to break down.

The growth temperature, T^* , of the tip will define a solute undercooling, ΔT_C , or via de phase diagram, the degree of supersaturation:

$$\Omega = \frac{\Delta C}{\Delta C^*} \quad (2.1)$$

The determination of Ω as a function of the other parameters requires the solution of the differential equation which describes the solute distribution (see Figure 2.6).

2.4 Hot tearing theory

The solidification process with its characteristic temperatures in steel is conventionally divided into three different stages^[9,10] schematically shown in Figure 2.7:

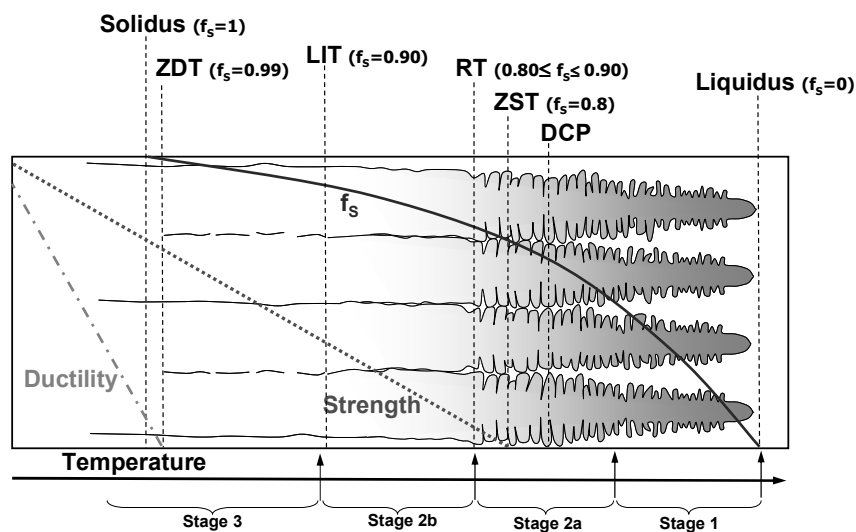


Figure 2.7 – Solidification structure with characteristic temperatures in hot tearing (see the text for explanations on abbreviations).

Stage 1: Formation of dendrites during solidification and liquid feeding. As the steel starts to solidify, it does so in a dendritic structure. While cooling, secondary dendrite arms form at a short distance behind the primary dendrite tips. These dendrites have no mechanical bond with each other being separated by liquid steel. Consequently, the shell at this location has little or no strength. However, as the melt cools, the dendrite tips of the growing crystals begin to touch one another until a coherent dendritic network is formed. This state is defined as dendrite coherency point (DCP). Only after the temperature has dropped below the coherency point, the mushy zone is formed ^[9,10].

If thermal strain is imposed on the semi-solid material at this early stage of solidification, the resulting opening in the structure will be filled by intergranular or interdendritic liquid. ^[11].

Stage 2: Coarsening and impingement of dendrites during solidification. This stage can be divided into two sub-stages:

- *2a, Coarsening of dendrites during solidification and interdendritic feeding:* secondary dendrite arms begin to reach out and interlock with each other and the individual dendrites start to connect with each other giving the solidified shell some strength. However, at this stage, the permeability of the network is still large enough to prevent defect formation by melt feeding.

- *2b, Coarsening of dendrite arms and interdendritic separation:* dendrites reach the stage when the interlocked secondary dendrite branches become indistinguishable. As the temperature drops further, the structure starts to resemble columns without visible dendrite branching. With increasing solid fraction, liquid is isolated in pockets or immobilised by surface tension ^[9,10].

During these sub-stages, as liquid is trapped between interlocking dendrites, the free passage for liquid is blocked, transforming continuous liquid films into isolated liquid droplets. As a result, the strength of the material is very low due to the existence of this non-continuous liquid film between the primary dendrites. If an external stress is applied to the material, hot cracking can easily occur. This type of cracking is defined as solidification cracking, interdendritic cracking, or hot tearing.

Stage 3: Grain formation at the end of solidification and bridging or solid feeding. At this stage, the boundaries of the primary dendrites of the same orientation become invisible on polished sections. This is called the transition from the dendritic structure to the grain structure. A thin liquid film can still exist at the grain boundaries due to the presence of segregated elements in the liquid, lowering the melting point of this film. Hot cracks formed at this stage are named grain-boundary or intergranular cracks, or hot cracks to distinguish them from the hot tears formed during stage 2. Solid-state creep is the only way to accommodate solidification shrinkage and thermal stresses ^[9,10].

Grain structures behave somewhat differently from the columnar structures of dendrites. The as-cast grains are formed by a pocket of dendrites with the same alignment. The gradual transition of a continuous liquid with isolated grains or clusters to a solid network with isolated droplets or films of liquid is called “percolation” ^[11]. At this point, if strain is applied

and separation of grains occurs, the isolated liquid droplets can form liquid bridges observed at the fractures.

The development of mechanical strength of the semi-solid steel can be characterized by two temperatures that also determine the hot cracking susceptibility of a steel grade.

The Zero Strength Temperature (ZST) is defined as the temperature during cooling at which forces can first be transmitted perpendicular to the solidification direction ^[12]. This ZST corresponds to a fraction of solid (f_s) in the range of 0.65 to 0.80. At this range (stage 2), a small strain leads to cracking, because a segregated liquid film still exists between the dendrites. This results in a crack or segregate-rich zone depending on whether or not liquid steel can still penetrate between the dendrites.

As the steel solidifies and cools further the strength of the material increases and at some point the material acquires plasticity (ductility) ^[12]. The temperature at which the transition occurs from brittle to ductile behaviour is known as the Zero Ductility Temperature (ZDT) and is commonly associated with a fraction of solid (f_s) between 0.98 and 1. In *Figure 2.5* a schematic representation of the ZST, ZDT and the solidification structure is shown.

The range between the ZST and ZDT is defined as the brittle temperature range (ΔT_B) and gives a qualitative guide to hot crack sensitivity ^[10,13].

$$\Delta T_B = ZST - ZDT \quad (2.2)$$

The wider the range, the longer the period of time (at a given cooling condition) that the semi-solid steel stays in this critical range, and the larger the stress concentration resulting from the thermal contraction restriction. It can be stated that the tendency to crack formation depends on the brittle temperature range of the alloy ^[10,13].

The application of this or any other hot tearing criterion is hindered by the lack of factual data on the mechanical properties of solidifying steel.

The ability to predict at least the tendency of hot tearing of solidifying steel is of great interest due to the continuous trend towards increased casting productivity by increasing casting speed, combined with higher quality demands, and the development of new steel grades.

Other authors ^[12,14] divided the mushy zone into the mass/liquid feeding zone and the cracking zone. Cracks formed in the mass/liquid feeding zone are refilled with the surrounding liquid, whereas cracks formed in the cracking zone cannot be refilled with the liquid because the dendrite arms are close enough to resist feeding of the liquid. Therefore the hot tears can take place under a small strain when the interdendritic liquid film is isolated to resist feeding of the surrounding liquid through the dendrite arms. In this case, the brittle temperature range it is defined as:

$$\Delta T_B = LIT - ZDT \quad (2.3)$$

Where:

L/T : Liquid impenetrable temperature, with a fraction of solid of 0.90, whereas the dendrites are compacted enough to resist the feeding of the liquid ^[12].

Another relevant temperature to consider in the study of the hot tearing phenomenon is the rigidity point (RT). The rigidity point is defined as the volume fraction of solid, or the temperature, at which a given alloy starts to develop mechanical resistance. On average, between $0.80 \leq f_s \leq 0.90$, the dendrite arms coalesce or bridge, transforming continuous liquid films into isolated liquid droplets. The temperature at which this takes place is designated as rigidity temperature, or rigidity point. Below $f_s \leq 0.80$, dendrite trunks do not pose much resistance to tensile stresses, whereas above $f_s \geq 0.90$, the mushy zone behaves as a coherent solid, slightly weakened by the presence of the liquid droplets.

2.4.1 Hot tearing definition

In literature many terms can be found with reference to the phenomenon of crack formation at temperatures close to the solidus temperature such as hot tearing, hot cracking or solidification cracking. Regardless of the name, hot tears are separations which might form during casting, when the temperatures of sub-areas of the material are between solidus (T_S) and liquidus (T_L) and are subject of simultaneously acting tensile stresses ^[2].

During solidification, metal experiences temperature differences, which induce convection in the liquid region and deformation in the solid. The former phenomenon involves very large displacements but low stresses, whereas the opposite occurs for the latter. This drastically different behaviour is due to the very large change of viscosity of a metal when it undergoes the liquid-to-solid transition (twenty orders of magnitude or more). The transition is made more complicated for an alloy because the presence of the mushy zone somehow “mixes” the two behaviours: the deformation of the dendritic network strongly depends on its coherency state and the flow of liquid now occurs in a porous solid phase ^[15].

Hot tears initiate above the solidus temperature and propagate in the interdendritic liquid film. They originate from a lack of liquid feeding of the mushy zone, especially towards the end of solidification, and, more precisely, when grains start to impinge and finally touch one another, but are still surrounded by a continuous liquid film ^[2].

In the course of solidification, the liquid flow through the mushy zone decreases until it becomes insufficient to compensate for the solidification shrinkage at which point the cavities (or voids) are formed. Cracks can initiate on these voids. The fracture has a bumpy surface covered with a smooth layer and sometimes with solid bridges that connect or have connected both sides of the crack ^[13].

The hot tearing mechanism includes phenomena occurring in two scales (see *Figure 2.8*) microscopic (crack nucleation and propagation, stress concentration, structure coherency, wet grain boundaries) and meso-macroscopic (lack of feeding, stress, strain or strain rate imposed in the structure).

The primary and secondary cooling causes strong macroscopic thermal gradients in the solidifying slab, which leads to uneven thermal contraction in different sections of the slab. As a result, macroscopic stress causes distortion of the slab shape, or may trigger hot tearing in the weak sections ^[14].

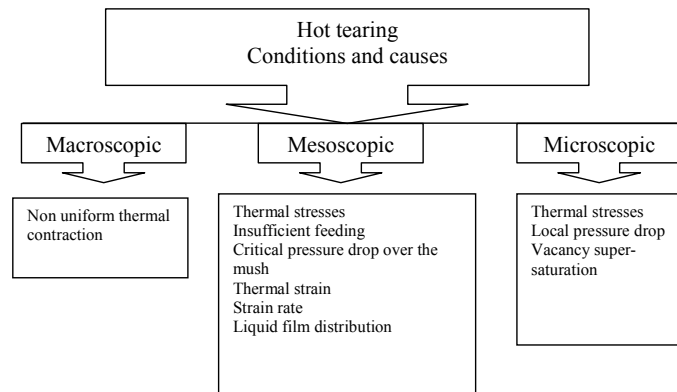


Figure 2.8. Summary of conditions and causes of hot tearing suggested by Eskin et al. ^[10,13]

On the microscopic level, the solidification shrinkage and thermal contraction impose strains and stresses on the solid network in the mushy zone, which creates the conditions for hot tearing. The deformation behaviour of the mush is very critical for the formation of hot tears ^[13].

The mesoscopic strain rate is believed to be the most important factor. The physical explanation of this approach is that semisolid material during solidification can accommodate the imposed thermal strain by plastic deformation, diffusion-aided creep, structure rearrangement and filling of the gaps and pores with the liquid. All these processes require time and the lack of time (high solidification speeds and/or strain rates) will result in fracture. Therefore, there exists a maximum strain rate that the semisolid material can endure without fracture during solidification ^[13].

Above the coherency temperature, a continuous liquid phase is still present in between the solid dendrite arms since they have not yet coalesced. Deformation induced by thermal stresses can pull these arms apart quite easily. If the interdendritic liquid flow can feed such regions and heal the cracks, then almost nothing is noticed in the microstructure except some local inverse segregation. These “healed” hot tears are often referred as segregation cracks, and they may cause defects due to anisotropy of the final material.

However, where the permeability between dendrites is very small, hot tears formed in the cracking zone cannot be refilled. The reason therefore is that the dendrite arms are compacted enough to resist feeding of the liquid ^[2].

The stresses are induced by differential thermal contractions upon cooling. When the dendritic network is coherent, it can sustain and also transmit stresses, and this is perhaps the reason why the stresses always find the weakest point in the solidifying shell to concentrate and develop a crack.

The formation of hot tears during continuous casting is mostly related to the macroscopic level of interaction between a reduced ductility of the solidifying steel in the mushy zone (the loss of ductility may also result from microsegregation in the liquid film between dendrites and grains) and stresses caused by different mechanisms, i.e. thermal contraction, bulging and bending^[12].

2.5 Hot tearing Criteria

Hot tearing remains as one of the major problems in casting technology. Existing models allow one to calculate the stress-strain and temperature situation in a casting, and to compare those with the chosen hot tearing criterion. In most successful cases, the simulation shows the relative probability of hot tearing and the sensitivity of this probability to such process parameters as casting speed, alloy composition, and casting dimensions.

Hot tearing however is just another example of material failure. Therefore it can be treated adequately, using the well developed methodology of fracture mechanics^[2].

The challenge nowadays lies not in the adequate description of macroscopic and microscopic stress-strains situations and their correspondence to the parameters and properties of the mushy zone, but rather in finding the real factors causing the nucleation and propagation of a hot crack due to the mesoscopic factors.

What is lacking is the completeness of the model. A comprehensive model and corresponding hot tearing criterion should include nucleation and propagation of hot tears and connect these processes to the microstructure evolution during solidification of the semisolid material, to the macroscopic and microscopic thermo-mechanical situation in the mushy zone, and to the mechanical (or fracture mechanical) properties of the mushy zone.

The existing hot tearing criteria can be conditionally divided into two categories: non-mechanical and mechanical criteria.

2.5.1 *Non-mechanical criteria*

These type of criteria deal with the vulnerable temperature range, the phase diagram and process parameters like casting speed (related to the rate of segregation during solidification) and alloy composition. Because of that, these criteria are applicable to most commercial alloys.

Feurer's criterion

Feurer's theory of hot tearing^[13] is based on a non-mechanical criterion that focuses on feeding and shrinkage during solidification. This approach considers that hot tearing occurs due to the lack of feeding, which is related to the difficulties of fluid flow through the mushy zone as a permeable medium in competition with solidification shrinkage.

Clyne and Davies' criterion

The hot tearing criterion proposed by Clyne and Davies ^[10] is based on the assumption of Feurer ^[13] that in the last stage of freezing, it is difficult for the liquid to move freely so that the strains developed during this stage cannot be accommodated by mass and liquid feeding. They consider this last stage as the most susceptible to hot tearing.

Katgerman's criterion

Katgerman's ^[10] model, combines the theoretical considerations of Clyne and Davies and Feurer^[13]. The model defines a hot tearing index, where the time when feeding becomes inadequate, t_{cr} , is determined using Feurer's criterion.

2.5.2 Mechanical criteria

In these criteria, the hot cracking sensitivity is based on mechanical effects during cracking. They are sub-divided in three groups: stress based-, strain based- and critical strain-rate criteria.

Stress-based criteria

The models are based on the assumption that a semi-solid body will fracture if the applied or induced stress exceeds a critical stress. The critical stress results either from the strength of the already solidified material or from the strength (surface tension) of the liquid film between dendrites or grains. The first type of these hot tearing criteria accounts for the fact that the material has a limit stress at which it fails. This approach can be subdivided into two sets of criteria.

The first set of equations is based on the strength of bulk material and the second group of equation, on the strength of a liquid film trapped between grain boundaries. Within the first type of stress-based criteria, the hot tearing susceptibility is derived from an assumption that the material contains defects or a weak point. Whether there will be a fracture or not depends on such parameters as: stress, defects dimensions, and configuration. The second mathematical approach is more comprehensive in describing the hot tearing phenomena. The effects of some parameters involved in hot tearing can be explained using this theory, for example: grain diameter, liquid viscosity, and liquid fraction.

A stress-based hot tearing criterion that uses the strength of liquid trapped between grain boundaries are reported by Novikov et al. and by Dickhaus et al. (described in detail in ref ^[10]). They refer to the stress needed to pull apart two parallel plates separated by a thin liquid film as to the strength of semi-solid metals. The assumptions that are applied in this model are the uniform distribution of liquid and no influence of sliding on the fracture strength ^[10].

Strain-based criteria

In these criteria it is assumed that materials associated with an existing liquid film can only sustain a certain amount of strain before tearing. The total strain that develops during the presence of a liquid film depends therefore on the strain rate and the length of film life. Novikov and Prohokov had their theories developed in the 1960's and more recently in the early 1990's, Yamanaka found out that hot tearing occurs when the total amount of strain within a certain critical (or brittle) temperature range exceeds the critical strain, independent of strain rate and manner of deformation ^[2].

Following this theory of an accumulated strain, the realisation of the strain-based hot tearing criterion for the continuous casting process can be done by comparing the strain due to the process to the critical strain of hot tearing. This criterion states that if the accumulated strain due to the process exceeds a critical value for hot tearing, hot tears will form ^[2].

According to this theory, hot tears are generated by an overcritical deformation of the mushy zone. In continuous casting, the mushy zone moves with the shell growth from the surface to the centre of the casting. Not only the position but also the width of the mushy zone changes due to variation of the solidification parameters over the metallurgical length ^[2].

The total strain in the solidifying shell and the mushy zone arises from thermal contraction, mould geometry like funnel shape, taper, bending, unbending – straightening, misalignment, bulging, and/or soft reduction. Only that part of the total strain accumulates in a critical temperature range ΔT_B and the associated residence time in the ΔT_B will contribute to the formation of hot tears ^[15].

Novikov's criterion

The mechanical criterion of Novikov ^[10] considers the hot cracking sensitivity determined by shrinkage strains in the mush in relation to the fracture strain of the mush. Novikov neglects the apparent strain (which is used in Prokhorov's criterion ^[10]), and proposes a "reserve of plasticity," p_r , in the solidification range, which is the integrated difference between the elongation to failure, ε_{fr} , and the linear shrinkage, ε_{sh} . This integration is performed from the coherency temperature until the solidus temperature, which Novikov calls the "brittle" (or "effective") temperature range, ΔT_{br} .

Magnin's criterion.

The criterion proposed by Magnin et al. ^[16,10] is based on the strain experienced during solidification in relation to the fracture strain in the last stage of solidification. The hot cracking sensitivity, HCS, is taken as the quotient of the circumferential plastic strain, $\varepsilon_{\theta\theta}$, at solidus temperature and the experimentally determined fracture strain, ε_{fr} , close to the solidus temperature. If HCS is higher than one, a crack will develop. Therefore, the model can be used to predict hot tearing both qualitatively and quantitatively.

Won's criterion ^[12].

A hot tearing crack criterion which is the best strain criterion for steels available from the existing literature found is by Y. M. Won ^[12]. This criterion takes into account the effects of

brittle temperature range, defined as the temperature range corresponding to solid fractions between 90% and 99% and the average strain rate within ΔT_B . It is seen that larger brittle temperature range and strain rate lead to smaller critical strain which implies easiness of crack initiation. The brittle temperature range includes the effects of the chemical compositions and the cooling rate, and the strain rate reflects the external loading conditions.

The critical strain decreases when the strain rate and the brittle temperature range are increased, which is dependent on the cooling rate and the content solute elements. With increasing the cooling rate and the content of solute elements, especially phosphorus and sulphur, the brittle temperature range increases largely due to the severe segregation of solute elements at the final stage of solidification, which is influenced by the cooling rate.

Critical strain-rate criteria

Most of these criteria are taking into account the mass balance within the mushy zone. Examples of these criteria are Prokhorov's, Braccini's and Rappaz-Drezet-Gremaud (RDG's) criteria.

Prokhorov's criterion

Prokhorov ^[10,16] formulated a mechanical criterion, in which the hot cracking sensitivity is determined by the shrinkage and the apparent strain rate in the mush in relation to the fracture strain rate of the mush.

In this approach, effects of the surrounding configuration are accounted for by the apparent strain rate. It is assumed that during solidification, alloys pass through a low-ductility temperature range that is called the brittle temperature range (BTR). The brittle temperature range runs from the coherence temperature until the solidus temperature.

Braccini's criterion

In the criterion of Braccini et al. ^[16], the strain rate is used for the crack initiation and propagation.

The critical strain rate for hot tearing, $\dot{\epsilon}$, is a measure for the hot cracking sensitivity, considering that this criterion only takes in account the critical strain rate in steady state, the hot cracking susceptibility is only influenced by the steady state casting speed. However, increasing casting speed leads to an increase of the critical strain rate ^[16].

RDG criterion (Rappaz-Drezet-Gremaud)

Up to now, the RDG criterion is the most complete criterion to be used in hot tearing of steels, and it is the intention to use this criterion for further analysis in this thesis, thus a detailed explanation is here presented.

In the RDG hot tearing criterion ^[15] the depression pressure, Δp , over the mush reads:

$$\Delta p = \Delta p_{sh} + \Delta p_{mec} - \rho g h \quad (2.4)$$

where:

Δp_{sh} and Δp_{mec} are the pressure drop contributions in the mush associated with the solidification shrinkage and the deformation induced fluid flow, respectively;

ρ : average density of the mush (g/m^3);

g : gravity constant ($\text{m/s}^2 = \text{N/Kg}$);

h : distance below the melt surface (m);

The pressure drop contributions in the mush associated with the solidification shrinkage and deformation-induced fluid flow are computed as follows:

$$\Delta p_{sh} + \Delta p_{mec} = \frac{180\mu\Delta T}{G\lambda_2^2} \left[v_T \beta A + \frac{(1+\beta)B\dot{\epsilon}\Delta T}{G} \right] \quad (2.5)$$

$$A = \frac{1}{\Delta T} \int_{T_{end}}^{T_{mf}} \frac{f_s^2 dT}{(1-f_s)^2} \quad (2.6)$$

$$B = \frac{1}{\Delta T} \int_{T_{end}}^{T_{mf}} \frac{f_s^2 F_s(T)}{(1-f_s)^3} dT \quad (2.7)$$

$$F_s = \frac{1}{\Delta T} \int_{T_{end}}^T f_s dT \quad (2.8)$$

Where:

μ : dynamic viscosity of the liquid phase (Pa.s),

T : temperature ($^{\circ}\text{C}$),

G is thermal gradient,

λ_2 is dendrite arm spacing (μ),

v_T is casting velocity, (m/s)

β : solidification shrinkage factor,

$\dot{\epsilon}$: viscoplastic strain rate, (s^{-1})

f_s is volume fraction of solid,

T_{end} : temperature at which bridging of the dendrite arms between grains occurs ($^{\circ}\text{C}$)

T_{mf} : mass feeding temperature ($^{\circ}\text{C}$).

The depression pressure Δp is a measure for the hot cracking sensitivity. A criterion for hot cracking is introduced by a critical depression pressure Δp_c . The hot tear will form if $\Delta p > \Delta p_c$.

2.6 The effect of alloying elements and non-metallic particles in steel

As the steel first solidifies it does so in the form of dendrites. Whilst growing these dendrites will reject the solute elements with the partition coefficient <1 to the liquid. As a result of incomplete equilibrating diffusion in the solid, the concentration of the solutes in the liquid

phase will progressively increase beyond that from equilibrium solidification and can result in the formation of low-melting phases. This process is known as microsegregation. The movement of the solidification front and flow motion may translate this microsegregation to the scale of the casting (sample), forming macrosegregation (uneven chemical composition on larger scale) in the solidified alloy ^[1]

Below the equilibrium solidus, the liquid phase rich in strongly segregating elements, such as sulphur and phosphorus, is located interdendritically and at the grain boundaries, i.e. between coherent dendrite arrays. Therefore, when the quantity of liquid phase drops, the sulphur and phosphorus concentration raises rapidly ^[14]. As a result of the strong segregation, the solidification temperature of this film is much lower than the solidus calculated from the initial composition of the steel ^[9,14,17].

Therefore, the segregating elements in the steel can influence the hot tearing susceptibility as they widen the ΔT_B displacing its lower limit to lower temperatures ^[2,9,14,17].

The upper temperature of the brittleness range depends mainly on the carbon concentration, the influence of sulphur or phosphorus will be more sensitive for the ZDT. Other elements in the steel, e.g. Mn, may adjust this temperature and fraction of solid through reactions with the segregating elements. The brittle–ductile transition temperature tends to be controlled by minor elements and their tendency to segregation.

Ti is the only micro-alloying element which is known to form nitrides at rather high temperatures, other micro-alloying elements will form carbo-nitrides at much lower temperatures. If precipitation as TiN or co-precipitation with other micro-alloying elements as (Ti,V,Nb)(C,N)^[18] can happen before solidification is finished, an influence of Ti on hot-cracking is possible, and the higher V and N content could influence the cracking susceptibility.

2.6.1 Fe-Mn-S system

The ability of manganese to react with sulphur during solidification of steel and its effect on hot tearing has induced great interest in the Fe-Mn-S system. In *Figure 2.9* and *Figure 2.10* the equilibrium ternary phase diagram of the Fe-Mn-S system, and the pseudo-binary Fe-MnS diagram, are shown respectively. These diagrams have been calculated with FactSage 6.2 and the FSstel database was used for the thermodynamic calculations^[19], the invariant points and their calculated composition is listed in *Table 2.1*. A liquid miscibility gap that originates on the Mn-MnS side of the ternary diagram, dominates this region. The eutectic from the same side close to the Mn corner runs parallel to the miscibility boundary.

Table 2.1. Four-phase intersection points from the ternary diagram Fe-Mn-S (three phases listed plus liquid).

Invariant point nr.	Four-Phase Intersection Points with LIQUID	S	Fe	Mn	T(°C)
1	Fe_liquid(liq) / MnS_mns(s) / Mn_liquid(liq)	0.2407	0.0837	0.6756	1665
2	Fe_δ(s) / Fe_liquid(liq) / MnS_mns(s)	0.3667	0.0824	0.5509	1538
3	Fe_δ(s) / Fe_liquid(liq) / MnS_mns(s)	0.3004	0.5597	0.1399	1538
4	Fe_δ(s) / Fe_γ(s) / MnS_mns(s)	0.0594	0.9385	0.0022	1394
5	Fe_δ(s) / Fe_γ(s) / MnS_mns(s)	0.3158	0.5570	0.1272	1394
6	Fe_δ(s) / Fe_γ(s) / MnS_mns(s)	0.3663	0.1595	0.4742	1394
7	Fe_δ(s) / Fe_γ(s) / MnS_mns(s)	0.0008	0.9266	0.0725	1394
8	MnS_mns(s) / Mn_bcc(s) / Mn_fcc(s)	0.0005	0.0723	0.9271	1138
9	MnS_mns(s) / Mn_cub(s2) / Mn_fcc(s)	0.0004	0.1119	0.8878	1087
10	FeS_fes(s) / Fe_γ(s) / MnS_mns(s)	0.3200	0.6581	0.0220	975
11	Fe_δ(s) / Fe_γ(s) / MnS_mns(s)	0.0000	0.6408	0.3592	911.7
12	FeS2_fes2_pyrite(s1)(s) / FeS_fes(s) / MnS_mns(s)	0.4918	0.3573	0.1509	778.0

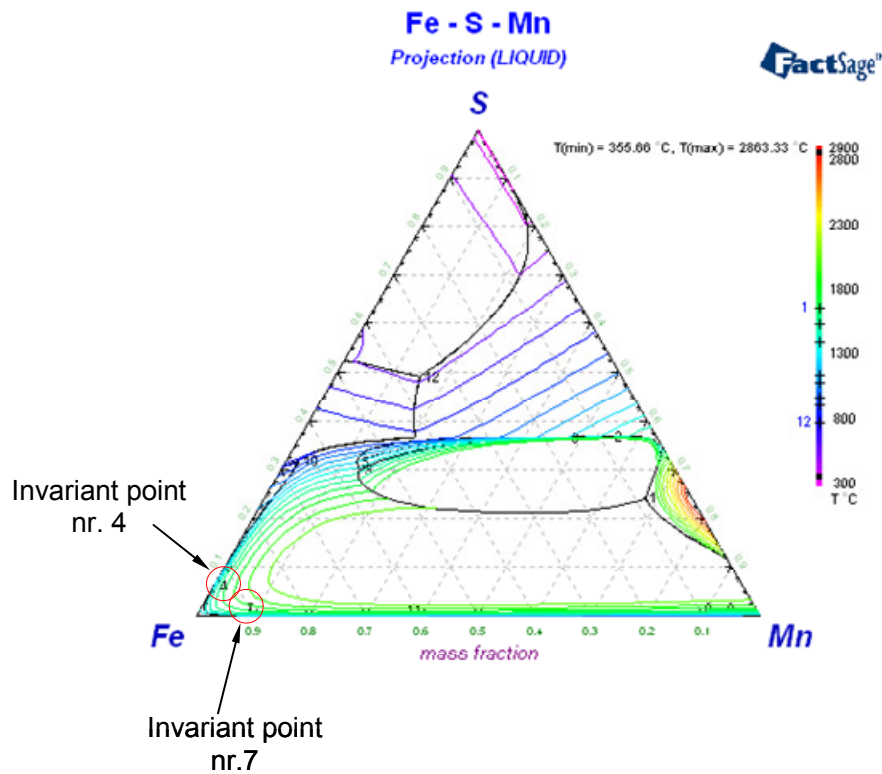


Figure 2.9. Fe-Mn-S ternary diagram (liquidus projection) [19].

Note: Fe-Mn-S ternary diagram is the liquidus projection thus the liquid phase has to be included in the analysis to the phases listed in Table 2.1.

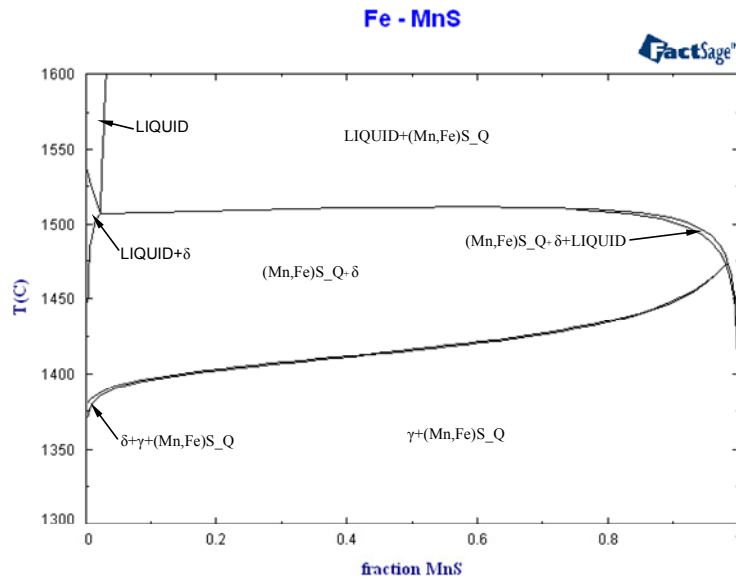


Figure 2.10. Fe-MnS Pseudo-binary diagram.

However, by studying the liquidus surface of the same system, there is also a univariant line from the monotectic reaction on the Fe-MnS pseudo-binary which starts at about 2300°C (this point is not shown in *Figure 2.10* due to scaling of the region of interest), where the MnS-rich liquid decomposes to an iron-rich liquid and MnS. Further at 1506°C there is an eutectic reaction through which the iron-rich liquid solidifies to δ -ferrite + MnS^[20].

Alvarez de Toledo et al.^[21] demonstrated that there is a critical value of the Mn/S ratio, below which a high susceptibility to cracking, is expected during casting or deformation of as-cast material. The value of Mn/S ratio increases as the S content of the steel decreases.

Many investigators have studied the influence of S and Mn/S ratio on the crack susceptibility of continuously cast steel^[2,14,17,21-25]. Some of them come to the conclusion that a low Mn/S ratio gives place to the formation of low-melting interdendritic liquid FeS phases during solidification. These low-melting phases enhance the internal cracking during continuous casting, or intergranular cracking during hot rolling^[21].

Calcium additions to the steel have been proven to be beneficial via a reduction of the total amount of free S in the steel, which in its turn reduces the volume fraction of sulphides precipitated in the interdendritic and austenitic boundaries.

However the paper of reference^[21] and its formulae were developed for *steels without calcium additions*, therefore the effect of Ca in reducing the S content and consequently the reduction of the cracking susceptibility is not included in this study.

2.6.2 The critical Mn/S ratio

As solidification takes place, the residual liquid increases its concentration in Mn and S. When the concentration of these two elements in the residual liquid is higher than the solubility product constant, MnS will begin to precipitate^[21]. Hence the phase composition starts to deviate from the equilibrium phase diagram. If there is some segregation of S and

Mn and the fraction of MnS reach above 0.75 in the interdendritic liquid, then the solidus will lower until 1400°C according to the pseudo binary Fe-MnS phase diagram.

When MnS begins to precipitate, depending on the amount of S consumed in the MnS precipitation, the S concentration of the residual liquid increases or decreases while the Mn concentration does the opposite.

Sulphur is expected to segregate strongly to grain boundaries because there is a difference in misfit strain energy, as compared to that of Mn; also the mobility of sulphur is about a thousand times greater than that of Mn at high temperature^[25]. Moreover, sulphur has a lower surface energy and will always try to form a precipitate on a grain boundary.

The influence of this change of the sulphur concentration profile in the crack susceptibility of the continuously cast steel can be predicted: if the sulphur concentration increases, or if some sulphur remains unreacted with the manganese, some proportion of FeS is expected to form, and the final solidification temperature of the interdendritic liquid will drastically drop, because the FeS has a low melting point. However the composition of the inclusions will further change as explained by Lankford^[25]. If pure FeS precipitates, it will be as liquid; for high cooling rates some Mn will be found in solution in the precipitates and as the cooling rate becomes slower, more Mn will have time to diffuse to the grain boundary and the precipitates will become more enriched with Mn because MnS is the stable phase. However, if the cooling rate becomes slow enough, MnS will nucleate and MnS precipitation will dominate.

The critical Mn/S ratio $(Mn/S)_c$, for which value the S concentration profile changes (increase or decrease of concentration), is calculated with equation (2.9). This formula is deduced based on solidification constants, where only one constant for MnS is not related to the solubility product of MnS in the liquid steel, but to this solubility in the solidified phases. This means that the liquid enrichment in S and Mn seems to be limited by the precipitation of MnS at the solid-liquid interface.

$$(Mn/S)_c = 1.345 * S^{-0.7934} \quad (2.9)$$

Steel grades with high Mn/S ratios, or more specifically higher Mn contents, are not embrittled because the solubility of MnS is less and the conditions of precipitation favour the precipitation of MnS in the matrix.

2.6.3 Mn/S ratio and brittle temp range

It is well known^[2,14,24] that the tendency to form internal cracks during continuous casting is related to the presence of solute-rich interdendritic films of segregated liquid, which is related to the temperature interval ZST—ZDT “brittle temperature range: ΔT_B ”.

For a given Mn/S ratio, an index was defined that would bear in mind the relation between Mn/S ratio and the critical ratio. This index is called MSC (manganese-sulphur-critical):

$$MSC = \frac{(Mn/S)_{steel}}{(Mn/S)_c} = \frac{(Mn/S)_{steel}}{1.345 * S^{-0.7934}} \quad (2.10)$$

When MSC is higher than 1, the best results are obtained: low ΔT_B and high ductility values.

In the range 700° to 1200°C steels (microalloyed steels are very sensitive to this phenomenon) exhibit a ductility minimum, commonly called “ductility trough” [26-28]; however theoretically this is the second through that steels have during cooling, as the first one is when liquid phases are still present, as explained in Section 2.4.

It important to note that the brittle temperature range evaluated in these studies^[21,25] is the second ductility trough, occurring at around 700°C to 1200°C, somewhat lower temperatures than the first ductility trough that is relevant for hot tearing. Therefore, the MSC index is another indication of the effect of MnS in the cracking susceptibility.

2.6.4 Sulphur-rich non-metallic particles

Sulphide inclusions have long been a major concern to steelmakers because inclusion morphology has a strong effect on ductility. Some types of interdendritic sulphides which are associated with the addition of a strong deoxidizer are particularly detrimental.

Some of the inclusions formed in commercial alloys are particles produced during growth of iron dendrites when segregation of manganese and sulphur into the interdendritic spaces reaches a sufficiently high level.

Traditionally, sulphides can be classified as type I, II and III [24,29,30]. Type I particles appear as individual spheroids of a wide size distribution scattered randomly in the interdendritic spaces, individual inclusions sometimes associated with an oxygen-rich second phase. Type II particles appear as a degenerate eutectic network made of irregular cylindrical rods, spread out in the interdendritic spaces, delineating the dendrite arm boundaries. These are usually seen as fan or chain-like distribution of fine inclusions. The classical “beads” and “stringers” are in reality intersections of a eutectic network by the polishing plane. Type III particles appear as idiomorphic crystals or angular inclusions scattered through the whole dendritic structure, but frequently situated in interdendritic spaces. They often project arms which join Type II particles [30].

The form of the sulphides is controlled by the steel composition and in particular by the degree of deoxidation [29]. Flemings^[30] concluded that type I inclusions form by exsolution (process through which an initially homogeneous solid solution separates into at least two different crystalline minerals without the addition or removal of any materials^[31]) of liquid sulphide pools from the melt; type II inclusions form by eutectic solidification of the sulphur-rich final liquid; and type III inclusions form by solidification of sulphide crystals out of the melt.

Interpretation of structures observed suggest that type I and possibly type III inclusions are “pushed” ahead of growing dendrites. Morphology of inclusions is adequately predicted on

the basis of only temperature and mode of solidification; such factors as surface energy differences between different inclusion types are not necessary to be postulated to explain their different morphologies ^[30].

As the major leading factor for the precipitation of type I MnS particles is the presence of oxygen in the molten steel, these non-metallic inclusions are not normally present in the continuously cast steel grades; therefore, type II are the most typical sulphur-rich particles encountered in these grades.

When Mn and S are present in the steel composition, MnS type II particles can form during solidification, it is sufficient to examine the Fe-MnS pseudo-binary system (*Figure 2.10*) to understand their formation. In the solidification of a steel with a fraction of MnS below 0.02, precipitation of iron continues until, just before the eutectic temperature is reached, there is a well-developed iron-dendrite structure mixed with sulphur-rich liquid of near eutectic composition. At the eutectic temperature this liquid solidifies to give type II MnS with its characteristic morphology ^[29].

2.6.5 Titanium nitrides precipitation during solidification

The intention of adding small amounts of carbide and nitride formers such as Nb, V and Ti is to control the austenite grain size (the particles hinder the boundary migration and grain growth) in the solid state. This, in turn, produces fine ferrite grain sizes, and by precipitation in the ferrite at lower temperatures (assisted by water cooling of the material out of the last rolling stand) gives a bonus of extra particle strengthening. These materials, the micro-alloyed or HSLA steels, are available in a variety of compositions ^[5]. Even at lower temperatures, in HSLA steels, precipitation of carbides or nitrides at the austenite or ferrite boundaries can lead to cracking in the second ductility trough ^[5]. By adding an appropriate concentration of these elements, the toughness, plasticity, wear- and corrosion-resistant properties could be remarkably improved ^[32].

Until now, just a handful of studies have focused on the combined effects of Nb, V, Ti and N on the refining of solidification microstructures for casting of steel grades.

Fu et al. ^[32] attributed the structure refinement from V + Ti and rare earths (RE) additions to the segregation of these elements to the solid/liquid interface during solidification, and corresponding growth restriction effect on the iron dendrites. This is also related to the nucleation of iron on carbides and nitrides of V and Ti that have a lattice mismatch less than 6% with iron.

The microsegregation of Ti and N during solidification at the solute enriched interdendritic zones leads to the precipitation of TiN in this interdendritic liquid.

According to Turkdogan^[18], the solubility product of TiN in low alloyed liquid steels is $[\text{wt}\% \text{Ti}] \times [\% \text{N}] = 6.15 \times 10^{-4}$ at 1500°C, which is taken to be the average solidus temperature of low-allowed steels. For a steel containing 0.02%Ti and 60 ppm N, about 55% of the nitrogen is converted to TiN precipitates at 99% local solidification. Upon complete solidification, most of

the remaining N in solution will precipitate as TiN, provided that $\%Ti/\%N \geq 3.42$. The TiN precipitated in the interdendritic liquid, which subsequently becomes the austenite grain boundaries, will be the sites upon which other carbides will precipitate during further cooling^[18].

Scheil and DICTRA calculations with several different Ti, N and Nb compositions, performed by Schneider et al.^[33], show a tendency to form TiN in the liquid, at the liquid region even at equilibrium conditions. Their Scheil calculations indicate TiN formation from the melt already for low Ti (0.003 wt%) but relatively high N (0.005 wt%) contents.

Moreover, the carbides and nitrides of vanadium, titanium and niobium show extensive mutual solubility's which arises from the fact that they have the same cubic crystal structure and have very similar lattice parameters. A combination of V with other microalloyed elements in the same steel can naturally lead to interactions since they compete for the same interstitial elements and may also form mixed compounds with one another. The stable TiN phase may incorporate a significant amount of vanadium. Since the (Ti, V)N particles are rather coarse such an effect reduces to some extent the contribution which the V can be expected to make towards precipitation strengthening^[34].

2.6.6 The combined effect of solutes in grain growth

Solute elements affect the dendrite growth and builds up a constitutionally undercooled zone in front of the interface. This undercooled zone facilitates nucleation and the new grain does the same to the next grain. The shape and magnitude of the constitutionally undercooled zone depend upon the dendrite growth, which is affected by solute elements, which in turn affects the subsequent nucleation behaviour^[35].

There are two reasons that can be proposed to explain why solute elements are essential for grain refinement. First of all, segregating elements act to restrict the growth of already existing solid/liquid interfaces so that there is more time for nucleation events to occur. This would be of importance if nucleation was spontaneous and non-directional. But probably of greater importance is that the segregating elements lead to a constitutionally undercooled zone in front of the interface. This constitutionally undercooled zone activates the nucleating particles in front of the interface, hence, interrupting the growth of the previous grain^[35].

The peritectic reaction does not usually take place at the peritectic temperature, as an undercooling is required to drive it. Therefore, it is equally probable that the secondary phase can crystallise directly from the melt before the reaction occurs^[35,36].

In literature^[35,37-41], there are two parameters that have been used to quantify the effect of solute elements on the grain size of a casting:

- The growth restriction factor, also known as GRF:

$$Q = m_l c_o (k - 1) \quad (2.11)$$

- The supercooling parameter:

$$P = \frac{m_l c_o (k - 1)}{k} \quad (2.12)$$

Where: m_l is the gradient of the liquidus slope, c_o is the concentration of the solute element in a binary alloy and k is the partition coefficient (see schematic representation in Figure 2.11).

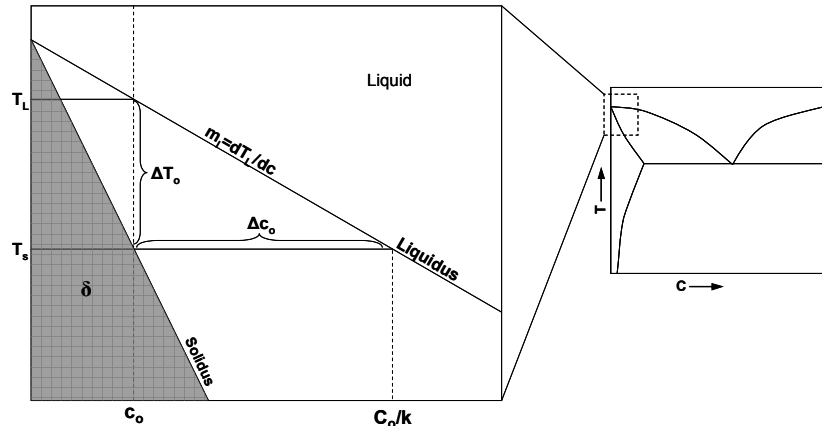


Figure 2.11. Schematic representation of a binary phase diagram^[1]

An assumption of the mechanism of grain refinement proposed by Easton and StJohn^[35,42] is that constitutional undercooling of ΔT_n is required for nucleation events to occur. ΔT_n is defined as the critical undercooling necessary for a nucleation event to occur on the most potent nucleant particles. Therefore, an increase in the rate of development of a constitutionally undercooled zone decreases the time and amount of growth required for a nucleation event to occur ahead of the interface and thus a smaller grain size is obtained. The effects of the development of a constitutionally undercooled zone on nucleation can be calculated, as long as a number of assumptions is made^[39,40]:

- The model assumes that the negative thermal gradient at the grain-liquid interface due to unconstrained growth is negligible in comparison to the amount of constitutional undercooling (Figure 2.12)
- There are sufficient substrates present and nucleation occurs as soon as the constitutional undercooling required for nucleation ΔT_n is achieved.

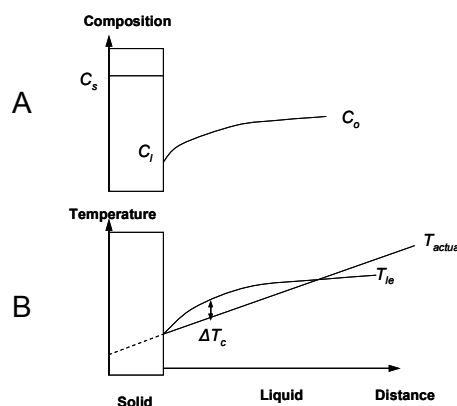


Figure 2.12. Constitutional undercooling^[40]

A: a hypothetical solute concentration profile in front of a grain in a peritectic system.
 B: The corresponding temperature profile showing the constitutionally undercooled zone ΔT_c , which is the difference between the actual temperature in the melt, T_{actual} , and the equilibrium liquidus temperature, T_{le} , for each increment of solute content in front of the interface^[40]

For the constitutional undercooling produced during the growth of a grain, the equilibrium liquidus temperature, T_{le} , and the actual temperature, T_{actual} , can be calculated using:

$$T_{le} = T_o + m_l c_o \quad \text{and} \quad T_{actual} = T_o + m_s c_s$$

Where T_o is the melting point of the pure metal, and m_s is the gradient of the solidus line^[39,40].

Assuming that the thermal gradient is zero and there is no thermal undercooling, the maximum constitutional undercooling, ΔT_c , can be calculated as follows:

$$\Delta T_c = T_{le} - T_{actual} = T_o + m_l c_o - (T_o + m_s c_s) = m_l c_o - \frac{m_l c_s}{k} = m_l (c_o - c_l) \quad (2.13)$$

If the growth of a single crystal is considered, then the amount of constitutional undercooling developed as solidification proceeds can be related to the fraction of solid f_s , by substituting the Scheil equation (i.e. assuming no diffusion of the solute in the solid phase and instantaneous diffusion of solute in the liquid phase):

$$c_l = \frac{c_o}{(1 - f_s)^p} \quad \text{where } p=1-k \quad (2.14)$$

to obtain:

$$\Delta T_c = m_l c_o \left(1 - \frac{1}{(1 - f_s)^p} \right) \quad (2.15)$$

By using this model a physical basis can be given to both the supercooling parameter P, and the growth restriction factor Q.

If the lever rule (assuming equilibrium solidification) analysis is used and the composition of the liquid:

$$c_l = \frac{c_o}{1 - (1 - k)f_s} \quad (2.16)$$

is substituted in equation (2.12), then:

$$\Delta T_c = m_l c_o \left(1 - \frac{1}{1 - (1 - k)f_s} \right) \quad (2.17)$$

When $f_s=1$:

$$\Delta T_c = \frac{m_l c_o (k - 1)}{k} = P \quad (2.18)$$

which is the supercooling parameter, P ^[39,40].

Another important parameter for comparing the effect of solute on the grain size achieved is the initial rate of development of the constitutional undercooled zone as this determines how quickly the undercooling necessary for nucleation is achieved.

When the initial rate of development of constitutional undercooling is with a $f_s=0$, is the growth restriction factor Q :

$$\frac{d\Delta T_c}{df_s} = m_i c_o (k - 1) = Q \quad (2.19)$$

Therefore the supercooling parameter is simply a measure of the solidification range, assuming no other reactions take place. In contrast, the growth restriction factor Q , is a calculation of the rate of development of the constitutional zone with respect to the fraction of solid, i.e. the beginning of growth. In other words, it is a measure of how rapidly the constitutional undercooled zone is formed at the earliest stages of growth^[39,40].

2.7 The pursuit for understanding of hot tearing during continuous casting

Hot tearing in aluminium alloys has been widely studied in the last decades, but in steels is a difficult research topic, particularly due to the high temperatures involved in solidification of commercial steel grades; therefore little information is available on the literature.

In addition, the continuous casting process adds a degree of complexity in the analysis.

The idea that the MnS plays a role in cracking of commercial steels is not new, but up to now this has not been linked with the presence of liquid phases and the effect in hot tearing, which is one of the main targets in this thesis.

Relatively small amounts of alloying elements can have a big effect in the microstructure and the consequences will be seen in the hot tearing susceptibility. Such a chain of effects is complex and is another challenge to fulfil in this thesis.

Therefore the study of a commercial steel grade by only analysing the phase diagrams is not sufficient enough to understand the hot tearing susceptibility during solidification.

It is the ambition of this thesis to set up an understanding of the most relevant subjects to link in a study for cracking susceptibility during solidification under continuous casting conditions.

References

1. Fisher, K. and Kurz, W., *Fundamentals of solidification*, 4th Edition, Ueticon-Zuerich, Switzerland, 1998, Trans Tech Publications.
2. Pierer, R., Bernhard, C., and Chimani, C., *A contribution to hot tearing in the continuous casting process*, La Revue de Metallurgie, 2 , 2007, 72-83.
3. Irving, W. R., *Continuous Casting of Steel*, 1st Edition, The Institute of Materials, London, UK, 1993, The University Press, Cambridge.
4. Thomas B.G., *Continuous Casting Consortium*, Urbana-Champaign, USA, 2006, University of Illinois, www.ccc.illinois.edu.
5. *The Making, Shaping and Treating of Steel*, 11th Edition, Casting, Pittsburg, Pa, USA, 2003, The AISE steel foundation.
6. Stahlinstitut Verein Deutscher Eisenhütten Leute, www.stahl-online.de.
7. Cornelissen, M. C. M., Kromhout J.A., Kamperman A.A., Kik, M., and Mensonides, F., *High Productivity and Technological Developments at the Corus DSP Thin Slab Caster*, European Continuous Casting Conference, Association Technique de la Siderurgie Francaise ATS, Nice, France, 2005
8. Flemings, M. C., *Solidification processing*, McGraw-Hill series in materials science and engineering, USA, 1974, McGraw-Hill.
9. Hansson K., *On the hot crack formationh during solidification of iron-base alloys*, PhD, Royal Institute of Technology, Stockholm, Sweden, 2001.
10. Eskin, D., Suyitno, and Katgerman, L., *Mechanical properties in the semi-solid state and hot tearing of aluminium alloys*, Progress in Materials Science, 49 , 2004, 629-711.
11. Dantzig J.A. and Rappaz, M., *Solidification*, 1st Edition, EPFL Press, Laussane, Switzerland, 2009, CRC Press.
12. Won, Y. M., Yeo, T. J., Seol, D. J., and Oh, K. H., *A new criterion for internal crack formation in continuously cast steels*, Metallurgical and Materials Transactions B, 31 (4), 2000, 779-794.
13. Eskin, D. and Katgerman, L., *A quest for a new hot tearing criterion*, Metallurgical and Materials Transactions A, 38A (7), 2007, 1511-1519.
14. Chojecki, A., Telejko, I., and Bogacz, T., *Influence of chemical composition on the hot tearing formation of cast steel*, Theoretical and Applied Fracture Mechanics, 27 , 1997, 99-105.

15. Rappaz, M., Drezet, J. M., and Gremaud, M., *A new hot-tearing criterion*, Metallurgical and Materials Transactions A, 30 (2), 1999, 449-455.
16. Suyitno, Kool, W. H., and Katgerman, L., *Hot tearing criteria evaluation for direct-chill casting of an Al-4,5 Pct Cu alloy*, Metallurgical and Materials Transactions A, 36A (6), 2005, 1537-1546.
17. Nakagawa, T., Umeda, T., Murata, J., Kamimura, Y., and Niwa, N., *Deformation Behavior during Solidification of Steels*, ISIJ International, 35 (6), 1995, 723-729.
18. Turkdogan, E. T., *Causes and effects of nitride and carbonitride precipitation during continuous casting*, Iron Steelmaker, 16 (5), 1989, 61-
19. FactSage, 6.2, www.factsage.com.
20. Raghavan, V., *Phase Diagrams of Ternary Iron Alloys. Part 2. Ternary Systems Containing Iron and Sulphur*, Delhi, India, 1988, Indian Institute of Metals.
21. Alvarez de Toledo, G., Campo O., and Lainez, E., *Influence of Sulfur and Mn/S ratio on the hot ductility of steels during continuous casting*, Steel Research, 64 (6), 1993, 292-299.
22. *ASM Handbook*, 8th Edition, 12: Fractography, Materials Park, OH, USA, 1987, ASM International.
23. *ASM Handbook*, 8th Edition, 09: Metallography and Microstructures, George van der Voort Editor, Materials Park, OH, USA, 2004, ASM International.
24. Flemings, M. C. and Bigelow, L., *Sulfide Inclusions in Steel*, Metallurgical and Materials Transactions B, 6 (2), 1975, 275-283.
25. Lankford, W. T., *Some considerations of strength and ductility in the continuous-casting process*, Metallurgical and Materials Transactions B, 3 (6), 1972, 1331-1357.
26. Mintz, B. and Abushosha, R., *Influence of vanadium on hot ductility of steel*, Ironmaking and Steelmaking(UK), 20 (6), 1993, 445-452.
27. Cho, Kyung Chul, Mun, Dong Jun, Koo, Yang Mo, and Lee, Jae Sang, *Effect of niobium and titanium addition on the hot ductility of boron containing steel*, Materials Science and Engineering: A, 528 (11), 25-4-2011, 3556-3561.
28. Turkdogan, E. T., *Causes and effects of nitride and carbonitride precipitation during continuous casting*, Iron Steelmaker, 16 (5), 1989, 61-
29. Baker, T. J. and Charles, J. A., *Morphology of Manganese Sulphide in Steel*, Journal of The Iron and Steel Institute, 210 , 1972, 702-706.
30. Flemings, M. C. and Kattamis, T. Z., *Investigation of Solidification of High-Strength Steel Castings*, Report Nr. AMMRC CR 63-04/F, Department of Metallurgy and Materials Science, Massachusetts, USA, 1968, Massachusetts Institute of Technology.
31. Encyclopaedia Britannica Online, 2012.

32. Fu, H., Qu, Y., and Xing, J., *Investigations of Solidification Structures of High Carbon Alloy Cast Steel Containing RE-V-Ti*, Journal of Materials Engineering and Performance, 18 (4), 2009, 333-338.
33. Schneider, A., Stallybrass, C., Konrad, J., Kulgemeyer, A., Meuser, H., and Meimeth, S., *Formation of Primary TiN Precipitates during Solidification of Microalloyed Steels - Scheil versus DICTRA simulations*, International Journal of Materials Research, 99 (6), 2008, 674-679.
34. Lagneborg, R., Siwecki, T., Zajac, S., and Hutchinson, B., *The role of Vanadium in microalloyed steels*, The Scandinavian Journal of Metallurgy(5), 1999, 186-241.
35. Easton, M. and Stjohn, D., *Grain refinement of aluminum alloys: Part I. The nucleant and solute paradigms—A review of the literature*, Metallurgical and Materials Transactions A, 30 (6), 1999, 1613-1623.
36. Stefanescu, D. M., *Microstructure evolution during the solidification of steel*, ISIJ International, 46 (6), 2006, 786-794.
37. Easton, M. and Stjohn, D., *An analysis of the relationship between grain size, solute content, and the potency and number density of nucleant particles*, Metallurgical and Materials Transactions A, 36 (7), 2005, 1911-1920.
38. Easton, M., Davidson, C., and Stjohn, D., *Effect of alloy composition on the dendrite arm spacing of multicomponent aluminum alloys*, Metallurgical and Materials Transactions A, 41 (6), 2010, 1528-1538.
39. Easton, M. A. and StJohn, D. H., *The effect of alloy content on the grain refinement of aluminium alloys*, Light Metals 2001, 2001, 927-934.
40. Easton, M. A. and StJohn, D. H., *A model of grain refinement incorporating alloy constitution and potency of heterogeneous nucleant particles*, Acta Materialia, 49 (10), 2001, 1867-1878.
41. Easton, M. A. and StJohn, D. H., *Improved prediction of the grain size of aluminum alloys that includes the effect of cooling rate*, Materials Science and Engineering: A, 486 (1-2), 2008, 8-13.
42. Easton, M. and StJohn, D., *Grain refinement of aluminum alloys: Part II. Confirmation of, and a mechanism for, the solute paradigm*, Metallurgical and Materials Transactions A, 30 (6), 1999, 1625-1633.

Chapter 3

Analysis of solidification path and phase diagrams of commercial steel grades

Low carbon steel is not expected to be sensitive to hot tearing and/or cracking, but in the Direct Sheet Plant (DSP) thin-slab caster in IJmuiden (The Netherlands) a low carbon aluminium killed (LCAK) steel grade has a high risk of breakouts due to cracking. On the other hand, a high strength low alloyed (HSLA) steel grade, a micro-alloyed steel grade with extra additions of vanadium, nitrogen and niobium, has a very low breakout occurrence due to cracking in the DSP caster; however, a similar steel grade, a low-range HSLA (LR-HSLA) with the same amount of niobium but a smaller amount of vanadium and nitrogen, is also very sensitive to breakouts due to hot tearing.

3.1 Problem background and statistical analysis

A breakout occurs when the solidified shell is not strong enough to resist the pressure of the molten steel. The shell bursts open and molten steel pours into the casting machine. This type of event severely limits the productivity, causes health hazard and may result in equipment damage.

The extensive damage to the machine results in loss of production. In total the financial benefit of eliminating breakouts can be estimated as above 1.5 M€ per year.

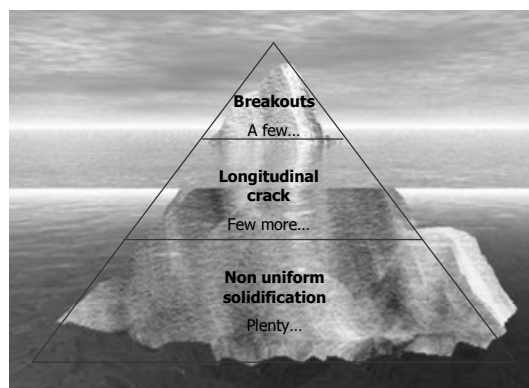


Figure 3.1. The "Iceberg" of breakouts...

A breakout is the tip of the iceberg (see *Figure 3.1*), underlying factors are less severe defects and process instabilities. At the bottom we have the root cause which is unstable solidification and process instabilities. Some of these instabilities will result in cracks and if severe enough can lead to a breakout (see examples in *Figure 3.2*).

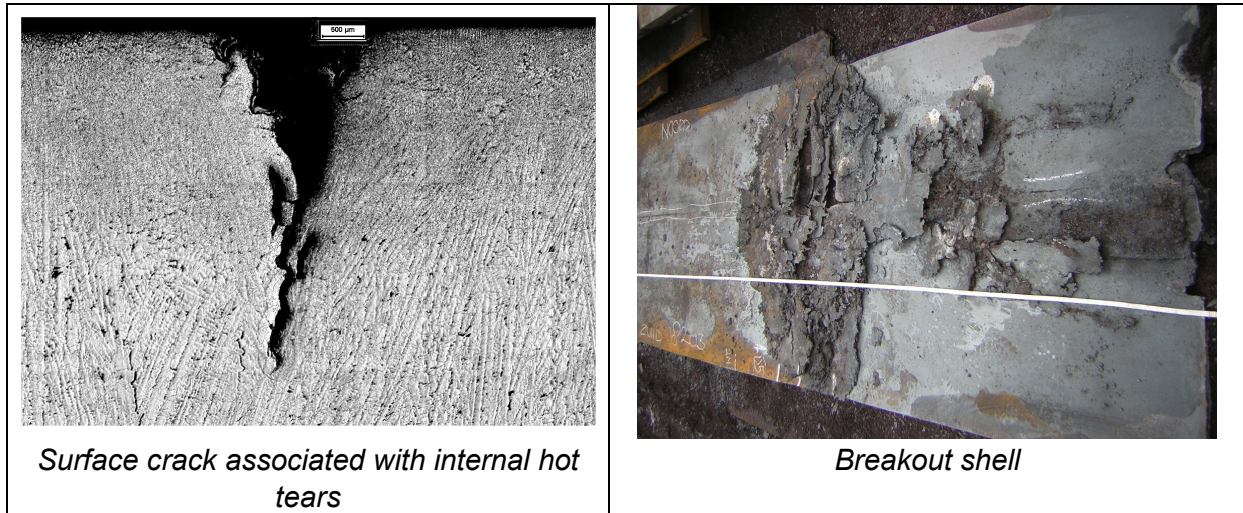


Figure 3.2. Examples of a cross-section of a longitudinal crack and a breakout shell.

Of course what is visible is always the tip of the iceberg, but when analysing a surface crack it is possible to see that it is associated with many more internal cracks and most of them are identified under microscopic analysis as hot tears as they propagate interdendritically (see *Figure 3.3*).

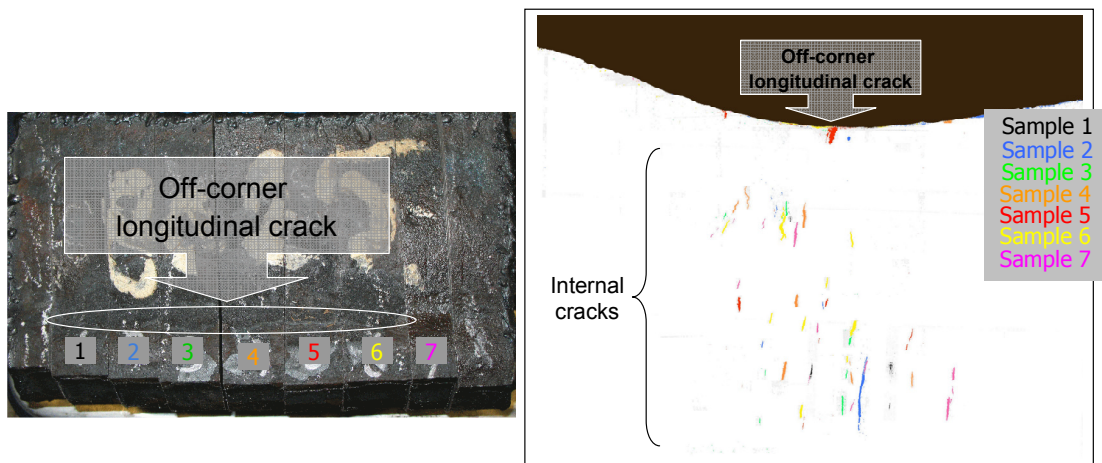


Figure 3.3. An off-corner crack and the associated internal cracks

Therefore, the purpose of this study is to investigate the differences between the three steel grades with respect to hot tearing sensitivity.

From the statistical analysis of the breakout occurrence related to cracking, in the years 2007 to 2011, the possibility of a breakout for the LR-HSLA is higher than that for the LCAK; and for the HSLA is smaller than that for the LCAK.

The only relevant parameter that differs between these two HSLA-type grades is the chemical composition, the rest of the casting parameters (casting speed, secondary cooling, mould powder, etc.) are equal for both grades, when cast in the DSP caster.

A binomial distribution has been used to calculate the expected values of a certain amount of breakouts per year (*Figure 3.4*).

If the HSLA grade would be cast at the same amount of heats and would have the same chance of a breakout as the LCAK, then how many breakouts should have per period of time? To answer, both grades have to be compared under the same conditions, thus giving the same chance of a breakout to an HSLA than to an LCAK.

Hence, the data used for this analysis consisted of the amount of heats cast per steel grade and the number of breakouts that occurred in these grades in the same period of time.

For the statistical analysis it is necessary to calculate:

- The probability that a breakout will occur. This possibility can be equal to the postulated as the fraction of breakouts in a bigger amount of heats, which is the normal expectation value for a large data set. In other words, it is the “true fraction” where the population is infinite. It is here designated as p in eq. (3.1).
- The chance that in a small group of heats a determined amount of breakouts will appear. It is the expectation value for a specific grade, in other words, a small number from the population, called a sample. This probability is designated here with P in eq. (3.1).

The relation between the two probabilities is ^[1]:

$$P(k, n, p) = \frac{n!}{k!(n-k)!} p^k (1-p)^{n-k} \quad (3.1)$$

where:

k : number of breakouts per steel grade

n : amount of heats per steel grade.

For the chance of a breakout “ p ”, within each period the fraction of breakouts for the LCAK is used.

This relation means the actual probability or true fraction of finding the chance that “ k ” amount of breakouts occur in an “ n ” number of heats.

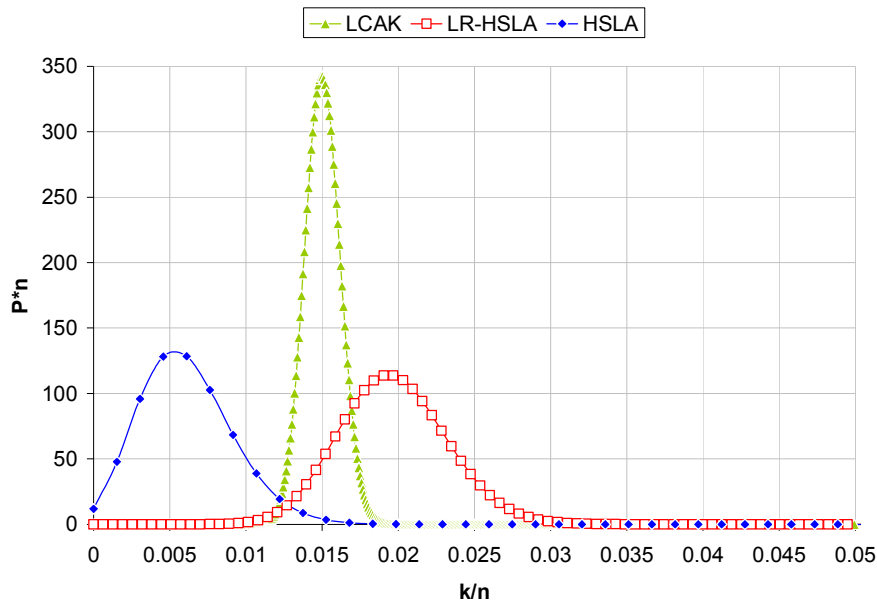


Figure 3.4. Binomial distribution of the breakouts probability in the years 2007 to 2011.

In the statistical analysis (see Table 3.1), the confidence interval means that 95% chance that the 'true' fraction is between lower and upper values, where the observed fraction is the calculated value from the actual data^[1].

The continuity-adjusted chi-square approximation, also called “2 x 2 tables” explains that if the fraction is the same, what will be the probability to get the actual value (or worse).

Table 3.1. Statistical results.

Grade	n	Observed fraction	Confidence interval	
			Lower	Upper
LCAK	10913	0.0150	0.0128	0.0175
LR-HSLA	1576	0.0197	0.0134	0.0278
HSLA	655	0.0061	0.0017	0.0156

	Continuity Adj. Chi-Square	Probability	Fisher's Exact Test Probability
LR-HSLA vs. HSLA	4.6688	0.0307	0.0229
LCAK vs. HSLA	2.8410	0.0919	0.0637
LCAK vs. LR-HSLA	1.6406	0.2002	0.1587

More information can be extracted from the probability calculated with the Fisher's Exact Test, where for this particular case, it can be concluded that:

- When the LR-HSLA is compared with the HSLA, the probability of exceedance (of finding these numbers) is less than 5%, thus it is generally considered statistically 'significant' and means that a true difference exists- so the grades behave different.

- For the comparison of the LCAK vs. HSLA, the probability is between 5% and 10%, which is generally considered 'weak' evidence.
- For the LCAK in comparison with the LR-HSLA, the probability is higher than 10%, which means that there is no evidence of difference, so these grades could well behave as the same.

From this statistical analysis, it can be concluded that even when the LR-HSLA and the HSLA grades are very similar in chemical composition, there is a difference that makes them to behave different in their cracking susceptibility. In contrast, the LCAK and the LR-HSLA could have the same performance in their cracking susceptibility.

3.2 Phase composition and solidification path analysis – Phase diagram assessment

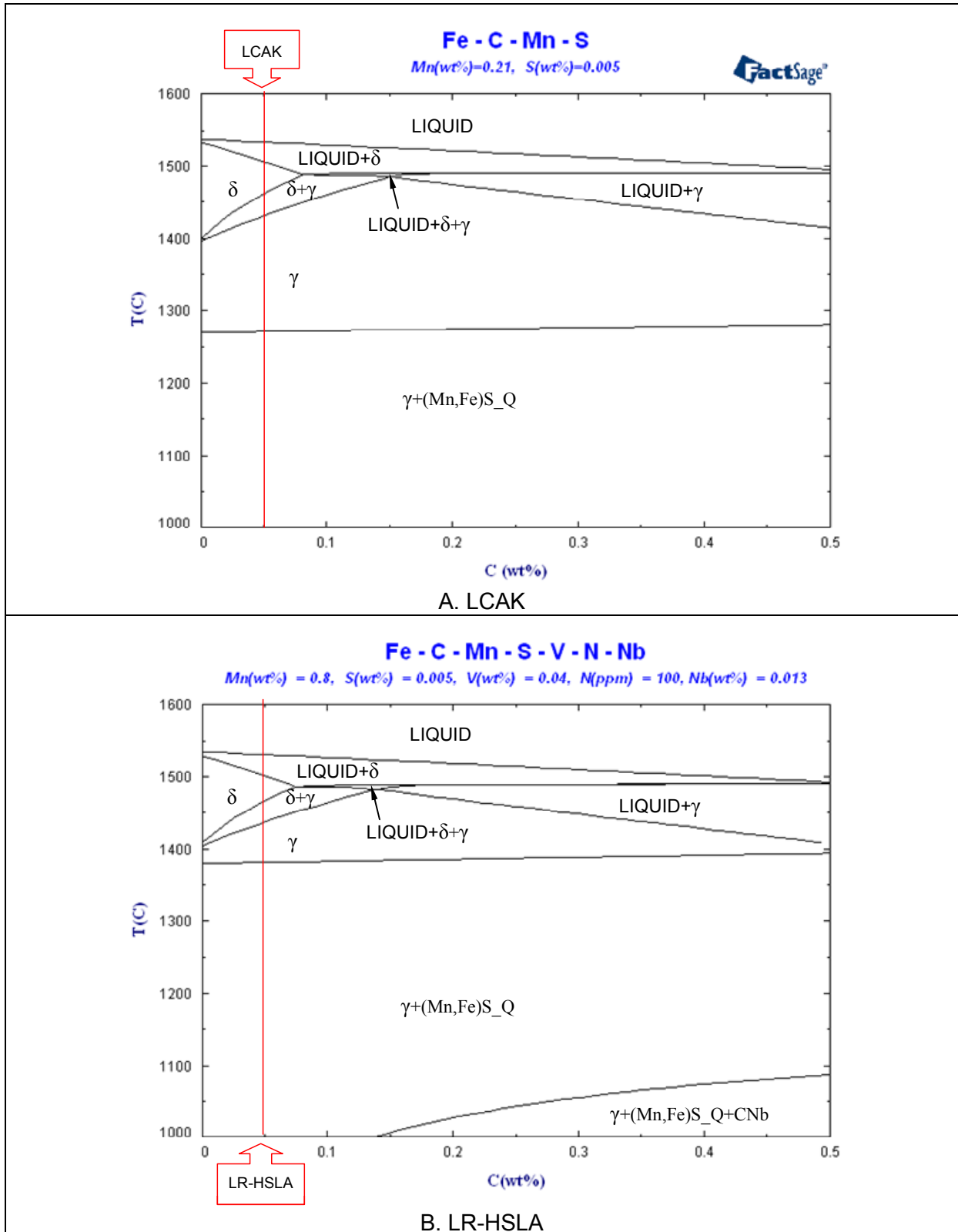
3.2.1 Equilibrium phase diagrams

One of the most powerful tools for studying the development of microstructure is the equilibrium phase diagram. A phase diagram embodies information derived from thermodynamic principles, specialised for a particular range of compositions and presented in a form that makes the data readily accessible. The equilibrium phase diagram shows the phases present in equilibrium and their relative quantities, as well as the composition of the phases over a range of temperatures. It should be noted that thermodynamics tells us what should happen in equilibrium but it does not guarantee that that is what will happen, as the real system may be constrained by kinetic processes ^[2].

The pseudo-binary phase diagrams of the steel grades considered in this study have been calculated with the FactSage software package and are shown in *Figure 3.5*.

From the assessment of these equilibrium phase diagrams it is not possible to gather the remarkable differences in hot tearing behaviour that these steels have, because these diagrams only show small differences in their solidification path but nothing that could lead to understanding of the cracking susceptibility.

However, the temperature at which the MnS will be expected to form is much higher for both HSLA grades than for the LCAK. As expected, the HSLA grade has at the right-side of the diagram, far from the compositional range given here, the carbo-nitrides phase formation.



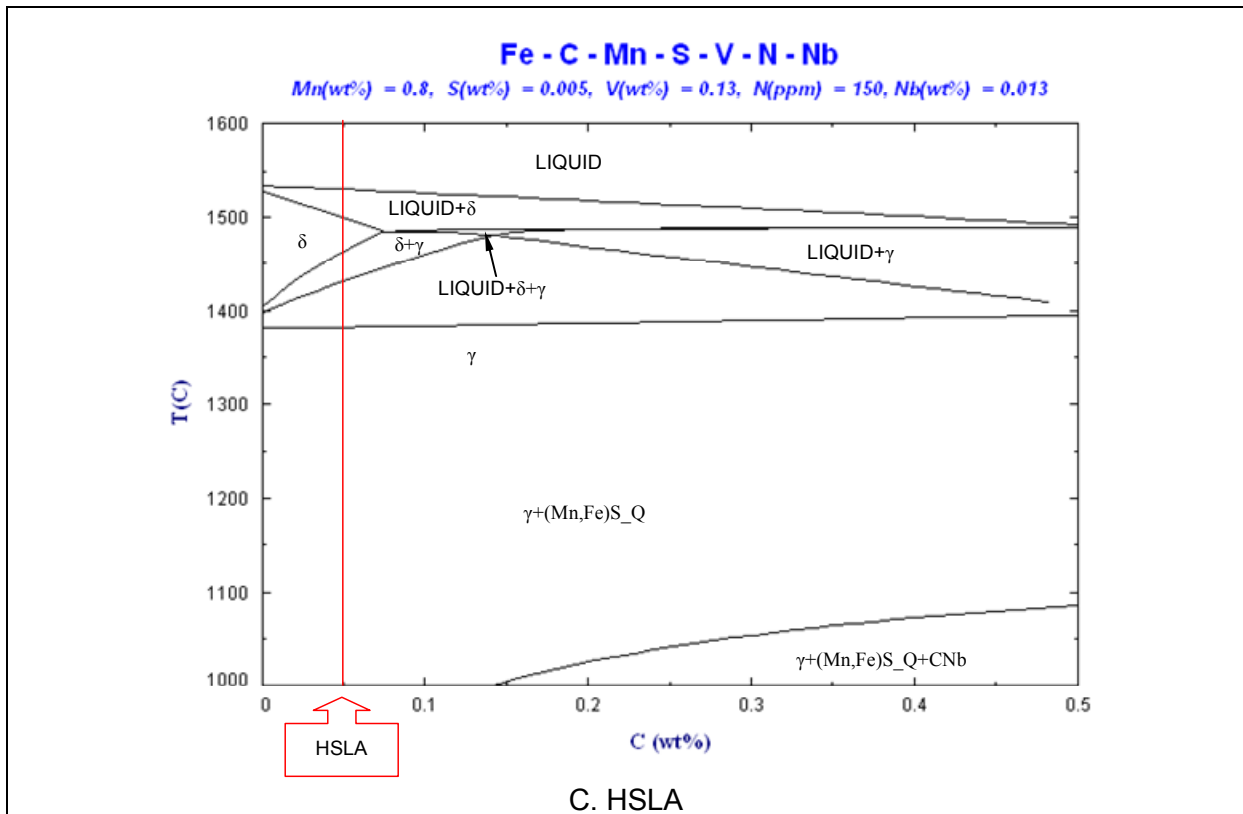


Figure 3.5. Equilibrium phase diagrams as calculated with FactSage.

3.2.2 Non-equilibrium Scheil calculations

In metallurgy, the Scheil-Gulliver equation (or Scheil equation) is often used to describe solute redistribution during solidification of an alloy. This approach approximates non-equilibrium solidification by assuming a local equilibrium of the advancing solidification front at the solid-liquid interface. This allows the use of equilibrium phase diagrams in solidification analysis.

Unlike equilibrium solidification, solute is treated as it does not diffuse back into the solid and is rejected completely into the liquid. Complete mixing of solute in the liquid is also assumed as a result of diffusion (that in reality can be assisted by convection or stirring)^[2].

For the formation of the solid phase, solution of the multi-component Scheil equation requires finding the composition of the liquid phase, $C_L^i(T)$, and fraction solid, $f_S(T)$. The Scheil solidification path is usually approximated by stepping through the temperature interval of interest and assuming local equilibrium to exist at the liquid/solid interface for each temperature step. In the first step, the liquidus temperature of the initial alloy composition is determined and in subsequent small temperature steps, the fraction solid is obtained from a lever rule calculation using the liquidus composition from the previous step. The actual increment of fraction solid is the product of that obtained from the lever calculation with the fraction liquid remaining.

Similarly, for two phase solidification, increments of solid fraction of the two phases are found from the three phase equilibrium condition. The calculation of the enthalpy versus

temperature during Scheil solidification requires that the variations in the compositions within the accumulated solid phases have to be considered.

Ideally the calculated compositions and increments of solid phase fraction are stored for each temperature step and the enthalpy is then calculated for the current temperature from the summation of the enthalpies of all solidified "layers" and the remaining liquid phase. This procedure is very time consuming. This problem can be avoided by averaging the composition for each individual solid at each temperature step. The enthalpy is then calculated using the average composition and the total fraction solid of each phase.

Since no diffusion is allowed in the solid phases, stepping is usually stopped after a eutectic equilibrium has been encountered or a predetermined fraction of solid phases has formed. However, calculation of the enthalpy may be continued if the results are needed for other calculations such as process simulations^[3].

The three steel grades considered in this thesis (see Table 1.1 in Chapter 1) have considerably low amount of sulphur in their composition (a maximum of 0.005 wt%), thus it is expected that the formation of MnS can be triggered only by strong segregation.

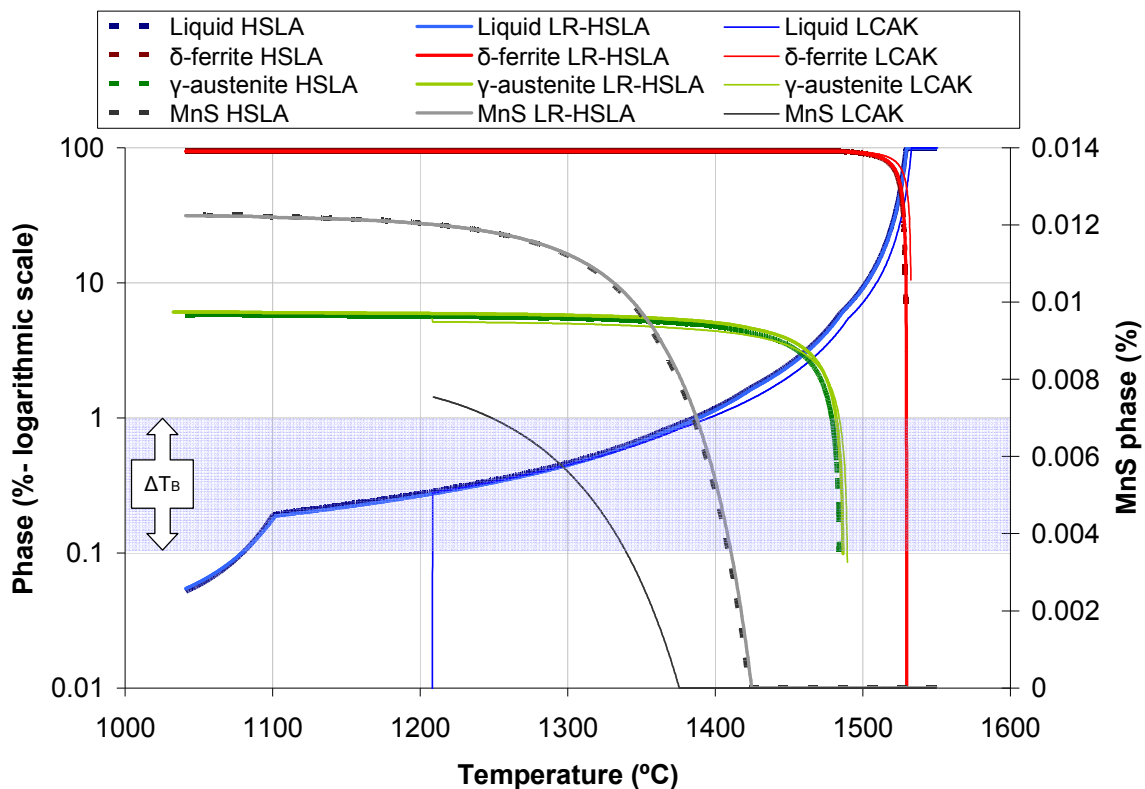


Figure 3.6. Phase fraction during solidification calculated with MTData and MnS percentage as function of temperature. ΔT_B is the brittle ductility range as theoretically expected for a fraction of solid (f_s) between 0.9 and 0.99.

Scheil calculations carried out with MTData until 0.01 f_L show that there are considerable amounts of liquid still present, about 2% for the HSLA's and 0.8% for the LCAK, when MnS starts to form, see Figure 3.6 and Table 3.2.

Table 3.2. Liquid phase present at start of MnS formation

Steel Grade	Temperature °C	Liquid %	[Mn] (wt%)	[S] (wt%)
LCAK	1375	0.820	0.007	0.004
LR-HSLA	1424	1.616	0.039	0.004
HSLA	1423	1.643	0.040	0.004

From these Scheil calculations it is possible to see that there are still considerable amounts of sulphur and manganese present dissolved in the liquid, particularly in the HSLA's when MnS starts to be formed (see *Table 3.2*). [Mn] wt% and [S] wt% in *Table 3.2* are the compositions of these two elements in the liquid at the starting temperature of the MnS formation.

As long as the partition ratio in the Scheil equation remains constant, some liquid will remain until an invariant temperature (e.g. eutectic) is reached and the remainder of the liquid then solidifies at the eutectic composition. Therefore the presence of liquid at lower temperatures (below 1300°C) is not realistic and is an artefact of the calculations. A common approach is to terminate the calculations when the fraction of solid f_s reaches the value 0.99, but in the steel compositions considered here this value is not reached even at 1100°C probably due to the presence of highly segregating elements like sulphur and phosphorus.

3.2.3 Thermal analysis for equilibrium phase diagram validation

A simple binary or ternary system could be evaluated with equilibrium phase diagrams and Scheil calculations with sufficient confidence that the thermodynamic systems and the databases available are adequate enough to describe the solidification of these systems. It is much easier and less time consuming to perform these thermodynamic calculations with any of the available software rather than trying to experimentally identify the phase transformations during solidification, but one has to be sure that the temperatures calculated are close to the real system. Moreover, when dealing with complex systems like commercial grades of steel, as is the objective of this thesis, where complex phases may be formed during solidification through various reactions, it is necessary to perform validation for these calculations.

A simple way to identify the phase transformations during solidification is the thermal analysis technique, developed originally for aluminium alloys^[4,5], that can easily be adopted to other systems^[6]. Particularly, the thermal analysis applied here uses two thermocouples^[4], located at the centre (T_c) and inner wall (T_w) of the crucible, respectively.

The experimental setup used for thermal analysis is shown in *Figure 3.7*. Two thermocouples are immersed from the top of the crucible that is insulated from the bottom. One thermocouple is placed at the centre of the crucible and the other in the inner wall, at exactly the same depth in the melt^[4]. Shielded thermocouples Pt–Pt30%Rh were used for the

experiments to register the temperature during solidification. The only alloy tested with this technique has been the LCAK steel grade.

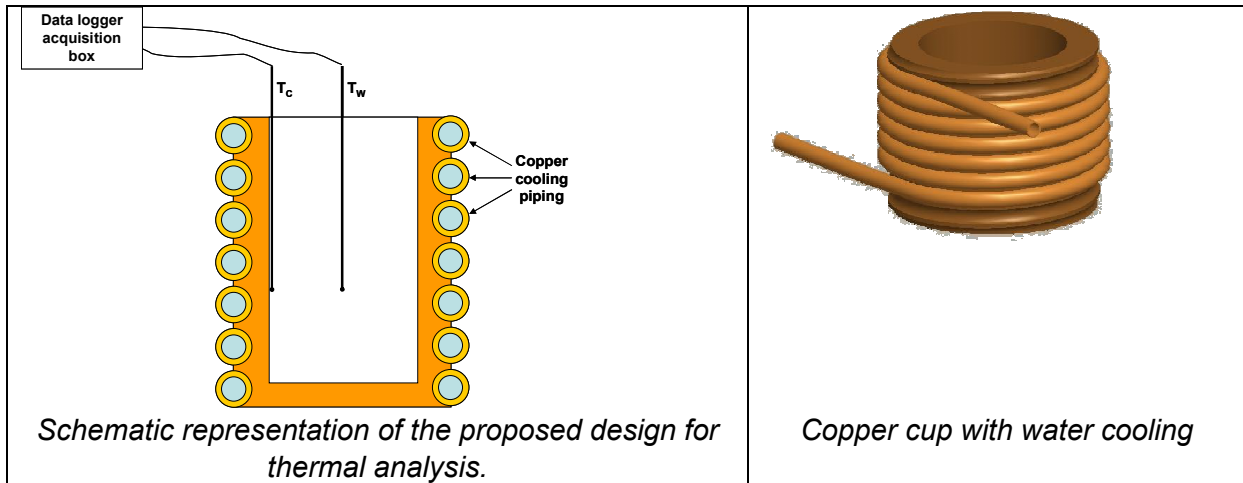


Figure 3.7. experimental setup for two-thermocouple thermal analysis

During the initial stage of solidification in a simple alloy system, a dendritic network develops from the mould wall at an almost constant dendrite tip temperature due to the release of latent heat that compensates the heat extraction through cooling. A constant temperature is recorded in the centre of the sample and during this period of time, the derivative of this “central” temperature is therefore zero. Meanwhile a temperature gradient develops in the sample, causing an increasing temperature difference (ΔT) between wall and centre. After the dendrites have penetrated through the entire sample volume, the central temperature falls and the temperature difference due to heat conduction through the dendrites trunks tends to equalize the temperature difference between wall and centre ^[4].

More detailed information on the solidification process may be obtained if the first derivative of the cooling curve is used in the data analysis. The derivative at each point of the curve is numerically equal to the slope of the cooling curve and therefore represents the rate of cooling in the solidifying sample. An increase of the derivative indicates that something has happened to slow down the rate of cooling, such as the appearance of a new phase that liberates extra latent heat.

Secondary reactions which release only small amounts of latent heat and which take place over a narrow temperature interval are only revealed by relatively small peaks on the derivative curve ^[4]. The first and second derivatives of the cooling curve with characteristic peaks and troughs can be associated with liquidus and solidus points, as well as phase transformations and dendrite coherency point. During early stages of solidification, dendrite crystals are separated and surrounded by liquid melt. However, as the melt cools, the dendrite tips of the growing crystals begin to touch one another until a coherent dendritic network is formed. This state is defined as dendrite coherency point (DCP). The DCP is a physical phenomenon; however, its direct detection in opaque metals is virtually impossible. Therefore indirect detection methods have been developed ^[5].

In the two-thermocouple technique here used, the DCP is determined by identifying the minimum point in the temperature difference curve ^[4,5], where the temperature difference is defined as:

$$\Delta T = T_w - T_c \quad (3.2)$$

where T_w is the temperature recorded by the thermocouple located close to the inner wall of the crucible and T_c is the temperature recorded by the thermocouple located at the centre of the crucible. The assumption that the DCP occurs at the minimum of the temperature difference curve is based on the change of the heat transfer path: from that through liquid to one through the solid phase.

The cooling rate is given by the difference between the liquidus and solidus temperatures, T_L and T_S respectively, divided by the time elapsed in the solid-liquid region t ^[7].

The DCP is determined by measuring the maximum point of the temperature difference between the two thermocouples.

An alternative way to detect the DCP uses only one thermocouple. All characteristic points on the cooling curve, including the dendrite coherency point, can be detected with the same accuracy with only one thermocouple. The minimum points in the ΔT curve and in the first derivative curve will correspond to the DCP.

For the thermal analysis considered here, the calculated average cooling rates based on the temperatures measured during testing, are shown in *Table 3.3*.

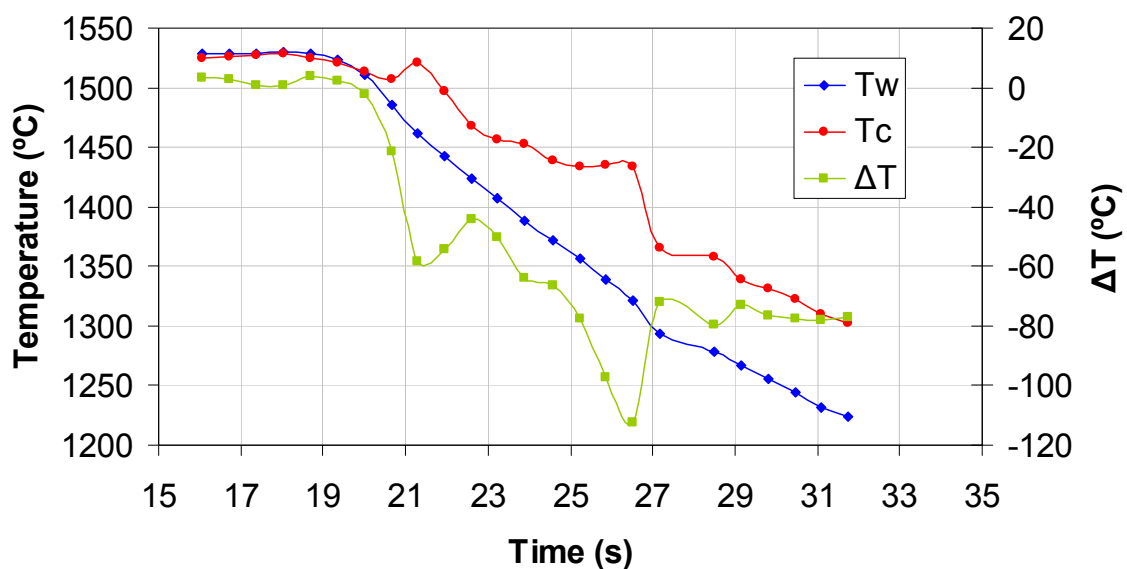


Figure 3.8. Thermocouple readings down to 1200 °C and ΔT .

Figure 3.8 shows the curves registered for the two thermocouples. Red and blue lines correspond to the thermocouples located in the centre of the crucible and close to the inner

wall, respectively. In green, the temperature difference between wall and centre thermocouples is shown.

Table 3.3. Calculated average cooling rates.

	T_C	T_W
$T_L - T_S$ (°C)	21	86
t (s)	1.95	5.2
Cooling rate (K/s)	10.7	16

The minimum points in the ΔT curve and in the first derivative curve will correspond to the DCP. The first derivative of the temperature change in time is shown in Figure 3.9.

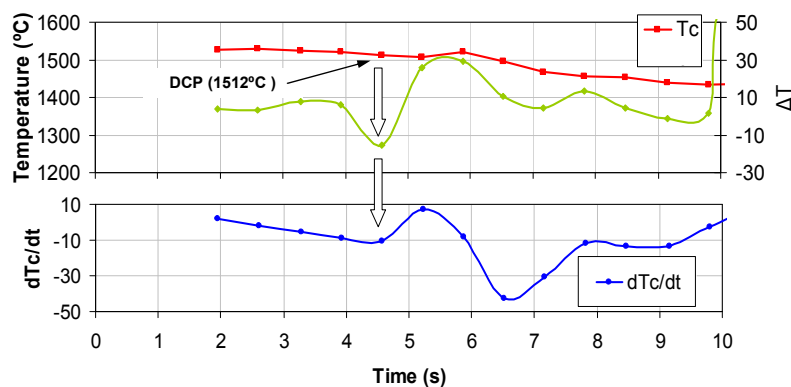


Figure 3.9. Determination of the dendrite coherency point for T_C using temperature difference and the first derivative of temperature over time.

In further analysis, we used the first derivative of the temperature change for the estimation of characteristic temperatures according to the phase diagram. In this analysis we used readings from both thermocouples.

As steel starts to solidify, the first peak in the first derivative can be associated with the liquidus temperature T_L . For both thermocouples this point is at the same temperature and equals to 1528°C. The next peak in the curves is associated with the T_S or solidus temperature. Because this point marks the moment when no more liquid is present in the material and, therefore, the heat extraction is at its maximum, the first derivative develops a sharp peak. This peak is measured at different temperatures at different thermocouple locations. The central thermocouple gives a higher reading of solidus temperature than the wall thermocouple, which is associated with a slower cooling rate in the central part of the mould (see Table 3.3) and may reflect stronger non-equilibrium solidification closer to the wall. Also the fact that the solidus temperature for the wall thermocouple is very low could be due to undercooling or due to an incomplete peritectic reaction.

The DCP close to the wall (a trough in the first derivative curve) corresponds to a lower temperature than the DCP in the centre. Although this measurement is less reliable than that from the central thermocouple as the solidification occurs too quickly and the difference in heat transfer mechanisms may be not registered correctly, the fact that the DCP is lower close to the wall may reflect the possibility of shrinkage during cooling, and therefore a detachment from the wall. Note that due to solidification the steel does shrink away from the

walls of the cups. This effect and its consequences for the heat extraction are also relevant at temperatures lower than the ones considered in this study.

The third peak in the first derivative curves corresponds to the transformation δ/γ (ferrite to austenite). This point also differ several degrees between the thermocouples located at the wall and in the centre, indicating the effect of the cooling rate in this phase transformation.

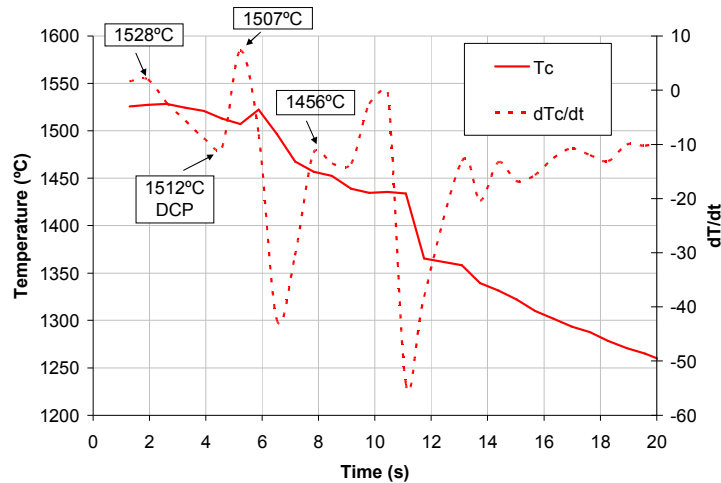


Figure 3.10. Temperature curve and the first derivative for T_c .

Table 3.4 summarizes the characteristic temperatures and Figure 3.10 shows the temperature curve and the first derivative for the T_c . The results emphasize a strong effect of the cooling rate on the characteristic temperature. The fraction of solid f_s as calculated with MTDData for the central thermocouple is also included in this table.

Table 3.4. Determination of characteristic peaks and comparison with calculations.

	T_w	T_c	f_L (%) as calculated with MTDData (Scheil)	Scheil (MTData)	Equilibrium (FactSage)
T_L	1528°C	1528°C	38.6	1532°C	1532°C
DCP	1510°C	1512°C	11.3	-	-
T_S	1442°C	1507°C	9.3	1513°C	1505°C
δ/γ	1388°C	1456°C	2.25	1489°C	1461°C

In Figure 3.11 (for the central thermocouple), the characteristic temperatures are plotted on the pseudo-binary phase diagram calculated with FactSage for this low carbon steel. The results correlate very well with the equilibrium phase diagram. However, the results have a small difference with the non-equilibrium Scheil calculations, thus considering the f_s from this data will not give a 100% fraction of liquid at T_L . In addition, because they are Scheil calculations, the fraction of solid will not be 100% at T_S .

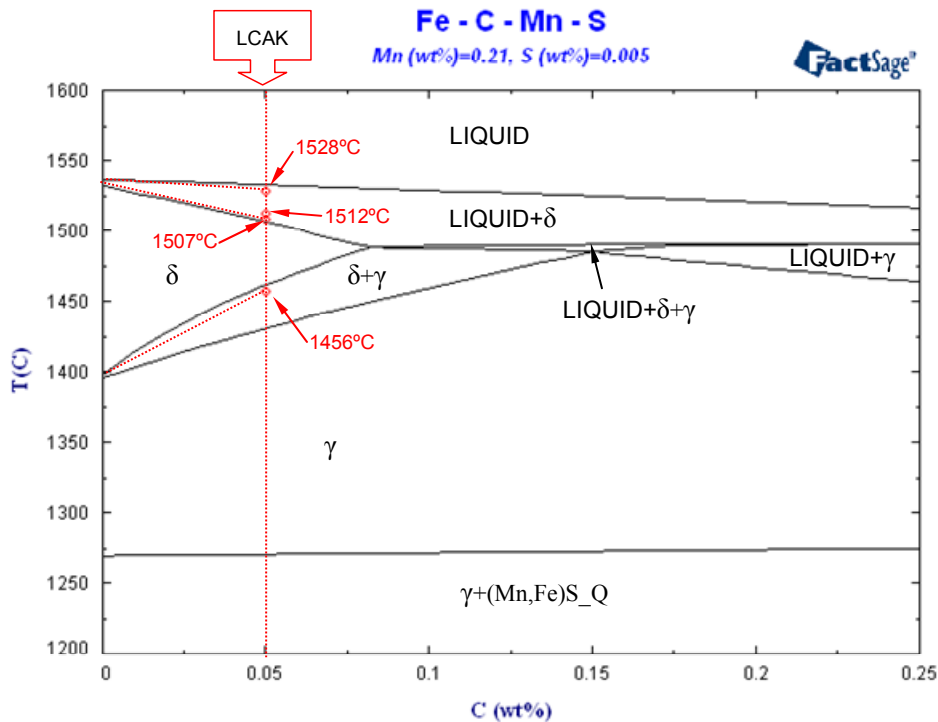


Figure 3.11. Simulated pseudo-binary phase diagram and measured characteristic temperatures for the central thermocouple.

3.2.4 Differential Thermal Analysis and Differential Scanning Calorimetry

Other and more accurate techniques to evaluate the solidification path and the complex phases formed due to non-equilibrium solidification are the Differential Thermal Analysis (DTA) and the Differential Scanning Calorimetry (DSC).

A set of tests were requested at Seteram Laboratories, France; for the LCAK and the HSLA grades.

The tests were done with a Setsys thermal analyser working with a high sensitive thermo-balance that can be combined with a DTA or DSC detector that allows the determination of respectively a difference of temperature or heat flux between the sample and the reference material contained in adequate crucibles.

The experiment profile was the following:

- From room temperature to 1360°C as quickly as possible
- First heating: from 1360°C to 1600°C at 1°C/min
- Fast cooling: from 1600°C to 1360°C at 20°C/min
- Second heating: from 1360°C to 1600°C at 1°C/min
- Second cooling: from 1600°C to 1360°C at 1°C/min

The tests were carried out under controlled atmosphere with helium flow rate at 20ml/min and an alumina 80- μ l crucible was used.

The TG-DSC rod was calibrated for temperature by using a palladium standard sample and measuring its melting temperature. The onset of the melting peak was determined at 1553.9°C whereas the literature gives 1554.8°C. Then, all measured temperatures on the samples curves were corrected according to the difference noticed between the measured and the literature temperatures. It has to be noticed that there is no method for the temperature calibration in the cooling mode. In fact there is always a difference between the melting temperature and the crystallization temperature for a metallic standard material due to undercooling. As a consequence the temperature calibration obtained during the heating mode was also used during the cooling mode.

From the melting/heating curves it generally is possible to distinguish some relevant temperatures ^[8,9]: The onset of the last peak upon melting as is the first visible onset of melting, is generally preferable over linear extrapolation methods for solidus determination. Moreover, from the freezing/cooling curves the end temperature at the first peak (offset upon cooling), means for metals the liquidus temperature, as it is the first point measured in this thermal event. From this point on, there will be some solid present.

For alloys that have a solidification range, including two or even three phases co-existing, as is the case of the Fe-C alloys in the peritectic range, it is plausible that the first thermal event shows an overlapping of peaks where the liquidus and the peritectic reaction and transformation occur.

LCAK Sample study

From the different heat flux signals recorded during the corresponding heating and cooling ramps it is possible to perform the following analysis:

Heating cycles

An exothermic peak (T_{1H1} in *Table 3.5*) at 1339.3°C is detected which indicates that there is a crystallization or dissolution effect (exothermic) prior to melting. After cooling, and during the second heating ramp this exothermic peak has disappeared; therefore this peak could be the effect of sample preparation or alloy reaccomodation, thus it is not relevant for this study.

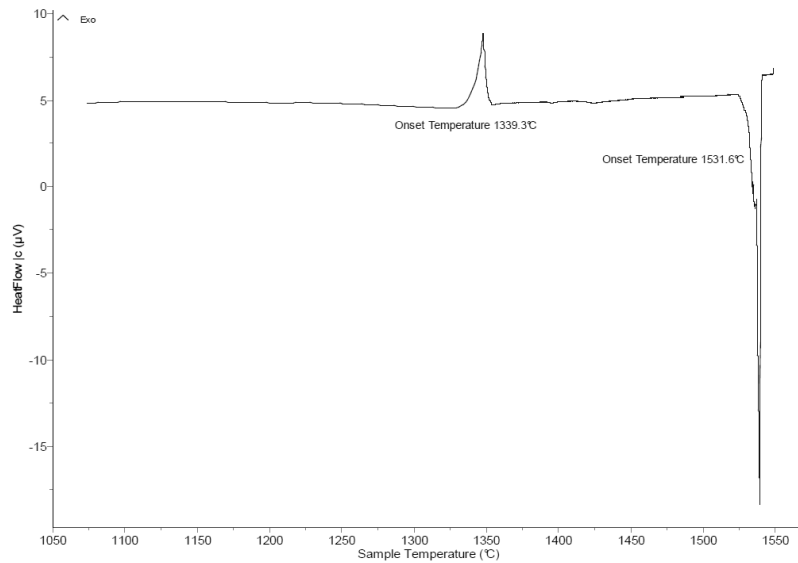


Figure 3.12. Heat flux recorded on sample LCAK during the first ramp - Initial mass: 272 mg

Upon heating, two small endothermic troughs at 1396.1°C and 1424.8°C T_{1H1} and T_{2H1} , respectively (Figure 3.13 and Table 3.5) are recorded on the first ramp and during the second heating ramp only one small endothermic trough at 1389.3°C is detected, T_{1H2} (Table 3.5 and Figure 3.14). This first endothermic trough in the first heating and the only one detected in the second cycle are consistent with the MnS dissolution. The second endothermic trough during the first heating cycle is consistent with the δ - γ transformation according to the calculated equilibrium phase diagram (see Section 3.2.1 previously in this Chapter)

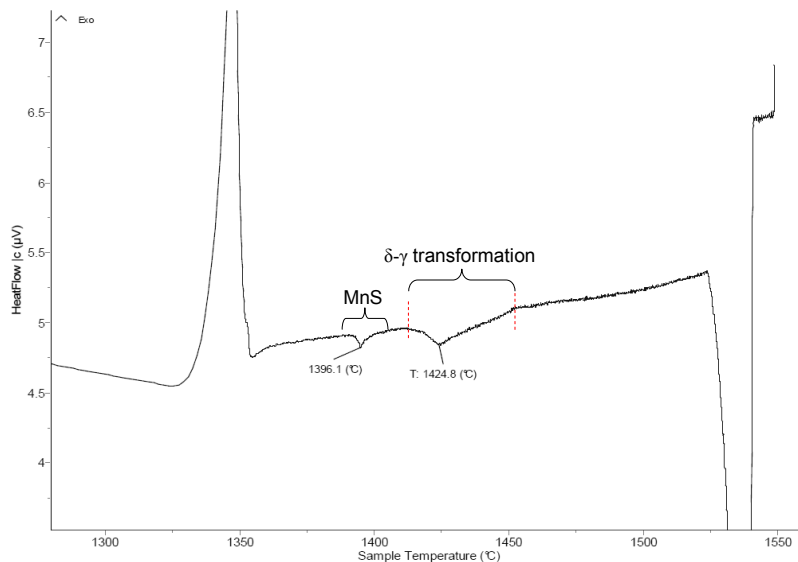


Figure 3.13. Magnification of heat flux recorded on sample LCAK during the first ramp - Initial mass: 272 mg

On both cycles a trough at 1531.5°C during the first heating ramp (Figure 3.12) and sharp trough at 1530.5°C during the second cycle (Figure 3.16) are detected marking the solidus

temperature (T_s); however, this temperature is much higher than expected from phase diagram calculations.

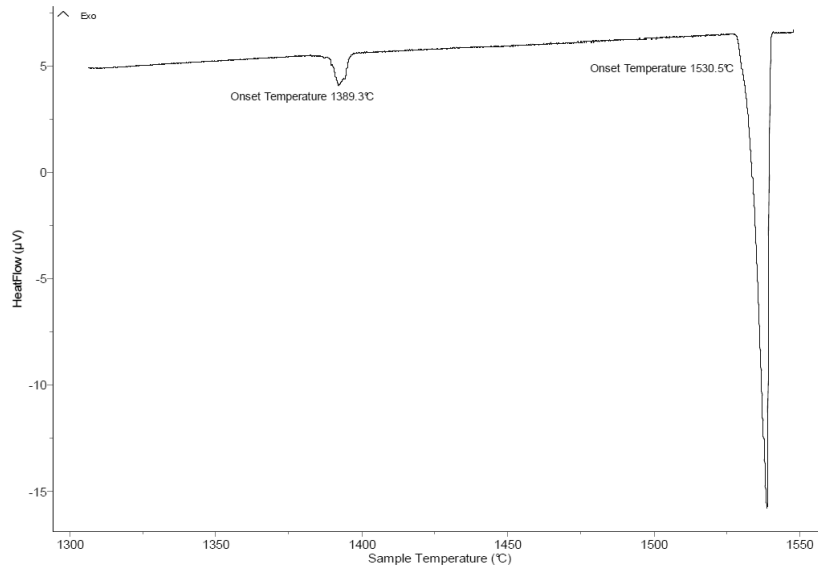


Figure 3.14. Heat flux recorded on sample LCAK during the second heating ramp - Initial mass: 272 mg

Cooling cycles

Two exothermic peaks are detected at 1498.6°C and at 1367.3°C T_{1C1} and T_{2C1} , respectively (Figure 3.15) during the first cooling ramp and another two exothermic peaks at 1533.4°C and at 1383.2°C, T_{1C2} and T_{2C2} , respectively (Figure 3.16) during the second cooling cycle. For this sample, no shoulder is detected on the peaks during cooling, indicating that there are only two phases in the alloy. However, the peaks and their recorded temperature are different for both thermal effects, but this difference could be due to the different cooling rate that both cycles had.

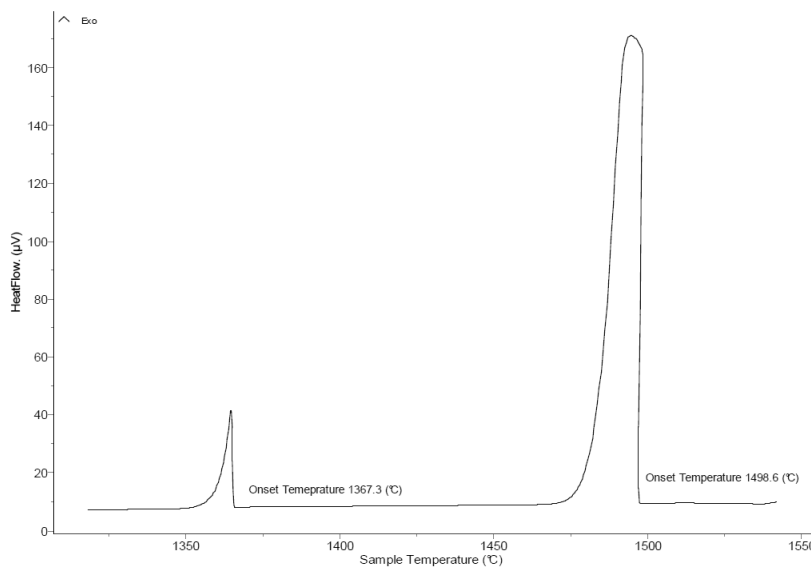


Figure 3.15. Heat flux signal recorded on sample LCAK during the first fast cooling - Initial mass: 272 mg

The first cooling peaks should correspond to the liquidus temperature, but it is uncertain if this is the case as it marks a lower temperature than the solidus previously detected during the two heating cycles.

Moreover, during these cooling cycles, the second peak detected corresponds again to MnS formation, where this phase also appears in the same temperature range, confirming that it is a liquid phase transformation because solid transformations do not undercool much.

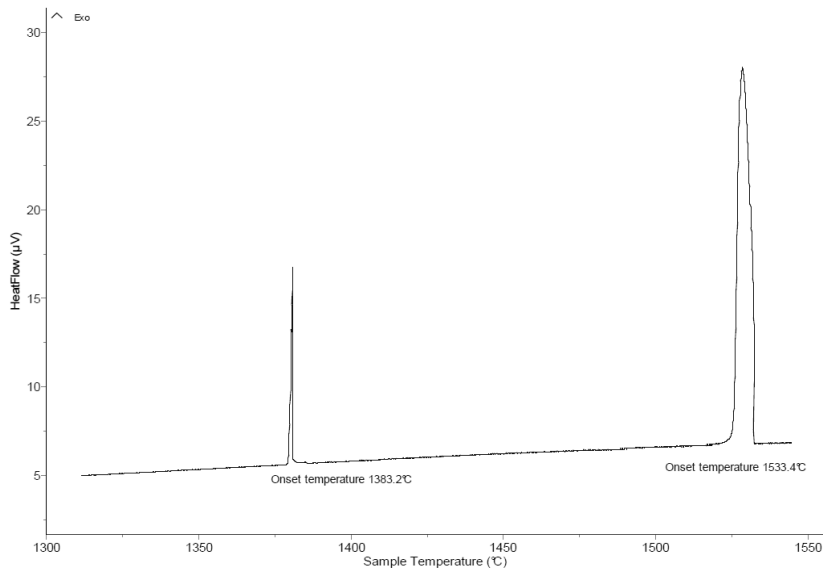


Figure 3.16. Heat flux signal recorded on sample LCAK during the second cooling - Initial mass: 272 mg

According to the literature review and phase diagrams analyses performed in Chapter 2, Section 2.6, the Fe–Mn–S system does have invariant points at 1394°C.

The importance of this finding supports the hypothesis that for this LCAK alloy manganese sulphides are formed during solidification due to alloy segregation, where this MnS phase will remain liquid until temperatures around 1390°C.

Table 3.5. Determination of characteristic peaks for LCAK.

First Heating (1°C/minute)	Second Heating (1°C/minute)
T _{1H1} :1338.3°C	
T _{2H1} :1396.1°C	
T _{3H1} :1424.8°C	T _{1H2} :1389.3°C
T _S :1531.6°C	T _S :1530.5°C
Fast Cooling (20°C/minute)	Second cooling (1°C/minute)
T _{1C2} :1367.3°C	T _{1C2} :1383.2°C
T _L :1498.6°C	T _L :1533.4°C

HSLA samples study

Performing a similar analysis for this steel grade, the following observations can be formulated:

Heating cycles

During the first heating ramp, a broad endothermic trough at 1426.7°C, T_{1H1} (δ - γ transformation) and a sharp trough at 1503.5°C, T_S (*Figure 3.17* and *Table 3.6*) with two shoulders, characteristic of an overlapping of events, are detected. In *Figure 3.17*, at the right hand side a magnification of the possible troughs overlapping is sketched in dotted-red and dotted-green lines. During the second heating cycle, again a broad endothermic trough at 1418.7°C, T_{1H2} (δ - γ transformation) and a sharp trough at 1504.8°C, T_S (*Figure 3.18* and *Table 3.6*) are detected. This sharp trough has a similar, but less pronounced overlapping of peaks than the trough in the first heating cycle. The offset of the two sharp troughs marks the solidus temperature for this alloy, which is consistent with the equilibrium phase diagram.

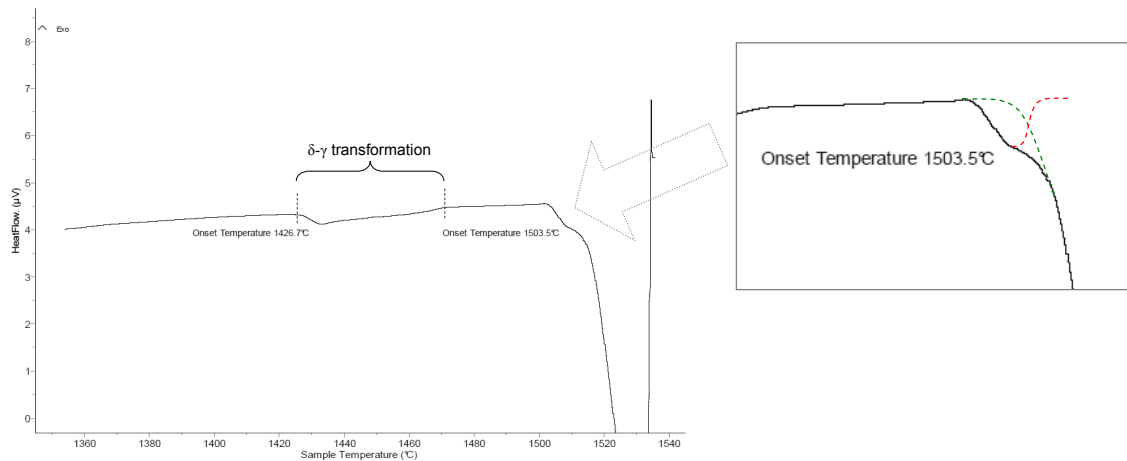


Figure 3.17. Heat flux recorded on sample HSLA during the first ramp - Initial mass: 344 mg

Both heating cycles display a trough with a double-shoulder, characteristic of an overlapping, denoting that there could be two transformations occurring in this temperature range (see *Figure 3.17* and *Figure 3.18*). The two possible transformations could be the TiN formation or the peritectic reaction, which is not necessarily fully developed, could be present in this steel grade.

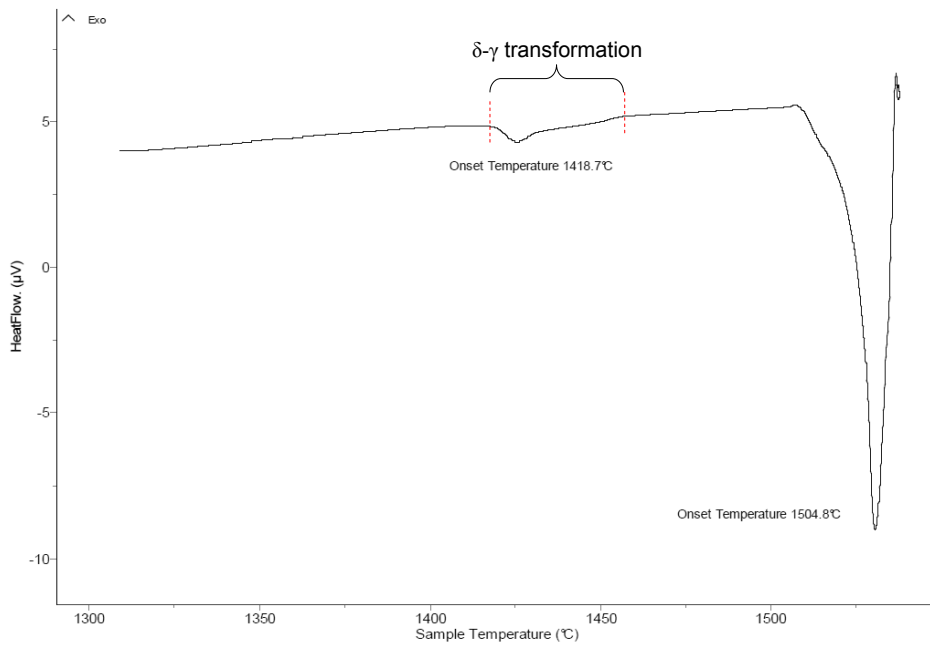


Figure 3.18. Heat flux recorded on sample HSLA during the second ramp - Initial mass: 344 mg

Cooling cycles

During the first fast cooling cycle, two peaks at 1525.3°C, T_L (intense and broad) and at 1433.8°C, T_{1C1} a broad peak (δ - γ transformation) are detected (Figure 3.19). During the second cooling ramp two exothermic peaks at 1527.8°C and at 1423.2°C (δ - γ transformation), T_L and T_{1C2} , respectively, are also recorded (Figure 3.20).

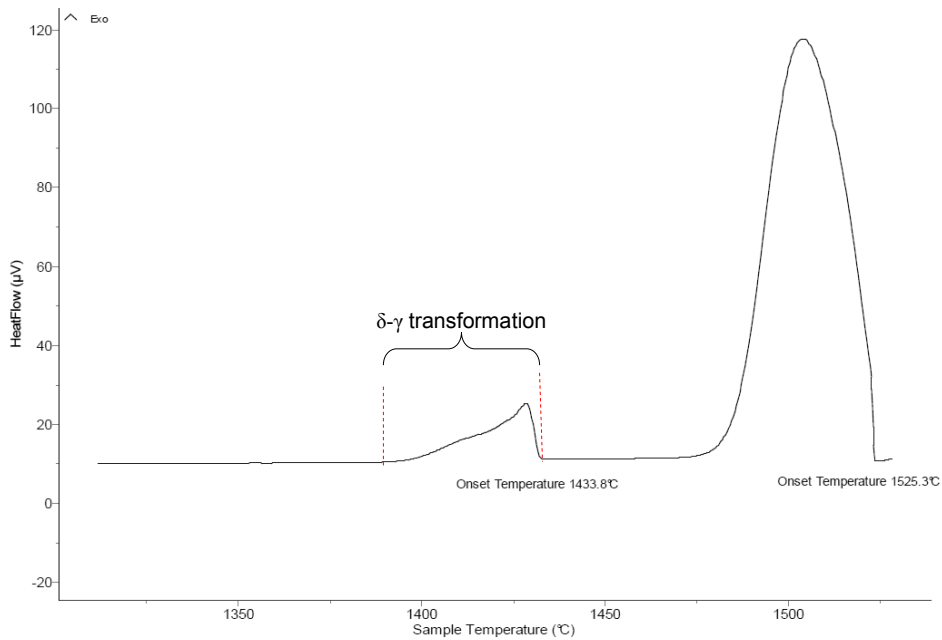


Figure 3.19. Heat flux signal recorded on sample HSLA during the first fast cooling - Initial mass: 344 mg

It is important to notice that the two cooling cycles run at different cooling rates, resulting in similar exothermic peaks, which means that in this case the thermal process has not modified the structure of the alloy.

This alloy has shown in all the cycles a broad transformation either upon cooling or heating, which is consistent to the δ - γ transformation.

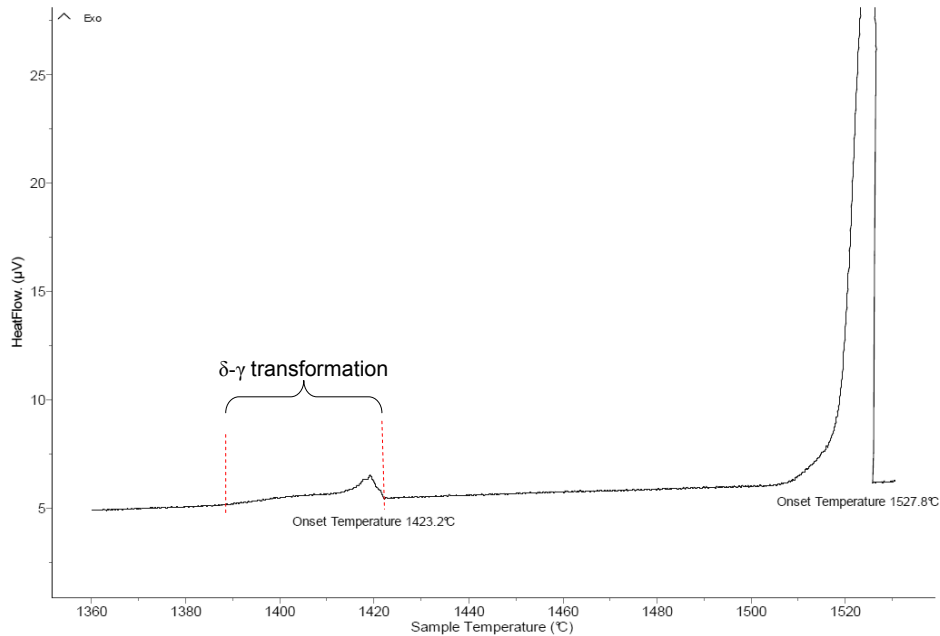


Figure 3.20. Heat flux signal recorded on sample HSLA during the second cooling - Initial mass: 344 mg

What is more important, for this steel grade it has been easier to determine the Liquidus and Solidus temperatures from the heating and cooling cycles, which are in the range of the calculated points for the equilibrium phase diagrams (see Section 3.2.1).

Table 3.6. Determination of characteristic peaks for HSLA.

First Heating (1°C/minute)	Second Heating (1°C/minute)
T _{1H1} : 1426.7°C	T _{1H2} : 1418.7°C
T _S : 1503.5°C	T _S : 1504.8°C
Fast Cooling (20°C/minute)	Second cooling (1°C/minute)
T _{1C1} : 1433.8°C	T _{1C2} : 1423.2°C
T _L : 1525.3°C	T _L : 1527.8°C

3.3 Peritectic phase transition

The terms *peritectic reaction*, *peritectic transformation* and *peritectic phase transition* have been used inconsistently in the past and hence, it is pertinent to define the terminology that will be used in this thesis. Following the terminology of Kerr et al. ^[10] also as explained by Dippenaar et al. ^[11], the peritectic phase transition is described as consisting of two separate stages: the peritectic reaction followed by the peritectic transformation.

The peritectic solidification starts with a ‘peritectic reaction’ in which all three phases, δ , γ , and liquid are in contact with each other. The peritectic γ phase will grow along the solid/liquid (S/L) interface δ/L , driven by liquid super-saturation. Solute rejected by the γ phase will diffuse through the liquid to the δ phase contributing to its dissolution. The γ phase will also thicken in the direction perpendicular to its growth, by direct growth in the liquid and at the expense of the δ phase by solid state diffusion. Once the reaction is completed and all the δ/L interface is covered by γ , the ‘peritectic transformation’ starts. The liquid and the primary δ phase are isolated by the γ phase. The transformation $\delta \Rightarrow \gamma$ takes place by long-range solid-state diffusion through the peritectic γ phase. The γ phase grows by direct solidification in the liquid [12].

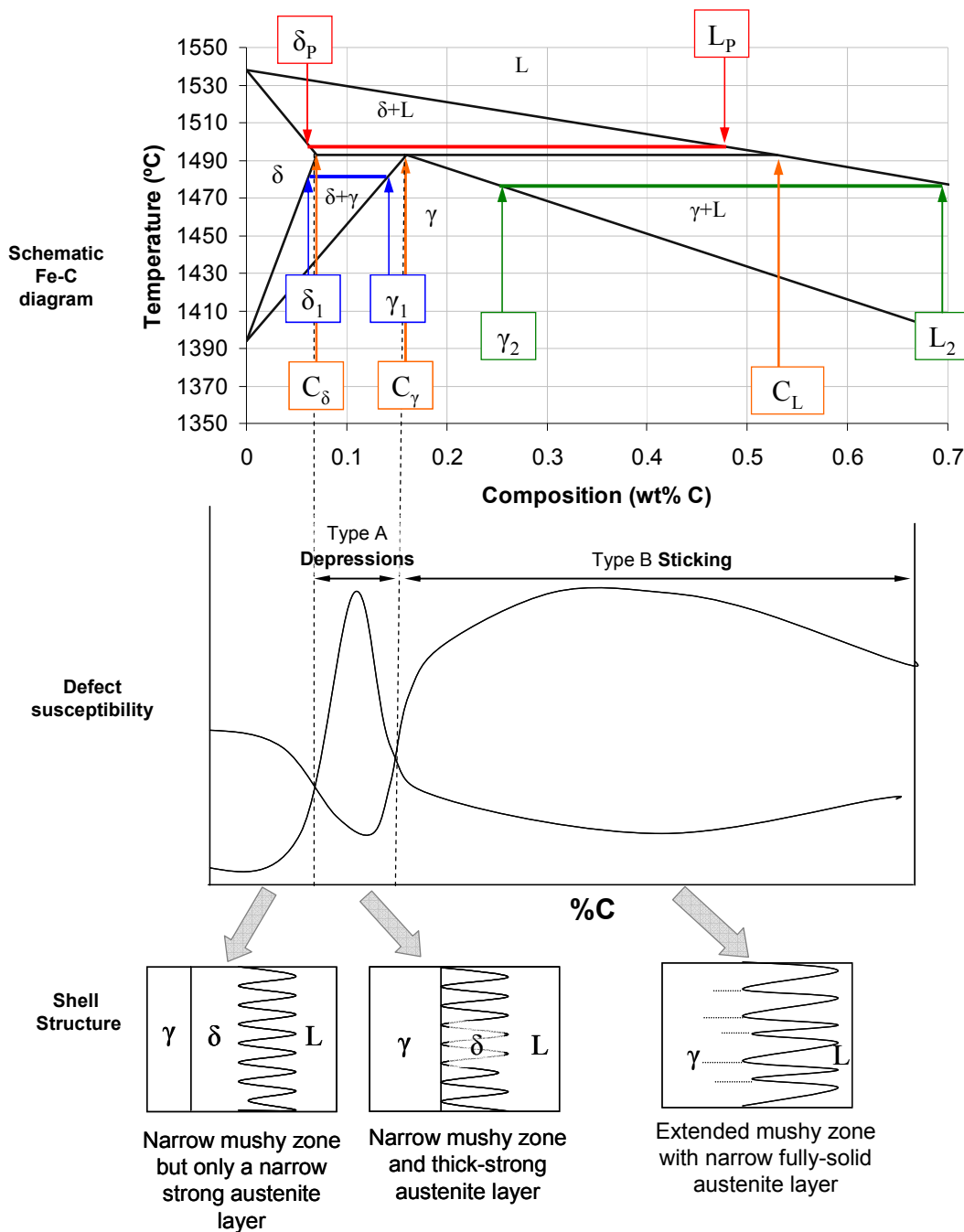


Figure 3.21. Suggested origins of the ‘Peritectic’ Surface Quality Problems [13]

During continuous casting of steel the solidification takes place under non-equilibrium conditions. The surface quality of the continuously cast slabs depends significantly on this early solidification conditions in and near the meniscus region in the mould. Cracks and weak spots in the newly solidified shell may propagate as the strand progresses through the caster and during downstream processing ^[14]. This has been attributed to uneven shell growth caused by the large volume contraction of the δ - γ transformation that makes the solidified shell detach locally from the mould wall. When stress is applied to the shell, this thin and weak area tears and cracks ^[15]. An important factor here is the proximity of the solidus to the rapid δ - γ transformation, represented in *Figure 3.21* ^[13]. The problem is particularly noted with near-net-shape or thin slab casting, which is thought to reflect the greater importance of a given surface defect size on thinner stock, and the faster casting speeds.

In view of its importance, several researchers have introduced factors to gauge the susceptibility of different grades and specific casts to these defects, which is assessed below for the three steel grades considered in this study.

3.3.1 Carbon equivalent formulae

The changes in the Fe–C phase diagram through chemistry can be described using an effective carbon content C_p expression of the form:

$$C_p = [\%C] + X_{Mn}[\%Mn] + X_{Si}[\%Si] + \dots \quad (3.3)$$

Several approaches have been given in the literature, where the coefficients for each formula have been developed either from thermodynamic databases (BSSTC and Howe's formulae), or based on plant experience (Trico, SMS and Wolf formulae). The coefficients and references for each of these equations are detailed in *Table 3.7*.

The equivalent weight concentrations of austenite forming elements are added to the C content and ferrite forming elements are subtracted. The actual peritectic covers the range C_δ to C_L in *Figure 3.21*, but regarding "peritectic grades" prone to defects the "peritectic" range is:

$$C_\delta < C_p < C_\gamma \quad (3.4)$$

with the proximity to C_δ (left hand /low C extremity) being considered particularly important. Since the key factor to assess the peritectic reaction is the primary ferrite fraction during solidification, a "ferrite potential" F_p can be defined by the following relationship:

$$F_p = 2.5(0.5 - \%C_p) \quad (3.5)$$

This highlights the left-hand /low C_p extremity of the peritectic which is around 0.1 %C, with F_p equalling 1 when C_p is 0.1 %.

- Ferrite stabilising elements are: chromium, tungsten, molybdenum, aluminium and silicon. The effect of a ferrite stabiliser is to decrease the peritectic A_4 temperature i.e. delay the formation of austenite.
- Austenite stabilising elements are nitrogen, nickel, manganese, cobalt and copper. The effect of an austenite stabiliser is to increase the peritectic A_4 temperature i.e. promote the formation of austenite

Table 3.7. Coefficients for selected carbon equivalent equations.

Reference	Mn	Si	Al(tot)	N	P	S	Nb	V	Ti	Cu	Sn	Cr	Ni	Mo	B	Ca
Wolf 1991 ^[16]	0.02	-0.1				-0.7						-0.04	0.04	-0.1		
Trico 1999 ^[16]	0.01	0.009	0.05	0.5	0.008	0.17	0.04	0.009	0.007	0.007	0.0006	0.003	0.02	-0.007	1.32	-0.24
BSSTC 1998 ^[16]	0.043	-0.14		1.06	0.029	0.11		-0.13	0.024	0.037		0.083	0.1	0.063		
SMS (DSP) ^[17]	0.014	-0.037			-0.04	0.222				0.003			0.023	0.004		
Howe ^[18]	0.04	-0.14		0.7					-0.24			-0.04	0.1	-0.1		

At the DSP IJmuiden steel plant, preference has been given to the SMS formulae since the developers of this equation also have experience with thin slab casters^[17]. However, for a more detailed study the formulae used should be the ones that are based on thermodynamic calculations, such as BSSTC and Howe’s formulae (see Table 3.7 for details on the coefficients for each formulae).

Following the plant experience of SMS Siemag^[17] for thin slab casters, boundaries for the ferrite potential and corresponding carbon equivalents are:

$$0.88 < F_p < 1.06. \text{ and } 0.076 < C_p < 0.148 \quad (3.6)$$

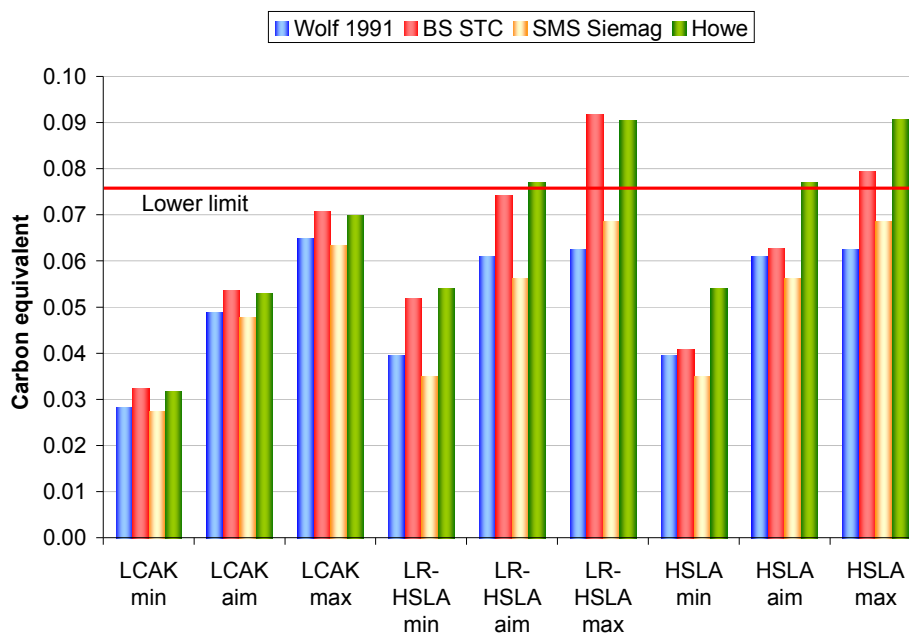


Figure 3.22. Carbon equivalent calculated for the LCAK, LR-HSLA and HSLA grades.

The given formulae of carbon potential are applied to the minimum, maximum and aimed compositions of the steel grades considered in this thesis and are shown in *Figure 3.22*. The red line marks the lower boundary of the peritectic range.

For all the formulae, the HSLA steel grades has a higher C_p than the other grades, particularly when the LR-HSLA C_p 's are calculated with BSSTC and Howe's formulae: in these cases, they fall within the limits of the peritectic range. For the case of Howe's formula, both grades LR-HSLA and HSLA are considered to be in the peritectic range; but for the BSSTC formula, only the LR-HSLA are fully in the peritectic range.

The ferrite potential reflects the same trend (figures not displayed in this study to avoid repetition of similar graphs), when calculating the C_p with the coefficients from BSSTC and Howe's the HSLA grades fall within the limits of the peritectic range. However, when using the other formulae, they are well below the lower limit.

3.3.2 Peritectic range

Up to now, most steel plants have used some type of carbon equivalent equation to calculate the effective carbon composition for a particular grade, and if the carbon equivalent was from 0.07 to 0.18% carbon (for DSP 0.076 to 0.148% carbon), the grade would be assumed to be peritectic. Therefore when continuously casting a peritectic grade determined in this manner, a peritectic-type mould powder would be used to improve the as-cast surface quality. Conversely, when the carbon equivalent equation would predict that the grade was not in the peritectic range, a non-peritectic powder would be used. ^[19]

Recently when casting new steel grades with a high content of alloying elements, the carbon equivalent calculations predicted that these steel grades would be non-peritectic but the cast product displayed characteristics belonging to a peritectic steel composition. This led Arcelor Mittal USA Burns Harbor to develop a peritectic predictor equation specifically for high aluminium steel composition but that could be used for all steel grades under the specified range ^[19]. The quantities of interest are the carbon levels shown as C_δ and C_γ in *Figure 3.21*. This is the so-called "peritectic range". Blazek et al. ^[19] spanned the entire range of all alloying elements used in the high alloyed steel grades. They developed a linear regression predictor equation for both the lower and upper peritectic points from Thermo-Calc calculated phase diagrams.

While these equations were valid for high alloyed steel grades, they could not be considered accurate for other steels containing comparable amounts of silicon and manganese with low aluminium. For this reason, and also to cover other steel grades, Blazek et al ^[19] carried out a more extensive parametric study of Thermo-Calc and predicted the peritectic equations. They used a more rigorous non-linear fit for their study to expand the useful range for the predictor equations.

Table 3.8. Ranges for alloying elements ^[19]

Element	Composition range (wt%)
Al	0 to 2.0
Cr	0 to 18.3
Mn	0 to 2.1
Mo	0 to 2.2
Si	0 to 2.05
P	0 to 0.1
S	0 to 0.15
Cu	0 to 1.35
Ni	0 to 10.3
V	0 to 0.03
Ti	0 to 0.33
Sn	0 to 0.03
Nb	0 to 0.075
W	0 to 0.5

Subsequently, Blazek could expand the range of alloys for which the peritectic equations were valid to include the entire range of alloys cast at Arcelor Mittal USA steel plants (entire range in *Table 3.8*). The net result is shown in *Table 3.10* which gives the elements and ranges included in the modelling. *Figure 3.23* shows the two regressions obtained for C_{δ} and C_{γ} .

Table 3.9. Regression equations.

Elements	Coefficient	
	C_{δ}	C_{γ}
C	0.0896	0.1967
Al	0.0458	0.0036
Mn	-0.0205	-0.0316
Si	-0.0077	-0.0103
Al ²	0.0223	0.1411
Al*Si	0	0.05
Ni	-0.0239	-0.0401
Mo	0.0106	0.03255
V	0.0134	0.0603
Cr	-0.0032	0.0024
Cr ²	0.00059	0.00142
Cr*Ni	0	-0.00059
W	0.0197	0.0266

Following the regression formulae from Blazek et al.^[19], the calculated C_{δ} and C_{γ} for the maximum, aim and minimum compositions of the three steel grades considered in this thesis, are listed in *Table 3.10*.

Table 3.10. Regression boundaries for the steel grades.

Range		Min	Aim	Max
LCAK	C_{δ}	0.087	0.087	0.086
	C_{γ}	0.19	0.191	0.188
LR-HSLA	C_{δ}	0.075	0.076	0.073
	C_{γ}	0.174	0.176	0.171
HSLA	C_{δ}	0.076	0.077	0.074
	C_{γ}	0.179	0.181	0.176

Considering the worst case scenario, thus taking into account the maximum composition for each steel grade, Figure 3.23 gives a graphical comparison of the expected peritectic ranges. In blue and red lines, the upper and lower boundaries, respectively, are shown for comparison. These values have to be taken as limits for each steel grade, particularly when considering a grade that is close to the limits. For some steel grades (LR-HSLA and HSLA) the inferior limits are lower, thus more strict than has been considered for DSP according to SMS Siemag^[17]. Moreover, the HSLA C_{δ} limit is slightly higher than of the LR-HSLA, where the only element considered in the formulae that differs in both compositions is vanadium. However, for most of the grades these limits are higher than 0.076 wt%.

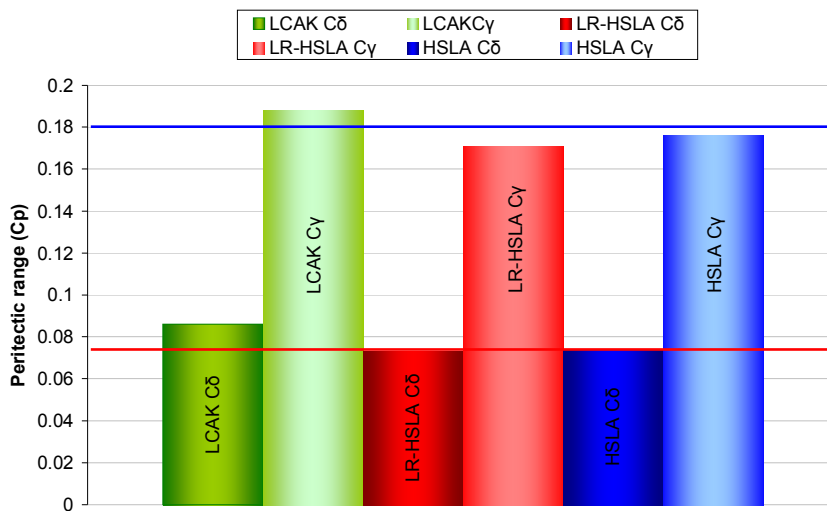


Figure 3.23. Graphical comparison of the expected peritectic ranges for the three steel grades.

3.3.3 Peritectic equivalent “Ep” in QuickSeg model

QuickSeg Peritectic (QSP) v2 is a standalone program written in Visual Basic 6 based on the finite difference model explained in ^[20], yielding the levels of micro-segregation during and after solidification and including liquidus, peritectic (if encountered) and solidus temperatures. It also predicts the homogenisation of the solute profile after solidification (if solidification ends as fully austenitic), TiN precipitation from the liquid, and NbCN precipitation from the partly homogenised solid. A further variable is the Peritectic Equivalent, which for each element (at a concentration of X wt% in the residual liquid) is given by:

$$E_p = [\%X] * \frac{(k_{\delta/L} * m_{\gamma/\delta} - m_{\delta/L})}{(T_{\delta/L}^0 - T_{\delta/\gamma}^0)} \quad (3.7)$$

Solidification should proceed as ferrite whilst the sum of these E_p terms in the residual liquid is less than unity, and change to austenitic solidification at the peritectic, once $\sum E_p \geq 1$.

It is derived from the binary phase diagrams, simplified to be linear. Thus constant equilibrium data are employed, restricting its applicability to dilute steels, but the parameters are designed to ensure that consistent temperatures and interface compositions are encountered through the peritectic, which requires one of the three sets of partition coefficients, k , and liquidus slopes, m , is a function of the other parameters.

Thus:

$$k_{\delta/\gamma} = k_{\delta/L} / k_{\gamma/L}, \quad (3.8)$$

and

$$m_{\gamma/\delta} = \frac{((T_{\delta/L}^0 - T_{\delta/\gamma}^0) * m_{\gamma/L} - (T_{\gamma/L}^0 - T_{\delta/\gamma}^0) * m_{\delta/L})}{(T_{\delta/L}^0 - T_{\gamma/L}^0) * k_{\delta/L}} \quad (3.9)$$

where $T_{\delta/L}^0 = 1537^\circ C$, $T_{\gamma/L}^0 = 1526^\circ C$, $T_{\delta/\gamma}^0 = 1392^\circ C$

The “QSP” tracks the changes in temperature, fraction solid and microsegregation of multicomponent steels during solidification, including the three-phase, peritectic transformation. It employs simplified thermo-physical data to enable rapid run times: these restrict its use to low alloy contents but is still suitable for the majority of Tata Steel Mainland Europe grades. One such aspect is the use of constant partition coefficient and liquidus-slope data per element for L/δ and L/γ . The selection of these must obey certain criteria such that the data are self-consistent regarding the onset and progress of the peritectic. From this, a “peritectic equivalent” E_p can be derived, such that the solidifying phase will be ferrite when the summed E_p of all the solutes is less than 1, whether for the initial, bulk liquid composition or for the enriching composition of the residual liquid during solidification (Section 3.3.3). For example, in the bulk liquid of a simple binary Fe–C alloy, $E_p = 1$ corresponds to 0.53%C, i.e. C_L in Figure 3.21. This differs from the peritectic carbon equivalents named above, however, as they relate to the composition C_δ in that figure, i.e. the left end of the peritectic, at about 0.09%C in the binary Fe-C phase diagram. In the binary phase diagram, this position equates to an E_p value of 0.09/0.53, i.e. 0.17.

Howe^[21] performed QSP calculations for the average compositions of steels LCAK, LR-HSLA and HSLA, and the result E_p values are 0.11, 0.14 and 0.17, respectively: therefore suggesting that LCAK is comfortably fully ferritic during solidification, LR-HSLA comes close to changing to austenite at the end of solidification, and HSLA should just about encounter the peritectic switch to austenite. However, upon running these compositions through the QSP program, the E_p of the residual liquid at solidus was 0.56, 0.62 and 0.69, reflecting the

same ranking order but remaining ferritic to solidus, never reaching the peritectic at $E_p = 1$. This is because the other elements are not behaving the same as carbon during solidification: they are not really “carbon-equivalent”; a concept which can only be an approximation.

This could still relate to a ranking order for peritectic crack susceptibility, even though the rapid δ - γ contraction occurs somewhat below solidus. Of note, here, however, is that according to the Thermo-Calc software, employing the Scheil approximation, the average steel HSLA composition does just reach the peritectic phase switch before solidus, as discussed below. It is not clear if the difference from the QSP program is simply due to their use of the Scheil approximation (zero solute diffusivity in the solid, as opposed to QSP’s use of temperature-dependent, finite diffusivities) or the implied partition coefficient data.

3.3.4 Thermo-Calc

Thermo-Calc is one of the most utilized software packages for thermodynamic simulations up-to-date which can also perform advanced calculations by the input of more complex thermodynamic and kinetic models (along with DICTRA).

The thermodynamic calculations here presented were performed by Dr. B. Böttger in RWTH-ACCESS, Germany as part of the M2i-Tata Steel-ACCESS Valorisation project “Thermodynamic calculations and MICRESS® simulations of microstructure evolution during continuous casting of technical steel grades” [22].

Four thermodynamic calculations (Scheil simulations) have been done for the LR-HSLA and HSLA steels. The first two, considering the aim values for C, Mn, Nb, N, V and the minimum value for Ti as alloying elements (see Figure 3.24). The last two consider the maximum values as listed in Figure 3.25. For all cases, fast diffusion has been considered for the interstitial elements C and N.

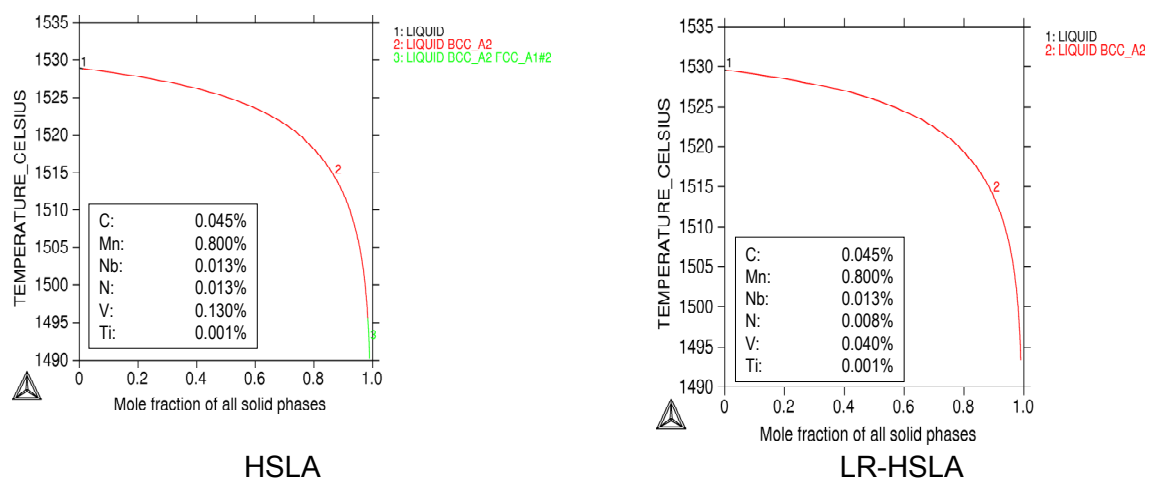


Figure 3.24. Scheil calculations for LR-HSLA and HSLA considering the aim values for the chemical composition.

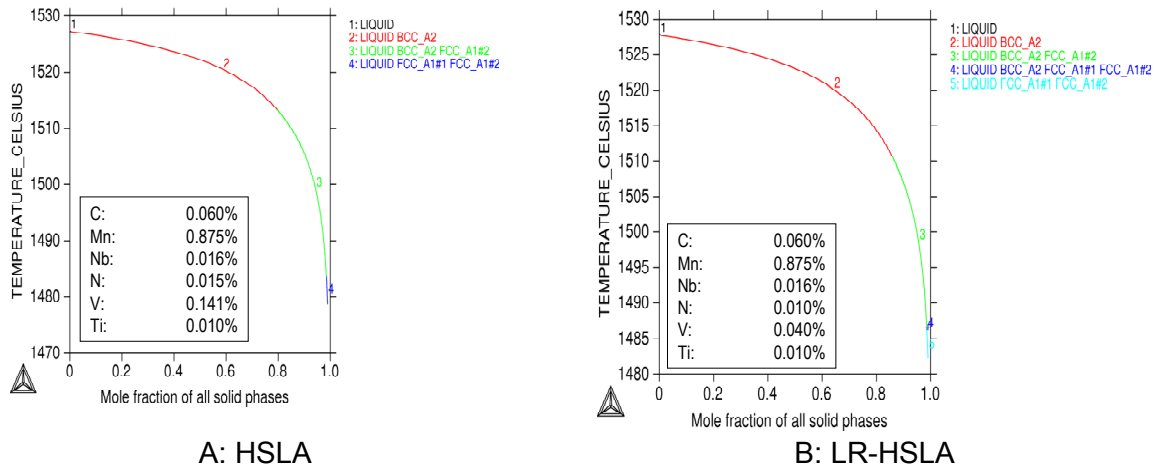


Figure 3.25. Scheil calculations for LR-HSLA and HSLA considering the maximum values for the chemical composition.

In Figure 3.25 A (for HSLA steel grade), the phases listed are as follows:

- 1: LIQUID: liquid steel
- 2: LIQUID BCC_A2: liquid and the δ ferrite (L+ δ)
- 3: LIQUID BCC_A2 FCC_A1#2: liquid, δ ferrite (L+ δ) and TiN
- 4: LIQUID FCC_A1#1 FCC_A1#2: liquid, γ austenite (L+ γ) and TiN

Consequently, in Figure 3.25 B (for LR-HSLA steel grade), the phases listed are as follows:

- 1: LIQUID: liquid steel
- 2: LIQUID BCC_A2: liquid and the δ ferrite (L+ δ)
- 3: LIQUID BCC_A2 FCC_A1#2: liquid, δ ferrite (L+ δ) and TiN
- 4: LIQUID BCC_A2 FCC_A1#1 FCC_A1#2: liquid, δ ferrite and γ austenite (L+ δ + γ) and TiN
- 5: LIQUID FCC_A1#1 FCC_A1#2: liquid, γ austenite (L+ γ) and TiN

When considering Ti as a component, (Figure 3.25), the LR-HSLA is showing the 3 phases coexisting with each other (reaction nr 4 in blue in Figure 3.25 B), thus full peritectic solidification. The idea why Ti was added as an alloying element is that it forms TiN precipitates in the temperature range which is relevant for hot crack formation, and that the amount of TiN precipitating already from the liquid phase is different between HSLA and LR-HSLA. The reason for this difference is mainly the different N content, but also, to a smaller extent, the different V content, as V is soluble in TiN (see Section 2.6.5, Chapter 2).

3.4 Concentric Solidification Technique

The concentric solidification experimental method is defined as the formation of a centralised pool of liquid metal contained by a rim of solid of the same material under a radial thermal gradient. More detailed information regarding this technique is described by Reid et al. [23]. This concentric solidification technique is also another powerful tool to evaluate the peritectic susceptibility of a steel grade during solidification. This is the main reason that it is used in this study.

3.4.1 Experimental data collection

In the system used for this study, a specimen of 10mm diameter was placed in an alumina crucible, which in turn is held in a platinum holder. The specimen was positioned at one focal point of an ellipsoid Infra-red heating furnace, with the heat source at the other point. The ability to establish a melt pool in the confocal microscope is dependent upon the existence of a radial thermal gradient across the 10mm diameter crucible holder. The technique is further explained in detail elsewhere^[23].

Samples of the LCAK, LR-HSLA and HSLA steel grades were sectioned from a slab and machined into the required discs. The temperature measured by thermocouples incorporated in the crucible holder is displayed on a monitor and simultaneously recorded with the digital image at the rate of 30 frames per second. Because the sample is positioned in the furnace chamber at one focal point of the ellipsoidal cavity and the heating element is situated at the other focal point, radiation heating is concentrated in the centre of the disk-shaped specimen and a radial temperature gradient develops within the specimen^[23].

Therefore, a pool of liquid metal forms in the centre of the specimen, which is contained by a solid rim of the same material under a radial thermal gradient, employing the concentric solidification technique. The centre of the sample is melted and maintained at constant temperature for a few minutes to establish local equilibrium at the ferrite/liquid interface. This procedure ensures that a stable liquid pool is formed with a solid rim surrounding the liquid pool and due to the geometry of the furnace relative to the specimen a thermal gradient is established across the liquid/solid interface^[24]. Specimens were then cooled to 1300°C at rates of 5, 10 or 20°C/min followed by cooling to room temperature at a rate of 100°C/min. The positions of the δ -ferrite/liquid and austenite/liquid interfaces were measured using frame-by-frame break down.

It is pertinent to note that the temperature recorded by the thermocouple during an experiment does not indicate exactly the temperature of the sample as the thermocouple is connected to a platinum holder and there is a gap between the holder and the alumina crucible as well as between the crucible and the sample. This temperature is used for control purposes and its relation with the actual sample temperature is treated with circumspect as explained in the analysis carried down by Aminorroaya et al.^[24].

3.4.2 Results evaluation

Moon et al.^[25], while performing a similar study on the peritectic transformation, indicate that a detailed understanding of the progression of the L/ δ interface is fundamentally important since it is the rate at which this initial solidification front progresses that will determine the thickness of the solidifying shell in the meniscus region of a continuous caster. Due to the instability of the solidification front, only the progression of the L/ δ interface in the samples tested at 10°C/min could be measured. However, the HSLA steel grade at these solidification conditions clearly has a lower progression of the L/ δ interface (see *Figure 3.26*).

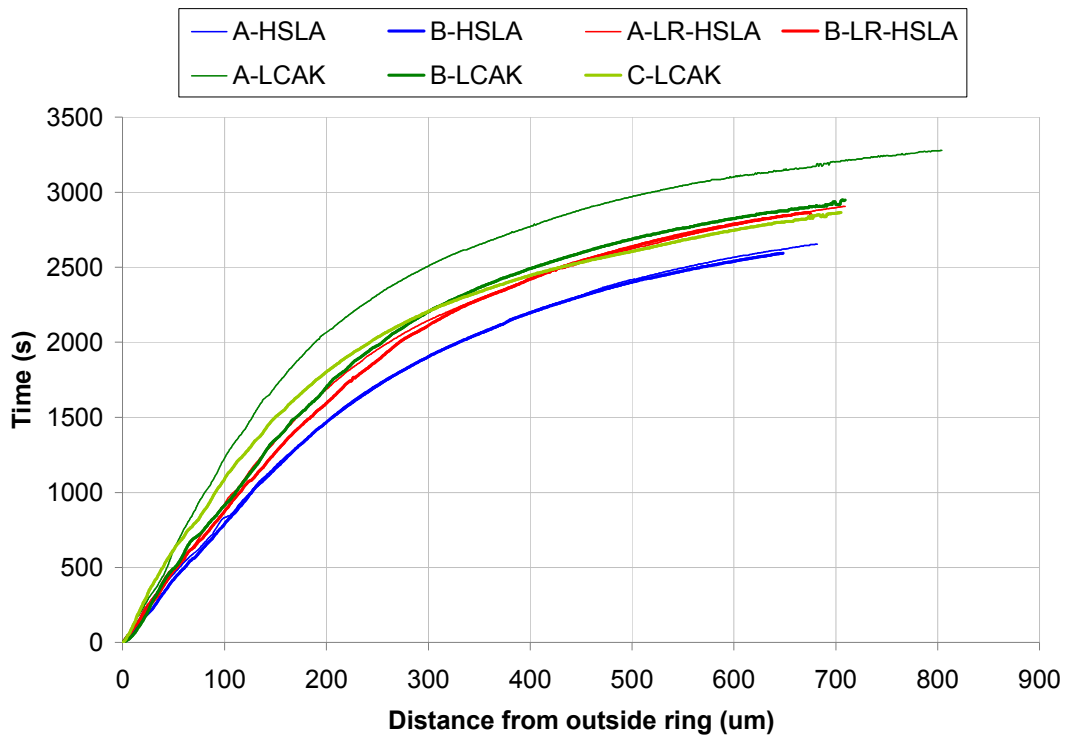


Figure 3.26. Progression of the L/δ interface in the samples tested at $10^\circ\text{C}/\text{min}$

Considering that in all samples analysed and at all cooling rates it is possible to see the peritectic reaction, a good comparison of the peritectic susceptibility of the alloys would be to rank them in respect to the temperature at which the peritectic reaction begins. The higher the onset temperature, the more prone the steel is to problems related to the peritectic phase transition as it takes a smaller alloy concentration to trigger this transition.

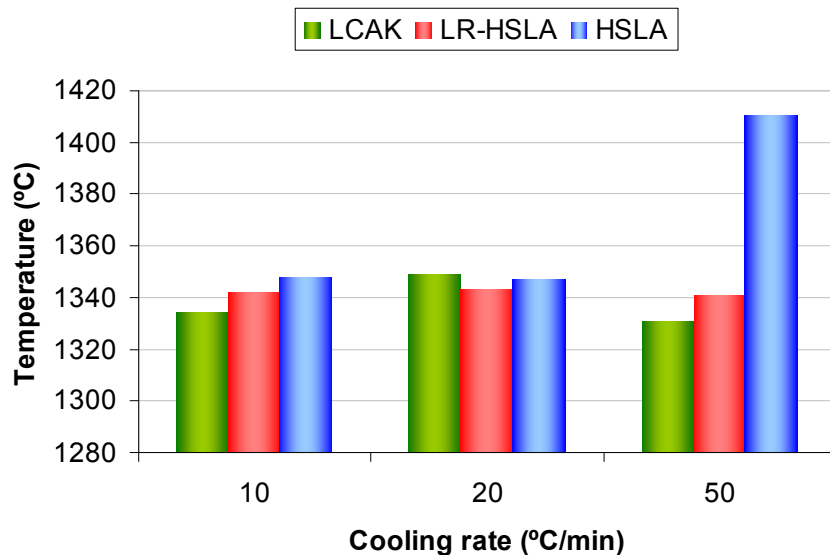


Figure 3.27. Temperature at which the massive peritectic transformation begins.

Following Moon et al. ^[25], the massive transformation as seen in Figure 3.27, appears to be temperature invariant with respect to the cooling rate for the LR-HSLA, while the HSLA steel grade has an increased peritectic transformation temperature with increasing cooling rate.

However, the two samples for the HSLA tested at 50°C/min do not show the massive transformation but rather show a massive solidification at the temperatures noted in *Figure 3.27*, where the last liquid remained directly solidify in fractions of a second, rather than experiencing the peritectic reaction and further continuing solidifying. Moreover, this massive solidification is accompanied with strong shrinkage, so evident that it shows an empty circle at the centre of the sample.

3.4.3 Non-metallic inclusions in the Concentric Solidification samples

The surfaces of the discs from the concentric solidification experiments were also analysed under SEM, showing non-metallic particles which confirms the segregating nature of the last liquid remained during solidification in this steel grade. In the analysed specimens, the sulphide particles grow in amount and size through the centre of the discs, and obviously, with decreasing temperature of the test, which agree with the assumption that they are formed from the segregated liquid.

The liquid phase in the centre of the discs has more time for sulphur segregation; therefore the MnS precipitates are bigger and more “eutectic” in appearance. This observation is in good agreement with Flemings and Kattamis ^[26] who showed a relation between the morphology and the size and type of inclusions with the distance from the ingot cooling surface. By increasing the distance, there is an increase in the average diameter of the Type I inclusions (see *Figure 3.29*) and an increase of the eutectic rod diameter and in average eutectic spacing in Type II inclusions. Even when the cooling rate of these discs is not the same as in Flemings’ research, each sample could be related with distance from the surface of an ingot/cast slab. Therefore the mechanism of particles growing fits very well with the reported one. Moreover, all three tested cooling rates, 10, 20 and 50°C/min, show the segregated features through the centre of the sample.

LCAK steel

Analysing the disc’s surface (see *Figure 3.28*), from the outside to the centre, the 10°C/min samples display the type’s II, III, and a ring of non-metallic particles very close to the centre. The 50°C/min discs show the types II and III but the ring of particles is absent and the type II inclusions are bigger and longer than on the other samples (see *Figure 3.29*). In between, the 20°C/min discs have again both types of MnS particles, the type I and II, but the ring that seems to be a cluster of type II particles, almost developing to form the type III as described by Flemings ^[27]: as particles with a cubic pattern often embedded in “dendritic” projections of the same inclusion which join the interdendritic network.

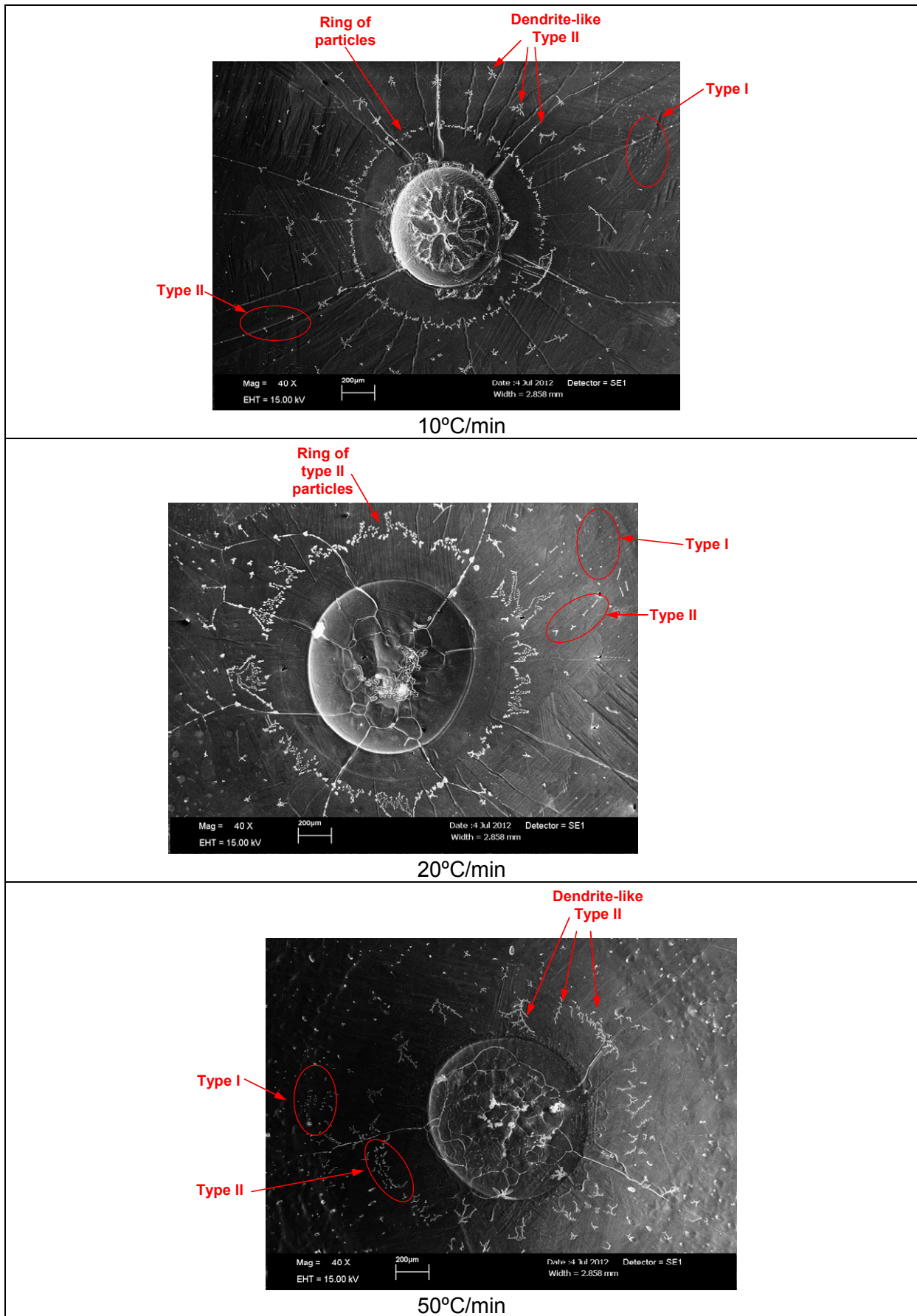


Figure 3.28. Overview of the surface of the 10, 20 and 50°C/min tested specimens for the LCAK steel grade.

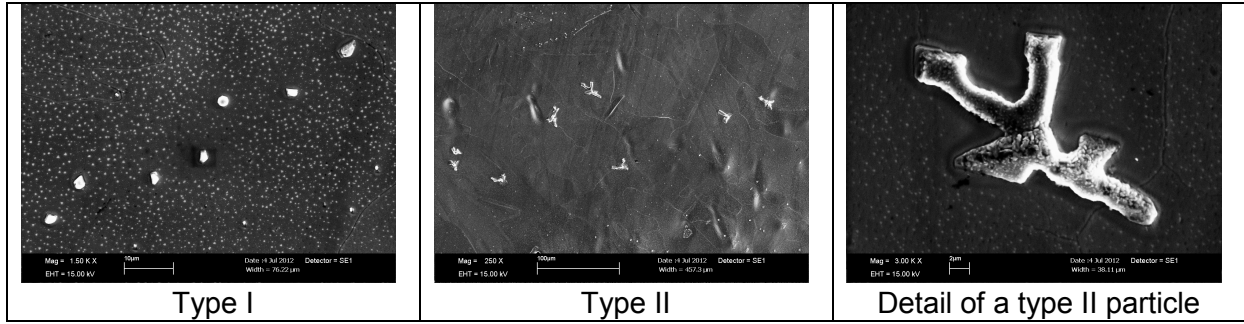


Figure 3.29. Examples of the non-metallic particles found at the specimen's surface.

LR-HSLA steel

Due to the solidification conditions of this technique, it is expected to have a high segregation towards the centre of the sample (see *Figure 3.30*). Because the LR-HSLA steel grade is more alloyed than the LCAK, the inclusions show a difference in composition in the so-called “MnS ring” and as expected the last liquid to solidify has also a high concentration of elements, and this can be seen at the centre of the sample. An example of one of these non-metallic particles found at the surface and the corresponding EDAX analysis is shown in *Figure 3.31*. For the two highest cooling rates, 20 and 50°C/min, this steel grade shows a very unstable solidification front, the most unstable of these three grades.

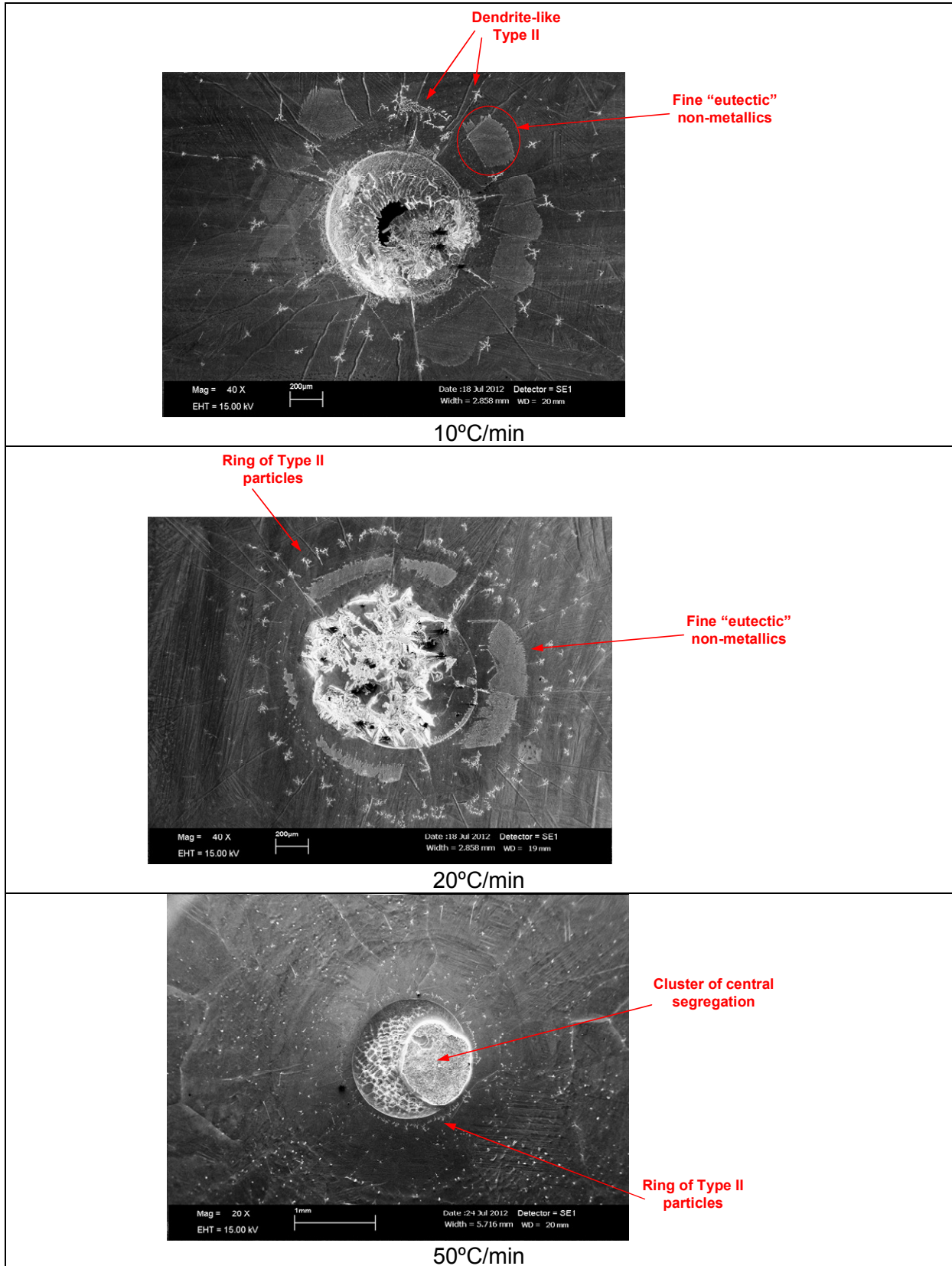


Figure 3.30. Overview of the surface of the 10, 20 and 50°C/min tested specimens for the LR-HSLA steel grade.

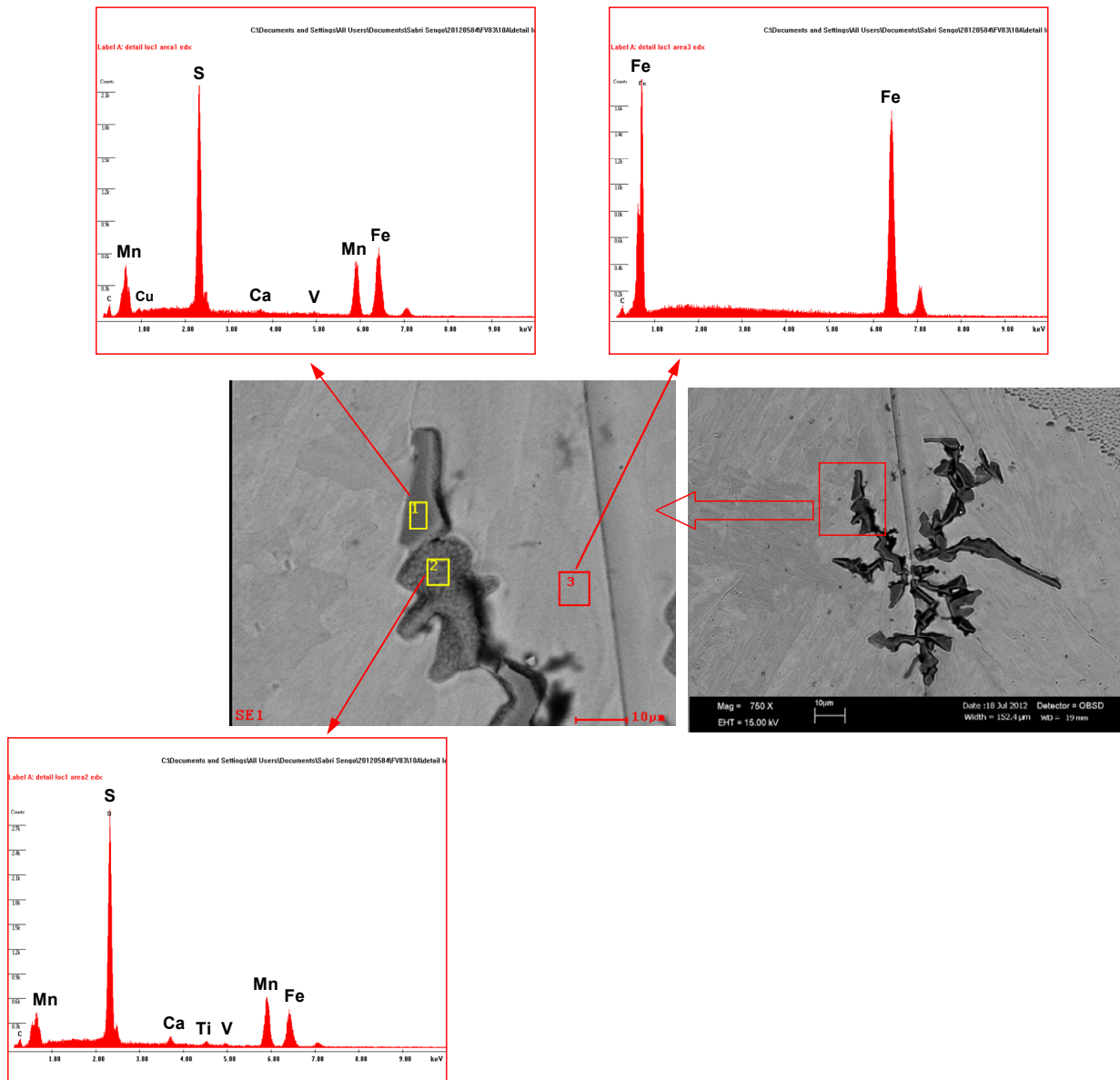


Figure 3.31. Detail and EDAX of a Type II MnS from the 10°C/min sample.

The LR-HSLA tested specimens did also present a fine eutectic-like structure, consisting of small rods of MnS with some vanadium, which in some cases display two different orientations, one almost parallel to the surface and the other at 90° from the former ones, thus perpendicular to the specimen's surface (see Figure 3.32).

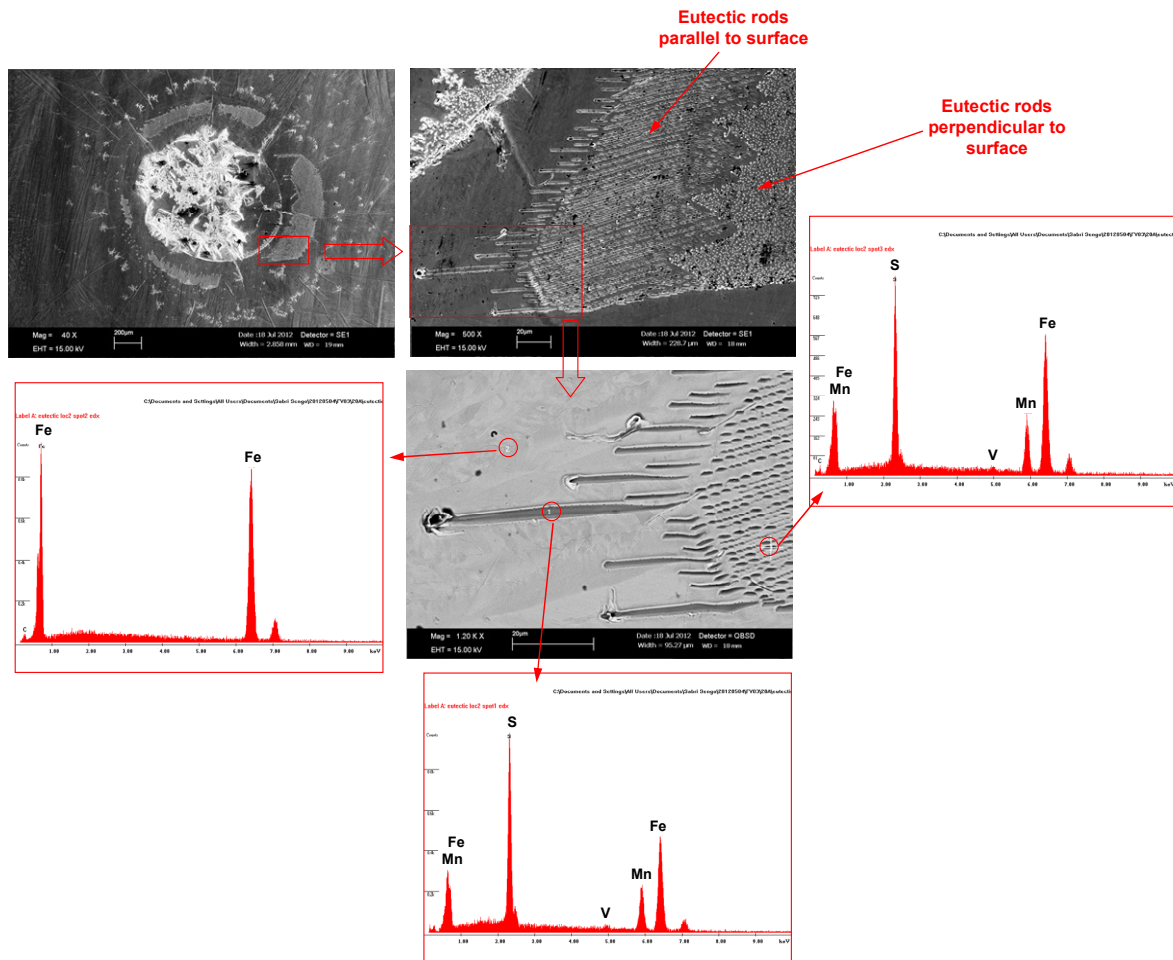


Figure 3.32. Detail and EDAX of the fine “eutectic” structure found at the surface of the 20°C/min sample.

HSLA steel

Almost the same solidification behaviour as the LR_HSLA is displayed at the HSLA grade (see Figure 3.33). However, the non-metallic particles encountered in these samples are richer in their composition, an obvious result, considering that this steel grade has a considerable amount of alloying elements (see Figure 3.34).

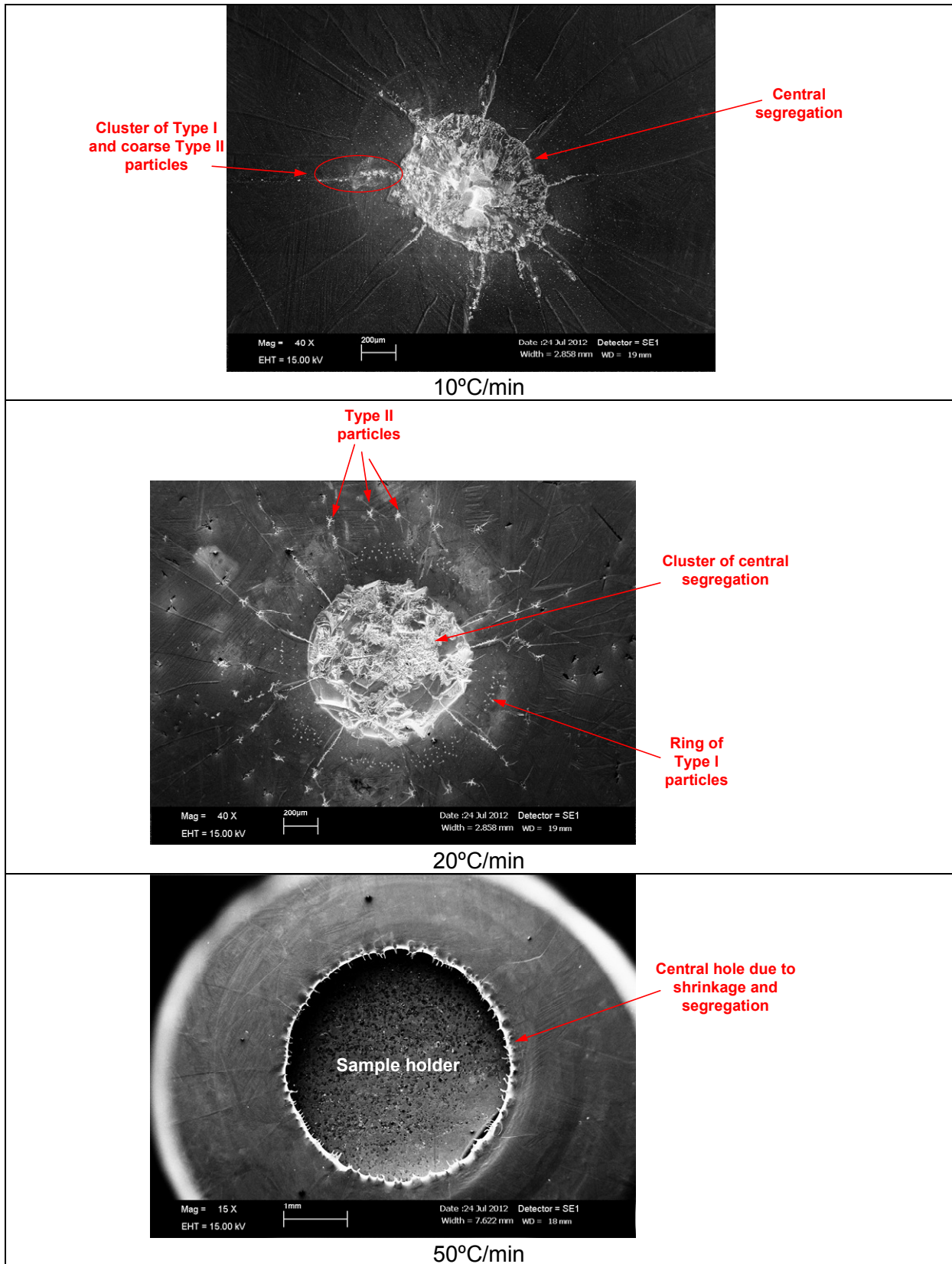


Figure 3.33. Overview of the surface of the 10, 20 and 50 °C/min tested specimens for the HSLA steel grade.

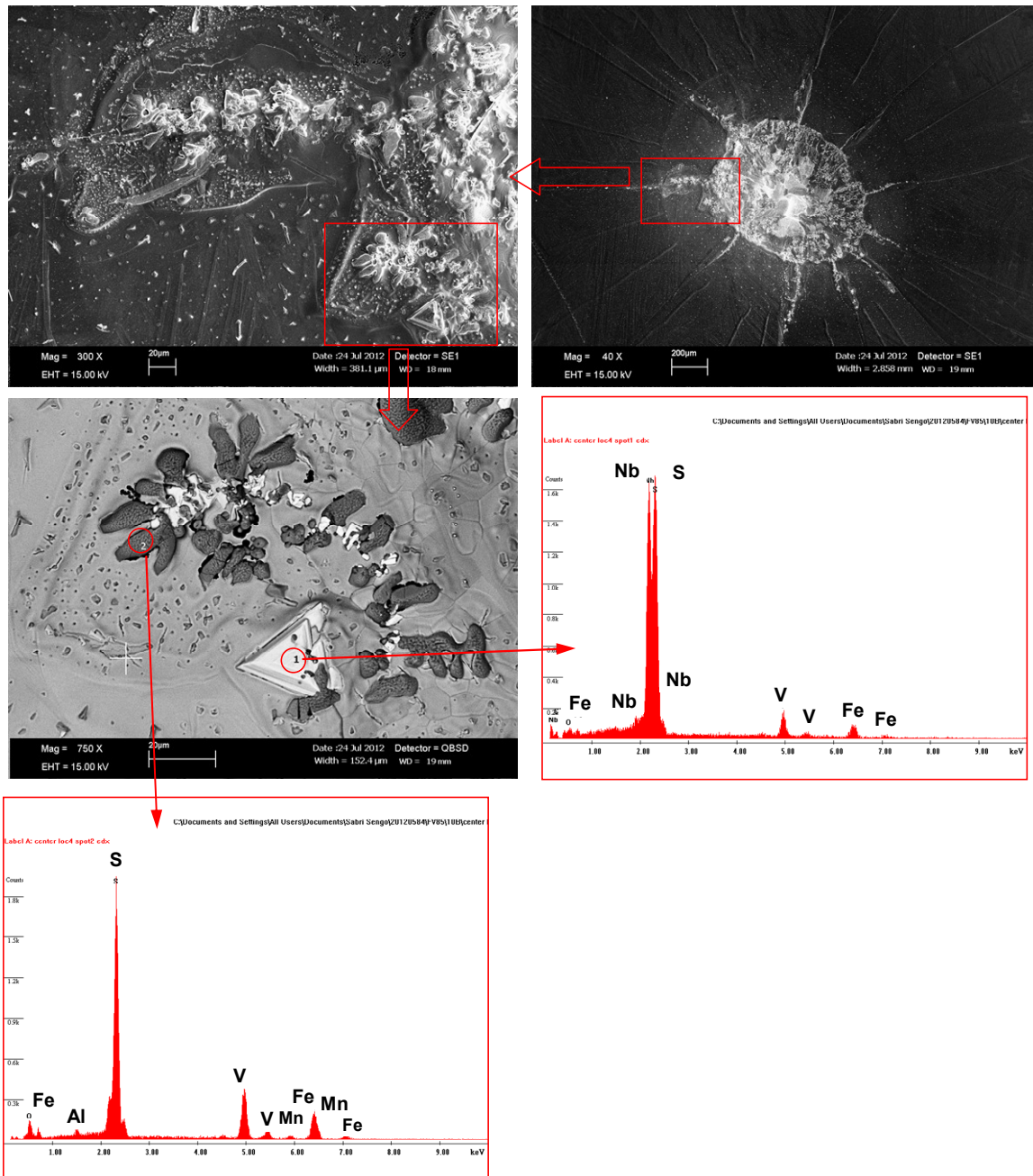


Figure 3.34. Detail and EDAX of the type I and II particles found near the centre of the sample at the surface of the 10°C/min tested specimen.

Nevertheless, there is a noticeable difference in the samples tested at high cooling rates (50°C/min), where the solidification shrinkage is so evident that it shows an empty circle at the centre of the sample, having as post-mortem sample a ring instead of a disc (see Figure 3.35). At the internal boundary of that ring it is not possible to see the elements concentrated as expected due to the end of solidification. In addition, there is no evidence that shows sticking of the centre of the sample or during extraction of the disc after testing, the disc could have been detached, leaving the centre attached to the crucible-sample's holder and the steel ring as a separate part.

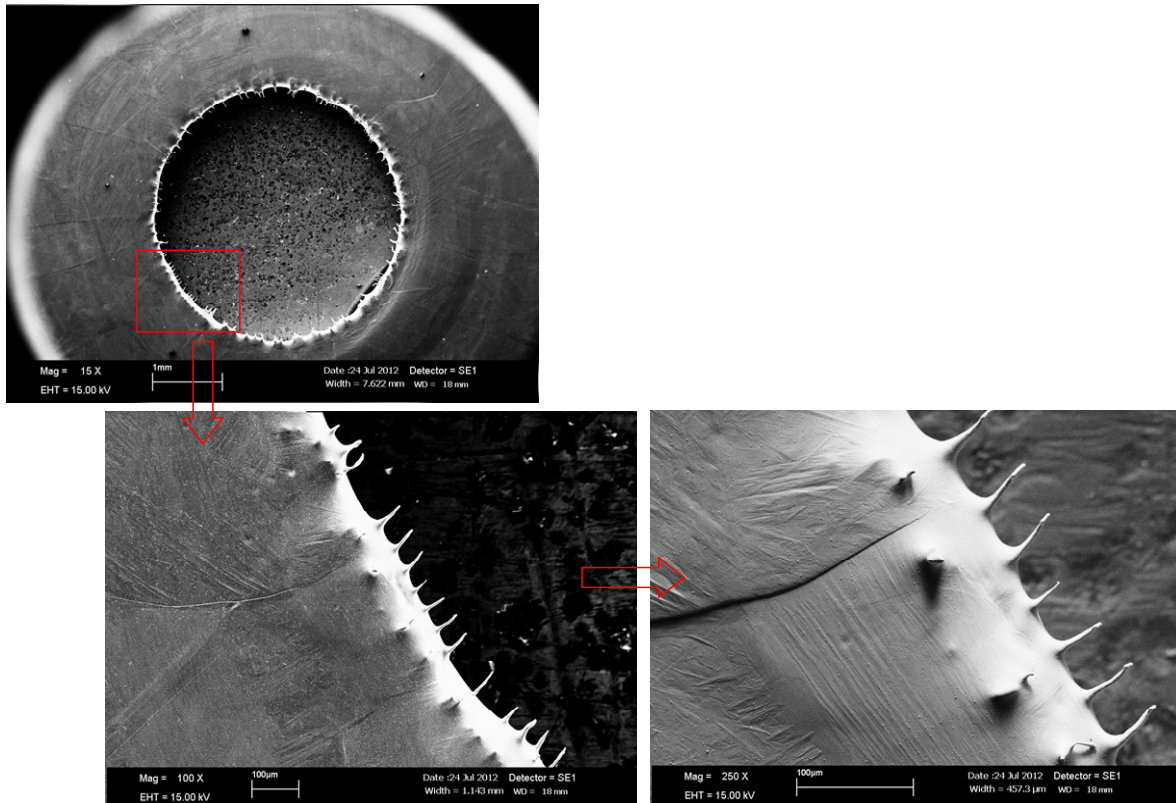


Figure 3.35. Overview of the internal border of the ring at the sample's centre from the 50°C/min specimen.

3.4.4 EPMA analysis in the Concentric Solidification samples

After SEM analysis of the disc's surface, they were cut in half following the transverse direction, and the elements present in the steel were measured with EPMA analysis.

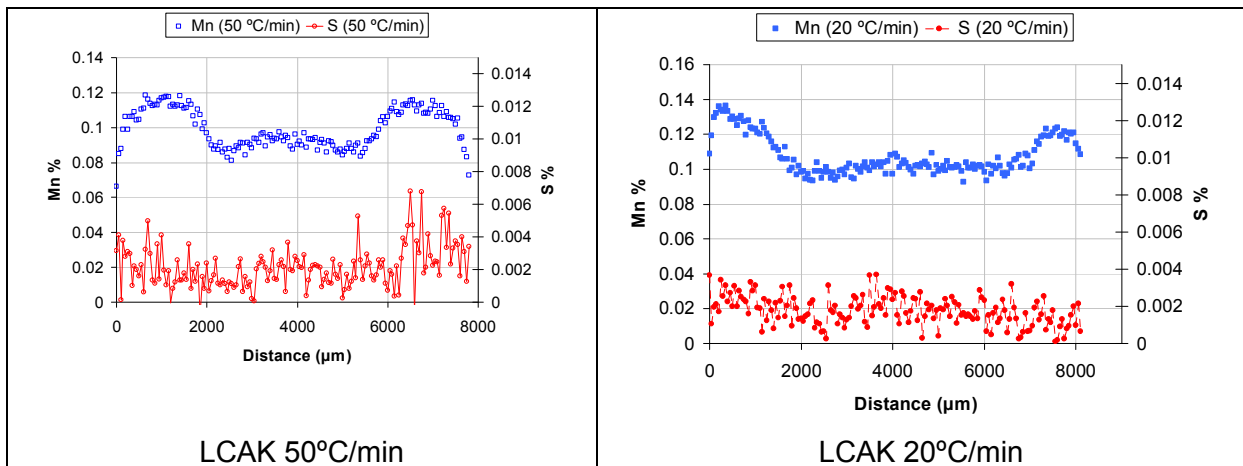


Figure 3.36. Mn and S % in the LCAK steel of the disk's samples

For all steels it is noticeable that at the point where the MnS particles are found at the surface of the samples, the Mn composition in the steel has a distinctive reduction, as a result of segregation and precipitation in the form of MnS at the surface. However, in the LCAK grade the S content does not seem to be affected by this Mn reduction in composition.

For the LR-HSLA grade it is relevant as here the reduction of Mn content is accompanied with a slight increase in S content. This could be due to the solubility changes due to the higher Mn content in the LR-HSLA steel grade in comparison with the LCAK (HSLA grades have 4 times more Mn in their composition than LCAK).

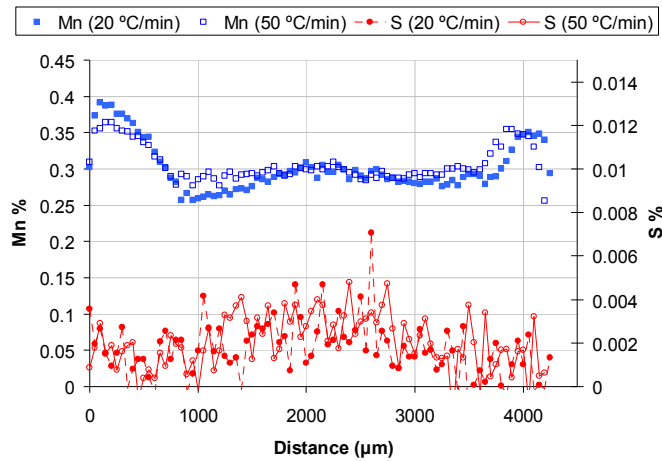


Figure 3.37. Mn and S % in the LR-HSLA steel of the disk's samples

Steel grades with high Mn content, or in other words, with a high Mn/S ratio, are not embrittled due to MnS segregation because the solubility of MnS is less and the conditions of precipitation favour the precipitation of MnS in the matrix^[28]. In steels with high Mn content there is an additional factor that favours MnS precipitation in the matrix, i.e., for a given temperature below the MnS solubility line, the degree of supercooling for precipitation will increase with increasing manganese.

On the contrary, for steels with a low Mn/S ratio, like the LCAK, the Mn/S ratio is low enough to nucleate and form fine precipitates or fine liquid droplets interdendritically. Further, as solidification continues, resulting in low ductility along the grain boundaries; which in either case, they serve as an easy path for crack propagation^[28].

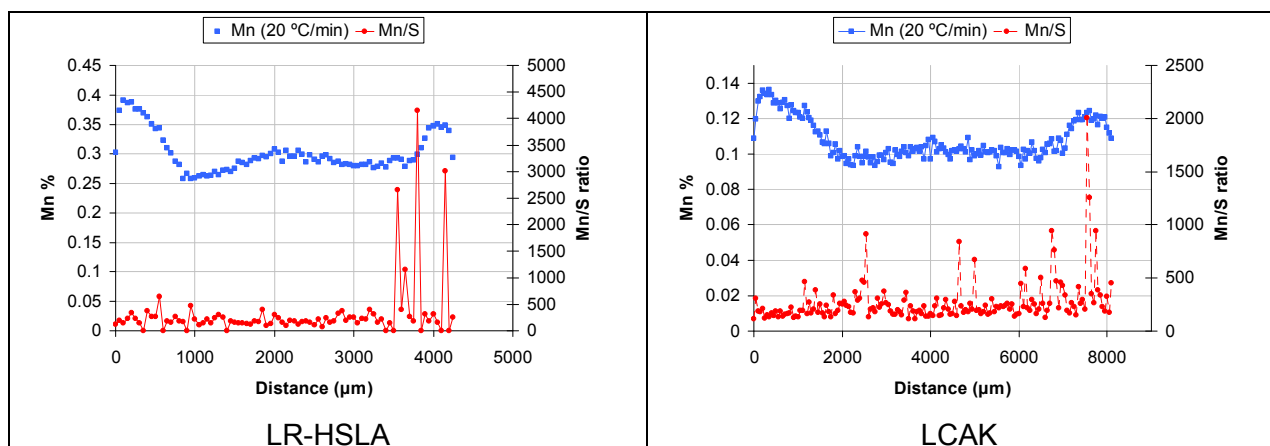


Figure 3.38. Mn/S ratio for the measured Mn and S content in the steel of the LCAK and LR-HSLA grades tested at 20°C/min.

The calculated Mn/S ratio based on the EPMA measured composition shows this trend; for the LR-HSLA it seems to be quite high in some parts of the sample. On the other hand, for

the LCAK samples, the Mn/S ratio is lower and stable through the whole line scan. For comparison, an example of the 20°C/min samples for the LCAK and LR-HSLA grades is shown in *Figure 3.38*. As Mn precipitates out, it will take out the S in 1:1 atomic proportions, thus if the S profile has not been affected by the MnS precipitation, which is the case of the LCAK, means there is still more S present but will precipitate out in such a way that the level measured stays within the scatter.

3.4.5 Growth restriction in the Concentric Solidification samples

As explained previously in Chapter 2, Section 2.6.6, solute elements affect the dendrite growth and builds up a constitutionally undercooled zone in front of the interface. This undercooled zone facilitates nucleation and the new grain does the same to the next grain. The shape and magnitude of the constitutionally undercooled zone depend upon the dendrite growth, which is affected by solute elements, which in turn affects the subsequent nucleation behaviour^[29].

There are two reasons that can be proposed to explain why solute elements are essential for grain refinement. First of all, segregating elements act to restrict the growth of already existing solid/liquid interfaces so that there is more time for nucleation events to occur. This would be of importance if nucleation was spontaneous and non-directional. But probably of greater importance is that the segregating elements lead to a constitutionally undercooled zone in front of the interface. This constitutionally undercooled zone activates the nucleating particles in front of the interface, hence, interrupting the growth of the previous grain^[29].

During the frame-by-frame analysis of the recorded video's it is possible to observe only for the HSLA and LR-HSLA grades the appearance of nucleation events ahead of the solidification front. Some of them do remelt as the solidification advances, but there is possible to distinguish two types that do remain stable upon cooling; the ones who visually have another colour, highly probable that are of a different composition, thus non-metallic particles, and the nuclei that seem to be δ -ferrite. An example of these observations is shown in *Figure 3.39*.

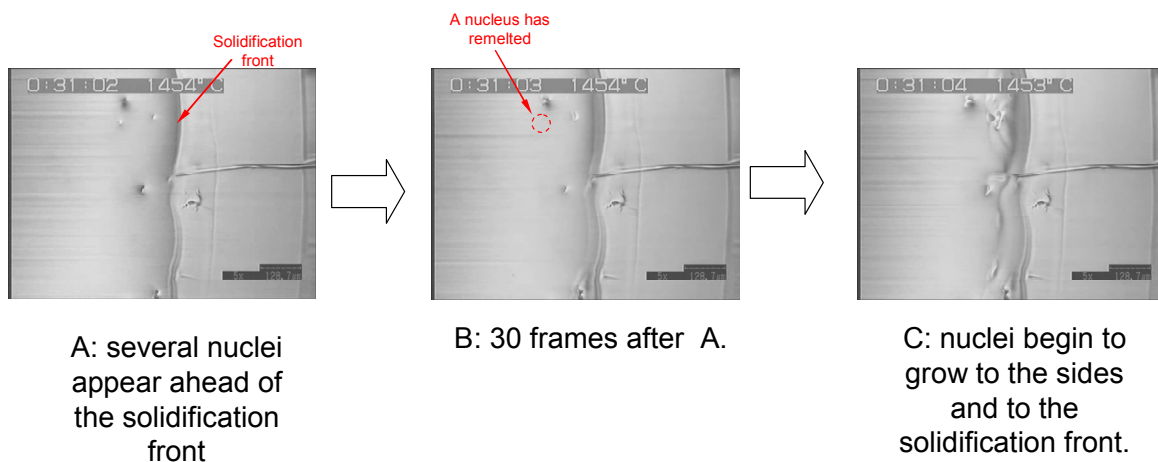


Figure 3.39. Nuclei growing and remelting ahead of the main solidification front. Snapshots taken from the HSLA steel tested at 50°C/min.

The non-metallic particles generate a very unstable solidification front, affecting the solidified structure which consequently has a very rough surface (see *Figure 3.40*).

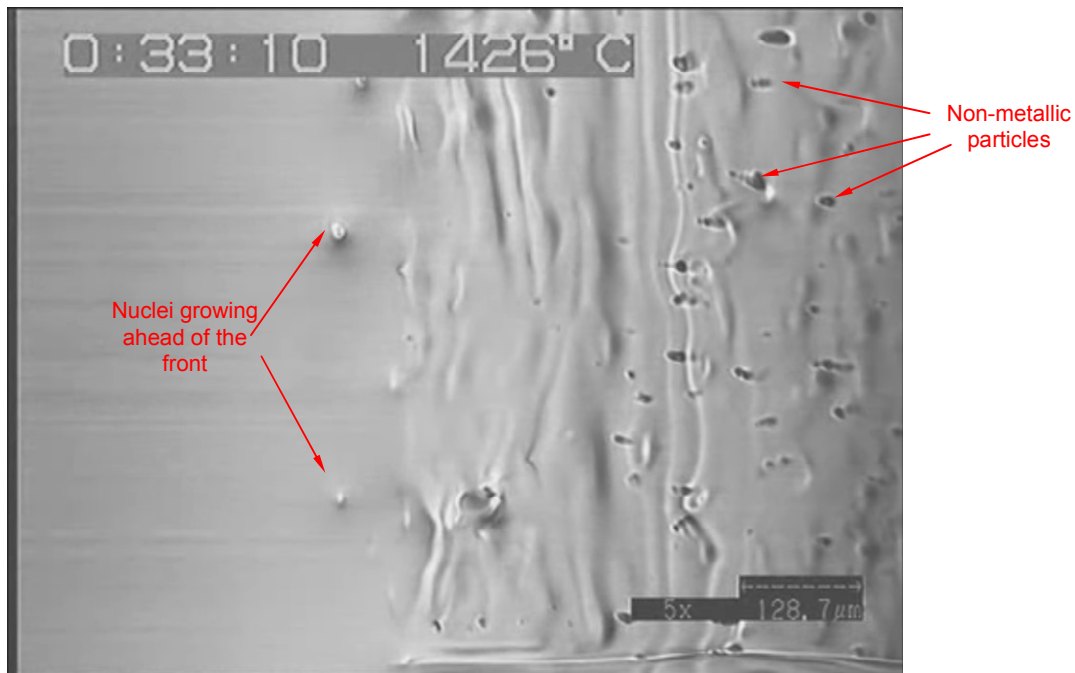
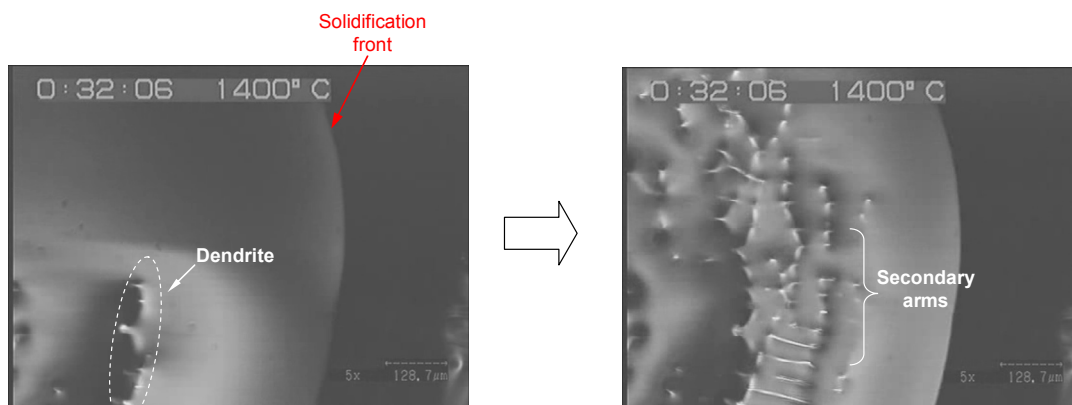


Figure 3.40. Non-metallic particles in the matrix and nuclei growing ahead of the main solidification front. Snapshots taken from the LR-HSLA steel tested at 50°C/min.

The δ -ferrite nuclei do sometimes further grow in a dendritic structure, where the primary arms are sometimes followed by the growth of secondary arms (see *Figure 3.41*). Dendrites growing ahead of the solidification front has been also observed by Reid et al ^[23], while analysing peritectic steel grades.



A: A dendrite developing ahead of the front

B: Secondary dendrite arms are visible after 3 frames

Figure 3.41. Dendrite developing secondary arms ahead of the main solidification front. Snapshots taken from the LR-HSLA steel tested at 50°C/min.

Both the non-metallic particles and the δ -ferrite nuclei are a sign that growth restriction occurs during solidification of these steel grades, thus is possible that the observed

microstructure refinement compared with that of the LCAK is due to the extra addition of alloying elements.

3.5 Concluding remarks: what additional studies are required for further hot cracking assessment of steels

Even when the equilibrium phase diagrams show very little differences in the three steel grades, the statistical analysis contradicts this fact. However, some indications in the DSC-DTA analyses of the LCAK and HSLA could be the input to analyse the hot tearing susceptibility due to an effect of alloying elements in the composition. The Concentric Solidification Technique studies can lead to an understanding of the LCAK hot tearing susceptibility due to the presence of MnS liquid films at low temperature; and the result of the peritectic susceptibility of the LR-HSLA is an indication of the weakness to cracking of this steel grade.

But more evidence is needed, thus a microstructure study, including microstructure modelling; and hot tensile testing will assist in complete understanding of the hot tearing susceptibility of these alloys under study. Not to forget, it is also important to learn the underlying mechanism of the strength during solidification of the HSLA to possibly modify other alloy compositions to make them less susceptible to cracking during solidification.

References

1. *Statistical methods in research and production*, 4th Revised Edition, Davies, O. L. and Goldsmith, P. L., Essex, UK, 1986, Longman Group Ltd.
2. Dantzig J.A. and Rappaz, M., *Solidification*, 1st Edition, EPFL Press, Laussane, Switzerland, 2009, CRC Press.
3. Kattner, U. R., Boettinger, W. J., and Banerjee, D., *Scheil Solidification Calculations*, The National Institute of Standards and Technology (NIST), 2013,
4. Arnberg, L., Bäckerud, L., Chai, G., and Thomas, S. P., *Solidification characteristics of aluminum alloys*, Department of structural chemistry, Arrhenius Laboratory University of Stockholm, 1996, American Foundrymen's Society.
5. Jiang, H., Kierkus, W. T., and Sokolowski, J. H., *Determining Dendrite Coherency Point Characteristics of Al Alloys Using Single-Thermocouple Technique*, Transactions of the American Foundrymen's Society, 107 , 1999, 169-172.
6. *A Guide to the solidification of steels*, Stockholm, Sweden, 1977, Jernkontoret.
7. Ruiz Mondragon, J. J., Herrera Trejo, M., de Jesus Castro Roman, M., and Solis, T., *Description of the hypo-peritectic steel solidification under continuous cooling and crack susceptibility*, ISIJ International, 48 (4), 2008, 454-460.
8. Differential Scanning Calorimetry (DSC) - Theory and Experimental conditions, <http://www1.chm.colostate.edu/Files/CIFDSC/dsc2000.pdf>.
9. Boettinger, W. J., Kattner, U. R., and Moon, K-W, *DTA and Heat-flux DSC Measurements of Alloy Melting and Freezing*, Special Publication -15th Edition, Washington DC, USA, 2006, National Insitute of Standards and Technology (NIST), Technology Administration, U.S.Department of Commerce.
10. Kerr, W., Cisse, J., and Bolling, G. F., *On equilibrium and non-equilibrium peritectic transformations*, Acta Metallurgica, 22 (6), 1974, 677-686.
11. Dippenaar, R., *The Peritectic Phase Transition in Steel*, Presentation to Corus RD&T , 2008,
12. Stefanescu, D. M., *Microstructure evolution during the solidification of steel*, ISIJ International, 46 (6), 2006, 786-794.
13. Howe A. and Apel, M., *VESPIISM – Virtual Experiments to Solve Problems in Steel Metallurgy*, Deliverable D12: "Peritectic /Thin Slab Casting Simulation, EU Project code GRD1-2000-25447 , 2004,
14. Carless, S., Kamperman, A., Westendorp, A., and Brockhoff, J., *Optimization of Surface Quality Through Mold Thermal Monitoring*, Iron & Steel Technology, 8 (7), 2011, 84-92.

15. Shibata, H., Arai, Y., Suzuki, M., and Emi, T., *Kinetics of peritectic reaction and transformation in Fe-C alloys*, Metallurgical and Materials Transactions B, 31 (5), 2000, 981-991.
16. EGKS Project, *Improving the surface quality of continuously cast semis by an understanding of the Shell development and growth*, EU, Project code 7210.PA/209 , 2000, 1-120.
17. SMS Siemag, www.sms-siemag.com, 2013,
18. EGKS Project, *Segregation and phase distribution during solidification of carbon, alloy and stainless steels*, EU, Projectcode 7210.CF/801 , 1989
19. Blazek, K. E., Lanzi, O., Gano, P., and Kellogg, D., *Calculation of the Peritectic Range for Steel Alloys*, AISTech 2007, 2007
20. Howe, A. A., *Micro-Segregation in Multicomponent Steels Involving the Peritectic Reaction*, PhD, The University of Sheffield, 1993.
21. Howe A., QSP calculations, Personal Communication.
22. Böttger, B, Apel, M., Santillana, B., and Eskin, D., *Phase Field Modelling of Microstructure Formation and Hot Cracking Susceptibility during Continuous Casting of Low Carbon and HSLA Steels*, Materials Science & Engineering - Conference Series, 33 , 2012
23. Reid, M., Phelan, D., and Dippenaar, R., *Concentric solidification for high temperature laser scanning confocal microscopy*, ISIJ International, 44 (3), 2004, 565-572.
24. Aminorroaya, S., Reid, M., and Dippenaar, R., *Simulation of microsegregation and the solid/liquid interface progression in the concentric solidification technique*, Modelling and Simulation in Materials Science and Engineering, 19 (2), 2011, 025003-
25. Moon, S. C., Dippenaar, R., and Lee, S. H., *Solidification and the δ/δ phase transformation of steels in relation to casting defects*, 27, 2012, IOP Publishing.
26. Flemings, M. C. and Kattamis, T. Z., *Investigation of Solidification of High-Strength Steel Castings*, Report Nr. AMMRC CR 63-04/F, Department of Metallurgy and Materials Science, Massachusetts, USA, 1968, Massachusetts Institute of Technology.
27. Flemings, M. C. and Bigelow, L., *Sulfide Inclusions in Steel*, Metallurgical and Materials Transactions B, 6 (2), 1975, 275-283.
28. Lankford, W. T., *Some considerations of strength and ductility in the continuous-casting process*, Metallurgical and Materials Transactions B, 3 (6), 1972, 1331-1357.
29. Easton, M. and StJohn, D., *Grain refinement of aluminum alloys: Part I. The nucleant and solute paradigms—A review of the literature*, Metallurgical and Materials Transactions A, 30 (6), 1999, 1613-1623.

Chapter 4

Thermo-mechanical behaviour of commercial steel grades for thin slab continuous casting

Cracking in continuously cast steel slabs has been one of the main problems in casting for decades. In recent years, the use of computational models has led to a significant improvement in caster performance and product quality. However, these models require accurate thermo-mechanical properties as input data which are either unreliable or non-existent for many alloys of commercial interest. A major reason for this lack of reliable data is that high temperature mechanical properties are difficult to measure. Several methods have been developed to assess the material strength during solidification, especially for light alloys.

The tensile strength during solidification of the three steel grades considered in this thesis from Tata Steel Mainland Europe –DSP plant in IJmuiden, the Netherlands, have been studied by a technique for high temperature tensile testing developed at Sumitomo Metal Industries, Japan. The experimental technique enables a sample to melt and solidify without a crucible, making possible accurate measurement of load over a small solidification temperature range.

In the present study, the tensile test results are analysed and the characteristic zero-ductility and zero-strength temperatures are determined for all the grades.

4.1 Hot tensile test of commercial steel grades at different temperatures

4.1.1 Introduction

Cracking during solidification of continuously cast steel slabs has been one of the main problems in casting for many years. Many of the cracks that occur during solidification are hot tears.

In recent years, the use of computational models has led to a significant improvement in insight in caster performance and product quality. However, these models require accurate thermo-mechanical properties as input data which are often unreliable or even non-existent for many alloys of commercial interest ^[1]. Moreover, the thermo-mechanical properties of steels are still poorly known at high temperatures, close to the solidus.

A major reason for this lack of reliable data is that high temperature mechanical properties are difficult to measure. Several methods developed to assess the material strength during

solidification and close to the solidus, particularly for aluminium alloys ^[2], could be adapted for steel.

On the other hand, the problem of hot tearing during continuous casting of steels has been extensively studied in the literature from the viewpoint of the casting process. Numerous studies refer to the influencing process parameters, such as chemical composition, cooling rate or strain rate. The treatment of hot tearing in steels has some peculiarities as compared to aluminium alloys. This is mostly related to the specific solidification structure that is formed during steel solidification.

Equiaxed grain structures behave somewhat differently from the columnar structures of dendrites. The arrangement of grain boundaries is random, causing the topology of any remaining liquid films to be very intricate. The gradual transition of a continuous liquid with isolated grains or clusters to a solid network with isolated droplets or films of liquid is called “percolation” ^[3]. At this point, if strain is applied and separation of grains occurs, the isolated liquid droplets can form liquid bridges observed at the fractures.

The development of mechanical strength of the semi-solid steel can be characterized by two temperatures that also determine the hot cracking susceptibility of particular steel.

As we have already discussed in Chapter 2, the Zero Strength Temperature (ZST) is defined as the temperature during cooling at which forces can first be transmitted perpendicular to the solidification direction ^[4]. This ZST corresponds to a fraction of solid (f_s) in the range of 0.65 to 0.80. At this range, because a segregated liquid film still exists between the dendrites, a small strain leads to cracking. This results in a crack or segregate-rich zone depending on whether or not liquid steel can still flow between the dendrites.

As the steel solidifies and cools further the strength and ductility of the material increases and at some point the material acquires plasticity ^[4]. The temperature at which the transition occurs from brittle to ductile behaviour is known as the Zero Ductility Temperature (ZDT) and is commonly associated with a fraction of solid (f_s) between 0.98 and 1.

The range between the ZST and ZDT is defined as the brittle temperature range (ΔT_B) and gives a qualitative guide to hot crack sensitivity ^[2,5].

$$\Delta T_B = \text{ZST} - \text{ZDT}. \quad (4.1)$$

The wider the range, the longer the period of time (at a constant cooling rate) that the semi-solid steel stays in this critical range, and the larger the stress concentration resulting from the thermal contraction restriction. It can be stated that the tendency to crack formation depends on the brittle temperature range of the alloy ^[2,5]. The application of this or any other hot tearing criterion is hindered by the lack of factual data on the mechanical properties of solidifying steels.

The ability to predict at least the tendency of hot tearing of solidifying steel is of great interest due to the continuous trend towards increased casting productivity by increasing casting speed, combined with higher quality demands, and the development of new steel grades.

This chapter is aimed at demonstrating the possibility of high-temperature tensile testing of steels and its application to the analysis of the hot tearing phenomenon.

4.1.2 Testing methodology

Tensile tests were performed in a temperature range from 1100°C to 1520°C using the apparatus shown in Figure 4.1.

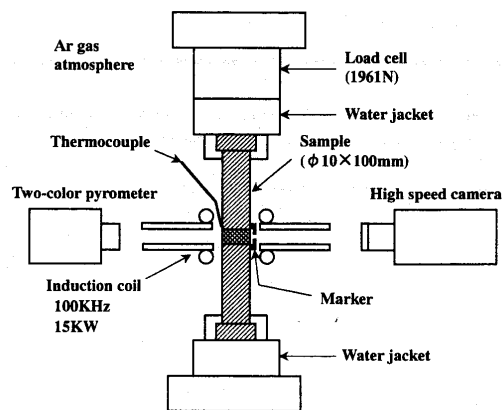


Figure 4.1. Scheme of the hot tensile test apparatus.

The testing rig is placed in a vessel that is, prior to test, evacuated by a diffusion pump to 1×10^{-3} (Pa) and then filled with argon. The high temperature tensile test apparatus is an assembly of a high frequency induction coil, a loading cell and a two-colour optical pyrometer [6-9]. The diameter of the sample is 10 mm and the length is 100 mm. [6-9].

The central region of 5 mm in length of the sample is melted by high frequency induction heating, and the load is applied and measured after reaching the prescribed conditions. The gravity force does not influence the measured load because the shape of the molten zone is maintained by the surface tension and the electromagnetic force.

The temperature of the molten zone is controlled by an R-type thermocouple welded to the sample surface at 5 mm from the molten zone. In addition, a two-colour optical pyrometer is used to control the temperature together with the R-type thermocouple.

The temperature of the molten zone is estimated using the regression line obtained in advance from a series of separate experiments where the relation between the temperature of molten zone and the control point has been determined [6-9]. The regression line is calculated using a set of samples equipped with a thermocouple in the centre of the sample, a thermocouple in the normal control location that is linked to the thermal controller, and the pyrometer. The procedure is to measure with all these devices every 100°C during heating the samples from 900°C to 1400°C and during cooling to 900°C. For the actual testing at

different temperatures, the controller is set including the error according to the regression line. The regression formula used is given in equation (4.2).

$$ST=1.017CT+7.4907 \quad (R^2=0.9988) \quad (4.2)$$

where ST is the sample thermocouple temperature and CT is the controller temperature.

The sample was heated, melted and solidified sequentially according to the control conditions of the high temperature tensile test. The temperature of the controlled zone was raised from room temperature to 30°C below the solidus temperature and maintained at this temperature for 30 seconds, and then the temperature was raised to 30°C above the liquidus temperature and maintained for 120 seconds to establish the steady state. Afterwards, the sample was cooled at a cooling rate of 0.17 (K/s). When the temperature of the molten zone reached a preset temperature, the sample was pulled at a strain rate of 1×10^{-2} (1/s).^[6-9]

After testing, the samples were cooled by turning off the heating coil until reaching room temperature inside the chamber.

The purpose of the high temperature range test is to measure the material strength in the solidification region, thus mimicking the mould region of a continuous caster.

Two sets of tests have been carried out. In the first set, one measurement was taken every 20°C and some uncertainties arose, leading to the second set of tests with one sample tested every 10°C starting from equilibrium solidus temperature. In addition, in the second set of tests, the elongation of the samples was estimated, from recorded displacement of the sample during testing.

From the tensile test data, the measured forces can be converted into nominal stress, if the area of the load is known, with the following equation:

$$\sigma = \frac{F}{A} \quad (4.3)$$

where: σ is the nominal tensile stress (Pa), F is the force to pull the sample (N), and A is the loaded area (m²).

Following the findings of Nakagawa et al.^[10], the loaded area is taken as the cross section area of the samples. It was not possible to evaluate the instantaneous area during testing (reduction of area). However, considering that there is no ductility in the brittle temperature range, the area of the sample will be nearly the same until failure.

This instantaneous gauge length (elongation with respect to the starting set point measured by displacement of the sample during testing), gives a non-zero starting point for the measurement. Consequently for the test results the point of Zero Ductility Temperature has non-zero elongation values, instead it is better to name this point as Minimum Ductility Temperature (MDT) for the test results analysed in this study.

The engineering stress-strain curve does not give a true indication of the deformation characteristics of a material because it is based entirely on the original dimensions of the specimen, and these dimensions change continuously during the test. Thus, measures of stress and strain which are based on the instantaneous dimensions are needed.

In plastic deformation the strains are frequently large, and during the extension the gauge length changes considerably. In the definition of true strain the change in length is referred to the instantaneous gauge length, rather than the original gauge length (see *Table 4.1*).

True stress is the load at any instant divided by the cross sectional area over which it acts. The engineering stress, or conventional stress, is the load divided by the original area.

In considering elastic behaviour it was not necessary to make a distinction, but in plasticity, particularly when dealing with the mathematics of the tension test, it is important to distinguish between these two definitions of stress (see *Table 4.1*).

Table 4.1. Formulae for true and engineering stress and strain.

	True	Engineering
Stress	$\sigma = \frac{F}{A}$	$s = \frac{F}{A_0}$
Strain	$\varepsilon = \ln \frac{L}{L_0}$	$e = \frac{\Delta L}{L_0}$

The engineering stress–strain curve does not give a true indication of the deformation characteristics of a material because it is based entirely on the original dimensions of the specimen, and these dimensions change continuously during the test. Thus, measures of stress and strain which are based on the instantaneous dimensions are needed.

The true stress can be determined from the engineering stress by the constancy of volume as follows ^[11]:

$$\sigma = \frac{F}{A} = \frac{F}{A_0} \frac{A_0}{A} = \frac{F}{A_0} (e + 1) = s(e + 1) \quad (4.4)$$

Here and in *Table 4.1*: σ is the tensile stress (Pa); F is the force to pull the sample (N); A is the loaded area (m²); A_0 is the original area (m²); L is the instantaneous gauge length (m); L_0 is the original gauge length (m); s is the engineering stress (Pa); ε is the True strain(m/m); and e is the engineering strain (m/m).

From the tensile data, having the load force, and instantaneous gauge length (elongation with respect to the starting set point measured by displacement of the sample during testing), the curves true stress and true strain for each temperature can be constructed.

4.1.3 Results and Discussion

The results of tensile testing are considered to be representative based on the previous experience of Sumitomo Metal Industries ^[8].

The fracture surfaces of tested specimens were preserved after testing and studied by naked eye and by scanning electron microscopy (SEM). The results were interpreted in terms of possible hot tearing mechanisms. With the test data and the post mortem study under SEM, the brittle temperature range defined is within the temperatures typical of the continuous casting mould.

Compositions of the LCAK, LR-HSLA and HSLA steel grades studied here are listed in *Table 1.1* in Chapter 1.

LCAK

Figure 4.2 shows the tested tensile specimens from 1st set (a) and 2nd set (a). From these figures, we can deduce that the MDT lies in the range from 1390°C to 1400°C and the ZST lies in the range from 1460°C to 1470°C. The elongation (ductility) increase is clearly visible in the sample tested at 1390°C (*Figure 4.2b*).

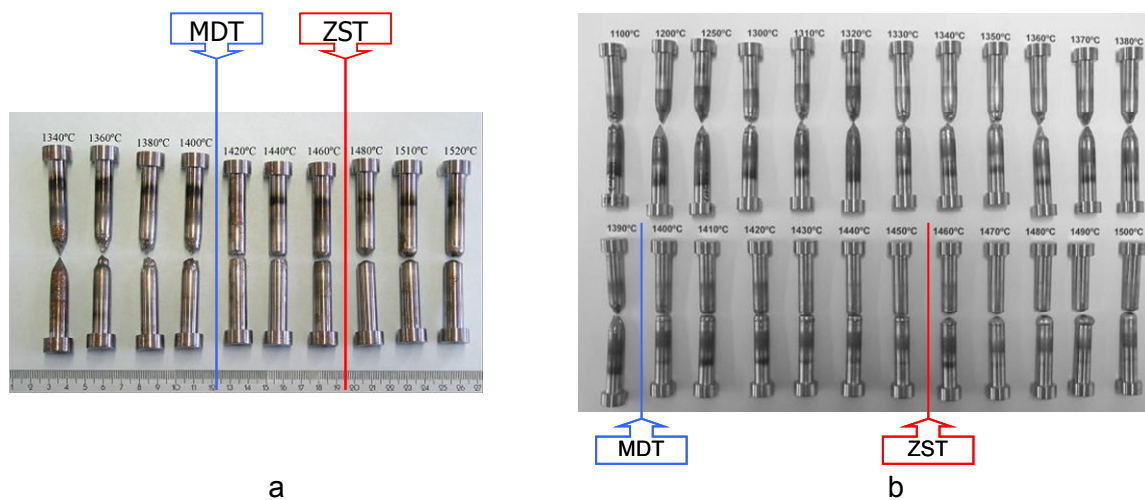


Figure 4.2. Post-mortem samples for the two sets of specimens: a, 1st set and b, 2nd set. Temperature is in degrees Celsius.

There is a difference between both sets of samples for the testing temperature 1400°C. In the 1st set this sample already shows some ductility and elongation; however, in the 2nd test this sample seems to be brittle with a flat fracture.

Nevertheless, this preliminary examination situates the brittle temperature range in almost the same temperature range for both sets, confirming good reproducibility of the test.

The comparison of tensile data for the two tests performed is shown in *Figure 4.3* (dark-green triangles: 1st set of tests; light-green triangles: 2nd set of tests). It can be noted, the accuracy and reproducibility of the data is within the standard error.

Having the displacement data as an instantaneous gauge length for each temperature, it is possible to build the elongation vs. temperature diagram and to determine not only visually with the post-mortem samples (*Figure 4.2*) but also with the actual data the ductility trough involved in the brittle temperature range (see dark-grey triangle points in *Figure 4.3*).

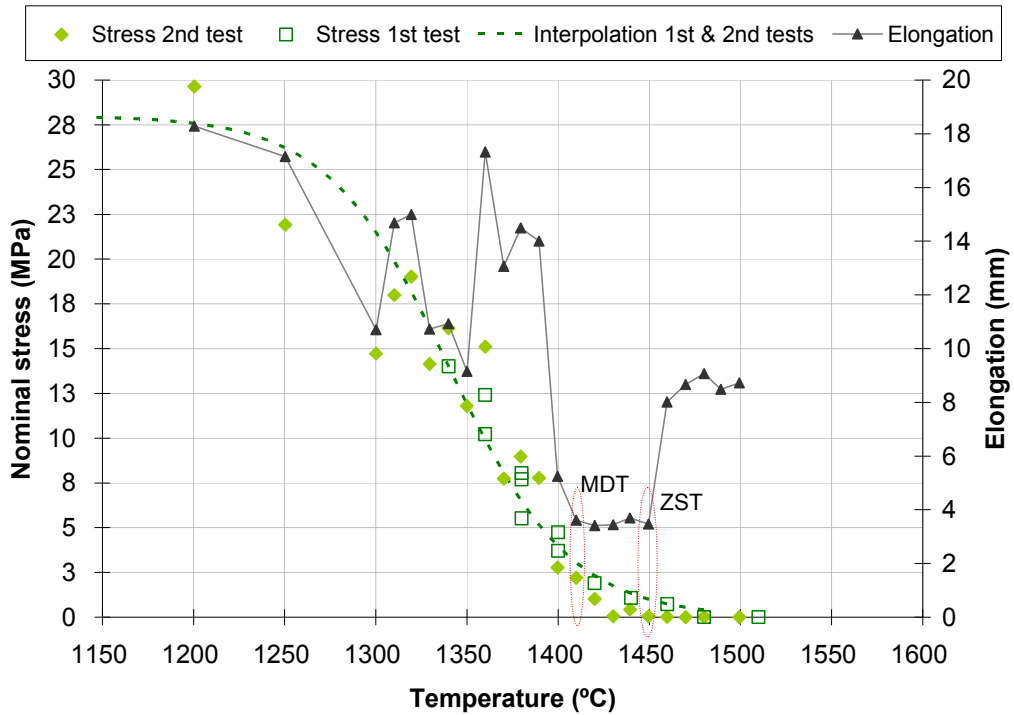


Figure 4.3. Determination of Zero Strength Temperature and Minimum Ductility Temperature for the LCAK steel grade.

The nominal stress shown in *Figure 4.3* is the value for each temperature at the ultimate tensile strength (UTS).

The elongation in the solidification range is minimum at the MDT (which can be around the non-equilibrium solidus) and increases at higher temperatures and to infinity at the liquidus and above. Note: The stress at high temperatures can be too low to be detected and yet enough to strain weak and highly ductile material. Actually, this is not really elongation but fluidity (as the reciprocal of viscosity).

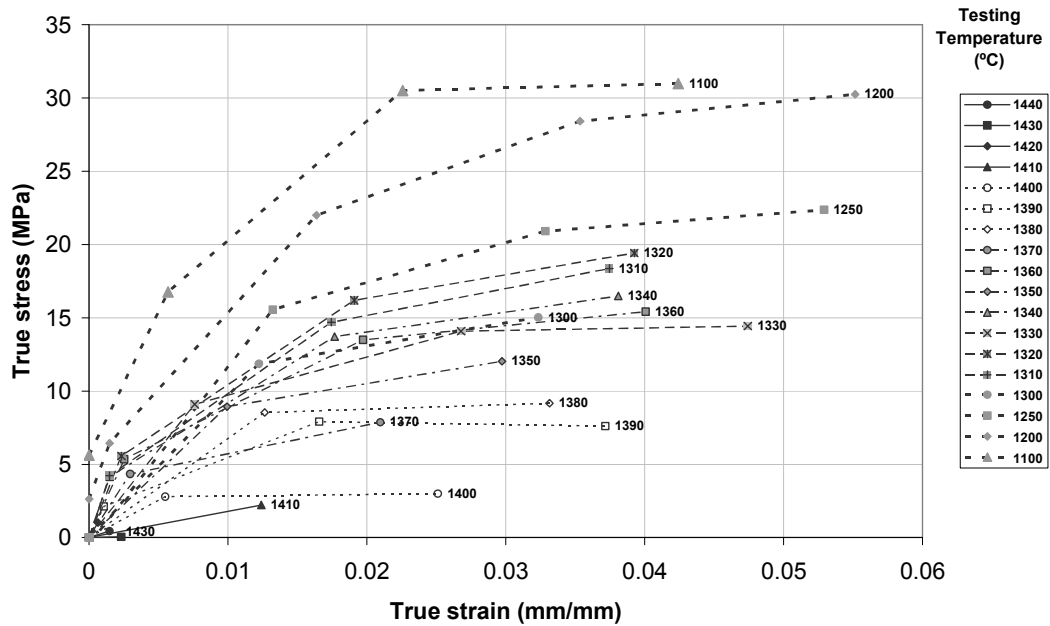


Figure 4.4. True stress-true strain curves for each temperature tested.

The true stress–true strain curves for each temperature (see Figure 4.4) are not only relevant data to determine the actual strength of this steel grade at each temperature, but also important as input data for mathematical modelling.

HSLA

The high temperature region tests were done to assess the material strength in the solidification region.

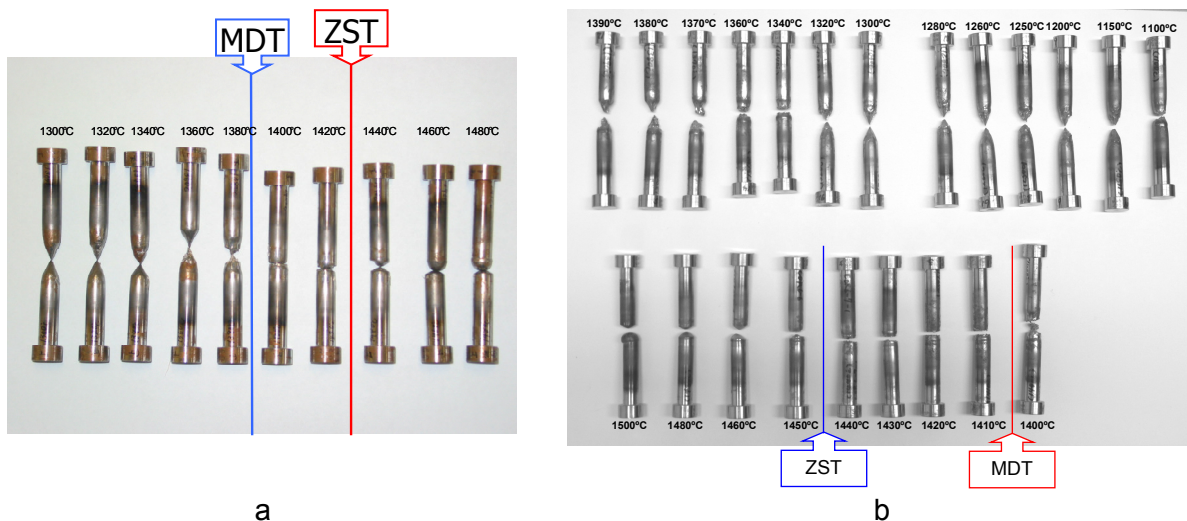


Figure 4.5. Two sets of specimens for the HSLA steel after tensile testing: (a) 1st set and (b) 2nd set.

Figure 4.5(a) shows the tensile specimens after testing from the first set of tests. For this HSLA, the MDT occurs in the temperature region of 1380°C -1400°C and the ZST occurs in the temperature region 1420°C -1440°C. This is evident from the flat fracture surface (no

ductile cone) and no elongation. As the temperature decreases the elongation/ductility increases. This is clearly noticeable in the sample tested at 1360°C.

Figure 4.5(b) shows the post-mortem samples from the second set of tests, again, the MDT occurs in the temperature region 1400°C -1410°C and the ZST occurs in the region 1440°C - 1450 °C. The elongation/ductility increase is clearly visible in the sample tested at 1390°C.

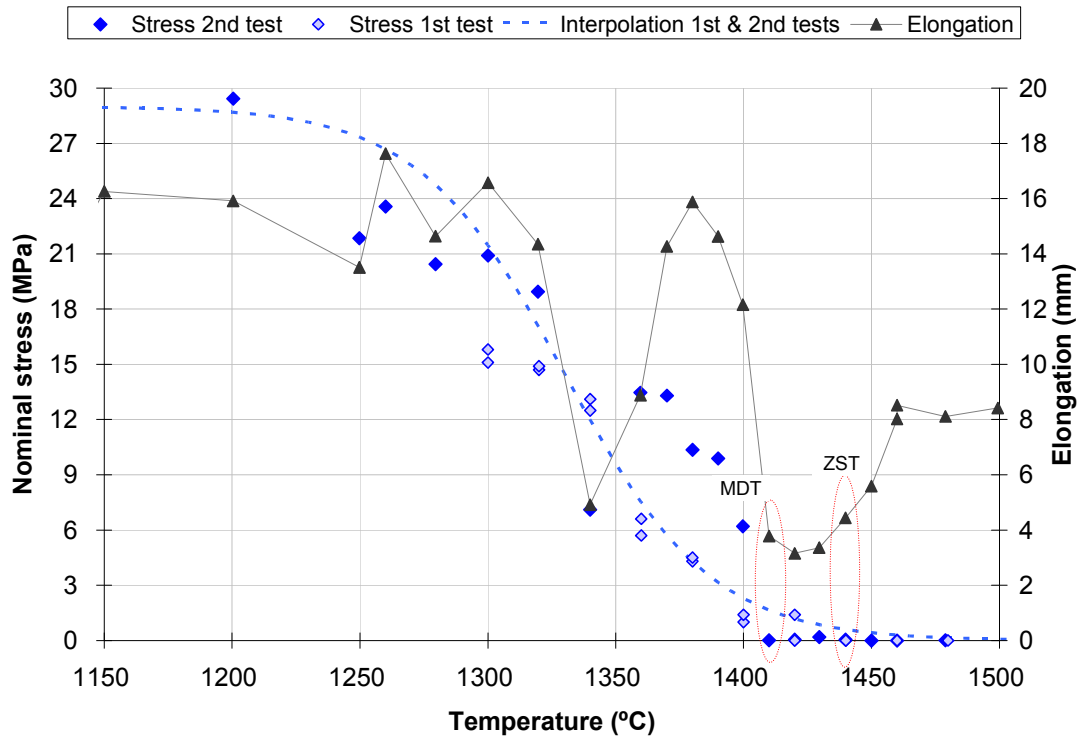


Figure 4.6. Determination of Zero Strength Temperature and Minimum Ductility Temperature for the HSLA steel grade.

There is a difference between both sets of samples in the specimen tested at 1400°C (see Figure 4.6). In the 2nd set of tests this sample already showed some ductility/elongation; however, in the 1st set, this sample showed no ductility/elongation and had a flat fracture. The values shown here in Figure 4.6 are also at UTS.

Nevertheless, the brittle temperature range is in the same temperature region, confirming the good reproducibility of the test.

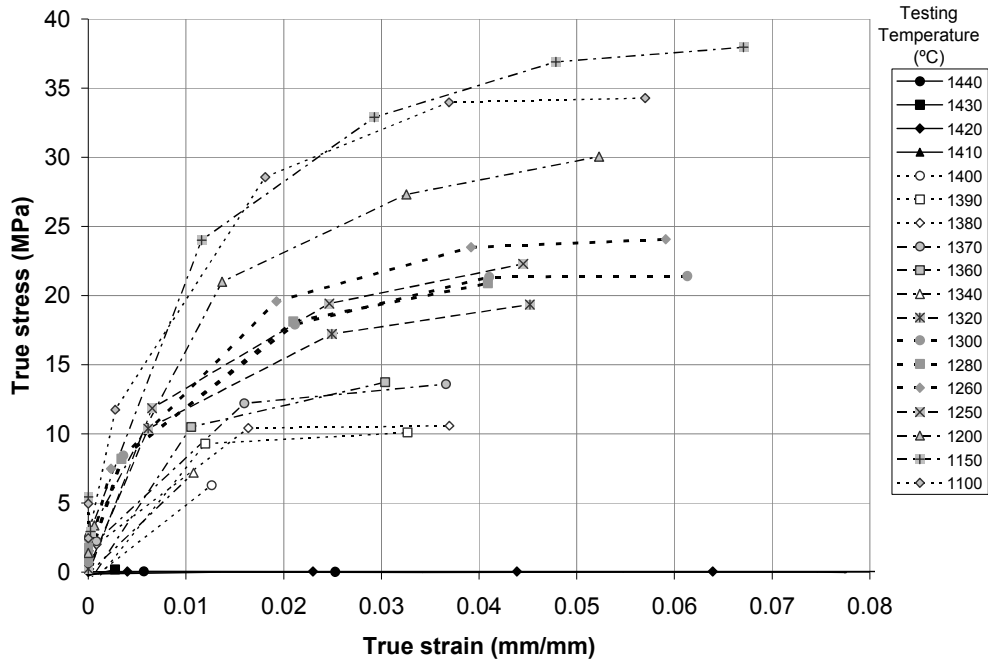


Figure 4.7. True stress-true strain curves for each temperature tested.

With the available data, the true stress-true strain curves are also created for the HSLA steel grade (see Figure 4.7).

LR-HSLA

Considering the good reproducibility of the test carried out on the LCAK and HSLA, it was decided to perform only one set of tests for the LR-HSLA.

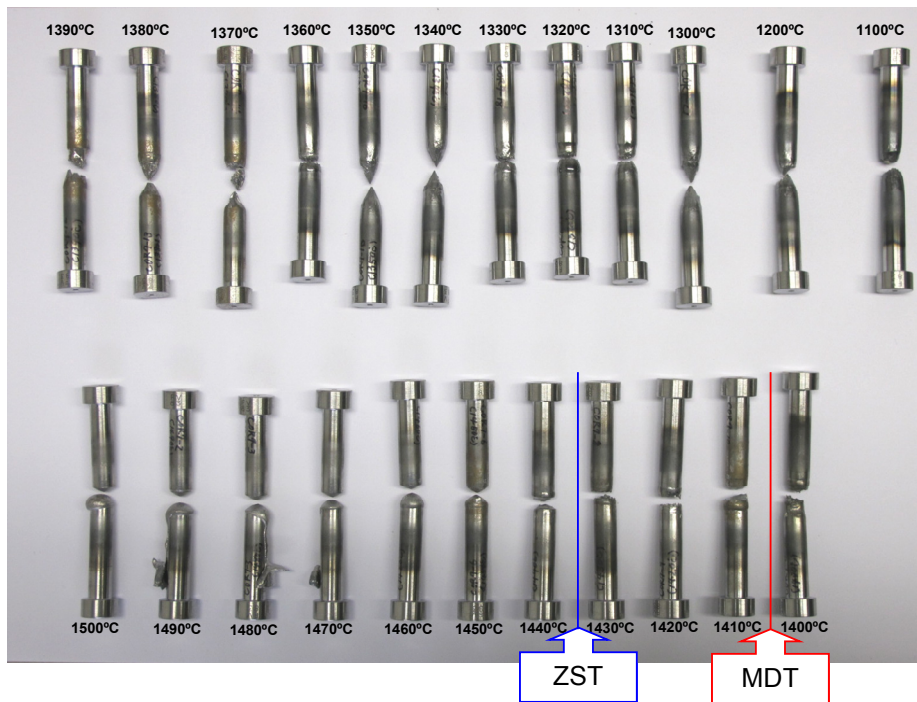


Figure 4.8. Post-mortem samples for the LR-HSLA

Figure 4.8 shows the tensile specimens after testing. For LR-HSLA, the MDT occurs in the temperature region of 1400°C -1410°C and the ZST occurs in the temperature region 1430°C -1440°C. This is evident from the flat fracture surface (no ductile cone) and the absence of elongation. As the temperature decreases the elongation/ductility increases. This is clearly noticeable in the sample tested at 1380°C (see Figure 4.8).

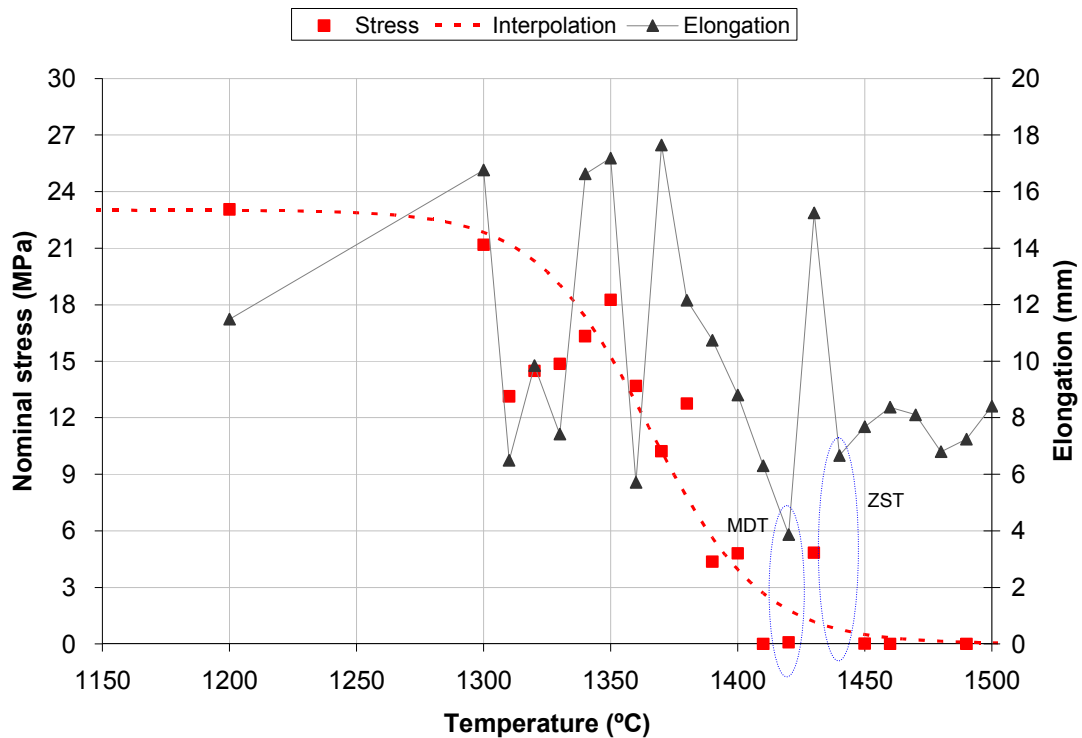


Figure 4.9. Determination of Zero Strength Temperature and Minimum Ductility Temperature for the LR-HSLA steel grade.

The brittle temperature range is in the same temperature region as visually seen in the post-mortem samples and the analysed data in Figure 4.9, confirming again the good reproducibility of the test.

However, one data point differs from the samples, in the 1430°C sample its fracture is flat but in the measured stress and the corresponding elongation, the data is far from what it is expected for a flat failure (see Figure 4.9). Nevertheless, the true stress-true strain curves are also built for this LR-HSLA steel grade (Figure 4.10). Once again, the values shown here are at UTS.

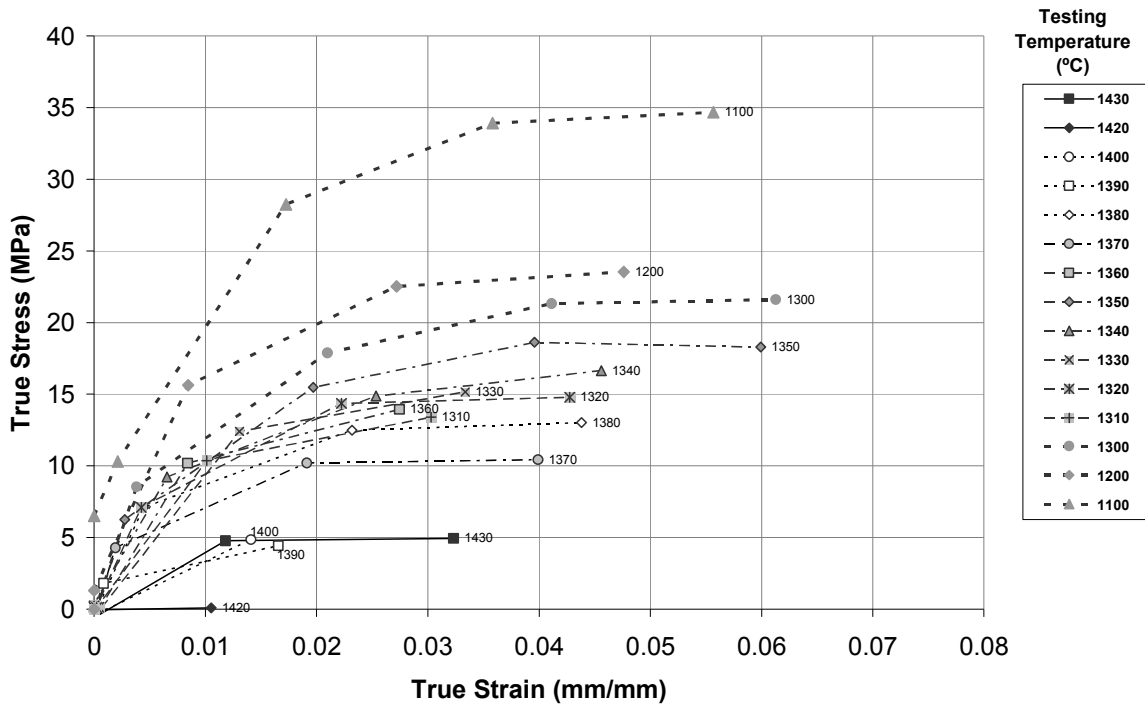


Figure 4.10. True stress-true strain curves for each temperature tested.

4.1.4 Characteristic temperatures

When comparing the brittle temperature ranges and their characteristic temperatures as measured by the hot tensile tests for the three steel grades, the LCAK has a broader ΔT_B .

Zero strength temperature

The zero strength temperature (ZST) should correspond to a fraction of solid (f_s) of around 0.65 to 0.80, which means that in the current experiment the solidification continues below the equilibrium solidus. At this stage of solidification a segregate-rich liquid film still exists between the dendrites therefore even a small strain may lead to cracking (see Chapter 2).

At this temperature, the stress starts to build up, but due to the lack of ductility in the material, the cracking will be brittle. Therefore ZST can be accurately measured by knowing the moment when the stress starts to increase from negligible values but the strain remains low.

Having the possibility of accurate measurements of stress and strain during tensile testing, the two characteristics of this particular temperature are easily determined by combining the data on temperature dependences of nominal stress and total elongation and the dependence of the true stress on true strain (see Figure 4.3).

It is concluded that for the LCAK steel grade, the ZST is between 1440°C and 1460°C (see Figure 4.3). It can be also concluded that for the HSLA steel grade, the ZST is around 1440°C to 1450°C (Figure 4.6). For LR-HSLA is 1440°C (Figure 4.9).

Zero ductility temperature

The temperature at which the transition occurs from brittle to ductile behaviour is known as the Zero Ductility Temperature (ZDT) and is commonly associated with a fraction of solid (f_s) between 0.98 and 1. As explained previously, for the test results the point of Zero Ductility Temperature has non-zero elongation values, thus it is better to name this point as Minimum Ductility Temperature (MDT) for the test results analysed in this study.

For the LCAK steel grade, by combining the temperature dependences of nominal stress and total elongation temperature and the dependence of true stress on true strain, the MDT could be determined around 1400°C (*Figure 4.3*), which is in good agreement with the preliminary assessment.

For the two HSLA steel grades considered here, by combining the data of nominal stress and total elongation versus temperature and the true stress versus true strain, can be determined that the MDT is for the HSLA is around 1400°C as well as for the LR-HSLA (see *Figure 4.6* and *Figure 4.9*).

4.1.5 Constitutive equations

The ability to understand and to predict crack formation during continuous casting has been always of industrial interest ^[12]. Moreover, the material behaviour in the as-cast condition can be described in the entire temperature range encountered by mathematical expressions that fit stress–strain curves.

For this purpose, it is common to use the Ludwik equation to characterise the material's mechanical behaviour. This equation is a phenomenological equation of the form ^[13]:

$$\sigma = K \varepsilon^n \left(\frac{\dot{\varepsilon}}{\dot{\varepsilon}_0} \right)^m \quad (4.5)$$

where:

σ : the stress; ε : the strain; $\dot{\varepsilon}$: strain rate; $\dot{\varepsilon}_0$: a constant taken equal to 1 (1/s); n : the strain hardening coefficient; m : the strain rate sensitivity; K : the material constant or consistency of the alloy.

Equation (4.5), at constant strain rate, becomes as follows:

$$\sigma = K' \varepsilon^n \quad (4.6)$$

Where K' will be:

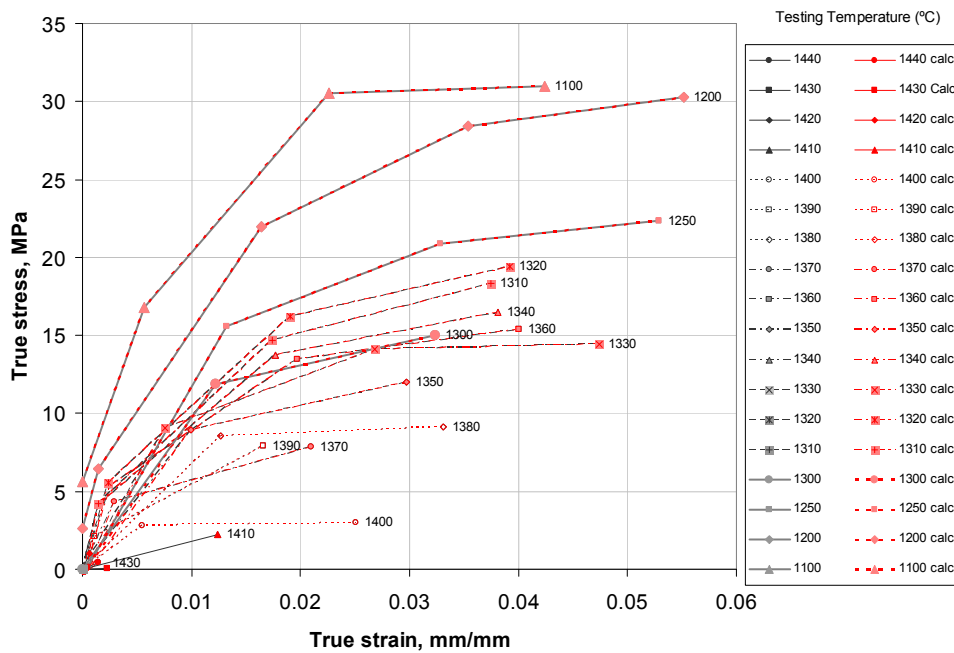
$$K' = K \left(\frac{\dot{\varepsilon}}{\dot{\varepsilon}_0} \right)^m \quad (4.7)$$

To avoid inaccuracy in the data fitting with the logarithmic approach, the method of least square fitting for power law curves has been used to approximate the parameters K' and n .

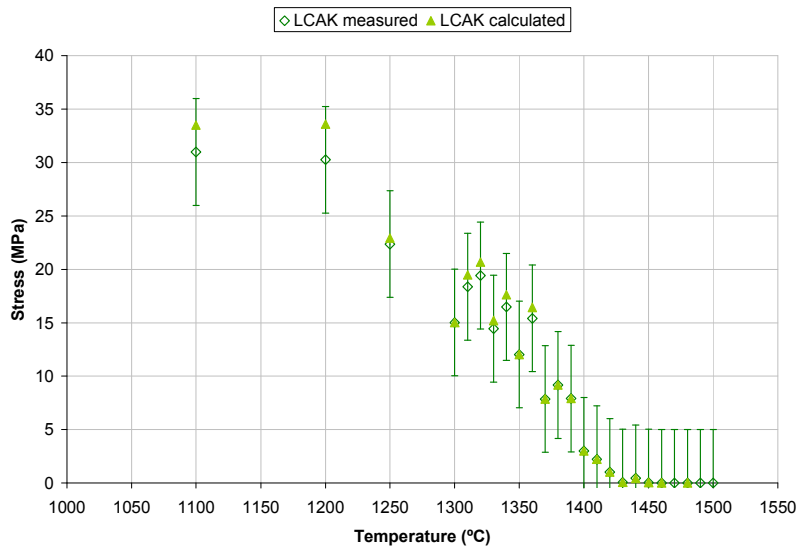
$$n = \frac{\sum \ln \varepsilon \ln \sigma - \frac{1}{N} (\sum \ln \varepsilon) (\sum \ln \sigma)}{(\sum (\ln \varepsilon)^2) - \frac{1}{N} (\sum \ln \varepsilon)^2} \quad (4.8)$$

$$K' = \exp \left[\frac{1}{N} \sum \ln \sigma - n \frac{\sum \ln \varepsilon}{N} \right] \quad (4.9)$$

Here N is the number of data points.



a



b

Figure 4.11. Application of the fitting procedure to LCAK steel: (a) full curves for measured (black) versus calculated (red) with least square fitting method and (b) UTS values for measured (dark-green triangles) versus calculated (light-green triangles)

Further, working with the standard deviation, it is possible to reduce the error and fine-tune the actual values for both parameters.

Figure 4.11 shows the results for the measured versus calculated curves for each temperature tested for the LCAK steel grade. For a better overview, the UTS values, measured and calculated are also shown, including a standard error for the measured values of $\pm 5\%$. It is important to note that the measured and calculated curves are overlapped considering that after the fine tuning with the sigma method the error is less than 3%. Figure 4.12 and Figure 4.13 show again for the LR-HSLA and HSLA steels, respectively, the measured versus calculated true strain–true stress from the UTS values.

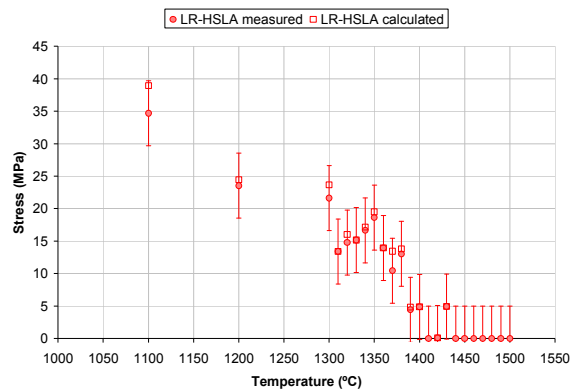


Figure 4.12. Measured (orange-crossed-squares) versus calculated (full-red squares) with least square fitting method for the LR-HSLA steel

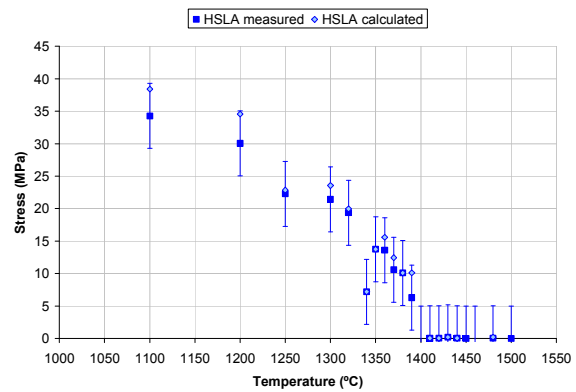


Figure 4.13. Measured (full-blue squares) versus calculated (light-blue rhomboids) with least square fitting method for the HSLA steel

Considering that K' and n are non-linear functions of temperature T and that the values of K' decrease when temperature increases, it is possible to fit the values to a Sigmoidal logistic equation ^[14] as follows (see Figure 4.15):

$$K' = \frac{a}{1 + e^{-b(T-T_0)}} \tag{4.10}$$

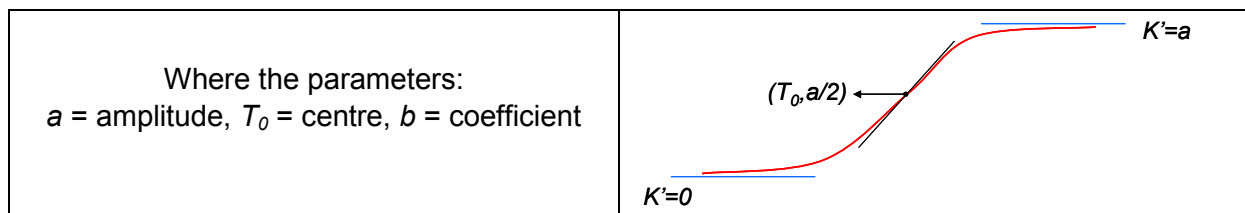


Figure 4.14. Schematic representation of a Sigmoidal Logistic equation

For all 3 steel grades considered in this study the parameters are as follows:

- $a= 95$
- $T_0=1335$
- $b= -0.042$

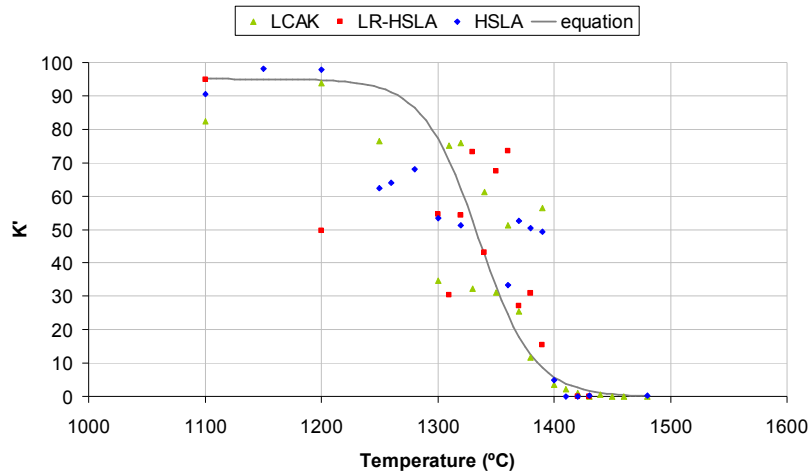


Figure 4.15. Coefficient K' for the three steel grades.

In the case of the strain hardening coefficient n , its temperature dependency denotes and confirms the presence of liquid phases down to 1400°C, the temperature at which this coefficient reduces its value to around zero. Therefore, this temperature is believed to be the zero ductility temperature for all 3 steel grades considered in this study ^[12].

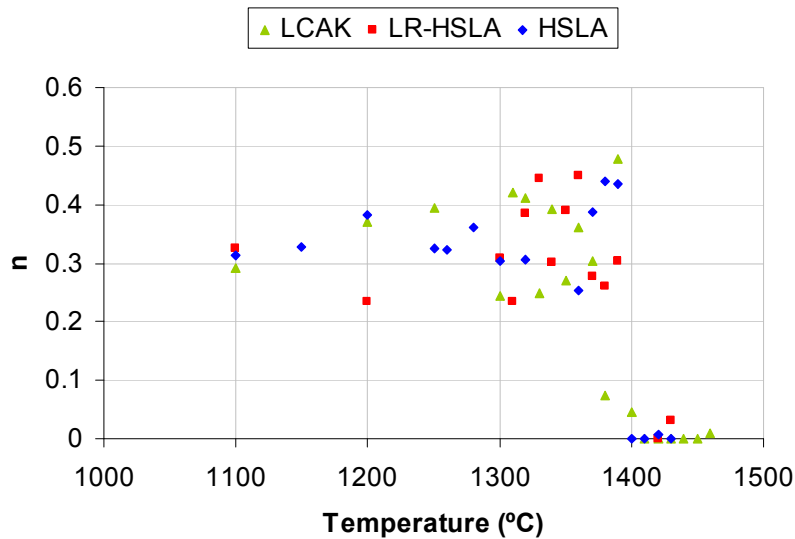


Figure 4.16. Strain hardening coefficient n

It is not possible to determine the temperature dependence of the strain rate sensitivity m because the tensile tests have been performed at only one strain rate, namely $1 \times 10^{-2} \text{ s}^{-1}$. Since thermo-mechanical data applicable to the solidification conditions of steel are scarce, particularly for the steel grades considered in this study, it has also not been possible to derive this coefficient from the literature.

4.2 Fractographic analysis on the hot tensile test samples

To get insight into the mechanisms of hot tearing susceptibility, the fracture surfaces of specimens tested at the limits of the brittle temperature range were analysed under SEM. All the samples tested above the ZST show a smooth fracture, typical of the fracture in the

presence of a continuous liquid layer separating dendrites, testifying for the non-equilibrium solidification that ends at a temperature below the equilibrium solidus.

4.2.1 LCAK

The results are shown for the specimen tested at 1460°C considered to be around ZST, the specimen tested at 1440°C as it is in the middle of the ΔT_B , and the specimen tested around the MDT at 1420°C.

ZST sample

The sample tested at 1460°C (from the 1st set) clearly shows brittle behaviour, being close to the ZST. In *Figure 4.17a*, a top view of the sample fracture is shown.

Towards the centre of the sample, there is an area with dendrites growing in several directions (*Figure 4.17b*). These dendrites could be growing into residual liquid pools which became voids upon testing.

The central part of the fractured sample exhibits smooth grain boundaries and bridges typical of the grain separation through liquid film, as shown in *Figure 4.18b*. This confirms the previous observations by Hansson ^[15] and Rappaz ^[3]. The amount of liquid present in the centre of the sample (as compared with the expected amount from the equilibrium phase diagram) is increased due to the segregation as a result of progressive solidification from the surface to the centre.

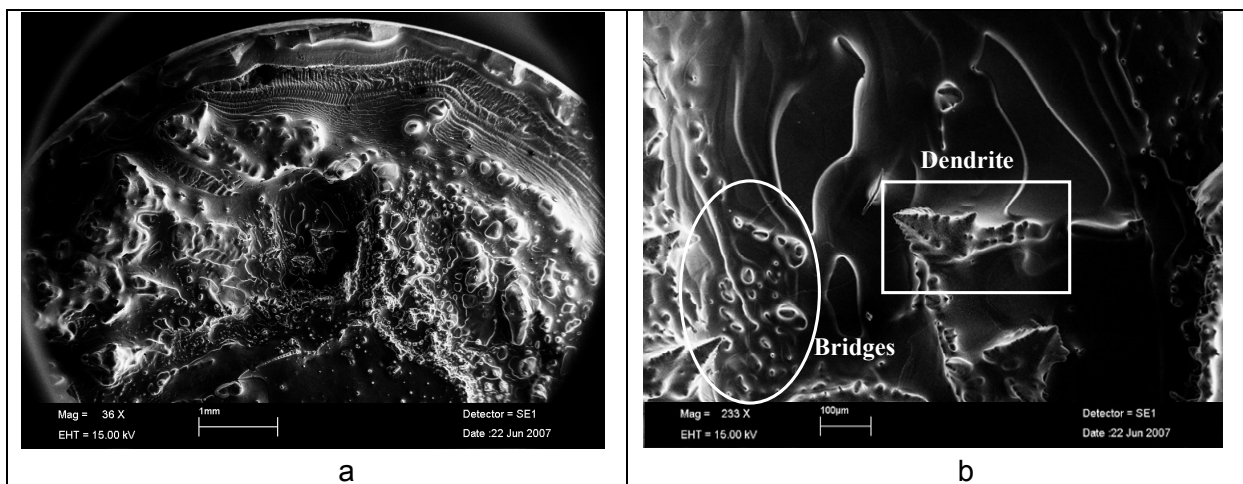


Figure 4.17. Surface fracture (a) and a detail with structural features (b) of the 1460°C specimen.

In the 2nd set of test samples, the fracture surface is similar, with the same type of dendrites and inclusions, particularly showing segregated interdendritic liquid, probably formed as a result of segregation of alloying elements (Mn, S, etc.) as can be seen in *Figure 4.18*.

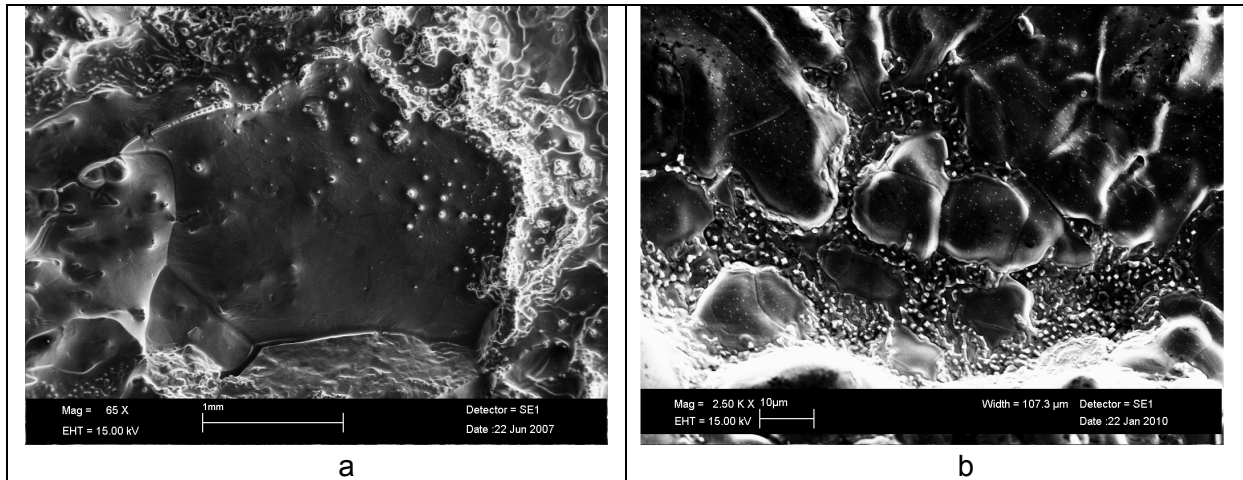


Figure 4.18. Centre of the specimen tested at 1460°C (a) and the detail (b) showing segregated liquid between dendrite branches.

The fracture of the samples tested at 1460°C shows Stage 2 of hot crack formation, with the dendrites covered with a thin liquid film. At this stage the material has just passed (or is in the vicinity of) the moment when the strength starts to build up (ZST) and liquid films are still trapped between the interlocking dendrites. Therefore, the resistance to external stresses is very low and hot cracking can easily occur. Consequently, the LCAK steel considered in this study will show an interdendritic cracking behaviour in temperatures around 1460°C.

1440°C samples

Figure 4.19 clearly shows the presence of a eutectic pattern on the fractures of the samples from both sets of tests, which testifies for the presence of a liquid film separating the grains at this stage of solidification.

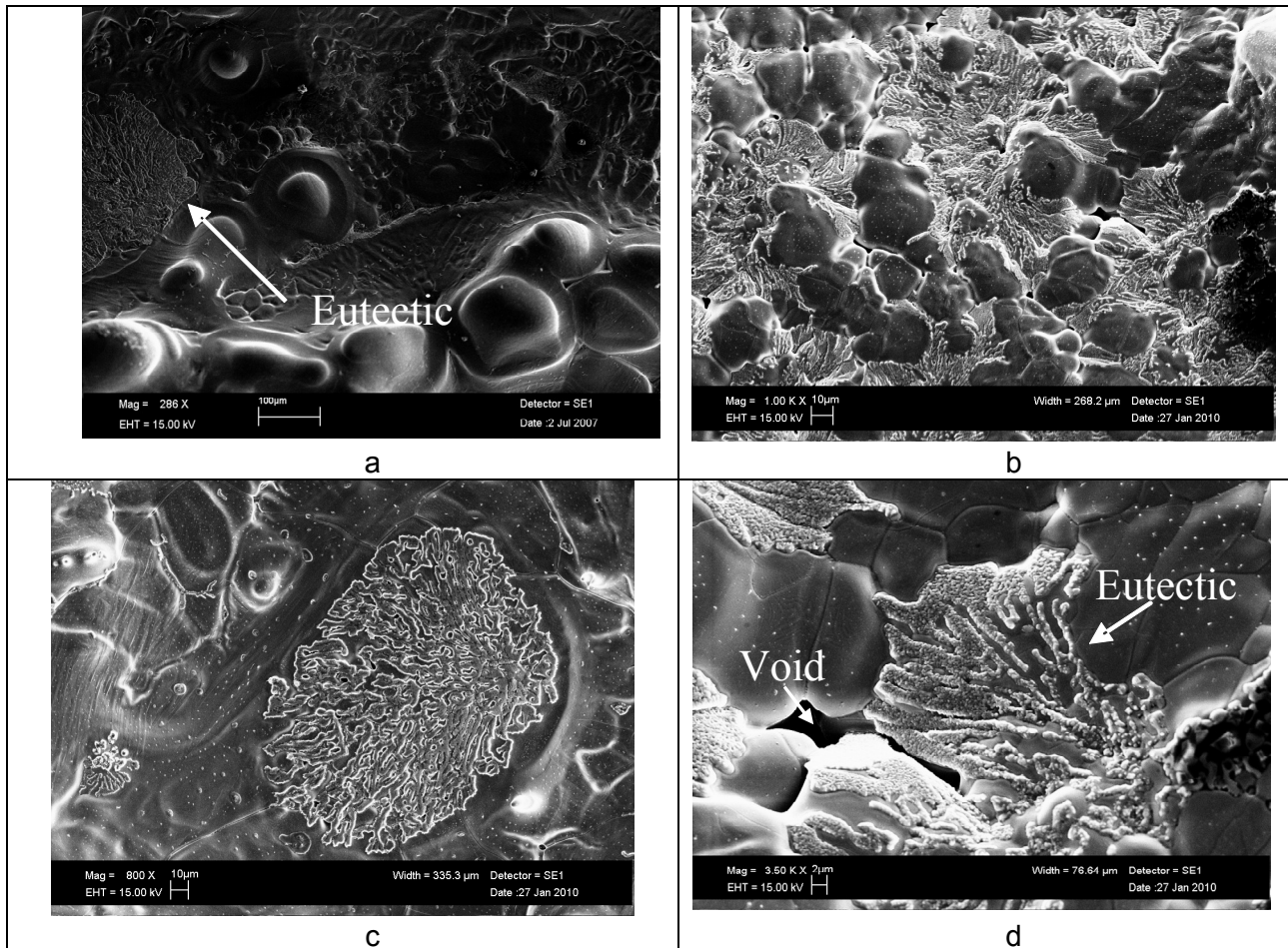


Figure 4.19. Eutectic structure features in the specimens tested at 1440°C: (a) and (b), general view with the eutectic between dendrite branches, (c), eutectic patch at the dendrite face; and (d), eutectic patterns close to the void between dendrite branches.

The eutectic pattern not only demonstrates that the liquid phase exists between the grains but also attests for the high solute concentration of this liquid due to segregation. In this case, the liquid phase may be preserved to temperatures considerably lower than the equilibrium solidus which is one of the reasons for low ductility^[10,16].

Similar eutectic structures have been observed by Nakagawa et al.^[10] when conducting comparable hot tensile testing on steel grades with higher carbon composition. They reported that at temperature about 100°C below the equilibrium solidus the samples did still had liquid and the displacement during testing remained small. This difference has also been attributed to the segregation in the interdendritic liquid and the temperature difference along the radius direction of the sample may be related to this macroscopic segregation^[10].

MDT samples

The samples tested at 1400°C are close to the MDT, showing in the centre of the sample as-solidified faceted ferritic grains (see Figure 4.20). The fracture is intergranular and brittle with some signs of the liquid present at the facets (wavy patterns in Figure 4.20a) and liquid film

in Figure 4.20d. In the second set of samples tested, bridges were found in the grains surface (see Figure 4.20b and c).

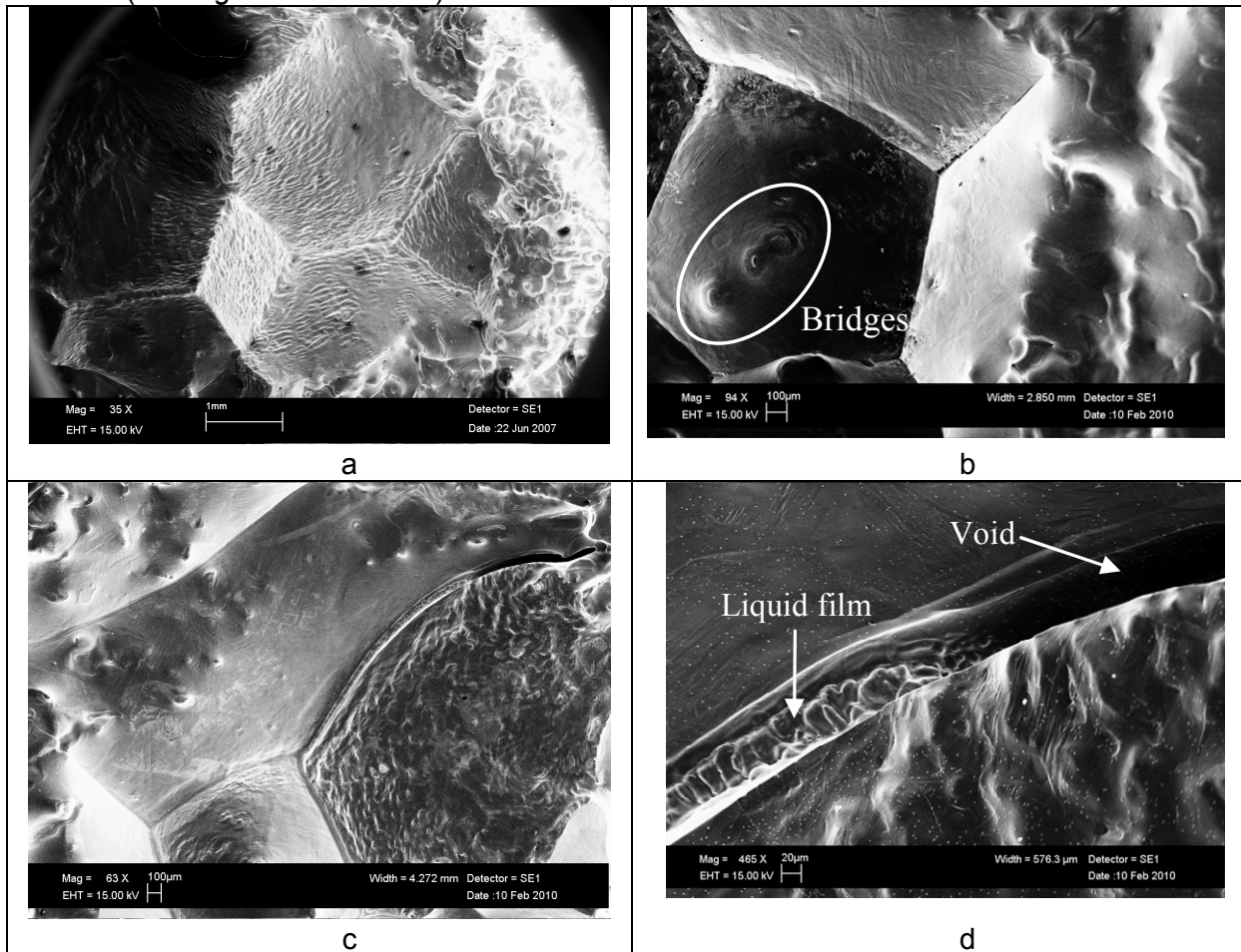


Figure 4.20. Fracture surface of the 1400°C LCAK specimens: (a), grain facets with wavy liquid patterns; (b), (c), bridges at the grain surface; and (d), void between two grains with a liquid film that seems to be percolating through the void.

The fracture of these specimens show Stage 3 of hot crack formation, only the grains were observed and no dendrite morphology can be seen in the fracture surface (except for the coarse dendrites close to the surface due to testing conditions). As a result of segregation of alloying elements, a thin liquid film, apparently with a low-melting point, is present between grains. Around this temperature the transition between brittle and ductile fracture begins (MDT), changing the fracture behaviour from interdendritic to intergranular. These findings are similar to a previous study carried out by Hansson for INVAR alloys [15].

4.2.2 LR-HSLA

From the tensile test specimens after testing, for the LR-HSLA, the MDT occurs in the temperature region of 1400°C-1410°C and the ZST occurs in the temperature region 1430°C-1440°C. The brittle temperature range is in the same temperature region as visually seen in the post-mortem samples and the analysed data, confirming the good reproducibility of the test.

ZST sample

The sample at a temperature around ZST was almost fully melted; therefore the surface of the sample was not possible to be analysed under the SEM. Nevertheless, the sample tested at 1430°C (see *Figure 4.21*) clearly shows brittle behaviour, being close to the ZST.

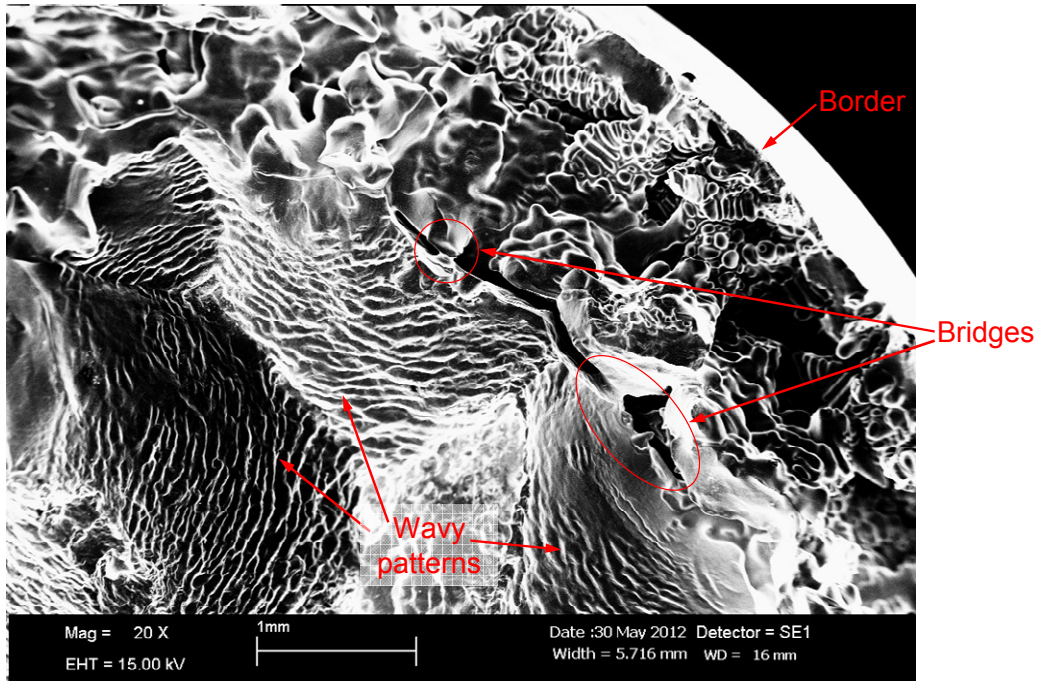


Figure 4.21. Overview of the fracture surface from the 1430°C LR-HSLA sample.

At the border of the sample, there is an area with dendrites growing in several directions, more developed ones clearly showing the secondary arms.

Towards the centre of the sample, a wavy pattern with a thin liquid film is present between grains and several bridges with also a liquid film, apparently with a low-melting point, are seen in some cracks (see *Figure 4.22*).

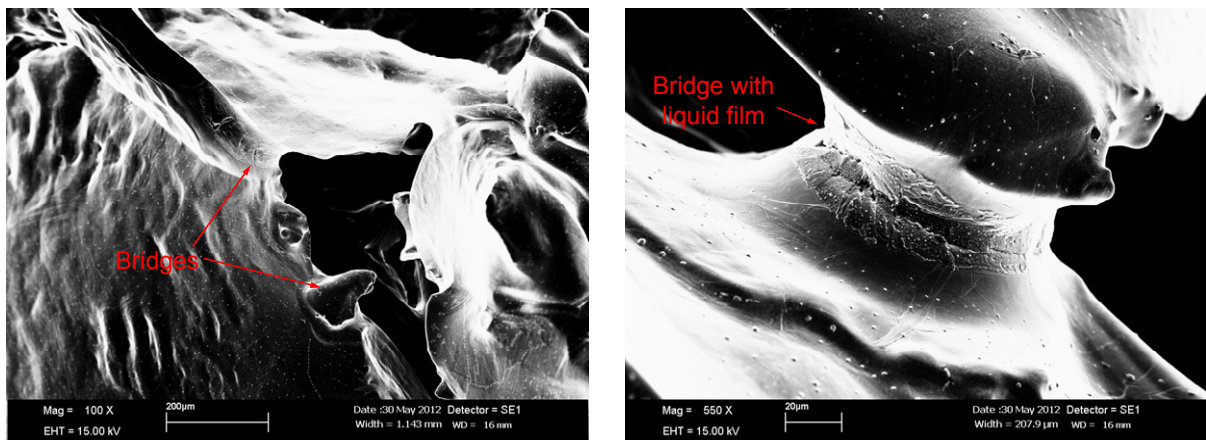


Figure 4.22. Bridges with liquid film between them.

The brittle temperature range is in the same temperature region as visually seen in the post-mortem samples and the analysed data. However, the 1430°C sample, its fracture is flat but

in the measured stress and the corresponding elongation, the data are far from what it is expected for a flat failure, and the SEM analysis confirms that the sample is close to the ZST.

MDT samples

The sample tested at 1400°C that according to the visual inspection and the data analysed is at the MDT, clearly shows ductility at the centre of the fractured surface.

On the other hand, between the ductile centre and the border of the sample it is still possible to see strings of MnS that are expected to have low melting point, *Figure 4.23*.

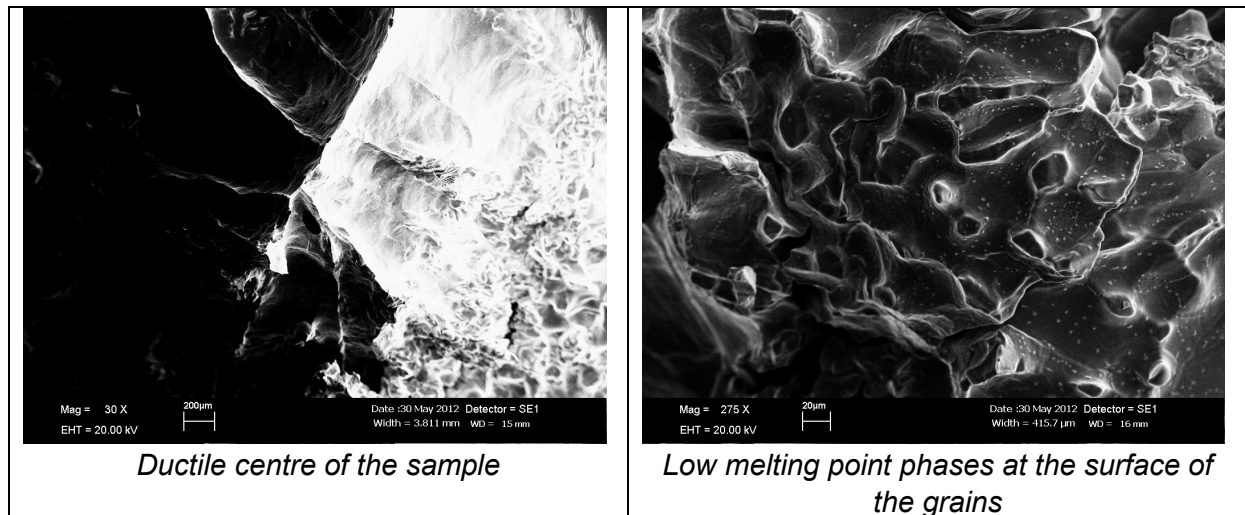


Figure 4.23. Features of the fracture surface from the 1400°C sample.

4.2.3 HSLA

Once again, the SEM study of the fracture surface of the samples for this steel grade, confirm the visual inspection and the measured data analyses.

ZST sample

According to the analysis, the 1440°C sample is in the region of the ZST, showing dendrites through the entire fracture surface, with visible signs of liquid films around the dendrites, as shown in *Figure 4.24*.

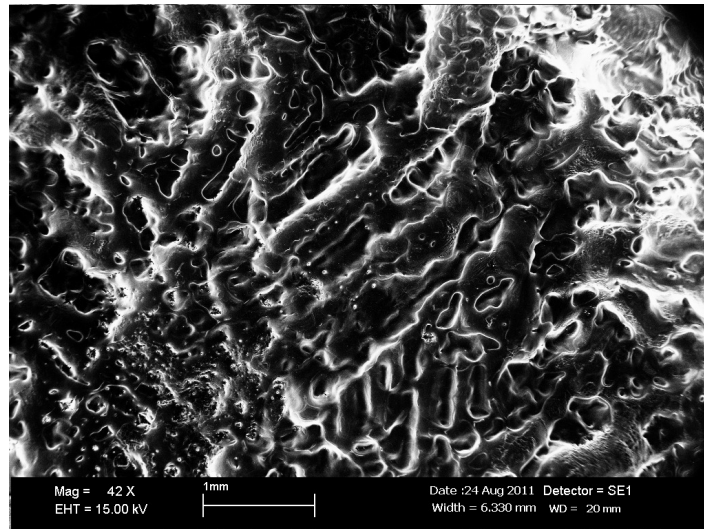


Figure 4.24. Overview of the fracture surface from the 1440°C sample.

MDT sample

The 1400°C sample, from the region at the MDT does also show dendrites until almost the centre of the fractures section. However, a small portion of its centre demonstrate some signs of ductility, confirming that this sample is in the vicinity of the MDT (see Figure 4.25).

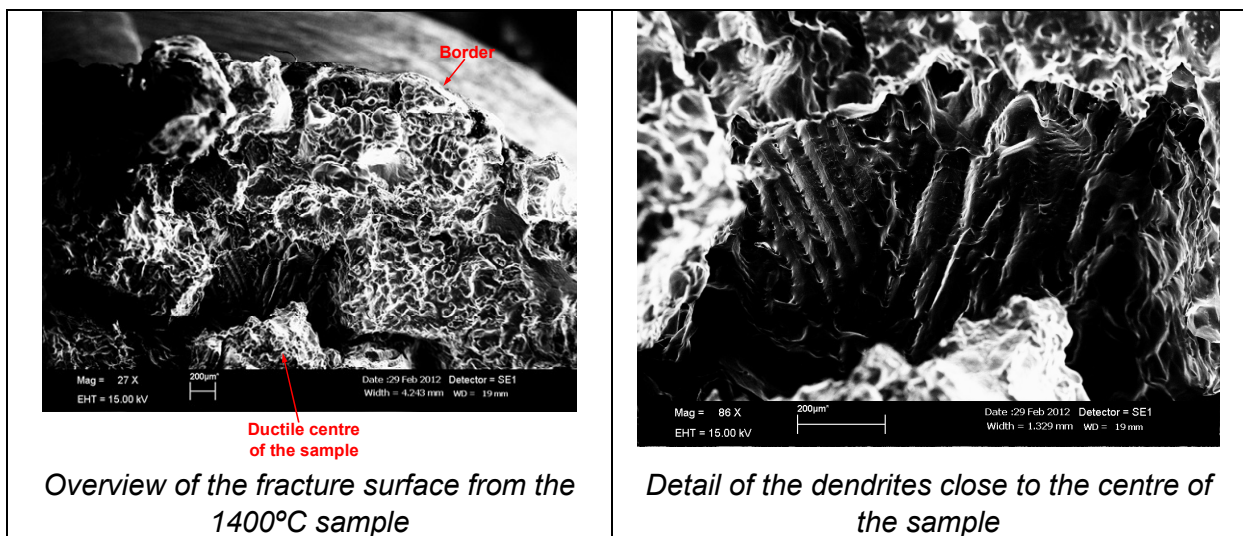


Figure 4.25. Features of the fracture surface from the 1400°C sample.

4.2.4 Non-metallic inclusions in the hot tensile test samples

The fracture surfaces of the examined samples show some interesting features that may help in understanding the nature of the last liquid remained during solidification in this steel grade.

LCAK steel

In support of the mechanisms described above, manganese sulphides (MnS) were found at the interdendritic fracture surfaces of all examined specimens of the LCAK hot tensile samples.

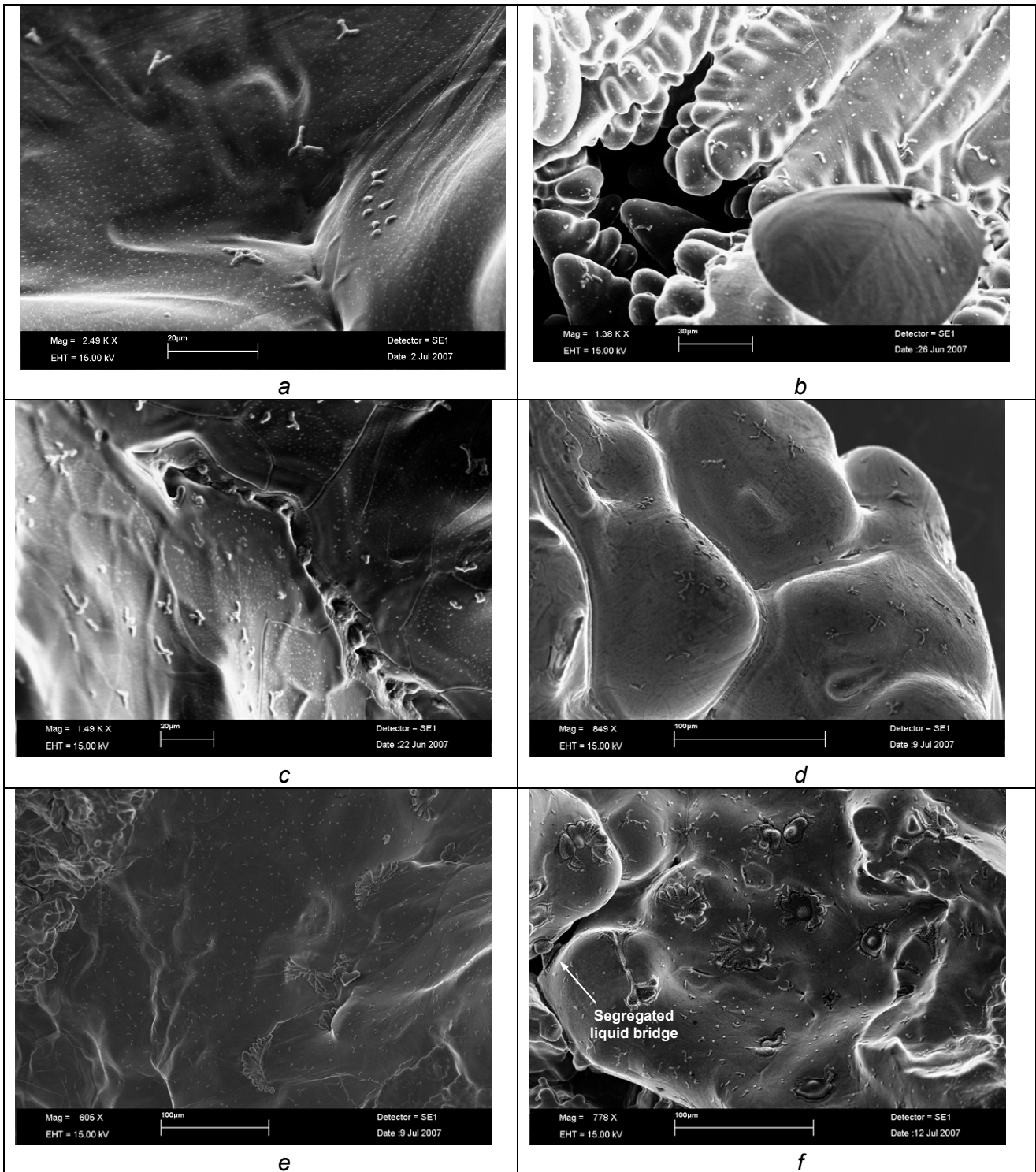


Figure 4.26. MnS inclusions found on the fracture surface of samples tested at: (a): 1460°C; (b): 1440°C; (c): 1420°C; (d): 1400°C; (e): 1380°C; and (f): 1360°C for the LCAK specimens.

Figure 4.26 gives representative examples of these inclusions at each test temperature, i.e. 1460°C, 1440°C, 1420°C, 1400°C, 1380°C, and 1360°C. Similar MnS particles have been found previously by other authors ^[10,15,17,18] The sulphide particles in the samples at lower temperature have the rosette shape typical of divorced eutectics.

These findings correlate very well with the type of particles reported in literature^[15,19,20]. Type I can be found at high temperatures (*Figure 4.26a, b*). The Type II particles are clearly visible in the samples at 1420°C and 1400°C (*Figure 4.26c and d*, respectively). Hansson has encountered exactly the same type of particles (interconnected stringers as a sort of degenerate eutectic) also on fracture surfaces of tensile specimens of rock tool steel grades (even though the test set-up was slightly different)^[15].

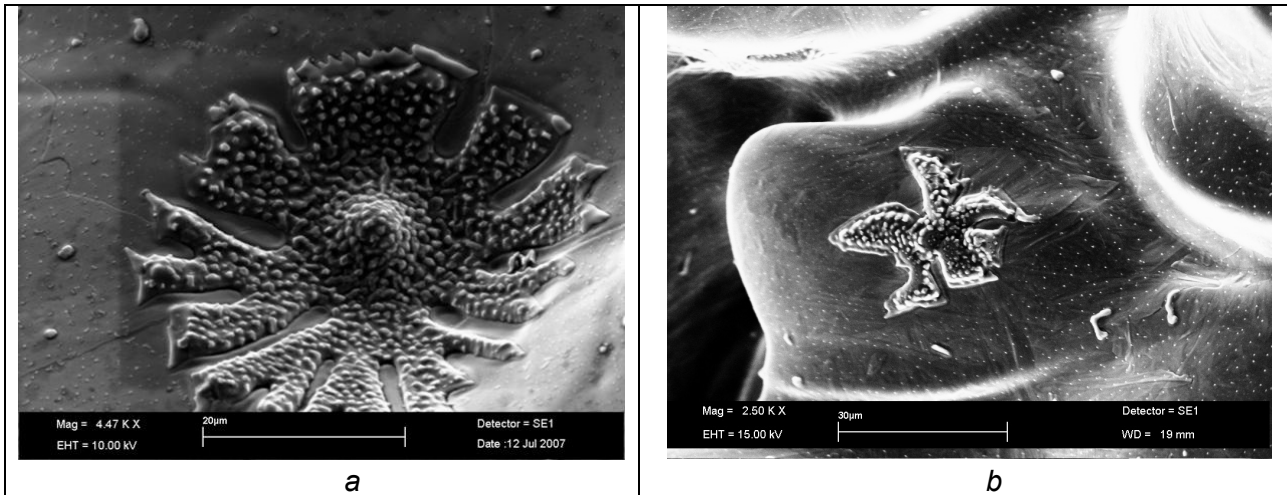


Figure 4.27. MnS rosette particle with microscopic particles containing Al and Ti from the 1360°C (a) and 1330°C (b) LCAK specimens

In a close study on the morphology of Type III inclusions, Flemings^[19] found that these particles show a cubic pattern often embedded in “dendritic” projections of the same inclusion and that they often surround regions of Type II inclusions, with projecting arms which join the interdendritic network. The particles found on the fracture surfaces of lower-temperature samples in this research compare very well with the findings of Flemings (*Figure 4.26 e, f*, and *Figure 4.27*).

In the analysed specimens, the sulphide particles grow in amount and size with decreasing temperature of the test, which concurs with the assumption that they are formed from the segregated liquid. The liquid phase in the samples tested at a lower temperature has more time to segregate the sulphur; therefore the MnS precipitates are bigger and more “eutectic” in appearance. This observation is in good agreement with Flemings and Kattamis^[19] who showed a relation between the morphology and the size and type of inclusions with the distance from the ingot cooling surface. By increasing the distance, there is an increase in the average diameter of the Type I inclusions and an increase of the eutectic rod diameter and in average eutectic spacing in Type II inclusions. Even when the cooling rate of the tensile samples is not the same as in this research, each sample could be related with distance from the surface of an ingot/cast slab; therefore the mechanism of particles growing fits very well with the reported one.

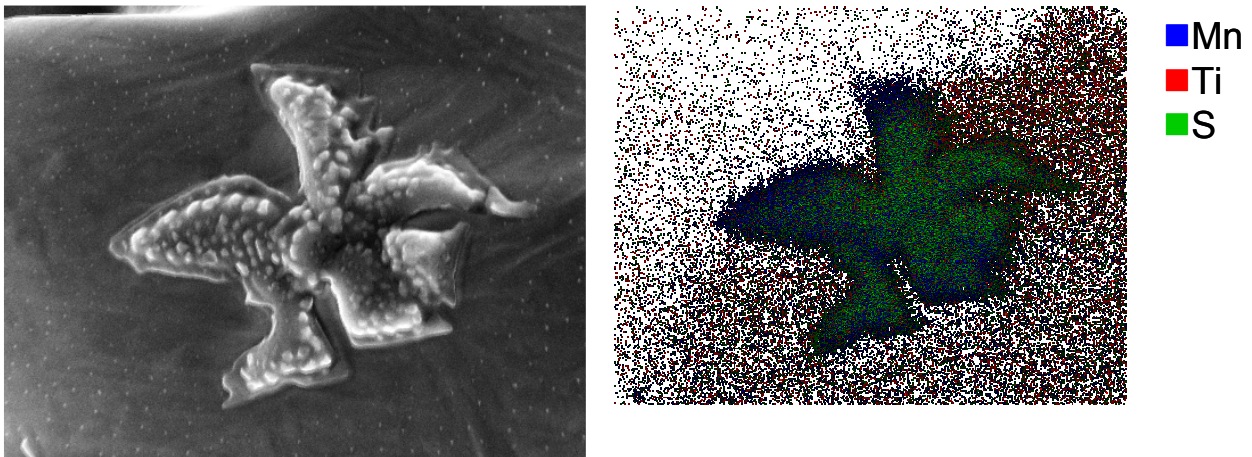


Figure 4.28. EDX analysis of the 1330°C LCAK specimen

It is interesting to note that microscopic particles containing Al (Al_2O_3 or AlN) and Ti have been found in the MnS rosette matrix (see Figure 4.27 and Figure 4.28). However it is not possible to determine the exact composition (TiN or TiO_2) of these “microparticles” due to their size, which are smaller than a micron, Figure 4.28. The occurrence of these particles may indicate the complex nature of the eutectics.

LR-HSLA steel

Similar particles were found at the samples from the low-range HSLA steel grade; however, the concentration of particles on the samples is visually slightly higher.

In addition, the sample at 1400°C has very long strings of MnS surrounding the grains, at an even distance, probably due to surface tension during formation of these particles (see Figure 4.29). Together with these strings, clusters of type I MnS particles are found also at the surface of this sample.

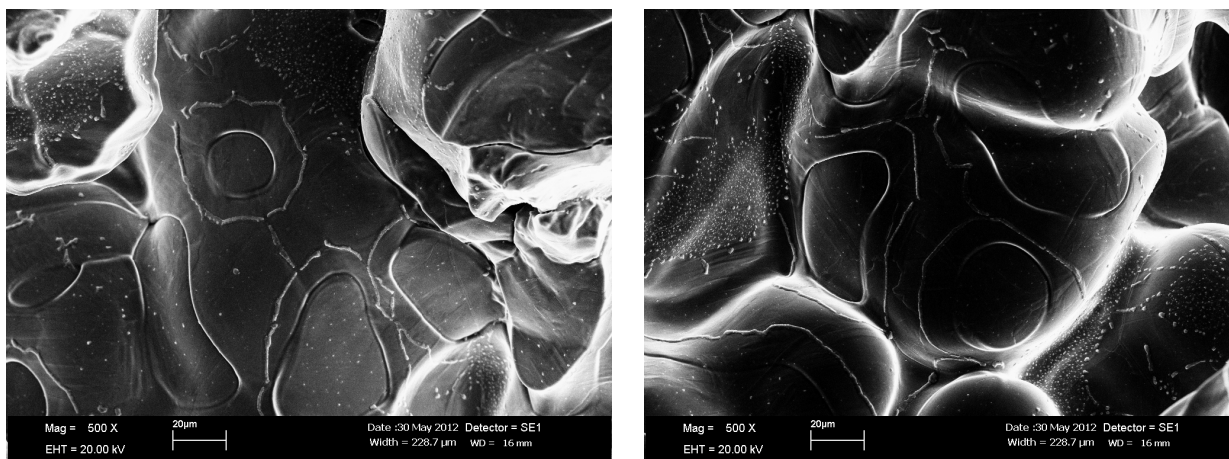


Figure 4.29. Long MnS strings surrounding the grains

Further, until 1360°C all the samples analysed showed MnS particles similar to the ones encountered at the LCAK steel.

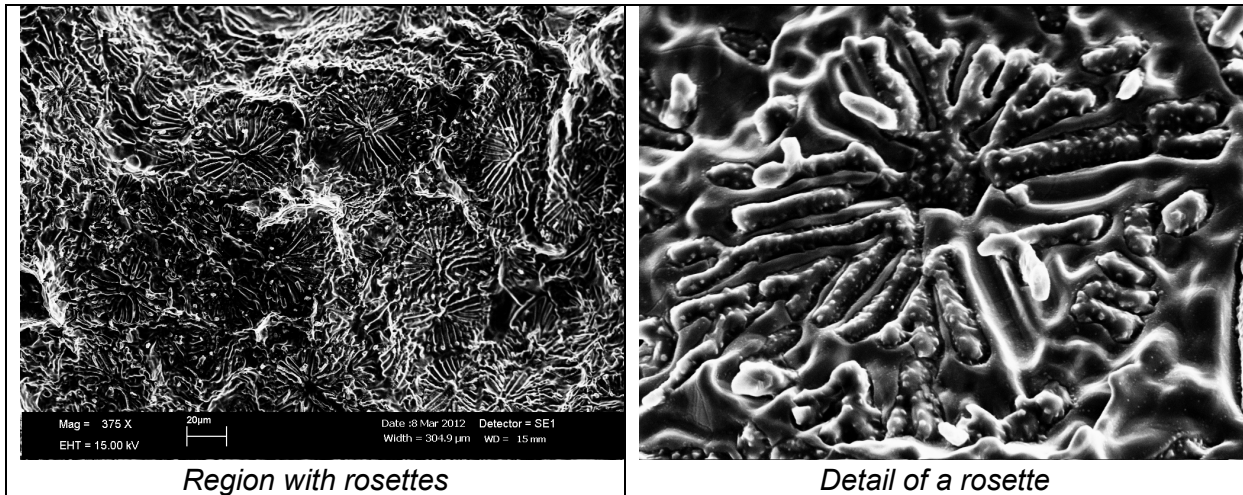


Figure 4.30. MnS rosettes encountered at the fracture surface of the 1360°C sample

However, the 1360°C sample has a vast concentration of big MnS rosettes which differ from those observed in the LCAK steel grade by having more and thinner limbs per rosette (see Figure 4.30).

HSLA steel

The non-metallic particles found on this steel grade are slightly different from the ones encountered at the fracture surfaces of the other two grades.

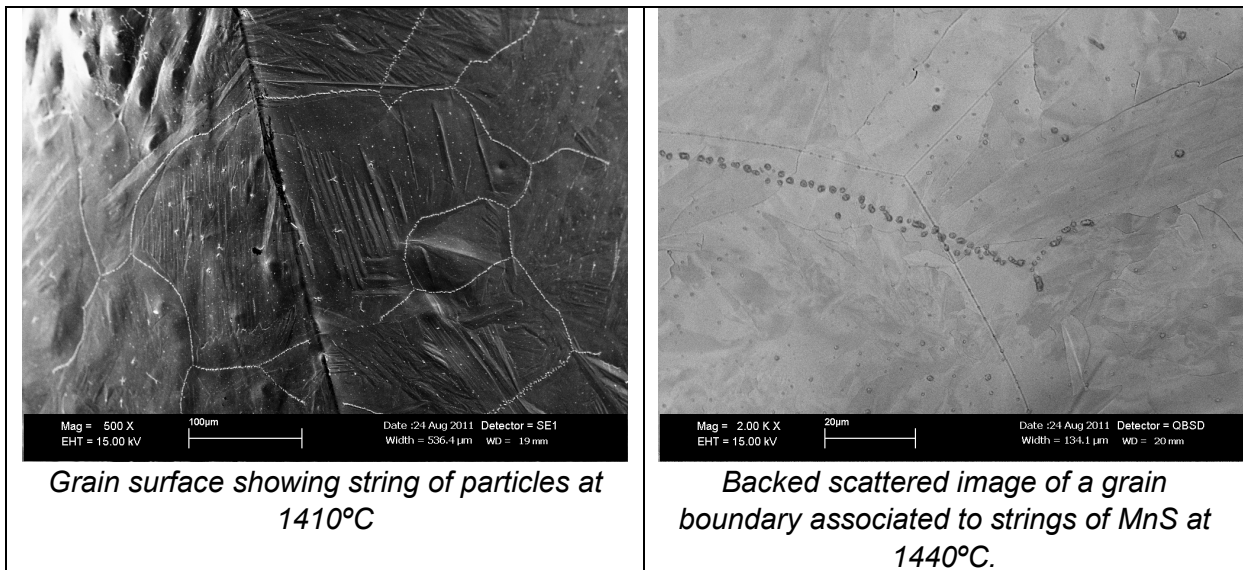


Figure 4.31. String of non-metallic particles at the samples in the ΔT_B region

At the samples in the ΔT_B (1400° to 1440°C), strings of particles associated with grain boundaries and especially triple-points are seen (see Figure 4.31).

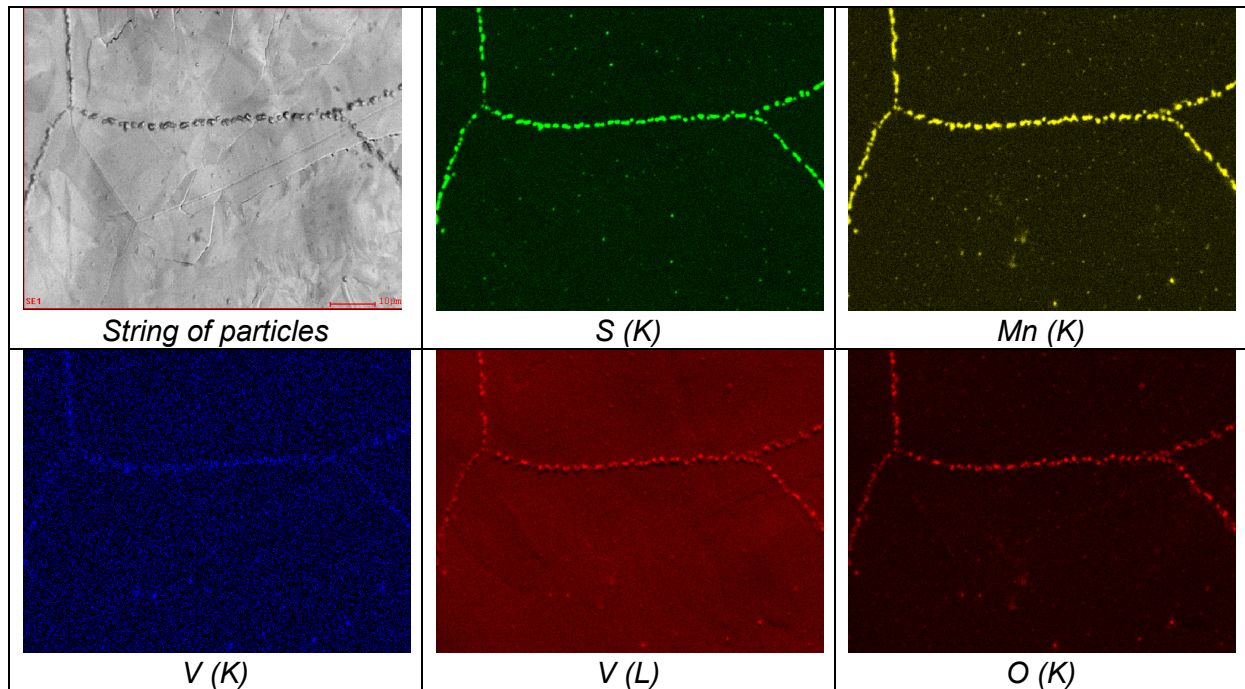


Figure 4.32. Mapping of elements for the strings of particles associated with grain boundaries.

It is well known that grain boundaries develop “grooves” under certain growing conditions^[21]. Sometimes the grooves fail to follow the grain growth process, remaining in their original positions whilst the actual boundary moved, with no associating grooving. It seems possible that in the case of the hot tensile samples a similar grooving associated with non-metallic particles can be seen. However, in this case the original boundary seems to stay pinned by the string of non-metallic precipitates and the actual grain boundary continues growing with a much smaller groove.

These strings of particles are in composition different from the other steel grades as they seem to have small amounts of vanadium, apart from manganese and sulphur. This fact is doubtful because the vanadium L-line and oxygen K-line are very close to each other, thus the clear vanadium L-line map could also come from an oxygen-signal (see mapping of elements in *Figure 4.32*)

At lower testing temperature, the size of the particles is much larger and the MnS rosettes are found even at the sample tested at 1340°C. Some of these rosettes have a shape similar to an ice-crystal and even display a 6-limb shape characteristic of the hexagonal structure (see *Figure 4.33*).

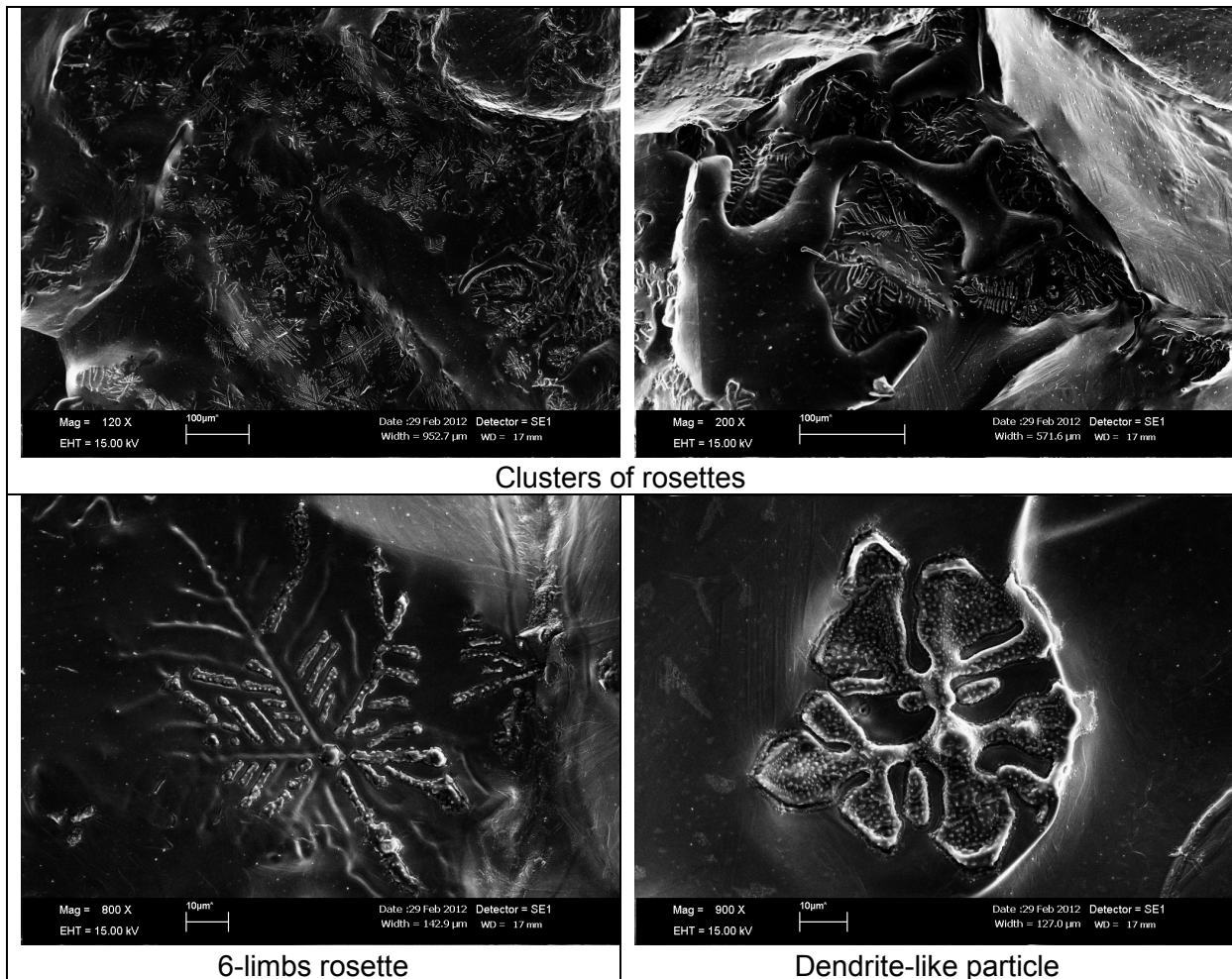


Figure 4.33. Non-metallic particles at the 1340°C sample

4.3 Thermo-mechanical behaviour and hot tearing susceptibility.

The findings of the hot tensile tests results suggest that the LCAK steel grade is, from the three examined grades, the one who has less strength during solidification and is particularly susceptible to cracking because it is also very much prone to develop non-metallic particles at the last stages of solidification.

In addition, according to the Scheil calculations (see Chapter 3) there is a substantial amount of liquid phase at the temperature ranges of the measured ΔT_B for all the three steel grades studied here, which is slightly higher than it is theoretically expected for the hot tearing susceptible range (see Table 4.2). Particularly the LCAK steel grade which has a broader ΔT_B , obviously does have more liquid still present at the ZST than the other two grades. However, the HSLA grade has a higher percentage of liquid present than the LR-HSLA.

Table 4.2. ΔT_B temperature range and fraction of liquid from Scheil calculations.

Steel Grade	ZST		MDT	
	Temperature (°C)	f_L (%)	Temperature (°C)	f_L (%)
LCAK	1460	2.44	1400	1.04
LR-HSLA	1440	2.04	1400	1.14
HSLA	1440	2.12	1400	1.19

To draw up a conclusion from the data analysed in this chapter, it is important also to relate the amount of liquid present and the permeability of the network, which may negotiate the effects of small fraction liquid through better feeding. The permeability depends on the structure as well as on the fraction solid. However, we have not analysed this aspect in our research.

A good approach to measure the hot tearing susceptibility is how much thermal strain is accumulated in the brittle temperature range, hence (under similar conditions), how broad is the brittle temperature range (ΔT_B). So what matters is how much time the steel spends on this ΔT_B , which is (under similar cooling condition) the function of ΔT_B width. The wider the ΔT_B the more thermal strain will be accumulated in the mushy steel and more incentive there will be for its fracture. Taking into account that the ΔT_B is typically between fractions solid f_S 0.8 and 0.99, combined with the measured strength and elongation; the ΔT_B is broader for LCAK while LR-HSLA is the least susceptible to hot tearing.

References

1. *Modelling for casting and solidification processing*, 1st Edition, Yu, K. O., New York, USA, 2009, Marcel Dekker.
2. Eskin, D., Suyitno, and Katgerman, L., *Mechanical properties in the semi-solid state and hot tearing of aluminium alloys*, Progress in Materials Science, 49 , 2004, 629-711.
3. Dantzig J.A. and Rappaz, M., *Solidification*, 1st Edition, EPFL Press, Laussane, Switzerland, 2009, CRC Press.
4. Won, Y. M., Yeo, T. J., Seol, D. J., and Oh, K. H., *A new criterion for internal crack formation in continuously cast steels*, Metallurgical and Materials Transactions B, 31 (4), 2000, 779-794.
5. Eskin, D. and Katgerman, L., *A quest for a new hot tearing criterion*, Metallurgical and Materials Transactions A, 38A (7), 2007, 1511-1519.
6. Baba, N., Ohta, K., Itoh, Y., and Kato, I., *Prevention of slab surface transverse cracking at Kashima n° 2 caster with Surface Structure Control (SSC) cooling*, La Revue de Metallurgie, 4 , 2006, 174-179.
7. Kato, T., Kawamoto, M., Yamanaka, A., and Watanabe, T., *Prevention of slab surface transverse cracking by microstructure control*, ISIJ International, 43 (11), 2003, 1742-1750.
8. Mizukami, H., Hiraki, S., Kawamoto, M., and Watanabe, T., *Tensile strength of carbon steel during and after solidification*, Tetsu to Hagane, 84 (11), 1998, 763-768.
9. Mizukami, H., Yamanaka, A., and Watanabe, T., *High temperature deformation behavior of peritectic carbon steel during solidification*, ISIJ International, 42 (9), 2002, 964-973.
10. Nakagawa, T., Umeda, T., Murata, J., Kamimura, Y., and Niwa, N., *Deformation Behavior during Solidification of Steels*, ISIJ International, 35 (6), 1995, 723-729.
11. George E. Dieter, *Mechanical Metallurgy*, SI metric edition Edition, 1998, McGraw-Hill Book Co. UK LTD.
12. Magnin, B., Katgerman, L., and Hannart, B., *Physical and Numerical Modelling of Thermal Stress Generation During DC Casting of Aluminium Alloys*, Modelling of Casting, Welding and Advanced Solidification Processes, Cross, M. and Campbell, J., London, UK, 1995, The Minerals, Metals and Materials Society.
13. Van Haften, W. M., *Constitutive Behaviour and Hot Tearing During Aluminium DC Casting*, PhD, Delft University of Technology, 2002.
14. Seber, G. A. F. and Wild, C. J., *Nonlinear Regression*, John Wiley & Sons, Inc., 1989

15. Hansson K., *On the hot crack formation during solidification of iron-base alloys*, PhD, Royal Institute of Technology, Stockholm, Sweden, 2001.
16. Emi, T. and Cramb A.W., *Surface Defects on Continuously Cast Strands - Casting Volume*, 11th Edition, 21, Pittsburg, USA, 2003, The AISE Steel Foundation.
17. *ASM Handbook*, 8th Edition, 12: Fractography, Materials Park, OH, USA, 1987, ASM International.
18. *ASM Handbook*, 8th Edition, 09: Metallography and Microstructures, George van der Voort Editor, Materials Park, OH, USA, 2004, ASM International.
19. Flemings, M. C. and Kattamis, T. Z., *Investigation of Solidification of High-Strength Steel Castings*, Report Nr. AMMRC CR 63-04/F, Department of Metallurgy and Materials Science, Massachusetts, USA, 1968, Massachusetts Institute of Technology.
20. Flemings, M. C. and Bigelow, L., *Sulfide Inclusions in Steel*, Metallurgical and Materials Transactions B, 6 (2), 1975, 275-283.
21. Seward, G., Prior, D. J., Bi, Y., Parker, S. V., and Howe, A. A., *Direct Observation and Modelling of Grain Growth Including Crystal Orientation*, International Conference on Thermomechanical Processing: Mechanics, Microstructure & Control, Dept of Engineering Materials, Sheffield, UK, 2002, The University of Sheffield.

Chapter 5

Effect of chemical composition on microstructure of commercial steel grades

It is observed that an LCAK steel grade has a high risk of cracking during solidification, while High Strength Low Alloyed (HSLA) steel has a very low cracking occurrence. This study assigns the unexpected effect of the chemical composition on the hot tearing sensitivity to the role of some alloying elements such as Ti, V and N as structure modifiers.

Furthermore, from the microstructural examination, two unexpected features were observed, the absence of an outer equiaxed zone, commonly called “chill zone” and the presence of “bent dendrites”. These two features are also investigated in this chapter.

Phase-field models have become very popular for the simulation of microstructure evolution during solidification processes.

This chapter also presents the microstructure simulations with phase-field for the three steel grades considered in this thesis, their microstructural differences due to chemical composition in the dendritic structure formed during the first stages of solidification and the relation of these alloying elements with the hot tearing susceptibility.

5.1 Introduction

The intention of adding of small amounts of carbide and nitride formers such as Nb, V and Ti to carbon steel is to control the austenite grain size (the particles hinder the boundary migration and grain growth) in the solid state. This, in turn, produces fine ferrite grain sizes, and by precipitation in the ferrite at lower temperatures (assisted by water cooling of the material out of the last rolling stand) gives a bonus of extra dispersoid strengthening. These materials, the micro-alloyed or HSLA steels, mentioned above, are available in a variety of compositions ^[1]. Even at lower temperatures, in HSLA steels, precipitation of carbides or nitrides at the austenite or ferrite boundaries can lead to cracking in the second ductility trough ^[1]. By adding an appropriate concentration of these elements, the toughness, plasticity, wear- and corrosion-resistant properties of the steel grade could be remarkably improved ^[2].

Until now, just a handful of studies have focused on the combined effects of V and Ti on the refining of solidification microstructures – all of them focused on casting steels.

Fu et al. [2] attributed the structure refinement from V + Ti and rare earths (RE) additions to the segregation of these elements to the solid/liquid interface during solidification, and corresponding growth restriction effect on the iron dendrites. This is also attributed to the nucleation of iron on carbides and nitrides of V and Ti that have a lattice mismatch in volume less than 6 % with iron.

Yu. Z. Babaskin [3] shows some experimental evidence that additions of V being bound with nitrogen and forming nitrides, e.g. VN, may act as structure refiners in a 40RL cast steel (see Table 5.1 for the chemical composition).

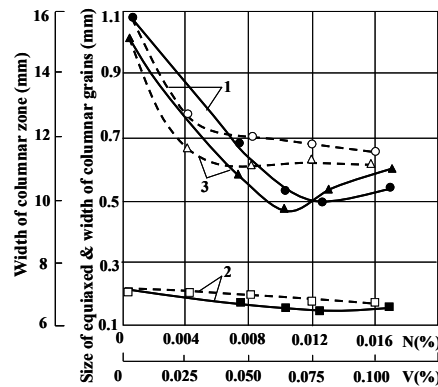


Figure 5.1. Effect of VN additions in a 40RL steel. (1) Width of the columnar zone, (2) average thickness of columnar dendrites, and (3) average size of equiaxed dendrites (45-mm billet; melt temperature 1560 °C). Effect of N (solid lines) and V (dashed lines).^[3]

Figure 5.1 shows that the increase in combined VN addition reduces the width of the columnar zone, decreases the thickness of the columnar dendrites, and the equiaxed dendrites show the minimum size at around 0.09 % VN.

On the other hand, it is shown that the effect of nitrogen is more pronounced than that of vanadium. Nitrogen seems to produce a minimum in curves 1 and 3 at around 0.010 % to 0.012 % N, while vanadium does not show this trend. Nevertheless, both elements cause the reduction in the width of the columnar zone, in the columnar dendrites average width, and in the average size of the equiaxed dendrites, when increasing V or N contents.

Table 5.1. Chemical composition of the 40RL steel [3].

Element	B	C	Cr	Mn	Ni	P	S	Si
(wt %)	0.0025 to 0.005	0.35 to 0.45	0.3	0.5 to 0.8	0.3	0.04	0.045	0.17 to 0.37

The grain refinement by VN additions was also shown in other alloyed casting steels. There is also evidence in Ref. [3] that additions of VN narrow the brittle (vulnerable) solidification range and increase the hot ductility.

5.2 Microstructural study of as-cast samples

To minimise the effect of heat transfer variation on the microstructure, special slab samples of the steel grades LCAK and HSLA were taken from the DSP caster for this study. The slabs were cast the same day (to reduce the effect on weather conditions and people), with new mould plates (to avoid effect on heat transfer), the same mould powder, and at the same casting speed. These slabs were sampled at the pendulum shear to avoid effect of the recrystallisation in the microstructure in the tunnel furnace before the rolling mill.

LCAK and HSLA macro- and microstructure was revealed with the Béchét–Beauchard etchant, shown in *Figure 5.2* and *Figure 5.3*, respectively.

Only dendrites are possible to see, the as-cast grain structure is possible to be seen due to recrystallisation of the samples during cooling.

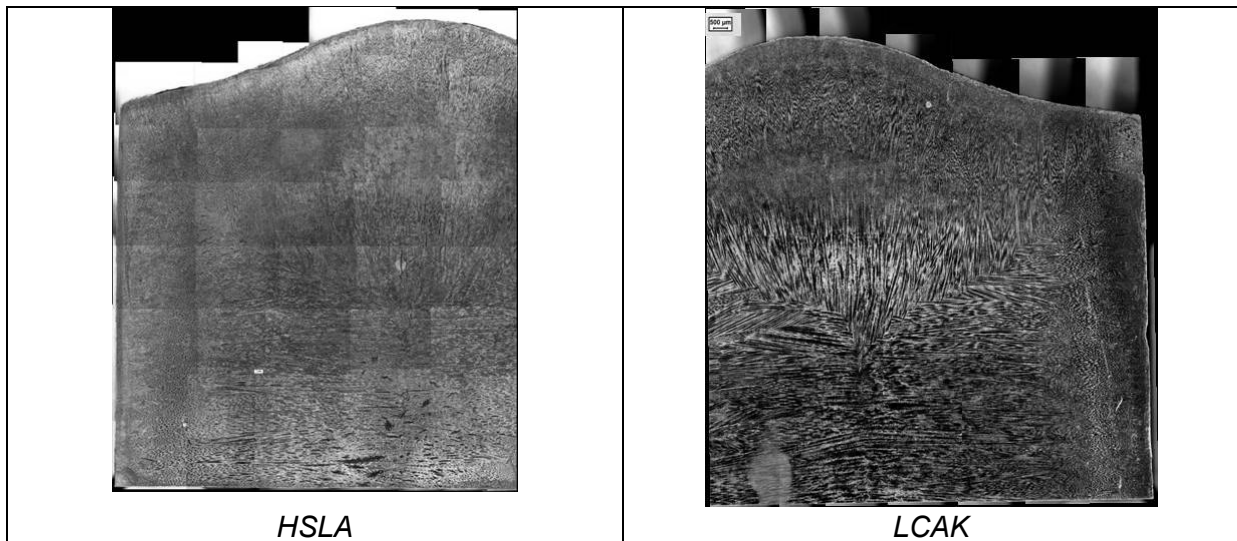


Figure 5.2. Macroetching for the two steel grades considered in this study.

The hypothesis is that V and N react during solidification with the corresponding structure refinement of the steel [3]. This refinement should have consequences for the mechanical behaviour of the steel, favourably affecting the strength of the semi-solid steel and its ductility. Eventually the hot tearing susceptibility will be decreased.

The macrostructures shown in *Figure 5.2* and *Figure 5.3* support the overall structure refinement in the HSLA steel as compared to the LCAK steel: dendrites are thinner and shorter, their internal constitution is finer.

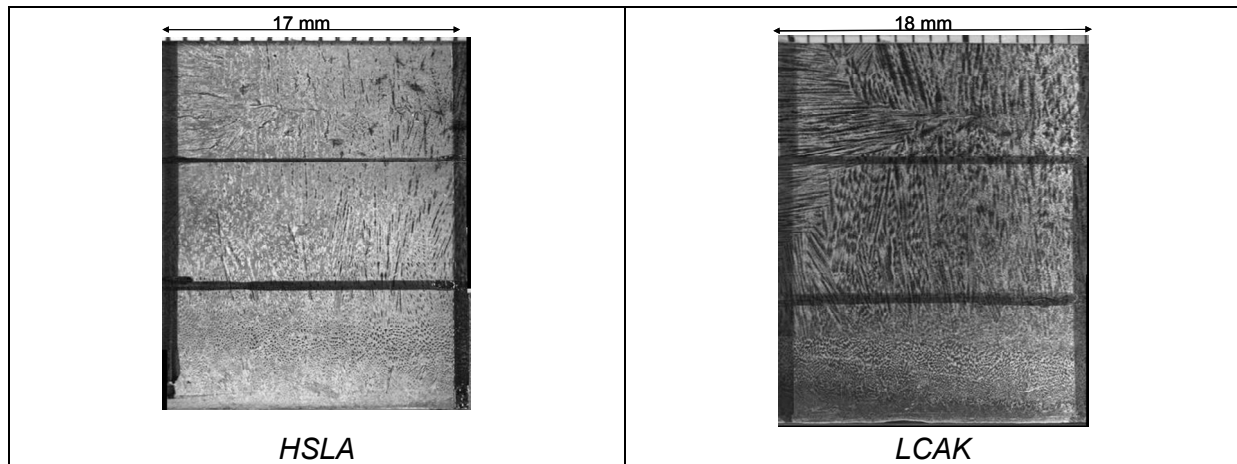


Figure 5.3. Macroetching for the two steel grades considered in this study.

From the microstructural examination, two unexpected features are observed, the absence of an outer equiaxed zone, commonly called “chill zone” and the presence of “bent dendrites”. These two features are further investigated in the following sub-sections.

5.2.1 Effect of fluid flow on dendrites growth

It is a well-known fact that dendrites growing in a flowing melt tend to bend towards the upstream direction^[4-8]. The mechanisms responsible for this bending have been studied and maybe classified into two cases. For free dendrites, that is for a pure metal growing in an undercooled substance, the thermal field around the dendrite tip determines the growth direction. The temperature around the tip in the downstream direction is higher than in the upstream direction due to the latent heat released on the surface. Therefore the driving force for the growth in the downstream direction decreases while it increases in the upstream direction^[4].

For columnar dendrites, that is for an impure metal growing with a positive temperature gradient, the solutal field around the dendrite tip plays an important role in determining the growth direction. The fluid flow has also an effect on the dendrite tip. Moreover, in the case of columnar dendrites, the dendrite tip may also determine the growth direction. A few studies have been performed on commercial grade steel^[4].

For microstructural analysis it is important to be aware of this effect on the microstructure, to avoid wrong interpretation of the results. For example, if the first few millimetres of shell solidified under the presence of strong fluid flow, their dendrite trunks could be seen on a cross-section as equiaxed dendrites, giving the impression that an equiaxed “chill zone” is present in the sample. Moreover, if one would correlate the thickness of this “chill zone” with some process parameters without a full 3D overview of the whole dendritic microstructure, it could lead to wrong conclusions. Therefore, to further investigate the dendritic structure smaller samples have been analysed, following the scheme from *Figure 5.4*.

The HSLA slab sample (from *Figure 5.2*) has been selected to illustrate here the effect of the fluid flow in the microstructure.

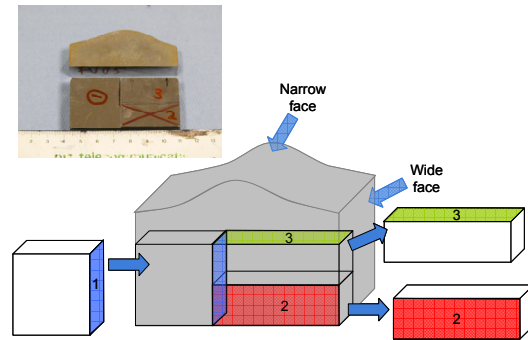


Figure 5.4. Schematic overview of the sample selection.

As the dendrites grow in the opposite direction of the fluid flow, in sample nr 2 it is possible to see the dendrites cut in a transverse direction ("bended dendrites" region marked in Figure 5.5).

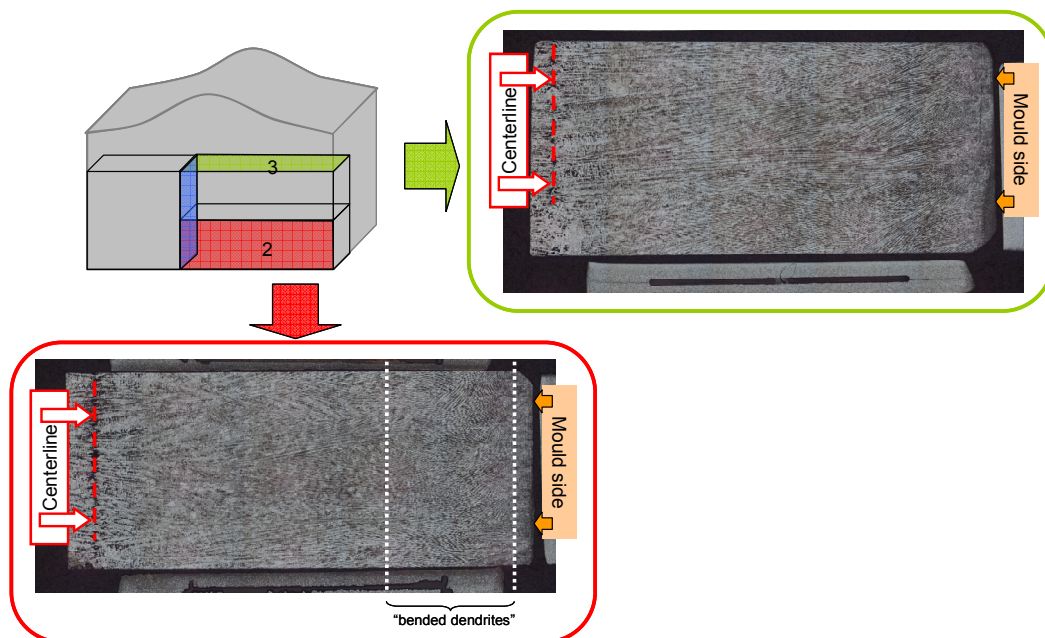


Figure 5.5. Overview of the microstructure in the samples.

As a result, the sample Nr. 3 shows the dendrites bending against the fluid flow. In Figure 5.6, the direction of the dendrites has been drawn in white-full-lines, together with the distance from the slab surface (light-blue dotted-lines).

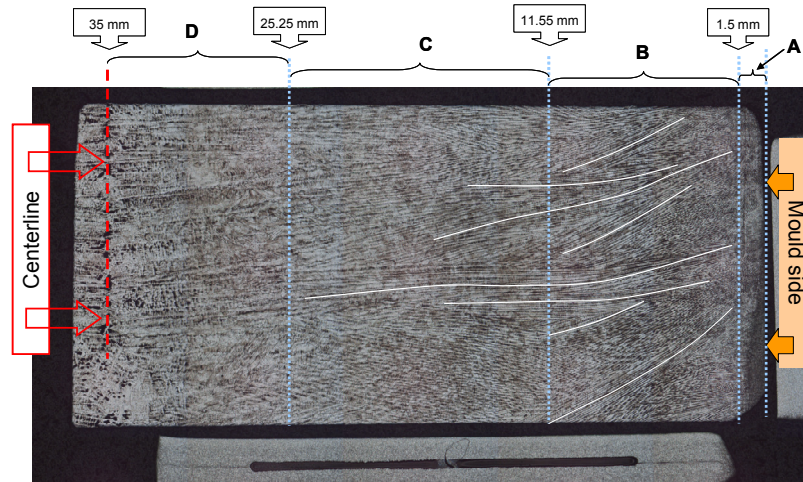


Figure 5.6. Detail of the bended dendrites.

The angle between a perpendicular line and a given dendrite trunk defines the deflection angle (see Figure 5.7).

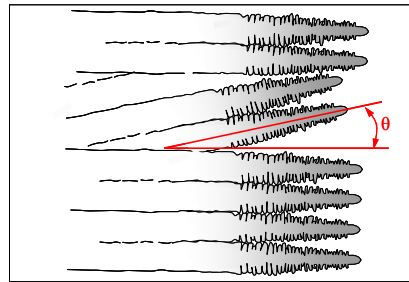


Figure 5.7. Schematic overview of dendrites and deflexion angle.

5.2.2 Outer equiaxed “chill” zone in continuous casting of steels

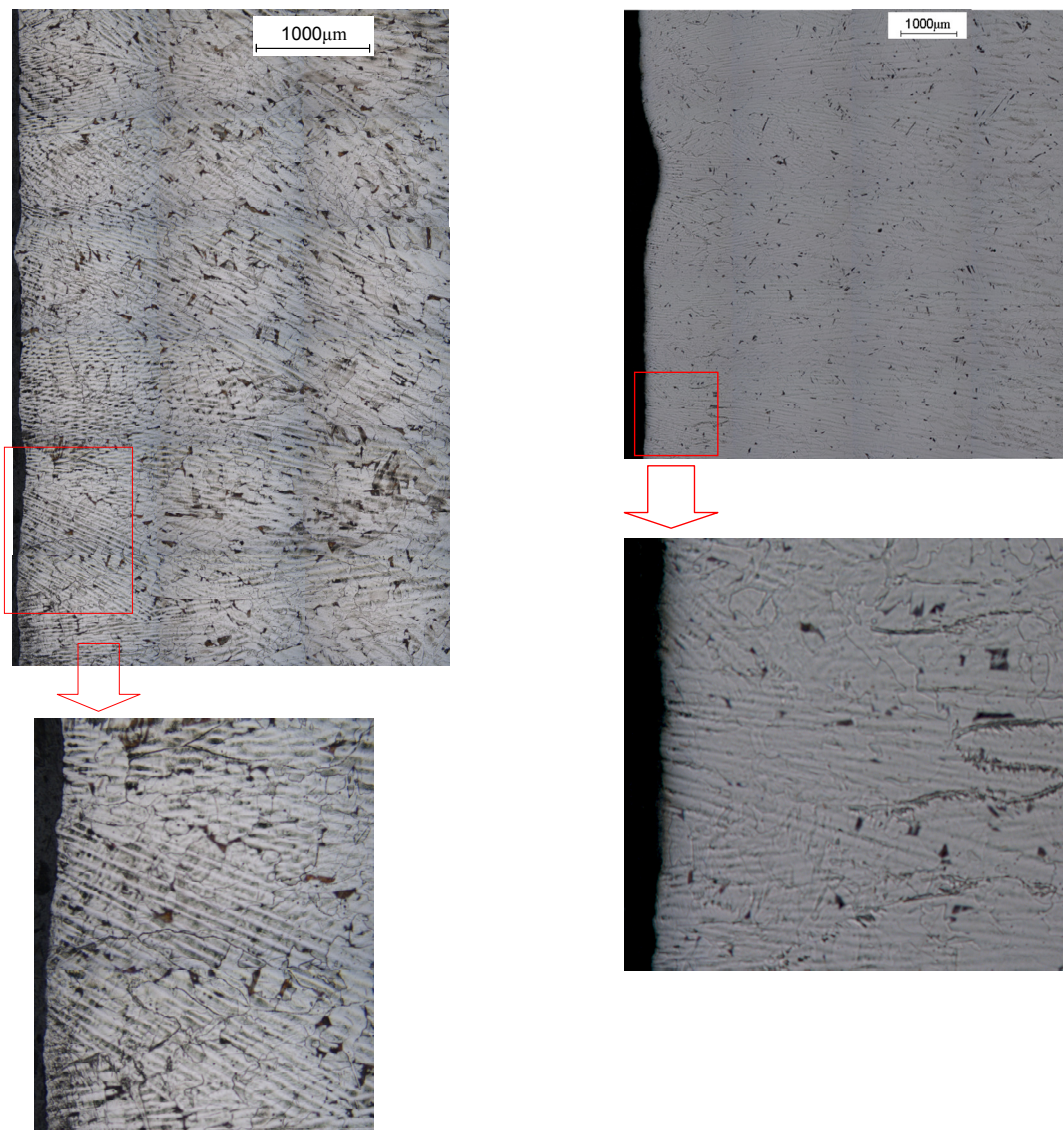
According to the literature ^[9,10], at the mould/metal interface, the cooling rate is at its highest due to the initially low temperature of the mould and good contact of the melt/casting powder with the mould. Consequently, many small grains having random orientations are nucleated at the mould surface and an “outer equiaxed” zone is formed. Moreover, equiaxed microstructure is characterised by crystals growing “freely” in the liquid melt.

However, the first nuclei to grow in a chilled surface will be the ones that are attached to that surface, which can later grow parallel and opposite to the heat flow direction, forming a columnar dendritic structure. In addition, if some crystals would appear growing freely in the melt, the high velocity of the fluid flow will wash the nuclei that are not attached to the chilled surface, giving no chance to develop an equiaxed structure, only columnar structure will be developed.

Mizukami et al. ^[11], in the analysis of initial solidification in small samples solidified over a chilled plate, found that the dendritic microstructure solidified unidirectionally from the chill plate side for each sample.

Xu et al. [12] found in samples taken from a 55 mm thin slab caster, where a low carbon steel shows a typical dendrite structure, the structure distribution with a fairly narrow central equiaxed crystal zone and no apparent dendrite inclination from the slab normal direction. At a larger magnification, the finer dendrites with different orientations competitively grow in the chill region, and the primary dendrite arms near the surface incline at different angles relative to the slab normal direction. The dendrites of which the growth direction coincides with the heat flux direction grow preferably, which consequently results in the columnar δ -ferrite grains in the middle layer and the apparently increased primary dendrite arm spacing.

Due to the high resolution of the metallographic images available for the steel grades considered in this thesis, it was possible to study the nature of the outer equiaxed region, commonly called “chill zone” [10].



HSLA LCAK
 Figure 5.8. Detail of the dendritic structure at the slab surface.

Contrary to the expectations, no equiaxed zone was found (see *Figure 5.8*). The whole microstructure is predominantly columnar, although some nucleation events occurred, because new orientations appear not only at the surface of the slab.

As explained before, in the first few millimetres of shell solidified under the presence of strong fluid flow, the dendrite trunks could be seen on a cross-section as equiaxed dendrites, giving the impression that an equiaxed “chill zone” is present in the sample, when in a full 3D analysis it is evident that there are no equiaxed dendrites.

5.3 Measurement of primary dendrite spacing

Depending upon the growth conditions, the dendrite (from the Greek, dendron=tree) can develop arms of various orders. A dendritic form is usually characterised in terms of the primary (dendrite trunk) spacing, λ_1 , and the secondary (dendrite arm) spacing λ_2 . Tertiary arms are also often observed close to the tip of the dendrite ^[9]. A schematic view of the primary and secondary dendrite spacing is shown in *Figure 5.9*.

It is important to note that the value of λ_1 measured in the solidified microstructure is the same as that existing during growth, whereas the secondary spacing is enormously increased due to the coarsening as a result of long contact between the highly-curved, branched structure and the melt ^[9].

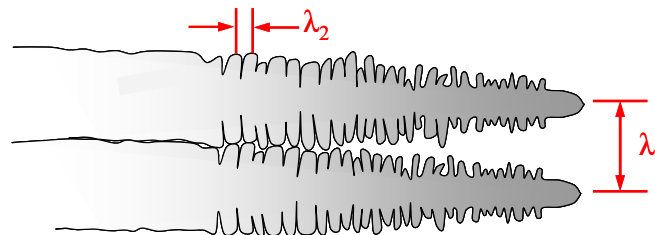


Figure 5.9. Schematic overview of the primary and secondary dendrite spacings.

The primary trunk spacing is an important characteristic of columnar dendrites and has a marked effect on the mechanical properties.

The secondary dendrite arms in the continuous cast structures of steel are difficult to see. However, the primary arm spacing is possible to measure.

The macrostructures support the theory of the structure refinement in the HSLA steel as compared to the LCAK steel: dendrites are thinner and shorter, their internal constitution is finer. *Figure 5.10* demonstrates this.

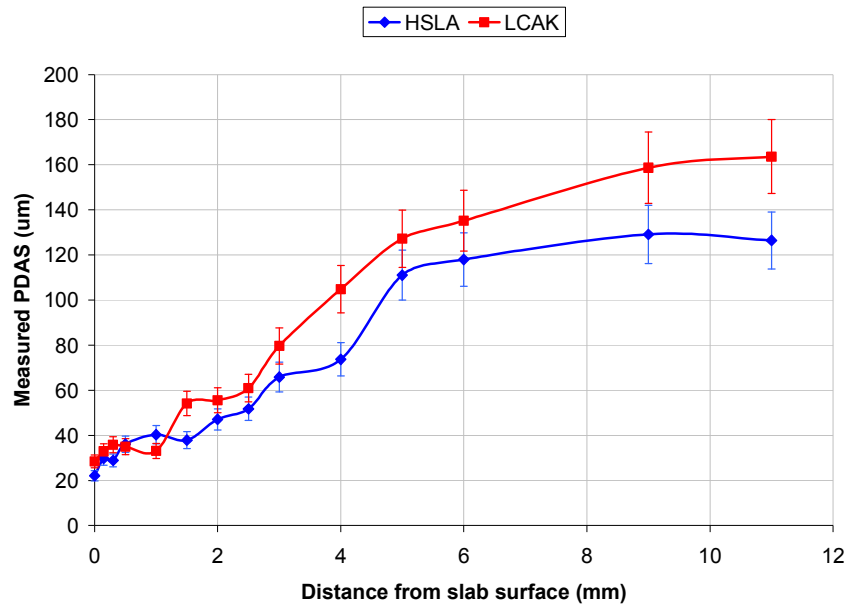


Figure 5.10. Primary dendrite arm spacing measured in the HSLA and LCAK steels.

5.4 Phase field modelling

Successful application of robust microstructure simulation software does help in understanding these microstructural differences. For the continuous casting process conditions, the effect on microstructure (grain size, orientation, morphology, microsegregation, precipitation) in the overall dendritic structure is investigated with the aim to exploit qualitative differences between these alloys.

The phase field calculations here reported have been done in collaboration with Dr. B. Böttger in RWTH- ACCESS, Germany as part of the M2i-Tata Steel- ACCESS Valorisation project “Thermodynamic calculations and MICRESS® simulations of microstructure evolution during continuous casting of technical steel grades” [13]. In addition, the cracking susceptibility has been considered in connection with the simulated microstructure evolution.

5.4.1 Introduction to the phase field

The phase-field method has widely been applied for alloy solidification. Idealized descriptions of the phase diagrams (ideal solution approximation [14], linear phase diagrams [15]) have been used for binary and pseudo-binary alloys. But this approximation in most cases is not suitable for use in multi-component multiphase systems, especially if the composition of the dissolved elements is too high for an ideal solution approximation, and if many phases are involved and, consequently, the complexity of the phase diagram descriptions increases. Instead, using Gibbs energy descriptions assessed from experimental data via the Calphad approach [16], together with software tools for Gibbs energy minimization [17], seems to be most promising.

Growing interest in the application of the phase-field method to technical alloys and industrial problems introduced a steep increase in complexity regarding thermodynamics as well as thermal boundary conditions. Most technical steels are multi-component, often containing

more than 10 relevant elements. Furthermore, several solid phases are typically involved in phase transformations, like fcc iron, bcc iron, manganese sulfide, carbides etc.

MICRESS®^[18] has been developed by ACCESS e.V. at Aachen University (RWTH). It is based on the phase-field concept for multiphase systems^[19] which has been applied to binary alloys^[15] and consequently extended to multi-component systems^[20,21] by direct coupling to thermodynamic databases via the TQ Fortran interface to Thermo-Calc^[17]. Since then the software has been developed further and applied to different alloy systems^[22-26] and also to steels^[27-30].

5.4.2 Multiphase-field model and MICRESS® software

The multiphase-field theory describes the evolution of multiple phase-field parameters $\phi_\alpha(\vec{x}, t)$ in time and space. The phase-field parameters reflect the spatial distribution of different grains of different orientation or of a number of phases with different thermodynamic properties. At the interfaces, the phase-field variables change continuously over an interface thickness η which can be defined as being large compared to the atomic interface thickness but small compared to the microstructure length scale. The time evolution of the phases is calculated by a set of phase-field equations deduced by the minimization of the free energy functional^[21,31]:

$$\dot{\phi}_\alpha = \sum_\beta M_{\alpha\beta}(\vec{n}) \left(\sigma_{\alpha\beta}^*(\vec{n}) K_{\alpha\beta} + \frac{\pi}{\eta} \sqrt{\phi_\alpha \phi_\beta} \Delta G_{\alpha\beta}(\vec{c}, T) \right) \quad (5.1)$$

$$K_{\alpha\beta} = \phi_\beta \nabla^2 \phi_\alpha - \phi_\alpha \nabla^2 \phi_\beta + \frac{\pi^2}{\eta^2} (\phi_\alpha - \phi_\beta) \quad (5.2)$$

In equation (5.3), $M_{\alpha\beta}$ is the mobility of the interface as a function of the interface orientation, described by the normal vector \vec{n} . $\sigma_{\alpha\beta}^*$ is the effective anisotropic surface energy (surface stiffness), and $K_{\alpha\beta}$ is related to the local curvature of the interface. The interface, on the one hand, is driven by the curvature contribution $\sigma_{\alpha\beta}^* K_{\alpha\beta}$ and on the other hand by the thermodynamic driving force $\Delta G_{\alpha\beta}$. The thermodynamic driving force, which is a function of temperature T and local composition \vec{c} , couples the phase-field equations to the diffusion equations

$$\dot{\vec{c}} = \nabla \sum_{\alpha=1}^N \phi_\alpha \vec{D}_\alpha \nabla \vec{c}_\alpha \quad \text{with } \vec{c} \text{ defined by} \quad \vec{c} = \sum_{\alpha=1}^N \phi_\alpha \vec{c}_\alpha \quad (5.3)$$

and \vec{D}_α being the multicomponent diffusion coefficient matrix for phase α . \vec{D}_α is calculated online from databases for the given concentration and temperature.

The above equations are implemented in the software package MICRESS®^[18] being used for the simulations throughout this study. The thermodynamic driving force ΔG and the solute partitioning are calculated separately using the quasi-equilibrium approach^[21], and are introduced into the equation for the multiple phase-fields. This allows the software package to be highly flexible with respect to thermodynamic data of a variety of alloy systems and not to be restricted by the number of elements or phases being considered. A multi-binary extrapolation scheme^[21] has been implemented in order to minimize the thermodynamic data handling, especially for complex alloy systems.

5.4.3 Boundary conditions

In continuous casting, during the initial formation of a solid shell, the local temperature field in the solidifying region is highly unstationary and non-linear. To obtain a realistic temperature boundary condition for the phase-field simulation, a temperature solver is integrated which, due to symmetry reasons, can be reduced to one dimension. According to the higher diffusivity of heat compared to solute diffusion, a lower resolution is required. This allows the temperature field to range deeply into the casting, ideally down to the centre of the casting, without causing too much computational effort (*Figure 5.11*). By this means, temperature can be explicitly solved in the 1D field including a boundary condition at both sides, while latent heat released from the simulation domain is averaged from the zone which corresponds to one grid cell in the low-resolution temperature field ^[32]:

$$\dot{T} = \frac{1}{C_p} \left(\nabla \sum_{\alpha} f_{\alpha} \lambda_{\alpha} \nabla T + \sum_{\alpha} H_{\alpha} \dot{f}_{\alpha} \right) \quad (5.4)$$

Here, f_{α} denotes the average phase fraction of phase α in this zone.

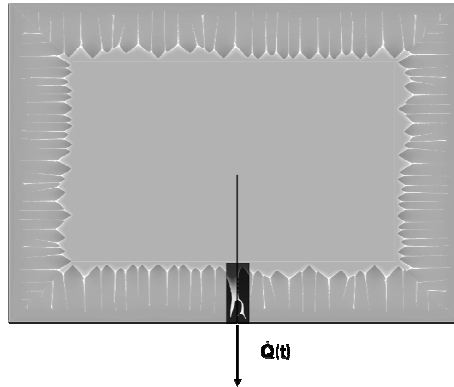


Figure 5.11. Schematic representation of the position of the simulation domain (small rectangular region) and the external 1D temperature field (black line) in the cross-section of the strand. The arrow below indicates the outer boundary condition for the temperature field.

Due to performance reasons, the simulation domain cannot cover the whole solidification length in the mould of the continuous caster. Instead, the solidification front is tracked by using the moving-frame option of the MICRESS® software (*Figure 5.12*). Tracking criterion can be a constant temperature at the bottom or a constant distance of the highest dendrite from the top of the simulation domain. The constant distance criterion was used in this study.

In the case of using the moving frame condition, for the extremely low-alloyed grades used in this study, it could be assured that the complete solidification interval and thus the major part of the latent heat release occurred inside the simulation domain (darker rectangular zone in *Figure 5.11*). But especially for the simulations with Ti where nucleation and growth of TiN at lower temperatures is investigated, the moving frame is switched off. Then, when the dendrites are touching the top boundary of the simulation domain, latent heat release outside the domain (but within the extension of the 1D temperature field in *Figure 5.13*) has to be taken into account.

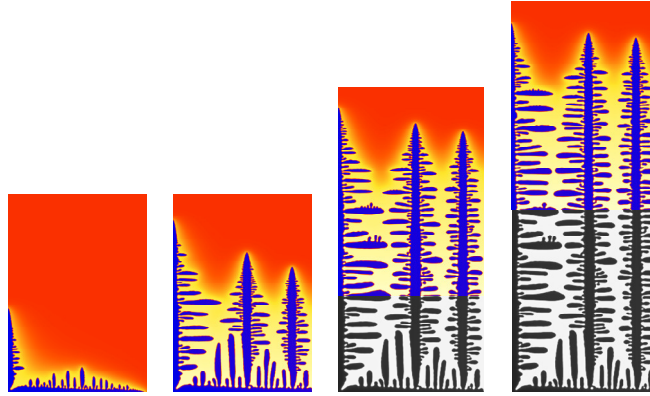


Figure 5.12. Schematic representation of the moving frame feature in MICRESS®. The (coloured) simulation domain is following the dendrite tips, the regions which are moving out (grey) are collected in a total view graphical output (whole image).

Latent heat formation is directly linked to microstructure formation, as this is not longer directly simulated, an approximated approach has to be used; instead of using the Scheil approximation. The latter would not be accurate because of the considerable dendrite tip undercooling, the results of a former simulation run from inside the simulation domain are abstracted in form of an enthalpy-temperature relation and used for the description of latent heat release outside the domain. This approach is called an iterative “homoenthalpic” approach, because a spatially independent enthalpy-temperature relation is assumed as described by Bottger et al. [32].

As shown in Figure 5.11, the bottom boundary condition of the 1D temperature field is a heat extraction rate which was obtained from a CON1D [33] simulation of the casting process for the DSP caster conditions. This time-dependent heat flow rate shows a strong peak at about 0.4 seconds (Figure 5.13). As casting simulations for different alloy grades gave very similar results, this curve was used for all grades in the MICRESS® simulation. Later, the use of the temperature of the outer edge of the slab as thermal boundary condition for MICRESS® (also obtained from the CON1D simulation) was preferred.

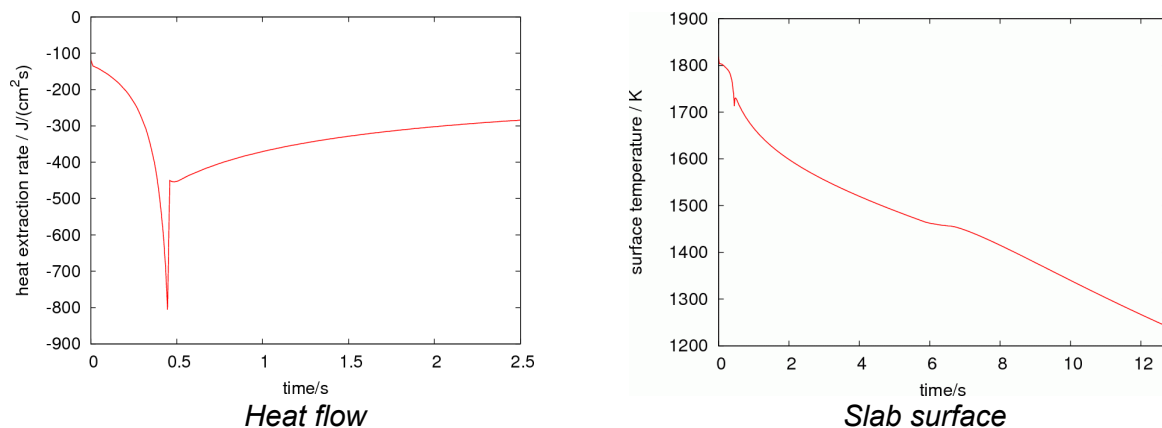


Figure 5.13. Heat flow and slab temperature used as boundary conditions.

The boundary conditions for the concentration fields and the phase boundaries (phase-field parameter field) which are chosen at the different sides of the simulation domain are of utmost importance if the simulation domain is not big. Only the bottom condition is uncritical

(isolating is used). At both sides, symmetric, periodic or isolating conditions can generally be applied. Symmetric conditions (mirror symmetry through the centres of the outermost row of grid cells) typically allow the use of the smallest domain, if symmetry is possible, like in the simulation of *Figure 5.12* where the dendrites are perfectly aligned along the y direction (direction of temperature gradient). Next best choice normally is the periodic condition, because this greatly reduces the effect of the boundary: Obliquely growing dendrites would “vanish” on one side and reappear on the opposite side without feeling any boundary.

But periodic conditions on the left and right boundary of the simulation domain turned out not to be the best choice because, in this project, selection of columnar dendrites with spontaneous nucleation of equiaxed grains was simulated. Under these circumstances, periodic conditions easily lead to the dominance of one dendrite orientation, even if it is not well aligned to the temperature gradient. Selection is stopped, while in reality there is always more than one grain or there is a real boundary somewhere, and thus selection leads to a dominance of highly favoured directions. Therefore, finally, isolated boundary conditions were used on the right and left side of the simulation domain.

In case of moving frame, for the top concentration boundary a fixed condition was used to assure that the far-field concentration remains constant (and equal to the average alloy composition). Otherwise, also an isolation boundary condition was used.

5.4.4 Nucleation model

As the existence of a chill zone was expected ^[9,10], and because nucleation can affect grain selection in columnar growth, a heterogeneous model for nucleation from the melt was used. The approach is inspired by a statistical approach to heterogeneous nucleation in equiaxed solidification ^[34,35] which is based on the assumption of a density distribution of heterogeneous nuclei with different diameters d . The critical undercooling for nucleation is then determined by:

$$\Delta T_{Nuc} = \frac{4\gamma}{\Delta S d} \quad (5.5)$$

where ΔS is the entropy of fusion, and γ the solid–liquid interfacial energy.

This basic idea has been extended to a fully spatially resolved model which further accounts for an inhomogeneous composition ^[22] and temperature ^[32] distribution and which is implemented in the MICRESS® software. At the beginning of each simulation run, the potential nucleation sites are randomly distributed over the domain, according to the given seed density distribution, and attributed with the critical nucleation undercooling given by the nucleant size according to Equation 5.7. If this critical undercooling is reached locally, a grain with random orientation is set.

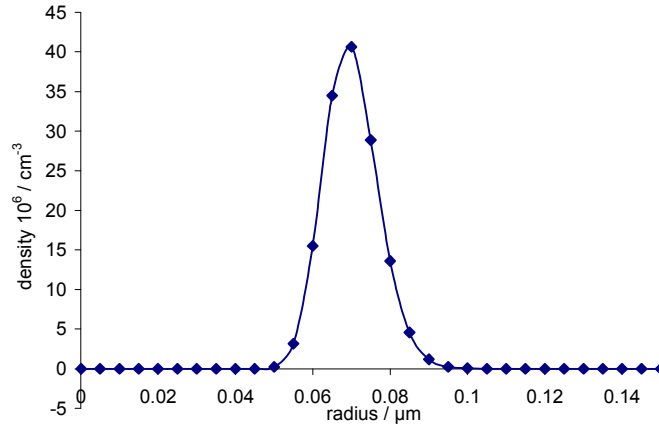


Figure 5.14. Typical seed density distribution used in this study. A log-normal distribution with $r_0=0.065$, $\sigma=10\%r_0$ and $N=107$ (Equations 5.8 and 5.9) is shown, the class width is $0.05 \mu\text{m}$.

The seed density distribution is defined by an arbitrary number of seed classes which have a different radius and as such a different critical nucleation undercooling. In this work, a three parameter log-normal distribution function is used:

$$\frac{dN}{dr} = \frac{N}{\sigma r \sqrt{2\pi}} \exp\left(-\frac{1}{2} \left[\frac{\ln(r)-\mu}{\sigma}\right]^2\right) \quad (5.6)$$

$$\mu = \ln(r_0) - \frac{\sigma^2}{2} \quad (5.7)$$

Discretisation into radius classes is done using an Excel sheet. The three parameters r_0 (average radius), σ (width) and N (total density) were varied, finding a final setting of parameters for these simulations (Figure 5.14).

5.5 Simulations of commercial steel grades

For the low alloyed steel grade (LCAK) only three elements (Fe, Mn, C) have been taken into account. Figure 5.15 shows a time series of results for LCAK and the carbon concentration distribution which demonstrates how morphology formation is proceeding. The solid-liquid interface and its development are clearly visible over the time range between 0.2 s and 3.0 s.

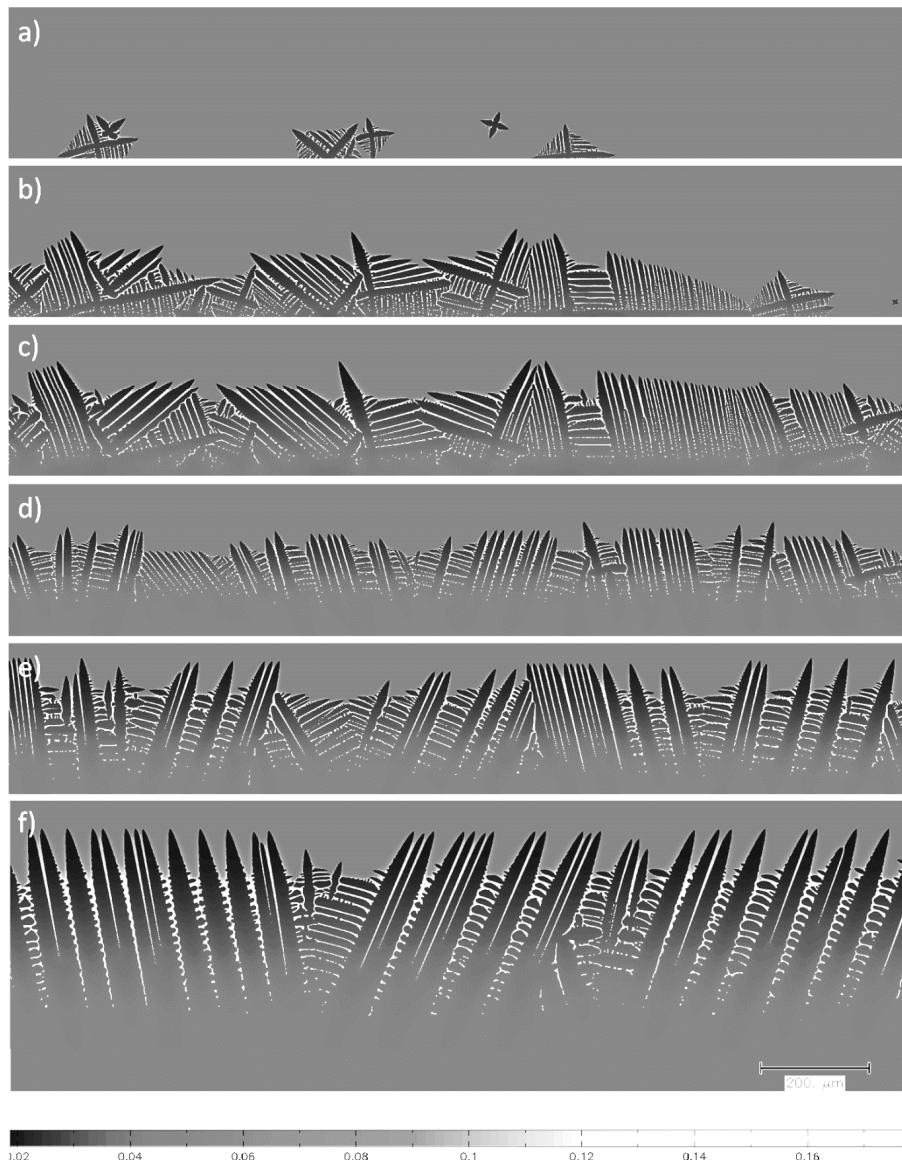


Figure 5.15. Time sequence for solidification of LCAK. The C distribution is shown after a) 0.20 s, b) 0.25 s, c) 0.30 s, d) 0.50 s, e) 1.0 s, f) 3.0 s.

The first seeds grow from the melt and form equiaxed grains (a)-(b). Due to the strong temperature gradient and dendrite selection the solidification front rapidly assumes a columnar structure (c-d). At this stage (d), the thickness of the mushy zone reaches a minimal value, which is due to the extremely strong cooling rate (see Figure 5.13) leading to a strong thermal gradient at this stage. At a later stage, (e)-(f), gradient and cooling rate are decreasing which leads to a coarsening of the microstructure. Nucleation of equiaxed grains ahead of the front is scarce. The choice of the nucleation parameter (Figure 5.14) is responsible for that, which is in accordance with experimental findings (Figure 5.17).

The simulation results, especially the grain structure after solidification, are very sensitive with respect to the choice of the seed density distribution for nucleation. In Figure 5.16, the grain structures obtained with two different seed density distributions is shown as orientation distribution. The two used distributions have the same shape, but the one used for the simulation shown in Figure 5.16 top has a 100 times higher total seed density. It can be seen

that a higher number of grains is nucleated in case of the higher seed density. In both cases, a strong grain selection occurs, and only grains with orientations close to 0° or 90° (i.e. with orientations close to the temperature gradient vector) are left.

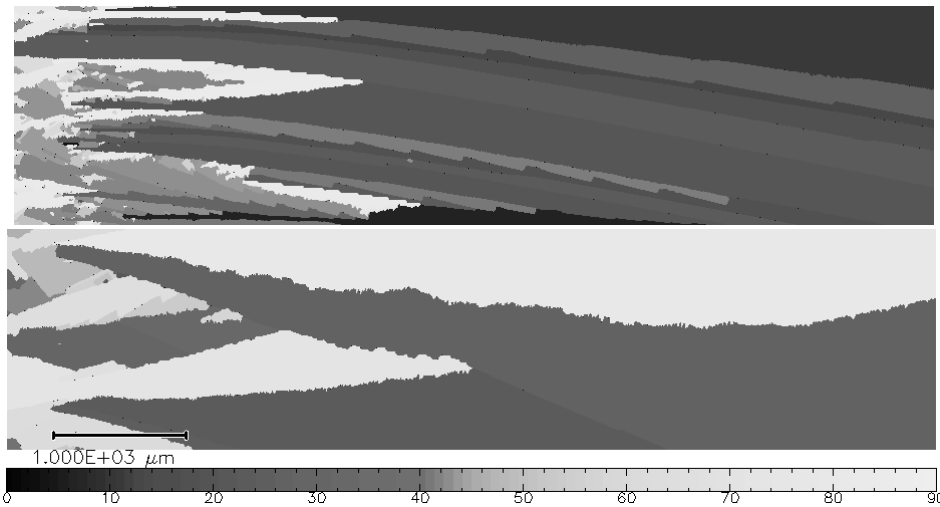


Figure 5.16. Simulated orientation distribution for LCAK and a simulation domain of 5000×2000 grid cells with seed parameter top: $r_0=0.05$, $s=0.14$ and $N=2 \times 10^8$ and bottom: $r_0=0.05$, $s=0.14$ and $N=2 \times 10^6$. The mould surface is on the left side.

In Figure 5.17 (left), a micrograph for LCAK shows a predominantly columnar structure. Nevertheless, some nucleation seems to have occurred. New dendrite orientations are appearing especially in the lower part close to the surface of the slab. In Figure 5.17 (right), this experimental microstructure is compared to the result of a simulation run. A good qualitative agreement can be seen, taking into account that the experimental micrograph is a cut through a 3D structure, and that after solidification other phase transformations have occurred which left their fingerprints there. Nevertheless, the average primary dendritic distances according to the simulation results appear to be smaller than in the experimental micrograph.

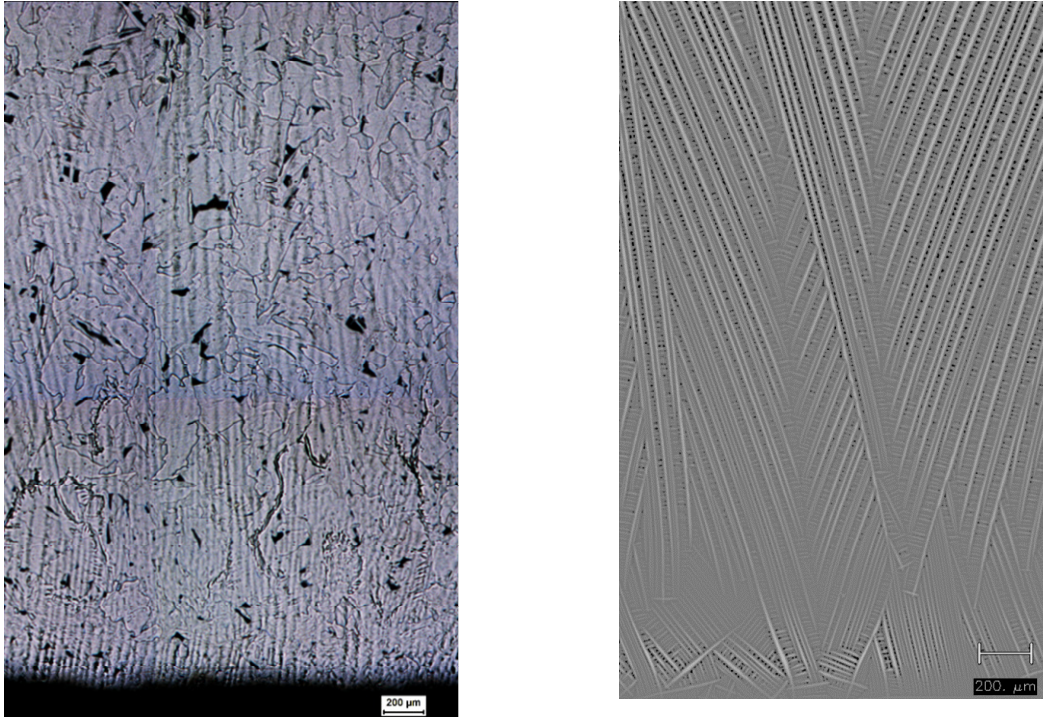


Figure 5.17. Comparison between a micrograph of the microstructure of LCAK (left) and simulation results (Mn distribution in grey scale, right). The strand surface is on the bottom side.

A check of the growth velocity of the dendrite front was possible by comparing the solidification length to the results of the heat transfer model CON1D^[33] which had been calibrated for the case of several breakout shells of LCAK^[36]. Figure 5.18 shows the measured shell thickness (up to the dendrite tips) in comparison to the front position predicted by the phase-field simulation. As can be seen, the fit is nearly perfect up to about 7 mm and the deviation does not exceed 5 % at the mould exit. This demonstrates that the 1D approximation of the temperature field is a useful approach under these conditions.

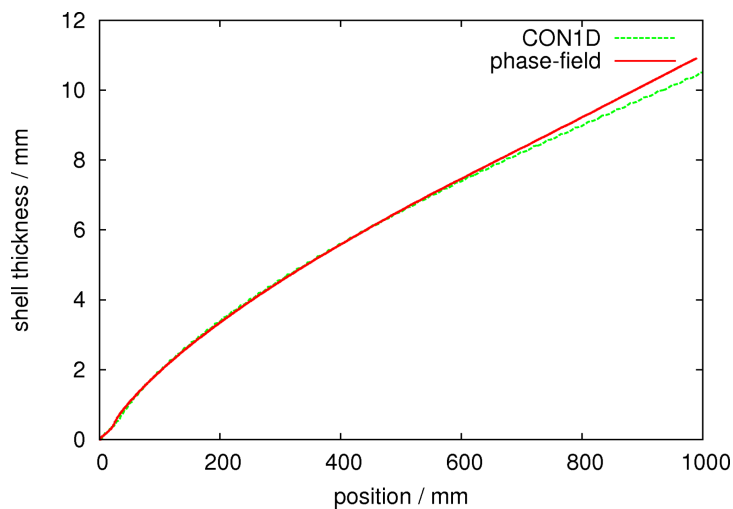


Figure 5.18. Shell thickness comparison for a LCAK slab between CON1D and phase-field simulation

Finally, a comparison of the PDAS (Primary Dendrite Arm Spacing) between experiment and simulation is shown (*Figure 5.19*). The measured PDAS values for two samples (Prep 2 and Prep 3) are opposed to the results of the phase-field simulation. Although the PDAS values are in quite good agreement for about the first 1 mm, there is a clear discrepancy for higher positions (>2 mm) in the solidified shell. Even uncertainties like insufficient calibration or measurement errors cannot explain why there is a strong increase in the PDAS between about 2 and 6 mm in the experimental results, which is not found in the simulation. It is believed that convective fluid flows, which are typically weak when the solidification process starts but get stronger with increasing solidification time, could have selectively altered the PDAS. The strong bending of dendrites typically found in micrographs (see Section 5.2) under these conditions suggests that a strong fluid flow is present in this region which could have altered the PDAS and which was not taken into account in the simulation.

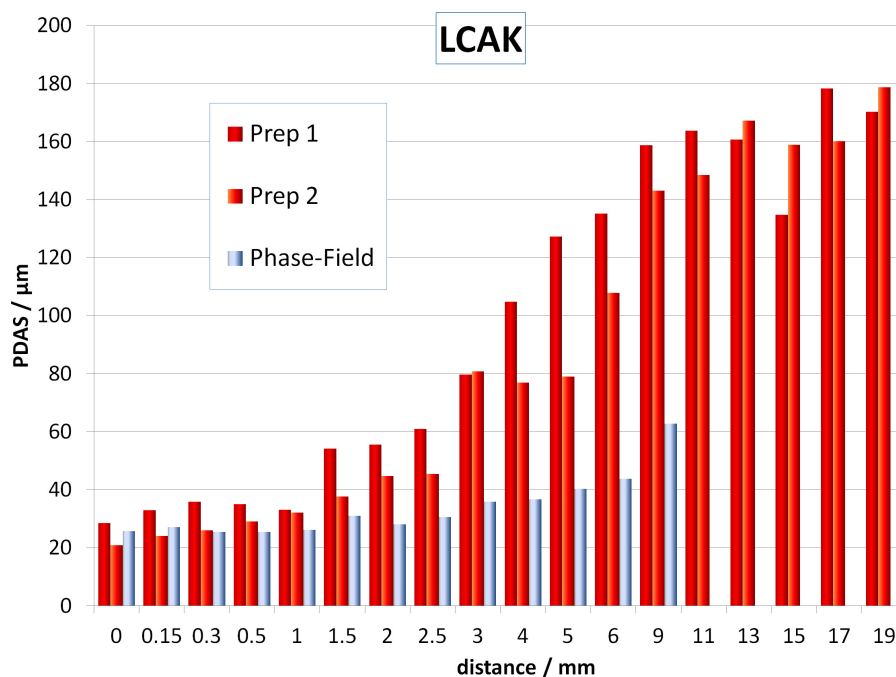


Figure 5.19. Comparison of the PDAS for LCAK between measurements (Prep 2, Prep 3) and simulation, as function of the distance from the shell surface.

For the LR-HSLA and HSLA steel grades, the micro-alloying elements Nb, V and N have been taken into account (*Table 1.1* in Chapter 1). This makes simulation considerably more time and memory consuming, but is needed to find out whether and how these elements are affecting microstructure and, thus, the hot cracking behaviour. Ti was still neglected at this stage, because no minimum content was defined in the alloy specification, and the typical concentration is very low (~0.003 wt%). *Figure 5.20* shows the concentration distribution of all five alloying elements for HSLA after 0.4 s solidification time, according to a phase-field simulation. All considered elements show a positive segregation, i.e. they are enriched in the interdendritic region during solidification. After complete solidification, C and N reach a rather smooth distribution, which is due to their high diffusivity in the solid. The other slow diffusing elements (Mn, V and Nb) retain their segregation pattern.

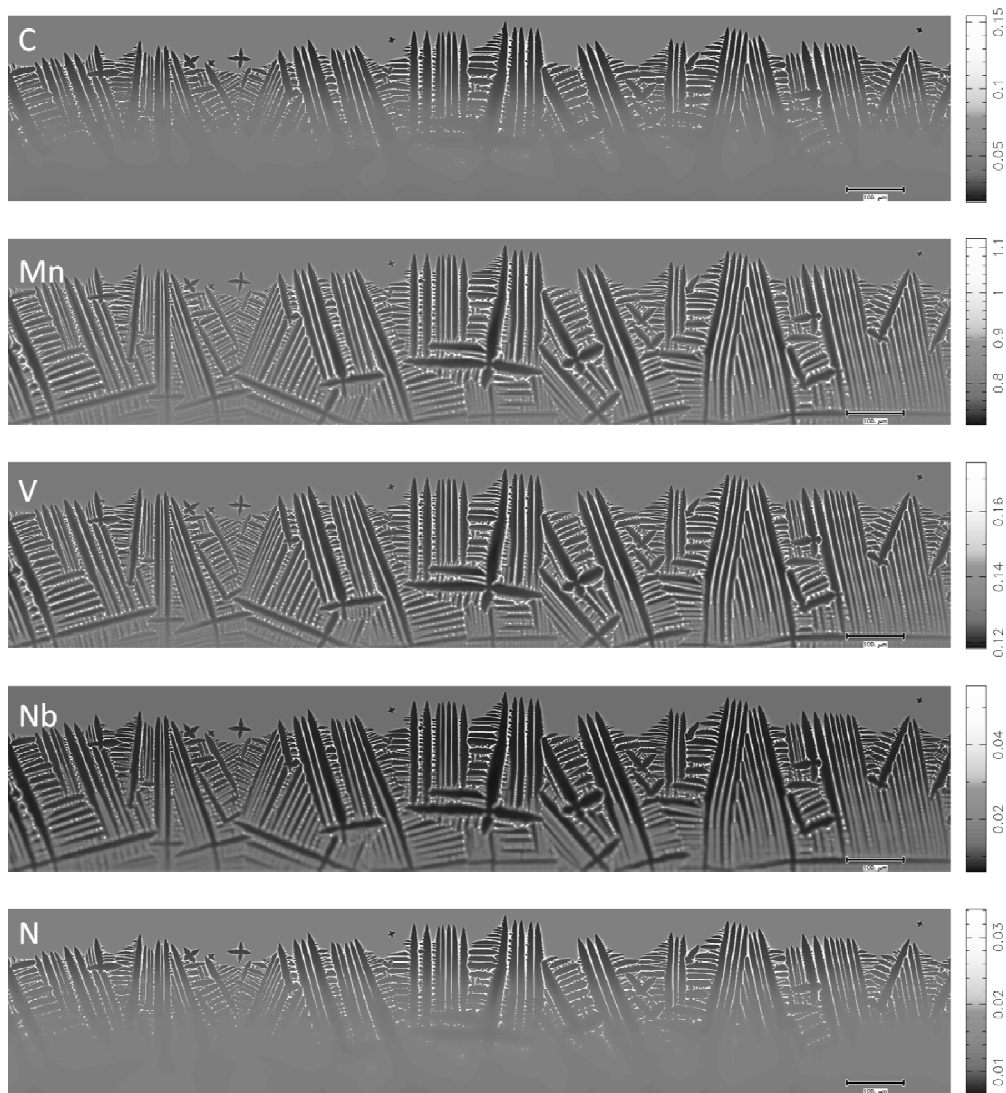


Figure 5.20. Concentration distribution of all elements in wt% for HSLA at $t=0.4$ s.

5.5.1 Quantitative evaluation of simulated microstructure

The microstructure differences between LR-HSLA and HSLA are by far smaller than those between LCAK and HSLA. This is reasonable if we look at the composition of the steel grades given in Table 1.1, Chapter 1. Apart from the lack of micro-alloying elements, the Mn content of LCAK is almost 4 times lower compared to the other two grades. Consequently, this difference should be visible in the simulated microstructures like those shown in Figure 5.21. Shown here is the Mn concentration distribution for the initial solidification microstructure of all three steel grades at the same stage of solidification. Mn is a strongly segregating element and outlines the dendrites well in both simulated and experimental structures. While the microstructures for HSLA and LR-HSLA are qualitatively identical, the dendrites and dendrite arms appear to be somewhat thicker for LCAK.

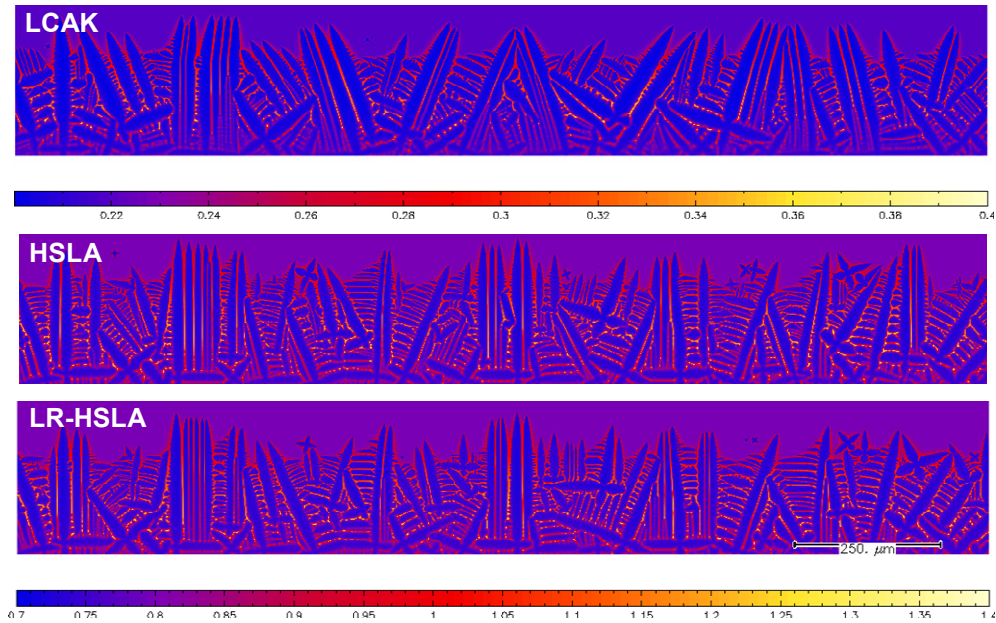


Figure 5.21. Microstructure of LCAK (top) after 0.32 s, HSLA (center) after 0.36 s and LR-HSLA (bottom) after 0.35 s, shown is the Mn distribution. Simulation domain 5000x2000 cells, $\Delta x=0.333 \mu\text{m}$.

A more quantitative evaluation includes the determination of the secondary dendrite spacing λ_2 . This has been done for different positions along the solidification path. In Figure 5.22, a log-log plot of the found λ_2 values versus the local solidification time (measured between $f_L=100\%$ and $f_L=1\%$) is shown. The coefficients for the empirical exponential relation $\lambda_2 = a\Delta t^b$ are given in Table 5.2. For all three steel grades, the exponent b is close to the theoretical value of 0.333, while the constants a are slightly different. Consequently, the secondary dendrite spacing λ_2 is biggest for LCAK and smallest for HSLA, which is in agreement with the increasing alloy content.

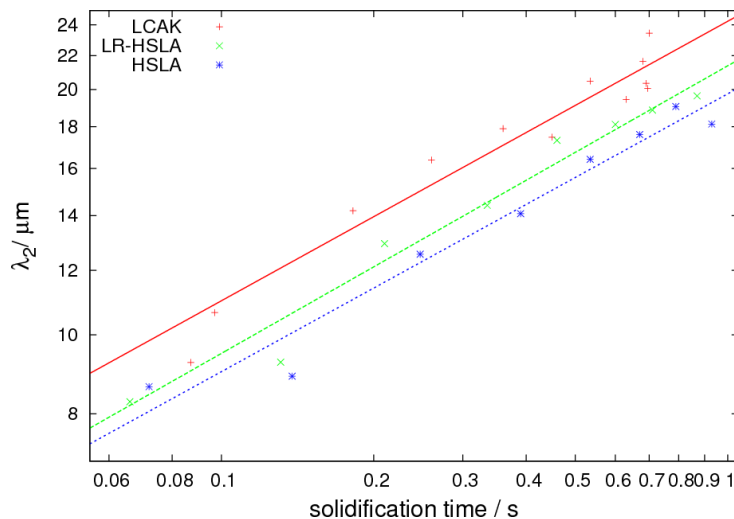


Figure 5.22. Dependency of λ_2 with local solidification time for LCAK, HSLA and LR-HSLA. The data can be represented by the exponential relation $\lambda_2 = a\Delta t^b$.

Another approach for a quantitative comparison of the microstructure is to analyse the specific surface of the dendritic network. For this purpose, the width of surface per area $S_i(T)$ is calculated in arbitrary units as a function of temperature for the three alloys. Each individual value is obtained by averaging the local phase-field gradient over row number i of the grid along the x direction, which corresponds to an isothermal line:

$$S_i(T) = \frac{1}{N_x} \sum_{i=1}^{N_x} \sqrt{\phi_\alpha^i \phi_\beta^i} \quad (5.8)$$

The resulting plot of S_i versus temperature, averaged for a reference distance range between 1.0 and 2.0 mm from the strand surface ($x=1.0-2.0$ mm), is smoothed using a cubic spline and shown in *Figure 5.23* (top). The three relations obtained for the alloy grades reflect both, the temperature range of the semisolid region, i.e. the length over which $S_i > 0$, and the value of S_i itself, which is a measure for the local fineness of the microstructure. The thickness of the semisolid region has a significantly lower value for LCAK compared to LR-HSLA/HSLA, and is only slightly higher for HSLA with respect to LR-HSLA. This can be more easily seen in *Figure 5.23* (bottom), where the three curves have been aligned to the same liquidus temperature. Interestingly, the maximum value of S_i is very similar for the three steel grades.

A total surface area of the mushy zone can be calculated by summing S_i over all rows i of the mushy zone, which is equivalent to an integration of the specific surface over the semisolid region:

$$S_{tot} = \int_x S_i(x) dx = \Delta x \sum_{i=1}^{N_y} S_i \quad (5.9)$$

The average values obtained at the reference position between 1 and 2 mm below the strand surface are given in *Table 5.2*. The difference between the values for LR-HSLA and LCAK is about 3-4 times bigger than the difference between HSLA and LR-HSLA.

Finally, the fraction liquid–temperature curves are compared in *Figure 5.24* (top). They were obtained in a similar way like the surface per area, namely by integrating the simulation results for various time steps between $x=1.0-2.0$ mm over all averaged isothermal rows of grid cells and subsequent smoothing. By shifting the resulting curves for HSLA and LR-HSLA, the curves could be aligned at a fraction liquid of $f_L=10\%$ (*Figure 5.24*, bottom). The relative shifting allows for a better comparison of the shapes of the curves and the length of the vulnerable temperature range between $f_L=10\%$ and $f_L=1\%$, which according to the RDG criterion is important for hot cracking (see Section 2.5.2, Chapter 2).

Table 5.2. Averaged microstructure parameters for the reference position (1-2 mm)

Steel grade	T_L (°C)	T ($f_L=10\%$) (°C)	T ($f_L=1\%$) (°C)	ΔT ($f_L=1-10\%$) (°C)	S_{tot} (a.u.)	$\lambda_2 = a\Delta t^b$ (μm)	
						a	b
LCAK	1528.3	1522.4	1515.4	7.03	3.49	24.25	0.3429
LR-HSLA	1523.7	1515.2	1506.4	8.75	5.76	21.38	0.3528
HSLA	1523.6	1514.2	1504.7	9.48	6.41	19.76	0.3409

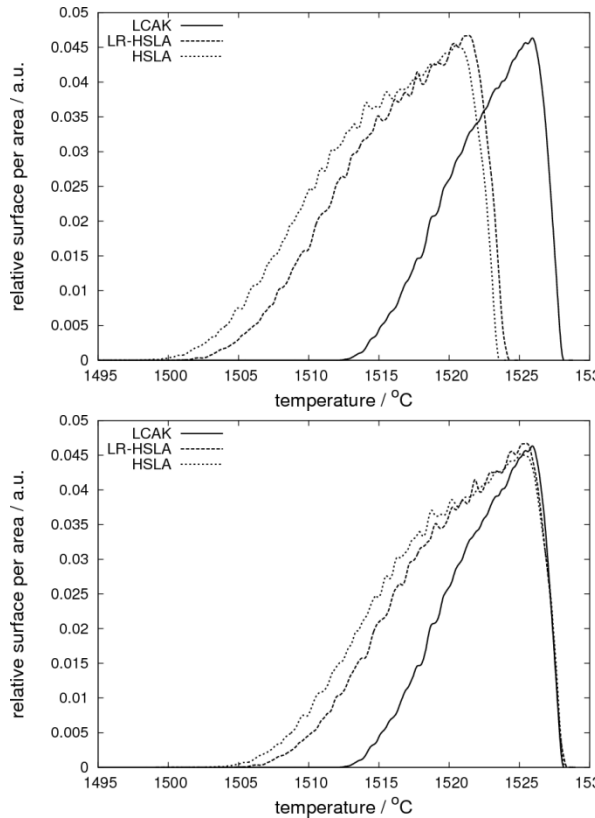


Figure 5.23. Top: Comparison of the smoothed average specific surface per area for LCAK, LR-HSLA and HSLA, plotted versus temperature. Bottom: The curves for HSLA/LR-HSLA are shifted to the same liquidus temperature as LCAK.

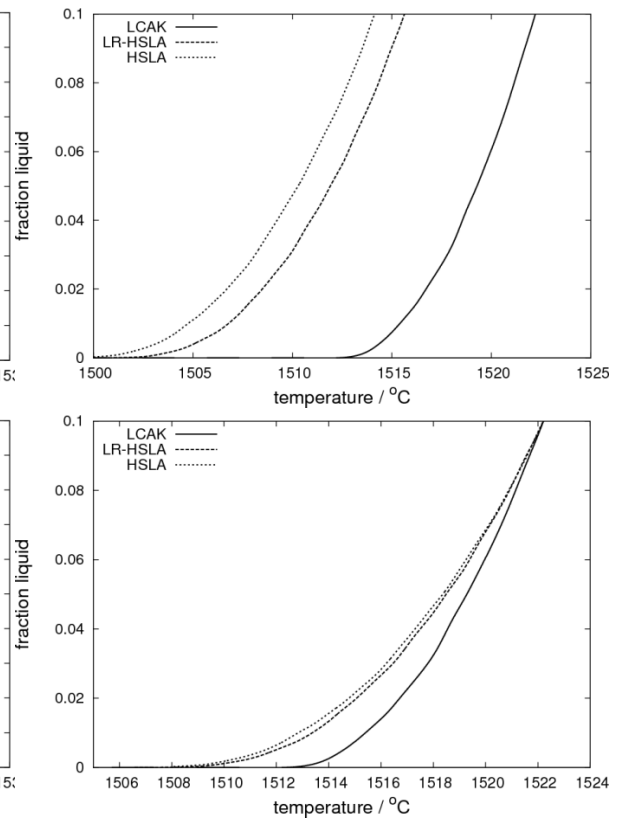


Figure 5.24. Top: Comparison of the fraction liquid-temperature curves for LCAK, HSLA and LR-HSLA for the $x=1.0-2.0$ mm. Bottom: For better comparison, the curves have been aligned at the temperature where $f_L=10\%$.

The results are in accordance with the thickness of the mushy zone found in Figure 5.23. While LCAK shows the steepest f_s / T curve and thus the smallest solidification temperature interval, HSLA and LR-HSLA exhibit an increased thickness of the semisolid region, which is due to the higher content of the alloying elements Mn, Nb, V and N. The difference between the two HSLA grades (which is only caused by the different content of V and N) is smaller but still significant. The obtained temperatures for $f_L = 100\%$, $f_L = 10\%$, and $f_L = 1\%$ as well as the vulnerable temperature interval ΔT ($f_L = 1-10\%$) are summarized in Table 5.2.

In summary, significant differences in microstructure have been found, even between HSLA and LR-HSLA, which are consistent with the different concentrations of alloying elements. The consequences for hot-cracking, according to the RDG criterion^[37-39], are evaluated in the following section.

5.5.2 Evaluation of the hot-cracking susceptibility using the Rappaz criterion

Hot tears are separations which might form during casting, when the temperatures of sub-areas of the material are between solidus (T_S) and liquidus (T_L) and are subject of simultaneously acting tensile stresses^[37-39]. Hot tears typically initiate above the (non-equilibrium) solidus temperature at volume fractions of the solid phase above 0.85–0.9 and

propagate mainly through the interdendritic liquid film. One of the conditions for hot tearing is the lack of liquid feeding of the mushy zone, especially at the end of solidification, and, more precisely, when grains start to impinge and finally touch one another, but are still largely separated by a continuous liquid film [38].

As explained in Chapter 2, a strain-rate-based criterion was developed by Rappaz et al. [39] for aluminium and adapted for steel by Drezet et al. [37]. The model is based on a mass balance for the liquid and solid phases and allows for calculating the pressure drop contributions in the mushy zone. It assumes a tensile deformation perpendicular to the growth direction of the dendrites, and describes the induced interdendritic liquid feeding flow. If this flow cannot compensate for thermal contraction (thermal strain) and for solidification shrinkage at a given strain rate, a void may form and initiate a crack.

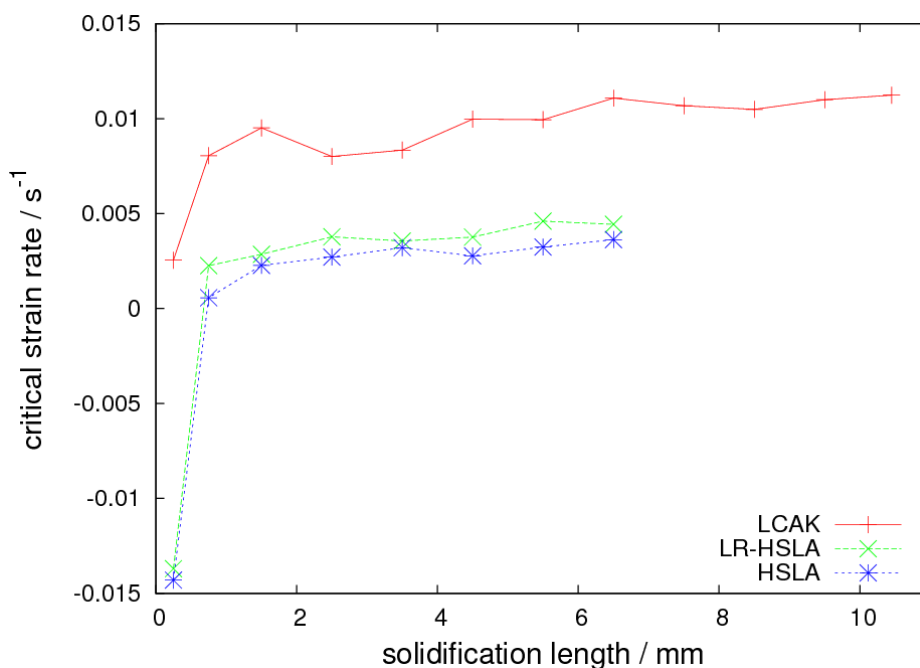


Figure 5.25. Critical strain rate according to the RDG criterion, as function of the solidification length.

Figure 5.25 shows the critical strain rates for different solidification lengths as calculated based on the phase field results. A low value of $\dot{\epsilon}_{crit}$ is equivalent to the prediction of a high risk of hot cracking. Very close to the slab surface ($x=0.25\text{mm}$), $\dot{\epsilon}_{crit}$ is very small, indicating an increased cracking risk. The negative values for HSLA and LR-HSLA even imply cracking (or porosity formation) without strain. However, at this early stage of casting and solidification, cracking susceptibility should not be critical as cracks can be easily healed by penetrating melt.

For higher depths inside the slab, corresponding to a later stage of solidification, the critical strain rate $\dot{\epsilon}_{crit}$ shows nearly constant values. If we compare the resulting hot-cracking risk with the observed frequencies of breakouts observed during production, we find agreement with respect to LCAK and LR-HSLA: Obviously, the higher concentration of Mn, but also of V, Nb and N, leads to a stronger segregation in LR-HSLA, a deeper mushy zone, and thus to an

increased risk of cracking. According to this analysis, HSLA should show an even slightly higher risk of breakouts compared to LR-HSLA. However, let us not to forget that the HSLA shows a strongly reduced breakout risk, which cannot be understood on the basis of this purely solutal analysis.

The critical strain rate $\dot{\varepsilon}_{crit}$ and critical strain ε_{crit} for the reference location $x = 1-2$ mm are given in *Table 5.3*.

Table 5.3. Critical strain rate $\dot{\varepsilon}_{crit}$ and critical strain ε_{crit} for the reference position (1–2mm) and for different steel grades (without Ti)

steel grade	$\dot{\varepsilon}_{crit}$ (s ⁻¹)	ε_{crit} (%)
LCAK	0.9514	0.06660
LR-HSLA	0.2855	0.02513
HSLA	0.2273	0.02205

5.5.3 Precipitation of carbo-nitride particles

The previous analysis shows that the low cracking risk of HSLA could not be explained only from the solutal effects of the elements V and N which have been added in comparison to LR-HSLA. The main purpose of the addition of these elements is the formation of VN at lower temperatures, which enables ferrite grain refinement in thermo-mechanically controlled processing (TMCP). The high solubility of VN (and also of Nb(C,N)) excludes the possibility that precipitation takes place at higher temperatures which are relevant for hot tearing. Ti is the only micro-alloying element which is known to form nitrides at rather high temperatures. Although it is not explicitly specified as an alloying element in the steel grades considered in this paper, this element is present with a typical content of 0.002–0.004 %. If its precipitation as TiN or co-precipitation with other micro-alloying elements as (Ti,V,Nb)(C,N)^[40] can happen before solidification is finished, an influence of Ti on hot cracking is possible, and the higher V and N content of HSLA perhaps could explain the altered breakout risk of this alloy.

In the following, the precipitation tendency for carbo-nitrides was simulated for LR-HSLA and HSLA. An additional small content of 0.003 % Ti was assumed. It must be pointed out that on the scale of the dendrites carbo-nitride particles cannot be properly resolved due to too coarse a grid. Each precipitate is typically represented by a single grid cell with a fraction of the carbo-nitride phase <1, and curvature is calculated using the assumption that this particle forms a sphere. In view of these restrictions, no morphological information apart from the integral particle size can be expected from the simulations. Also, the particle size and density are not representative, because nothing is known about nucleation data and no experimental data were available for calibration. For this reason, the evaluation presented here is focusing only on the temperature when carbo-nitrides are formed, and on their phase fraction.

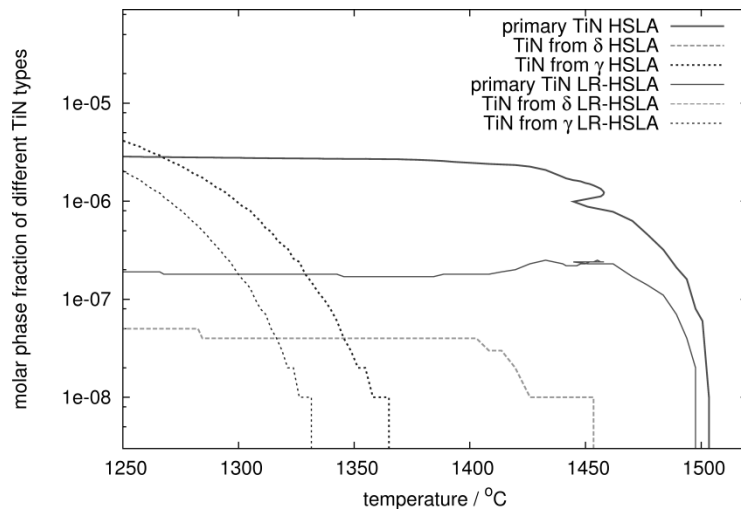


Figure 5.26. Logarithmic plot of the carbo-nitride phase fraction versus temperature down to 1250°C for a Ti composition of 0.003wt%. Independent values are given for those particles which nucleated in the melt, in the δ -ferrite and the γ -austenite phase.

In order to find out whether carbo-nitride particles could affect the hot-cracking behaviour of the selected steel grades, the first question to be addressed is at which temperature and at which sites precipitation of this phase can occur. For this purpose, a simulation setup with a rather small simulation domain of 300x2000 grid cells and a resolution of 0.333 μm was chosen. No moving frame was applied in this case, because the focus was also on precipitation of carbo-nitrides in ferrite and austenite at lower temperatures. Figure 5.26 shows the amount of carbo-nitrides for HSLA and LR-HSLA in a temperature range between 1250°C and 1520°C. Particles which were nucleated from the melt, the δ -ferrite and the γ -austenite were distinguished and evaluated separately.

According to the simulation results, most of the total amount of carbo-nitrides forms either in the melt at temperatures above about 1450°C, or from the γ -austenite at much lower temperature. Furthermore, in the considered temperature range, the precipitates mainly consist of TiN. This means that, in accordance with empirical knowledge^[40], the formation of particles which could affect the mechanical behaviour at high temperatures strongly depends on the Ti and N content of the alloy.

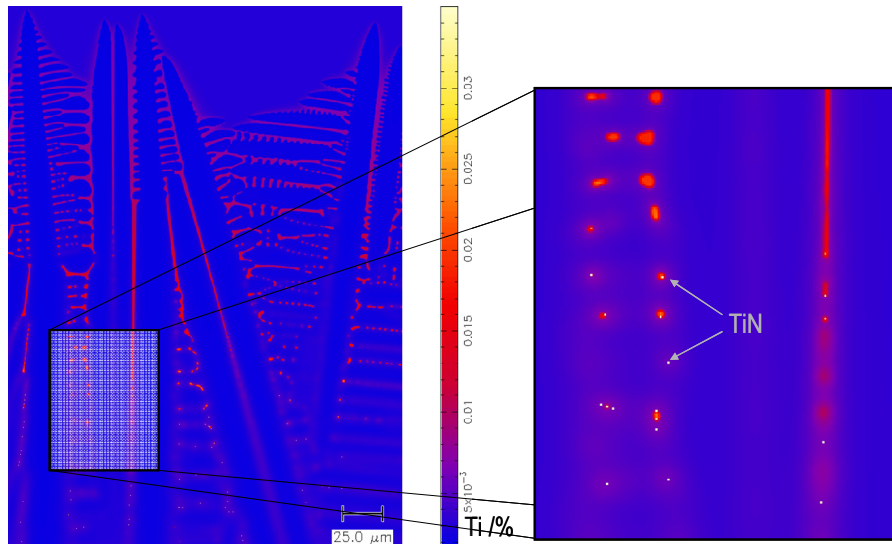


Figure 5.27. Concentration distribution of Ti in HSLA+0.003 wt% Ti after 0.7 s for a small section of the simulation domain, showing interdendritic TiN precipitation.

Although TiN precipitation from the γ -austenite, which is shifted to a slightly higher temperature in HSLA compared to LR-HSLA, could also somehow affect crack propagation at temperatures below 1350 °C, the focus in this study is on those precipitates which form in the interdendritic liquid. For this purpose, a conventional simulation with moving-frame and 2000 x 5000 grid points was performed, which takes into account a Ti content of 0.003 wt% and nucleation of TiN in the melt. Figure 5.27 demonstrates where this type of TiN precipitation is taking place. Shown is the Ti distribution for a small section of the simulation domain at $t=0.7$ s. A further magnified subsection in Figure 5.27 reveals that TiN is forming at low temperatures just before solidification is completed. It should be quite reasonable and straightforward to assume that during this eutectic reaction, which is taking place in the thin channels of remaining liquid, the neighbouring dendrites are fused together, i.e. coalescence is triggered. If this is the case, TiN precipitation from the melt could increase the coalescence temperature and thus reduce the hot cracking risk. And, as has been shown in Figure 5.26, TiN precipitation depends strongly on the N content of the alloy and thus is expected to be different in HSLA and LR-HSLA.

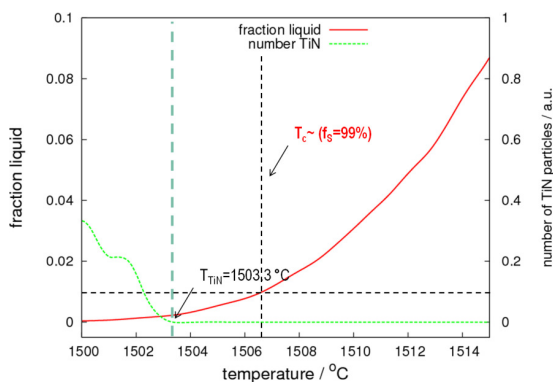


Figure 5.28. Number density of TiN precipitates and fraction liquid plotted versus temperature for LR-HSLA + 0.003% Ti.

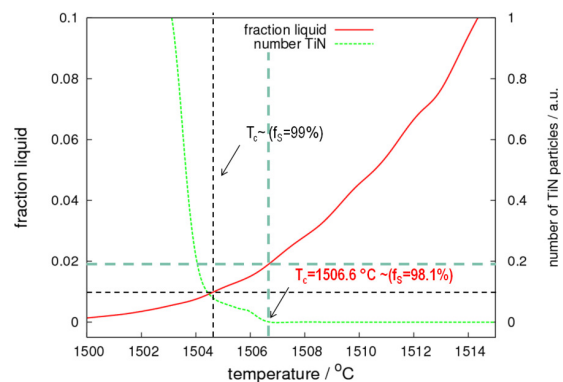


Figure 5.29. Number density of TiN precipitates and fraction liquid plotted versus temperature for HSLA + 0.003% Ti.

In the following it shall be assumed that the coalescence temperature is determined by the temperature where TiN starts forming, if this happens at a fraction of solid below 0.99. Otherwise, the default criterion $f_s=0.99$ is used for determining the coalescence temperature T_c . The TiN onset formation temperature, as well as the corresponding value of f_s for LR-HSLA and HSLA are evaluated in *Figure 5.28* and *Figure 5.29*, where a dimensionless number density of the TiN precipitations is plotted together with the fraction liquid against temperature. As can be seen, for HSLA the TiN onset formation temperature lies nearly 2 degrees above the default coalescence temperature for $f_s=0.99$, and a strong effect of TiN precipitation on hot cracking could be expected. On the other hand, for LR-HSLA TiN forms well below the default coalescence temperature, and TiN precipitation should not alter the hot-cracking behaviour.

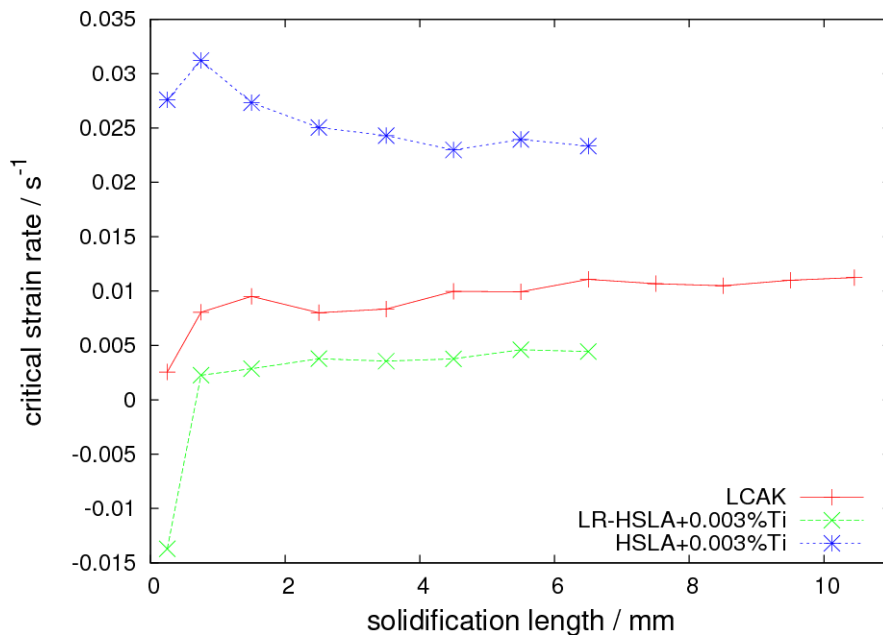


Figure 5.30. Critical strain rate according to the RDG criterion including the effect of TiN precipitation.

Finally, *Figure 5.30* shows the resulting prediction of hot cracking using the RDG criterion, if we take the corrected coalescence temperature for HSLA into account, thus with TiN, compared with the results in *Figure 5.25*, the critical strain rate $\dot{\epsilon}_{crit}$ as well as the critical strain ϵ_{crit} are for HSLA with TiN more than a factor of 10 higher than for LR-HSLA, which is in very good agreement with the breakout behaviour observed during production. The criteria for coalescence, the corresponding coalescence temperature as well as the resulting critical strain rate $\dot{\epsilon}_{crit}$ and critical strain ϵ_{crit} for the reference location $x = 1-2\text{mm}$ are summarized in *Table 5.4*.

Table 5.4. Critical fraction solid for coalescence, corresponding coalescence temperature T_c , critical strain rate $\dot{\epsilon}_{crit}$ and critical strain ϵ_{crit} for HLSA and LR-HSLA with and without Ti

steel grade	f_s	T_c (K)	$\dot{\epsilon}_{crit}$ (s^{-1})	ϵ_{crit} (%)
LR-HSLA	0.99	1506.42	0.2855	0.02513
LR-HSLA+0.003%Ti	0.99	1506.42	0.2855	0.02513
HSLA	0.99	1504.74	0.2273	0.02205
HSLA+0.003%Ti	0.981	1506.60	2.733	0.2651

5.6 Influence of microstructure on hot tearing susceptibility

The results show that there is a direct reason to look at the microstructural difference even when the chemical composition differs only slightly between steel grades.

A good analogy is a wall built with bricks, if the same force is applied to a wall constructed with few, big bricks, and to another wall of the same dimensions but with many small bricks, the wall with the fewer bricks will fail first to the same applied force. This is explained as few-big-bricks have less points to intersect and distribute the load, where in the case with many small bricks, the load will be further distributed along the joints between bricks.

For a microstructure the same correlation holds, the mushy zone consisting of few big dendrites/grains is weaker than the one with many small ones. This is the case of the LCAK, where the microstructure analyses of the as-cast samples and the phase field simulations have proven that this steel grade will solidify with a coarse microstructure.

Additionally, the higher the amount of alloying elements, the higher the segregation, thus the smaller the grains will be developed during solidification. Therefore, a steel grade with higher amount of alloying elements will have a tendency to solidify with a stronger, much compact structure, and this is probably the case for the LR-HSLA and HSLA steel grades. However, in general, the higher the amount of alloying elements, the lower the Solidus temperature will be. For the steel grades studied here, there is a very small difference on their Solidus temperature (see Chapter 3), in comparison with the big effect that the alloying elements make in the strengthening of the structure.

The special behaviour of the HSLA grade, compared with the LR-HSLA, can be better understood by taking into account the precipitation of TiN, even if Ti is not specified in the alloy grades and only very low amounts of this element are present. With the hypothesis that TiN particles can trigger the coalescence of dendrite trunks it is possible to understand why, for a given Ti content, an increased N content can help to reduce the risk of hot tearing. This effect of TiN precipitation could be quantified by assuming an increased coalescence temperature that shifts above the default coalescence temperature at $f_s=0.99$.

To summarize, the LCAK grade is susceptible to cracking during solidification because its microstructure is coarse due to the lack of alloying elements. The HSLA grade is not cracking susceptible during solidification due to earlier coalescence of dendrites as a result of TiN formation, much earlier than for the LR-HSLA grade.

References

1. *The Making, Shaping and Treating of Steel*, 11th Edition, Casting, Pittsburg, Pa, USA, 2003, The AISE steel foundation.
2. Fu, H., Qu, Y., and Xing, J., *Investigations of Solidification Structures of High Carbon Alloy Cast Steel Containing RE-V-Ti*, Journal of Materials Engineering and Performance, 18 (4), 2009, 333-338.
3. Babaskin, Y. Z., *Structure and properties of cast steel*, Kiev, 1980, Naukova Dumka (in Russian).
4. Esaka, H., Suter, F., and Ogibayashi, S., *Influence of carbon content on the growth angle of steel dendrites in a flowing melt*, ISIJ International, 36 (10), 1996, 1264-1272.
5. Okano, S., Nishimura, T., Ooi, H., and Chino, T., *Relation between Large Inclusions and Growth Directions of Columnar Dendrites in Continuously Cast Slabs*, Tetsu to Hagane, 61 (14), 1975, 2982-2990.
6. Takahashi, T., Ichikawa, K., and Kudou, M., *Effect of Fluid Flow on Macrosegregation in Steel Ingots*, Solidification and Casting of Metals Conference, Sheffield, UK, 1977, University of Sheffield, UK.
7. Turchin, A. N., Eskin, D., and Katgerman, L., *Effects of Solidification Range on the Structure of Aluminium Alloys Obtained under Conditions of Constant Melt Flow*, Materials Science Forum, 519-521 (2006), 2006, 1789-1794.
8. Turchin, A. N., Eskin, D., and Katgerman, L., *Deflection of Columnar Grains During Solidification of Aluminium Alloys under Forced Flow Conditions*, International Journal of Cast Metals Research, 20 (6), 2007, 312-318.
9. Fisher, K. and Kurz, W., *Fundamentals of solidification*, 4th Edition, Ueticon-Zuerich, Switzerland, 1998, Trans Tech Publications.
10. Flemings, M. C., *Solidification processing*, McGraw-Hill series in materials science and engineering, USA, 1974, McGraw-Hill.
11. Mizukami, H., Hiraki, S., Kawamoto, M., and Watanabe, T., *Initial Solidification Behavior of Ultra Low, Low and Middle Carbon Steel*, ISIJ International, 39 (12), 1999, 1262-1269.
12. Xu, P. G., Yin, F., and Nagai, K., *Solidification Cooling Rate and As-cast Textures of Low-Carbon Steel Strips*, Materials Science & Engineering A, 441 , 2006, 157-166.
13. Böttger, B, Apel, M., Santillana, B., and Eskin, D., *Phase Field Modelling of Microstructure Formation and Hot Cracking Susceptibility during Continuous Casting of Low Carbon and HSLA Steels*, Materials Science & Engineering - Conference Series, 33 , 2012

14. Nestler, B. and Wheeler, A. A., *A multi-phase-field model of eutectic and peritectic alloys: numerical simulation of growth structures*, Physica D: Nonlinear Phenomena, 138 (1-2), 2000, 114-133.
15. Tiaden, J., Nestler, B., Diepers, H. J., and Steinbach, I., *The multiphase-field model with an integrated concept for modelling solute diffusion*, Physica D: Nonlinear Phenomena, 115 (1-2), 1998, 73-86.
16. Saunders, N. and Miodownik, A. P., *CALPHAD (calculation of phase diagrams): a comprehensive guide*, 1st Edition, Materials Science, Oxford, UK, 1998, Pergamon, Elsevier Science Ltd.
17. *Thermo-Calc software*(www.thermocalc.se), 2012,
18. *MICRESS*(www.micress.de), 2012,
19. Steinbach, I., Pezzolla, F., Nestler, B., Seesselberg, M., Prieler, R., Schmitz, G. J., and Rezende, J. L. L., *A phase field concept for multiphase systems*, Physica D: Nonlinear Phenomena, 94 (3), 1996, 135-147.
20. Böttger, B., Grafe, U., Ma, D., and Fries, S. G., *Simulation of microsegregation and microstructural evolution in directionally solidified superalloys*, Materials Science and Technology, 16, 11 (12), 2000, 1425-1428.
21. Eiken, J., Böttger, B., and Steinbach, I., *Multiphase-field approach for multicomponent alloys with extrapolation scheme for numerical application*, Physical Review E, 73 (6), 2006, 066122-
22. Böttger, B., Eiken, J., and Steinbach, I., *Phase field simulation of equiaxed solidification in technical alloys*, Acta Materialia, 54 (10), 2006, 2697-2704.
23. Böttger, B., Eiken, J., Ohno, M., Klaus, G., Fehlbier, M., Schmid-Fetzer, R., Steinbach, I., and Buhrig-Polaczek, A., *Controlling microstructure in magnesium alloys: a combined thermodynamic, experimental and simulation approach*, Advanced Engineering Materials, 8 (4), 2006, 241-147.
24. Rosler, J., Gotting, M., Del Genovese, D., Bottger, B., Kopp, R., Wolske, M., Schubert, F., Penkalla, H. J., Seliga, T., and Thoma, A., *Wrought Ni-Base Superalloys for Steam Turbine Applications beyond 700 deg C*, Advanced Engineering Materials, 5 (7), 2003, 469-483.
25. Steinbach, I. and Apel, M., *The influence of lattice strain on pearlite formation in Fe-C*, Acta Materialia, 55 (14), 2007, 4817-4822.
26. Warnken, N., Ma, D., Mathes, M., and Steinbach, I., *Investigation of eutectic island formation in SX superalloys*, Materials Science and Engineering: A, 413 , 2005, 267-271.
27. Böttger, B., Apel, M., Eiken, J., Schaffnit, P., and Steinbach, I., *Phase-Field Simulation of Solidification and Solid-State Transformations in Multicomponent Steels*, Steel Research International, 79 (8), 2008, 608-616.
28. Böttger, B., Stratemeier, S., Subasic, E., G+Ähler, K., Steinbach, I., and Senk, D., *Modelling of Hot Ductility during Solidification of Steel Grades in Continuous Casting– Part II*, Advanced Engineering Materials, 12 (3), 2010, 101-109.

29. Nakajima, K., Apel, M., and Steinbach, I., *The role of carbon diffusion in ferrite on the kinetics of cooperative growth of pearlite: a multi-phase field study*, Acta Materialia, 54 (14), 2006, 3665-3672.
30. Senk, D., Stratemeier, S., Böttger, B., Göhler, K., and Steinbach, I., *Modeling of Hot Ductility During Solidification of Steel Grades in Continuous Casting* Part I, Advanced Engineering Materials, 12 (3), 2010, 94-100.
31. Steinbach, I. and Pezzolla, F., *A generalized field method for multiphase transformations using interface fields*, Physica D: Nonlinear Phenomena, 134 (4), 1999, 385-393.
32. Böttger, B., Eiken, J., and Apel, M., *Phase-field simulation of microstructure formation in technical castings A self-consistent homoenthalpic approach to the micro-macro problem*, Journal of Computational Physics, 228 (18), 2009, 6784-6795.
33. Santillana, B., Hibbeler, L. C., Thomas B.G., Kamperman A.A., and van der Knoop W., *Heat Transfer in Funnel-mould Casting: Effect of Plate Thickness*, ISIJ International, 48 (10), 2011, 1380-1388.
34. Greer, A. L., Cooper, P. S., Meredith, M. W., Schneider, W., Schumacher, P., Spittle, J. A., and Tronche, A., *Grain Refinement of Aluminium Alloys by Inoculation*, Advanced Engineering Materials, 5 (1-2), 2003, 81-91.
35. Quested, T. E. and Greer, A. L., *The effect of the size distribution of inoculant particles on as-cast grain size in aluminium alloys*, Acta Materialia, 52 (13), 2004, 3859-3868.
36. Santillana, B., Thomas B.G., Botman, G., and Dekker, E., *3D Thickness Measurement Technique for Continuous Casting Breakout Shells*, 7th European Continuous Casting Conference Proceedings, Düsseldorf, Germany, 2012, Steel Institute VDEh.
37. Drezet, J. M., Gremaud, M., Graf, R., and Gäumann, M., *A new hot tearing criterion for steel*, 4th European Continuous Casting Conference Proceedings, Birmingham, UK, 2002, IOM Communications Ltd., London , UK.
38. Grasso, P. D., Drezet, J. M., and Rappaz, M., *Hot Tear Formation and Coalescence Observations in Organic Alloys*, JOM, web-only supplement: <http://www.tms.org/pubs/journals/JOM/0201/Grasso/Grasso-0201.html> (January), 2002
39. Rappaz, M., Drezet, J. M., and Gremaud, M., *A new hot-tearing criterion*, Metallurgical and Materials Transactions A, 30 (2), 1999, 449-455.
40. Lagneborg, R., Siwecki, T., Zajac, S., and Hutchinson, B., *The role of Vanadium in microalloyed steels*, The Scandinavian Journal of Metallurgy(5), 1999, 186-241.

Chapter 6

Physical modelling of cracking during continuous casting solidification

The study of the thermo-mechanical properties of commercial steels helps in understanding hot tearing and cracking in solidifying steels. The need for such understanding is motivated by the continuous trend towards improved casting productivity by increasing casting speed and higher quality, as well as for the development of new steel grades.

However, the thermal and mechanical conditions under which the initial solidification takes place are difficult to assess. Physical modelling is a useful tool to simulate processes conditions at a laboratory scale, under a controlled environment, which makes it easier to evaluate results than in the complexity of a full-scale process.

6.1 Introduction

The first attempts to develop a physical model to simulate casting conditions in a mould for continuous casting at lab scale were done in the early 1980's^[1]. With this first design of a mould simulator, the initial stages of solidification of molten metal in a continuous casting mould, including the oscillation marks on the solidified metal, can be studied in detail. Moreover a desired oscillation pattern can be tested and different heat extraction levels can be simulated and measured. Tata Steel RD&T installed a similar mould simulator in 1998. To broaden the capabilities of this device, an adaptation was developed, under the scope of this PhD study, to include the possibility to generate cracks during solidification as a relevant step in the assessment of hot tearing at continuous casting conditions.

This chapter describes the development of this physical model of cracking during continuous casting solidification, including the detailed evaluation of the first tests results.

6.2 Mould cracking simulator (MCS)

6.2.1 Description of the original mould simulator

In order to study the influence of major casting parameters such as casting speed, oscillation characteristics and mould slag viscosity on shell growth and slag infiltration, a mould simulator is available at Tata Steel RD&T. The design of the simulator is similar to the one described by NKK Research ^[1].

The schematic diagram of the mould simulator is shown in *Figure 6.1* ^[2]. The simulator is placed on top of an induction furnace containing 150 kg of liquid steel. It consists of a compact unit designed to lower a water-cooled copper tube into a liquid steel bath. At the start of an experiment the tube is protected with a steel cap. The mould tube consists of two concentric copper tubes. The diameter of the outer tube is 70 mm with a wall thickness of 5 mm. The diameter of the inner tube is 45 mm thus creating a cooling water channel with a gap width of 7.5 mm. Cooling water flows from the inside of the tube and then enters the cooling water channel from the bottom side. The system oscillates by means of a generator that can vary the oscillation frequency between 0 and 10 Hz with a maximum amplitude of 4 mm. Frequency and amplitude can be varied independently. It is possible to oscillate in different types of non-sinusoidal mode such as a saw tooth.

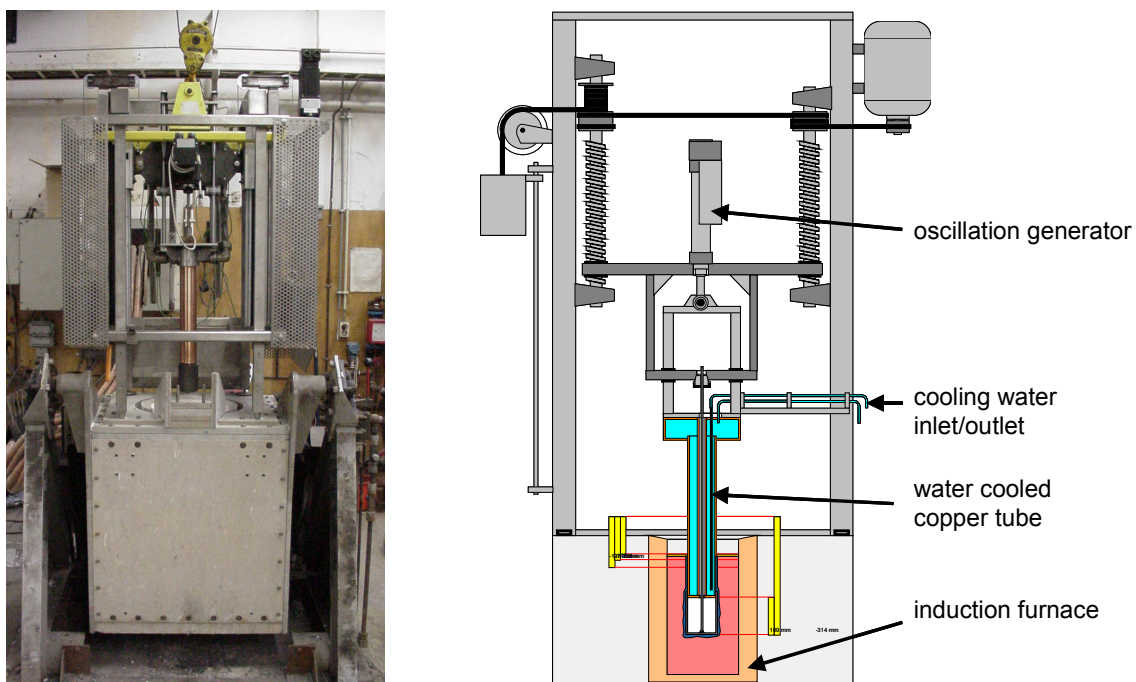


Figure 6.1. Photo and schematic view of the mould simulator ^[2]

The actual mould is a cylindrical copper tube with a cylindrical steel cap, which is positioned at the bottom of the cylinder. The cap is attached to a steel shaft, which runs through the cylinder and can push down the steel cap.

In the initial part of the experiment the copper mould tube together with the steel cap is lowered into the liquid steel bath. The submersion depth is chosen in such a way that the cap is positioned completely below the meniscus. The actual experiment begins, when approximately 30 mm of steel has solidified on the copper tube. The cap is then pushed down into the steel bath at a preset speed. During the experiment the copper tube oscillates. When the cap is pushed down into the bath, fresh steel solidifies on the copper tube on each oscillation cycle as shown in *Figure 6.2*. The speed at which the cap is pushed down is equal to the speed at which the solidifying steel shell moves down the mould and is therefore equivalent to the casting speed of a continuous casting machine.

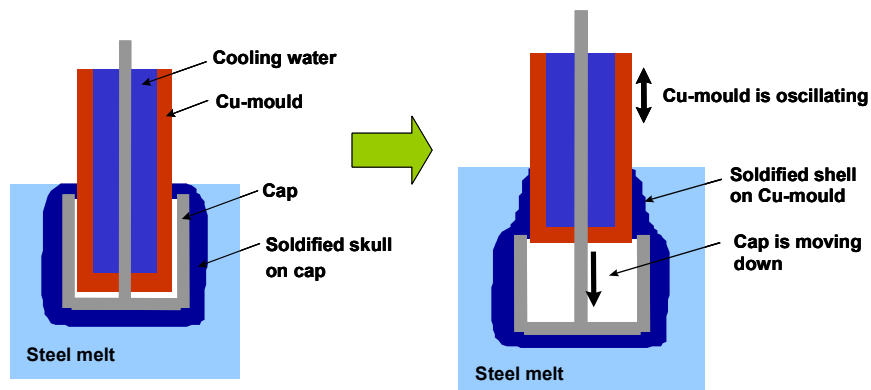


Figure 6.2. Schematic drawing of the mould simulator at Tata Steel RD&T.

6.2.2 Development of the Mould cracking simulator [3]

The submerged split-chill tensile test (SSCT) [4,5]

An in-situ tensile test method, the SSCT test, has been developed by the Christian Doppler laboratory in Leoben, Austria [4,5] offering a laboratory experiment with conditions similar to those in the actual process, to determine the high-temperature mechanical properties and crack susceptibility of steel.

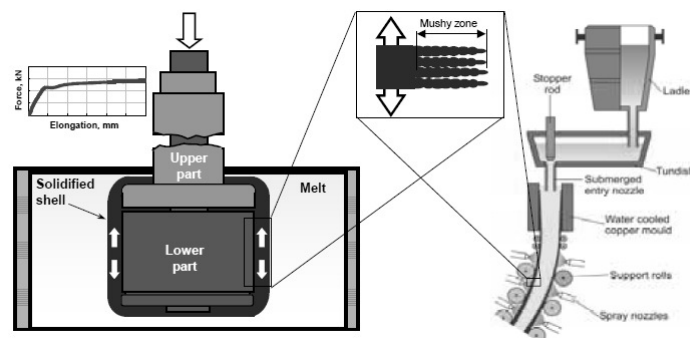


Figure 6.3. Schematic representation of the SSCT test [5].

The major aspects of the method related to its comparability with the continuous casting process can be summarized as follows. The SSCT test is performed in-situ during solidification, and the main load direction is perpendicular to the main dendrite growth axis – identical to the continuous casting process. The microstructure of the solidifying shell can be regulated by adjusting the cooling rate used in the test according to continuous casting conditions. Low strain-rate testing can be applied, whereas the typical strain rate in continuous casting ranges from 10^{-4} to 10^{-3} 1/s. A deformable mushy zone exists in order to simulate crack formation, in particular hot tearing (see Figure 6.3).

SSCT Experimental procedure [5]

A solid steel test body, split in two halves, is submerged into the liquid melt in an induction furnace. The surface of the test body is spray-coated with a thin zirconium oxide layer. The coating controls the cooling conditions and minimizes friction. A steel shell solidifies around

the test body with the main crystallographic orientation perpendicular to the interface, similar to the situation in a continuous casting mould. The force between the upper and lower parts of the test dummy is measured by a load cell, the position of the lower part by an inductive position sensor. A servo-hydraulic controller controls force and position. This allows a number of different testing procedures, including the hot tensile test, in which after a certain holding time, the lower half of the test body is moved downwards at a controlled velocity at strain rates typically between 10^{-3} and 10^{-2} 1/s while displacement and tensile force are recorded.

Design and development of the hot cracking rig

The SSCT device has the disadvantage that it is a static model, meaning that the device is not able to simulate the dynamics of a continuous casting process, particularly the oscillation cycles and its great influence on the solidification particularly via the mould slag influence.

To expand the capabilities of the mould simulator, it is possible to modify the existing device (schematically shown in *Figure 6.2*) by combining the features of SSCT with generating cracks under continuous casting conditions, including oscillation parameters, primary cooling and mould slag.

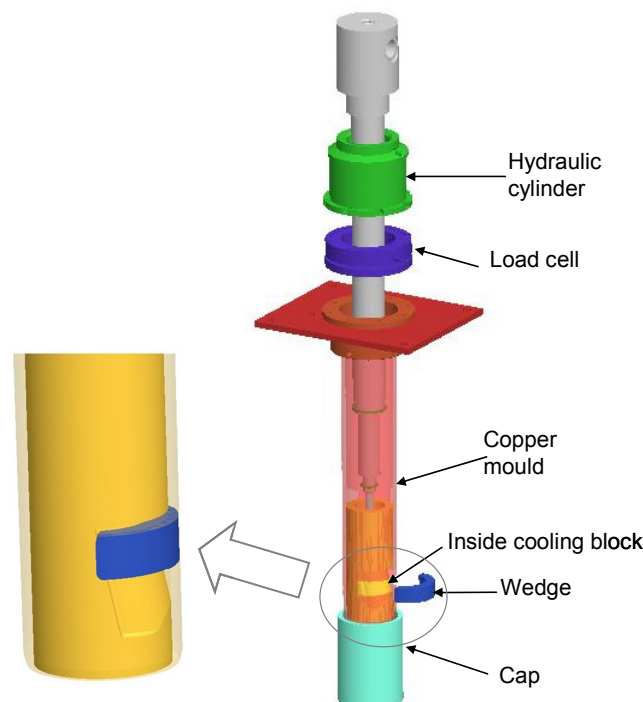


Figure 6.4. Schematic representation of the Mould Cracking Simulator [3].

The proposed modification is further called Mould Cracking Simulator (MCS) and its design is shown in *Figure 6.4*, where the blue half-ring will create an extra tensile stress in the solidifying steel shell, producing cracking in the longitudinal and transverse directions.

By providing a separate section that is movable in outward direction (yellow-wedge cooling block), different tensile forces can be imposed on the metal adhered to the copper tube-mould (transparent-orange in *Figure 6.4*) which corresponds to the tensile forces occurring during continuous casting; as in continuous casting transverse as well as longitudinal cracks can occur in the cast slab.

The internal wedge-block is water-cooled and it provides indirect heat extraction to the copper tube-mould by closed contact between both surfaces. It has been chosen for this indirect cooling system to reduce the risk of leakage during mechanical testing, considering that the mechanical part of the test should be free of movement even inside the liquid metal.

The steps performed during testing are described in *Table 6.1*

Table 6.1. Testing steps for the MCS.

Step	Description
1	Lowering the system until the steel cap is fully submerged in the liquid metal
2	9 seconds of freezing time to form a scull around the cap
3	Mould tube starts oscillation
4	Cap starts to move down and mould keeps oscillating
5	After 10 oscillation cycles, a solidified shell is created and the system goes up
6	While the system moves upwards, the hydraulic system is open and the load is applied via the wedge

6.2.3 First experiments in the MCS with Al- 2%Cu

To test the proposed modifications under solidification conditions, a set of experiments were recommended with a hot-cracking sensitive aluminium alloy. The alloy chosen was Al with 2% Cu. An aluminium alloy was chosen because the melting temperature is almost half that for steels and there were some concerns about indirect cooling during testing.

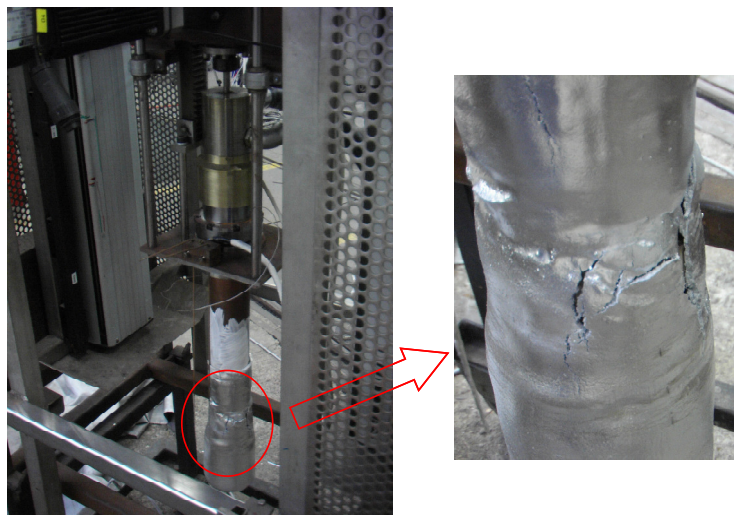


Figure 6.5. Overview of the first test with aluminium alloy and a detail of the cracked shell after testing

Two successful trials were performed. In *Figure 6.5* an overview of the first test with the aluminium alloy and a detail of the cracked shell after testing are shown. In *Figure 6.6* the cracked specimens of the two successful trials are compared.

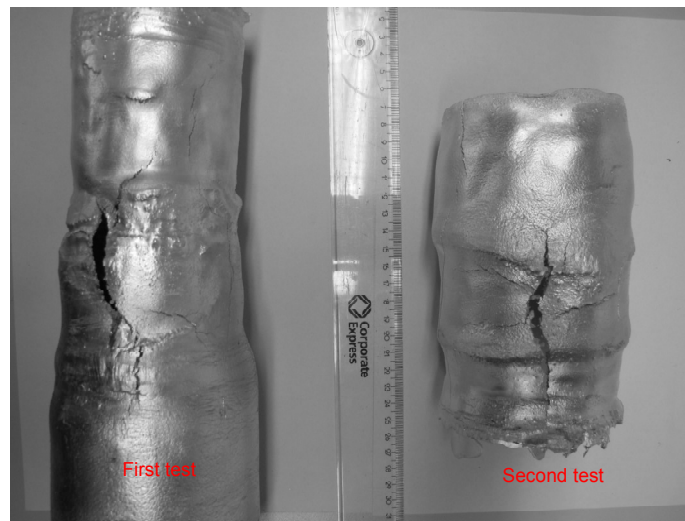


Figure 6.6. Cracked specimens of the two successful trials

Unfortunately, during the first trial the data gathered during testing was not properly recorded and during the second test, it was evident that the data-acquisition system was not fast enough to properly record in detail the full testing procedure as can be seen in the oscillation cycle in *Figure 6.7*. The load cell is sensitive enough to be able to trace all the movements of the whole device. However, the oscillation cycle as recorded by the data acquisition system during this experiment is incomplete and uneven, it does not agree with the applied settings of a sinusoidal cycle, showing the lack of data points recorded.

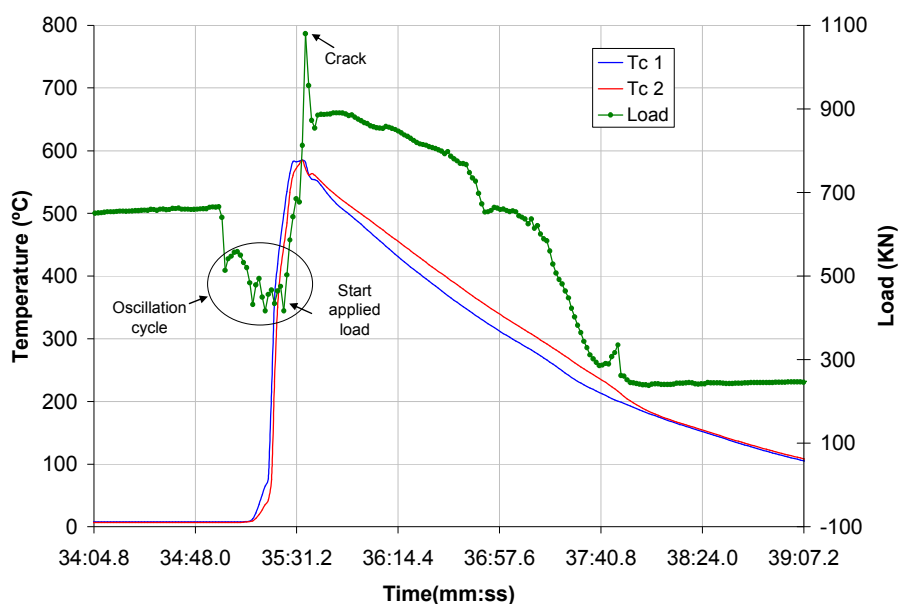


Figure 6.7. Thermocouples and load signals during the second test with Al 2%Cu alloy.

Two thermocouples were positioned on the opposite side of the half-ring, embedded in the copper tube-mould. Their signal shows a slight increase on temperature at the start of the

loading procedure. This is coherent with the fact that the shell is pulled away from the copper mould on the opposite side by the wedge. As a result, it is pushed to the mould where the thermocouples are located, increasing the contact with the mould surface. However, it is evident from the data analysis that the thermocouples have a delay in their signal acquisition.

6.2.4 *A priori cold test procedure for steel*

It is important to know the internal resistance, namely: friction, opening of the hydraulic systems, and movement of the different apparatus parts during testing to be able to gather accurate information of the strength of the solidifying steel shell. Considering that some of these internal resistances are related to the surface condition of the parts, for each test it is necessary to perform a “cold” test where the apparatus is fully tested under room temperature conditions without liquid metal. In *Figure 6.8* the measured load-signal for a test without load (light-blue line) and two cold tests (red and green lines) including the load procedure prior to the first steel test are shown.

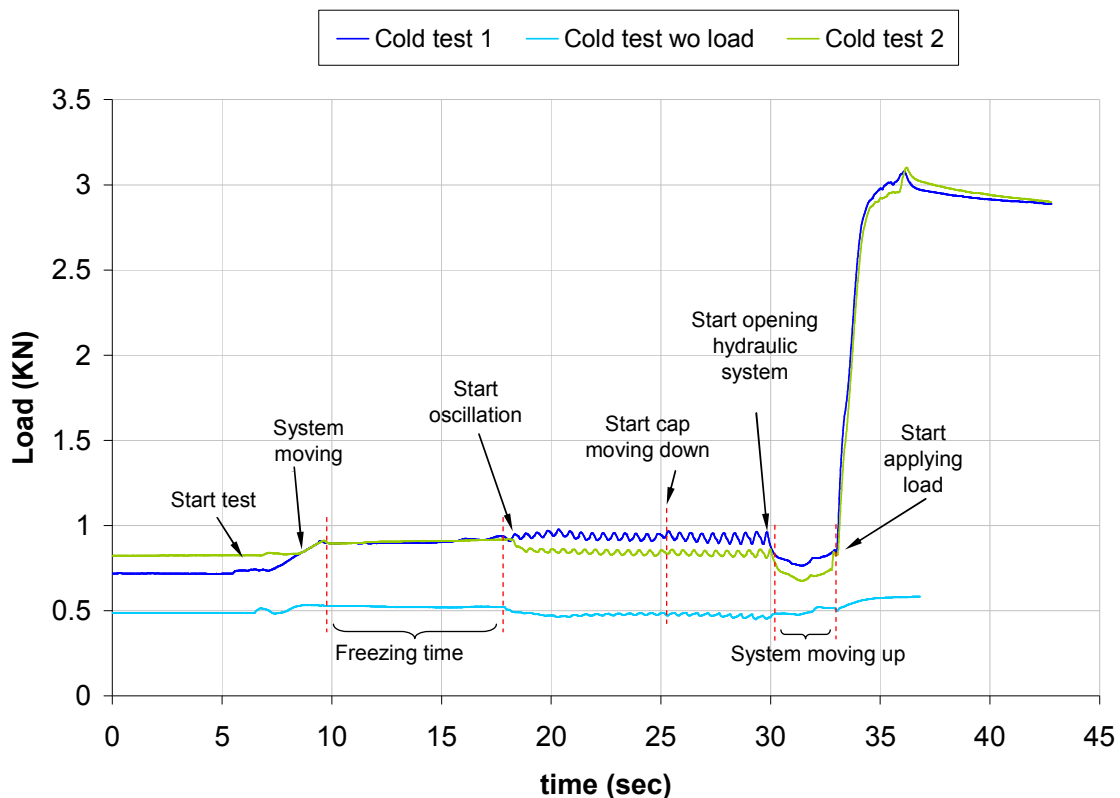


Figure 6.8. Recorded signals during the cold-test

The steps described in *Table 6.1* can be seen in the load signal as the signal is sensitive enough to record all these details (see *Figure 6.8*). The use of a high sensitivity data acquisition system is evident in the data recorded here as the full oscillation cycle and detailed information regarding the load signal can be seen.

6.2.5 MCS steel experiments

The tests done with the aluminium alloy were performed with an oxygen-free-Cu mould but the steel tests are executed with a bronze alloy mould (Cu-12%Sn), the same alloy as the inner cooling block, the same material was chosen in order to reduce the friction between the two parts. To reduce the friction between the inner-cooling block and the mould tube, boron-nitride is used as dry lubricant and the mould tube is coated on the outside surface with a thin-sprayed layer of zirconium oxide to protect the surface from the high temperature and avoid melting or sticking to the steel shell.

While performing the test with liquid steel, the signals are slightly different, particularly the lowering of the cap because it accounts for the ferrostatic pressure. The first test with liquid steel has been performed with an LCAK alloy. The test was performed at a temperature of 1560°C, thus a superheat of about 30°C for the liquid steel. Mould powder has been used to control the heat transfer during testing and to protect the liquid bath from reoxidation.

The tests are performed in an open furnace, thus the chemical composition of the steel bath is difficult to control particularly due to reoxidation. Therefore, the chemical compositions of the steel grades tested differ from the nominal. Nevertheless, the reported values do reveal the sensitivity on the mechanical properties of different steel grades.

Table 6.2. Chemical composition of the first steel grades.

Steel	C	Mn	Al	S	P	Nb	V	N
1	0.042	0.212	0.026	0.002	0.001	<0.001	<0	0.0062
2	0.05	0.07	0.004	0.004	0.003	<0.001	<0	0.0027
3	0.024- 0.014	0.384- 0.345	0.022- 0.002	0.005- 0.004	0.003	0.002- 0.003	0.015- 0.014	0.0165
4	0.054- 0.061	1.082- 1.027	0.064- 0.129	0.004	0.005	0.047- 0.043	0.108- 0.11	0.0113- 0.0117
5	0.049	0.55	0.075	0.004	0.003	0.006	0.021	0.012
6	0.051	0.608	0.283	0.005	0.004	0.009	0.05	0.0139

In the first steel trial (see chemical composition for steel nr. 1 in *Table 6.2*), the load has been applied 3 oscillations before the end of the test, in contrary to the cold tests when it was applied just after finishing the oscillations. This change can be also seen in the load signal as shown in *Figure 6.9*. There is a big difference between the recorded signal during testing with steel and the signals of the cold tests, where the latter have higher values. It is not expected as the system does not have a resistance during cold testing except the internal friction. Post-mortem analysis showed that this 1st steel tested had some signs of reoxidation, showing at the crack region some porosity characteristic of a rimming steel, this could easily explain why the steel had a lower strength than the force measured during the cold test.

Nevertheless, two cracks were formed; the first one is a longitudinal crack and the second one a transverse crack in the lower border of the wedge at the end of the test.

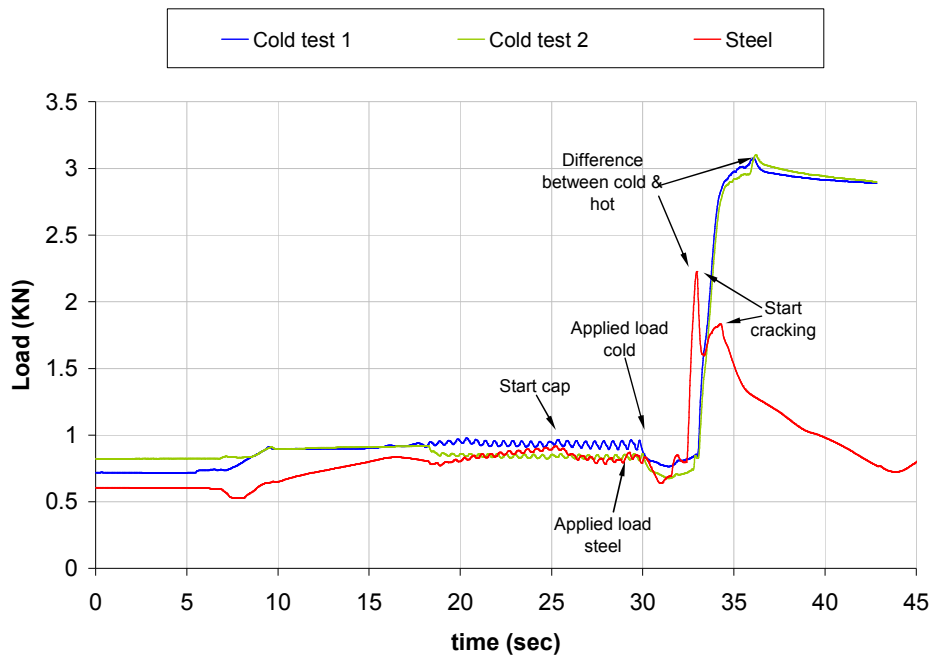


Figure 6.9. Recorded signals during the first steel test

These cracks are also recorded in the signal, as the start of relief of the load applied is believed to be at the start of each trough (Figure 6.9). However, the second crack and its corresponding trough in the signal are difficult to see as it overlaps with the end of the system's movements. The same pattern has been seen during testing steel nr. 6, while in this case no reoxidation was visible (see Figure 6.10).

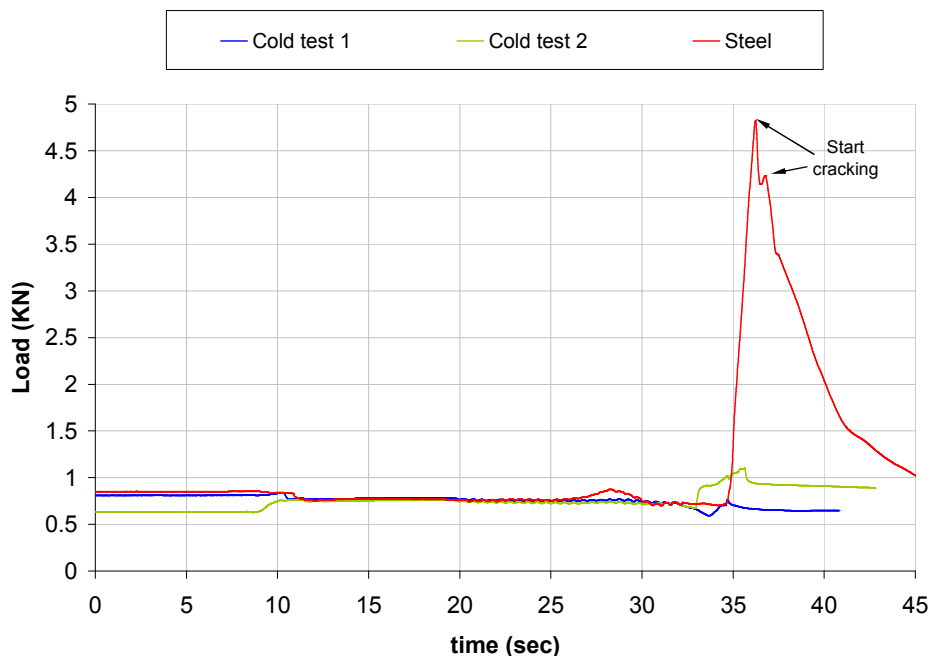


Figure 6.10. Recorded signals during testing steel nr. 6

While testing steel compositions 2 and 3, the data acquisition was set to record signals up to 5 kN and the apparent measured strength was higher than that but the real value is not

known because after those 5 kN the signal was not recorded. Another problem encountered during testing was the torsion of the system due to a malpositioning of one of the thermocouples, resulting in too high friction in the system even during oscillation steps, ending with the wedge being jammed at the beginning of the test.

Considering all the encountered problems, three successful tests were performed proving the usefulness of this physical modelling (see measured load in *Figure 6.11*). The load signal has a characteristic pattern for all the grades tested, confirming the reproducibility of the test.

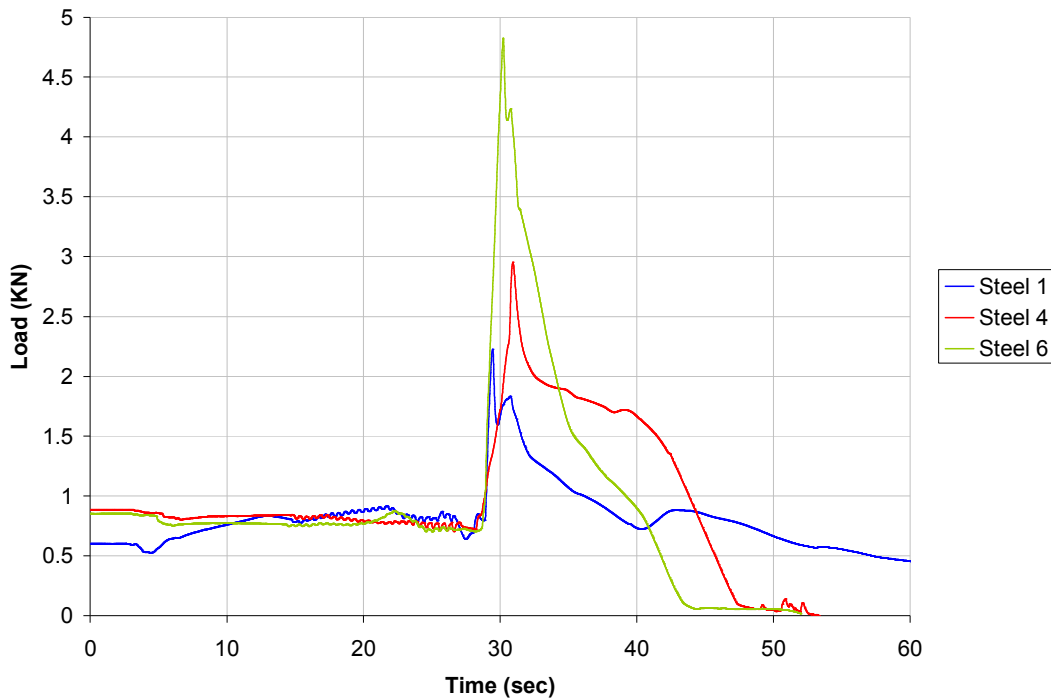


Figure 6.11. Load signals during the three successful steel tests.

Obviously the measured load is specific to each chemical composition, thus steel nr. 4 with the higher content of Mn and microalloyed elements is less strong than steel nr. 6.

The same as in the aluminium tests, two thermocouples were inserted in the mould tube, positioned at the opposite side of the wedge's location. These thermocouples are fed through a small channel in the surface of the inner-cooling block. Due to the upward movement of the block during testing, the thermocouples have been cut during the loading part of the test, thus the thermocouple signals are unreliable just after initialization of the loading procedure (see green and blue line in *Figure 6.12*).

As the thermocouples are positioned at the mould surface, the maximum temperature values recorded by the upper thermocouple are consistent with the 600 °C to 800 °C expected values from the surface of a continuous casting mould ^[6,7]. These temperatures are slightly higher than actually measured in industrial casters^[8-7] but this is mainly due to the indirect cooling of the MCS.

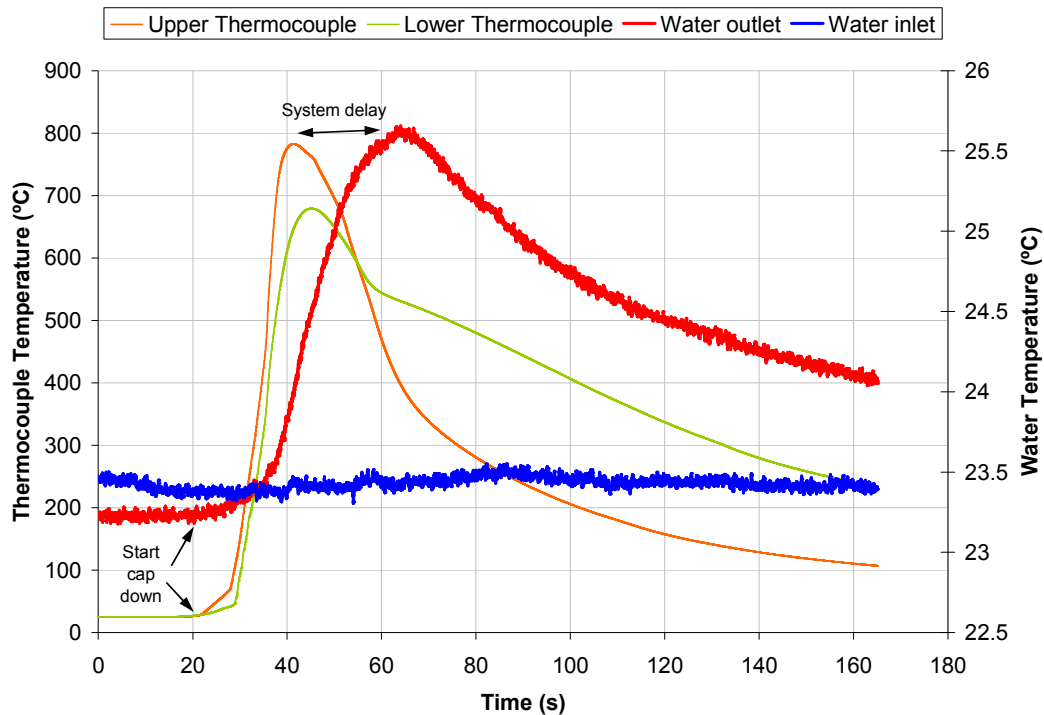


Figure 6.12. Temperature signals during the test of steel nr. 4.

The cooling water system is also equipped with thermocouples positioned in the inlet and outlet water pipes, for two main reasons: to measure the temperature difference between inlet and outlet to calculate the heat transfer, and as a safety precaution to avoid boiling during testing. *Figure 6.12* shows the two temperature signals for the cooling water system during this test. From the red-line signal is possible to see the slight but noticeable temperature rise in the water outlet since the immediate moment that the mould tube is in contact with the liquid steel, which occurs when the cap starts to move down. There is a system delay because the thermocouples installed in the water system were chosen to be thicker so that they will remain stationary in the system.

6.2.6 Fractography of the MCS steel samples

To understand the nature of the cracks created during testing of a steel shell in the MCS, a complete fractographic study has been performed. The steel alloy chosen for this study was steel nr. 4, considering that no problems were encountered during testing and its chemical composition fits the requirements of a commercial steel grade that could be cast in a continuous casting process. In *Figure 6.13* an overview of the steel shell after testing is shown, where the cracks can be easily seen.

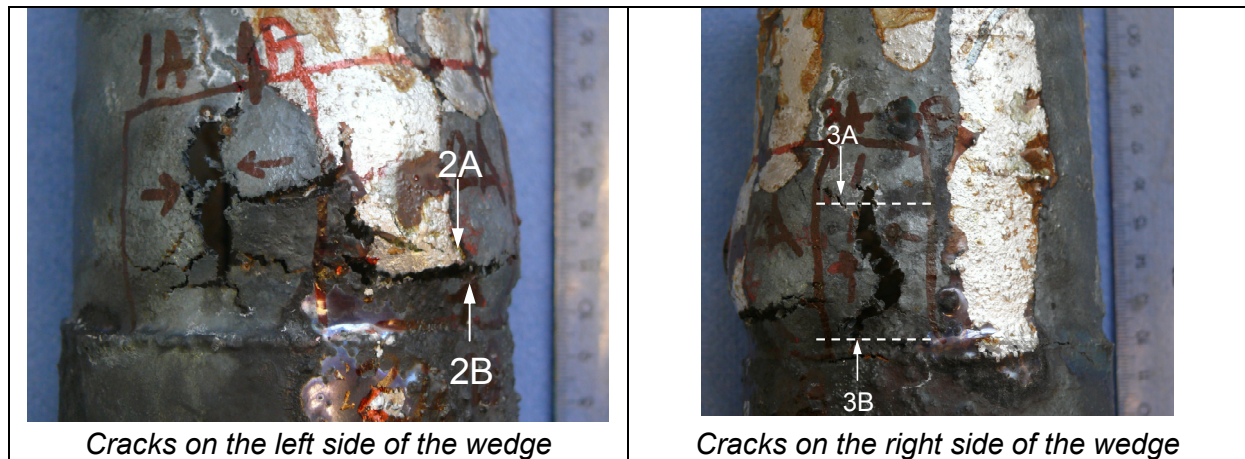


Figure 6.13. Cracks on the steel shell after testing of alloy 4

Several samples were cut for further microscopic analysis. The crack in the region 2A-2B (see Figure 6.13) was opened up to be able to see the fracture surface under SEM.

The SEM overview of the 2B-crack surface can be seen as a collage of images in Figure 6.14. There is a region where the surface is smooth, which is because during cracking some mould slag present at the steel surface was still liquid enough to penetrate the crack and coat part of the fracture. It is important to note that up to now the tests are performed when the testing rig is just above the liquid bath for safety reasons, but the steel and the slag are hot enough to remain liquid during testing. Moreover, this fractographic analysis proves that the cracks induced in these tests are interdendritic.



Figure 6.14. Fracture surface of crack sample 2B

Considering that the primary and secondary dendrite arms were easily revealed at the fracture surface, both arm spacings were also possible to be measured.

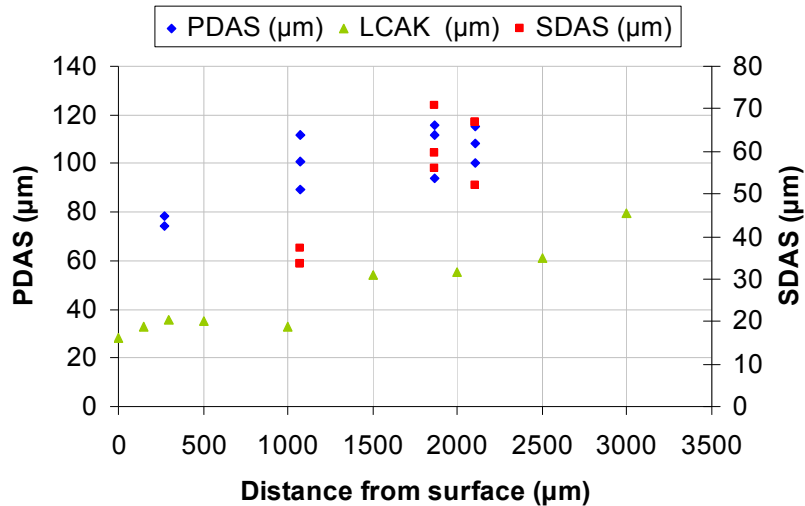


Figure 6.15. PDAS and SDAS at the fracture surface, compared with PDAS from slab samples (marked LCAK)

In Figure 6.15, the PDAS and SDAS are compared with the previously measured PDAS from the LCAK steel grade from slab samples (see Figure 5.10 in Chapter 5). The results denote the influence on the cooling rate (the MCS has an indirect cooling) which is possible to see in the lower PDAS values. Due to safety reasons, the water cooling is already running prior to testing, thus the steel will solidify under the condition of a relatively cold mould surface, where the shell will solidify with a mould temperature between 50 °C and 250 °C (see Figure 6.16). Therefore, the shell formed under these conditions will have a lower PDAS than with a stable continuous casting condition where the mould is to some extent warmer than at the start of casting. However, both measurements are generally in agreement, being another validation of the MCS as a physical model for continuous casting.

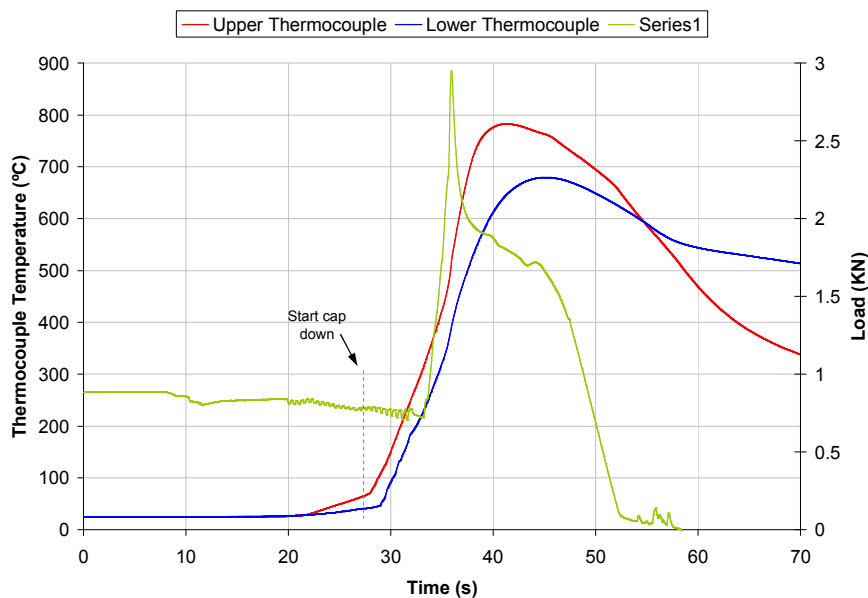


Figure 6.16. Temperature and load signals during testing for the steel nr. 4.

Transverse cuts of Samples 3A and 3B were embedded and polished for microscopy and etched with Beché-Bauchard etchant to reveal their dendritic microstructure.

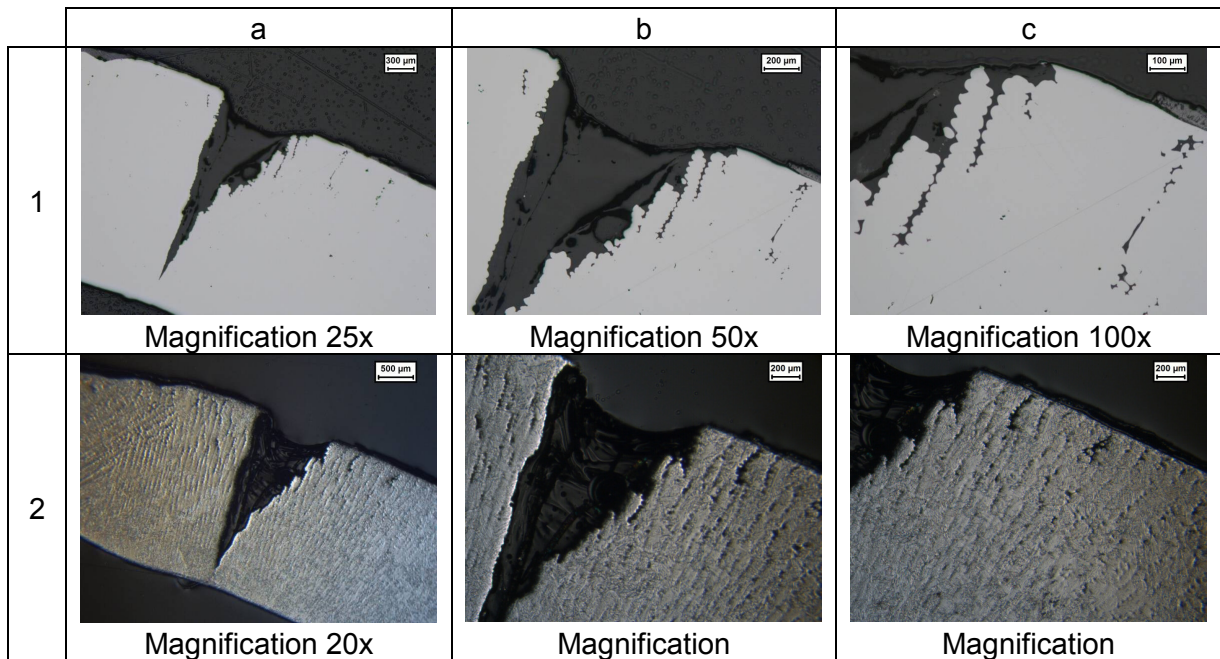


Figure 6.17. Detailed overview of the transverse cut of the crack in sample 3B

The transverse cut on sample 3B was chosen to be as close as possible to the opening of the crack where the light microscopic analysis of this crack shows the dendritic structure tore apart, as expected in a hot tear. In Figure 6.17 the first-top row of images show the as-polished view of the crack and in the row below the same locations are visible but after Bechet-Beauchard etching. This etching revealed in more detail the dendritic microstructure, corroborating the dendritic structure around the crack.

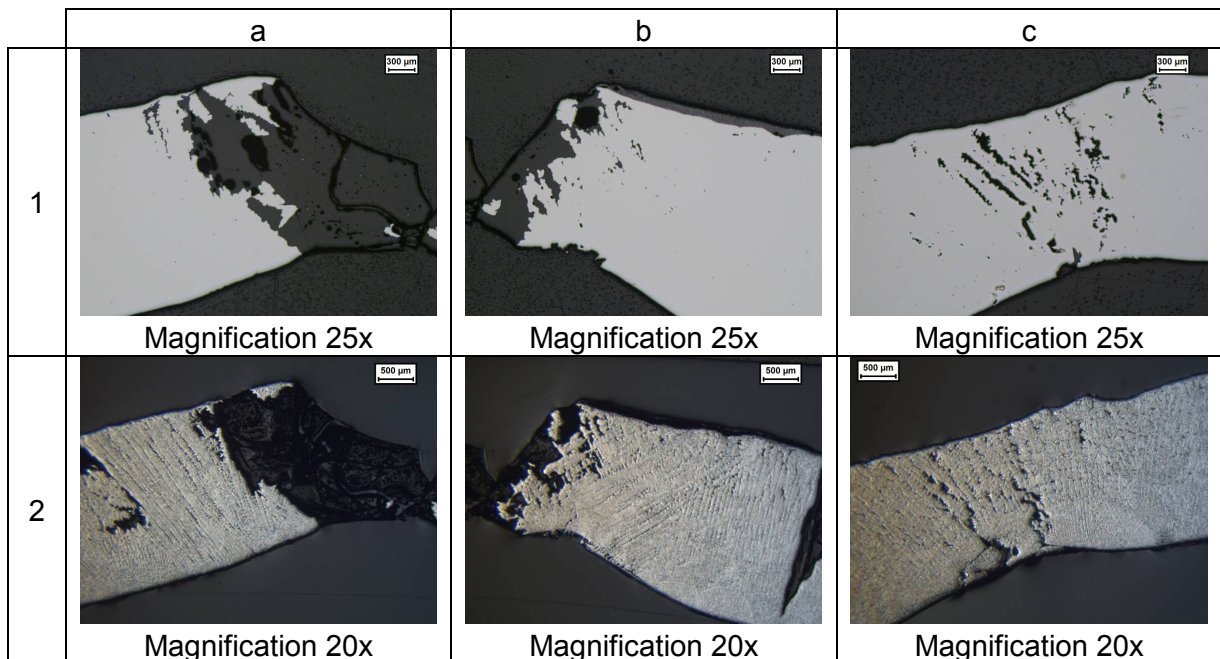


Figure 6.18. Detailed overview of the transverse cut of the crack in sample 3A.

The 3A sample was chosen to be in an open region of the crack to also verify the structure of the crack. Likewise, in *Figure 6.18* the first row shows the as-polished samples and the second lower row shows the images after etching.

The first two columns show the left and right hand sides of the crack, and the third column is another region in the same sample where it is possible to see a group of hot tears with the associated necking of the steel shell in a stage previous to an open crack. Similarly, these images also confirm the hot tear nature of these cracks.

6.3 Assessment of the physical modelling results

The modifications of the mould simulator to the MCS are novel in the way that no other physical model of cracking during continuous casting is able to simulate the process in such a way that it resembles the industrial process.

These modifications are simple and inventive adaptations to the original design, and the results have a potential to bring new insight on thermo-mechanical properties of steels under continuous casting processing.

Despite the alloys tested during the first few experiments did not have the same alloy compositions studied in this thesis, the results of the MCS are very promising;

- The adaptations on the MCS compared with the industrial process show little influence on parameters, such as mould surface temperature and heat extraction.
- It is possible to measure qualitatively the strength of a steel shell during continuous casting solidification conditions.
- The dendritic structure of the steel shell formed during testing is comparable to the industrially cast steel slabs.
- The cracks generated in that steel shell have the characteristics of hot tears, i.e. they are formed with the presence of semi-solid material.

It is expected that this new physical model developed in the framework of this thesis will help in the study of the thermo-mechanical properties of commercial steels motivated by the continuous trend towards improved casting productivity by increasing casting speed and higher quality, as well as for the development of new steel grades.

References

1. *Simulator for solidification in continuous casting mold*, ISIJ International, 25 (1985), 1985, 352-352.
2. Van der Knoop W., Visser H.H., and Abbel G., *A better understanding of initial solidification phenomena during continuous casting by using a mould simulator.*, Proceedingsg 1st SteelSim Conference, Brno, Czech Republic, 2005
3. Santillana, B. and Cruijff, M., *Mould Simulator*, Application Nr. EP11002966, Patent Pending, 2011.
4. Bernhard, C., Hiebler, H., and Wolf, M. M., *Simulation of shell strength properties by the SSCT test*, ISIJ International, 36 (Supplement), 1996, 163-166.
5. Pierer, R., Bernhard, C., and Chimani, C., *Evaluation of common constitutive equations for solidifying steel*, Berg- und Hüttenmannische Monatshefte (BHM), 150 (5), 2005, 163-164.
6. Santillana, B., Hibbeler, L. C., Thomas B.G., Kamperman A.A., and van der Knoop W., *Heat Transfer in Funnel-mould Casting: Effect of Plate Thickness*, ISIJ International, 48 (10), 2011, 1380-1388.
7. Thomas B.G., Li G., Moitra A., and Habing D., *Analysis of the thermal and mechanical behavior of copper molds during continuous casting of steel slabs*, Iron & Steelmaking, 10 (1998), 2008, 125-143.
8. Ramirez-Lopez, P. E., Lee, P. D., Mills, K. C., and Santillana, B., *A New Approach for Modelling Slag Infiltration and Solidification in a Continuous Casting Mould*, ISIJ International, 50 (12), 2010, 1797-1804.
9. Thomas B.G. and Parkman, J. T., *Simulation of Thermal Distortion of a Steel Droplet Solidifying on a Copper Chill*, TMS Annual meeting, Solidification Proceedings, TMS, Indianapolis, IN, USA, 1998

Chapter 7

Discussion and conclusions

7.1 Results analysis and hot tearing susceptibility

The purpose of this study has been to investigate the differences between three steel grades with respect to hot tearing sensitivity upon solidifying in a thin slab caster.

One of the steel grades chosen for this study, is a low carbon aluminium killed (LCAK) steel grade which theoretically is not expected to be sensitive to hot tearing, but in the Direct Sheet Plant (DSP) caster from Tata Steel in IJmuiden, The Netherlands, this grade has a high risk of breakouts due to cracking during solidification. The other two grades selected are a high strength low alloyed (HSLA) steel grade, a micro-alloyed steel with extra additions of vanadium, nitrogen and niobium, with a very low breakout occurrence due to hot tearing and a similar steel grade, a low-range HSLA (LR-HSLA), with the same concentration of niobium but a lower concentration of vanadium and nitrogen, which is very cracking sensitive during solidification.

Although these steel grades are not very different in chemical composition, thermodynamic calculations described in Section 3.3, Chapter 3, showed that the two HSLA steel grades have different propensity to the peritectic reaction upon solidification due to the combination of elements in the chemical composition that are either ferrite or austenite stabilisers. When considering Ti in both chemical compositions, the LR-HSLA is showing the 3 phases liquid, ferrite, and austenite coexisting with each other, thus full peritectic solidification (see Section 3.3.4, *Figure 3.25*). However, the higher content of N and V in HSLA steel, both elements being known as ferrite stabilisers, shifts the composition back to a safe point where the peritectic susceptibility is not relevant.

The DTA and DSC analysis of the HSLA steel grade has shown that in all heating and cooling cycles a broad transformation occurs that is consistent with the δ - γ transformation (*Figures 3.17 to 3.20* in Section 3.2.4, Chapter 3). Both heating cycles (*Figures 3.17 and 3.18*) display a double-shoulder trough, characteristic of a peak overlapping, denoting that there could be two transformations occurring in this temperature range. The two possible transformations could be either the TiN formation or the peritectic reaction, which is not necessarily fully developed, but could be present in this steel grade.

Titanium is the only micro-alloying element which is known to form nitrides at rather high temperatures during solidification. If precipitation occurs as TiN or co-precipitation with other micro-alloying elements as (Ti,V,Nb)(C,N)^[1] can happen before solidification is finished, an influence of Ti on reducing the hot tearing is possible. This could be the case of the HSLA steel grade, which is known to have a low hot tearing susceptibility.

In order to better understand this special behaviour of the HSLA grade, compared with the LR-HSLA and the potential precipitation of TiN, phase field microstructure simulations have been performed as summarized in Chapter 5, Section 5.5. The results show that TiN can form already during the latest stage of solidification, even when very low amounts of this element are present (see *Figure 5.26*). If TiN particles trigger the coalescence of dendrite trunks as shown in *Figure 5.27*, then it is possible to understand why, for a given Ti content an increased N content present in the HSLA grade can help to reduce the risk of hot tearing. The effect of TiN precipitation in hot tearing can be quantified by assuming the coalescence temperature as the TiN precipitation temperature instead of the ZDT, when this temperature is above the expected ZDT temperature at $f_s=0.99$.

Another important point to consider is the difference in microstructure, even when the composition differs slightly, the microstructure seems to be affected by these variations in composition, as demonstrated in Chapter 5, Section 5.2 and 5.3. The dendritic microstructure of the HSLA steel grades is finer than the one of the LCAK. For a solidification microstructure, few big dendrites are much less strong than many small ones, a finer structure is better for hot tearing because of greater strength.

Additionally, the higher the amount of alloying elements, the higher the segregation, thus the smaller the grains will be developed during solidification. Therefore, a steel grade with higher amount of alloying elements will have a tendency to solidify with a stronger, much compact structure, and this is the case of the HSLA steel. These HSLA steel grades contain certain elements that may act as grain refiners and can restrict growth, Both non-metallic particles and δ -ferrite nuclei appeared ahead of the solidification front during the observations with the Concentric Solidification Technique only for the HSLA and LR-HSLA grades as seen in Section 3.4.5, Chapter 3.

Unique hot tensile tests were carried out in the temperature range involving solidification. The results given in Chapter 4 suggest that among the studied steel grades, the LCAK steel grade has the lowest strength during solidification and a broader ΔT_B .

During non-equilibrium solidification (calculations with the Scheil approximation), a substantial amount of liquid phase remains in all the three studied steel grades at the temperature ranges of the measured ΔT_B , in the range theoretically expected to be susceptible to hot tearing. Particularly the LCAK steel grade which has a broader ΔT_B , has more liquid still present at the ZST than the other two grades. The HSLA grade has a higher percentage of liquid present than the LR-HSLA.

Fractographic studies of the samples fractures above the non-equilibrium solidus (see Chapter 4, Section 4.2, *Figures 4.26, 4.30 and 4.33*) revealed low melting phases even at

temperatures as low as 1360°C. These low-melting films do have an effect on the hot tearing behaviour of commercial steel grades^[2,3]. The LCAK is particularly prone to develop non-metallic particles at the last stages of solidification as demonstrated in Section 4.2, Chapter 4.

Steel grades with high Mn content, thus with a high Mn/S ratio, are not cracking susceptible because the solubility of MnS in the liquid is less than in the matrix, thus the conditions of precipitation favour the precipitation of MnS in the matrix. For a given temperature below the MnS solubility line (see *Figure 2.10*, Section 2.6.1, Chapter 2), the degree of supercooling for precipitation will increase with increasing manganese content. On the contrary, for steels with a low Mn/S ratio, like the LCAK, the Mn/S ratio is low enough to nucleate and form fine liquid droplets interdendritically and, as solidification continues, along the grain boundaries. This results in both cases in low ductility as shown in Section 4.2, Chapter 4; these liquid films serve as an easy path for crack propagation^[4].

The thermal analysis performed with DTA and DSC supports the assumption that for the LCAK alloy, MnS is formed during solidification due to segregation of Mn and S to the liquid phase, and that MnS may not precipitate until temperatures around 1390°C, keeping the liquid phase at such a low temperature as demonstrated in *Figure 3.13*, Section 3.2.4, Chapter 3. According to the literature and phase diagrams evaluation, the Fe-Mn-S system has invariant points at 1394°C (see *Figure 2.9*, Section 2.6.1, Chapter 2).

Whilst the study with the Modified Mould Simulator (see Chapter 6) did not confirm the increased hot tearing susceptibility of the LCAK and LR-HSLA, it did partially substantiate that the modifications on its design are novel in the way that no other physical model of cracking during continuous casting is able to simulate the process in such a way that it resembles the industrial process.

These modifications described in Section 6.2.2, Chapter 6, are simple and inventive adaptations to the original design, and the results have a potential to bring new insight on thermo-mechanical properties of steel grades during continuous casting.

Despite the alloys tested during the first few experiments were not the same alloy compositions studied in this thesis, the results of the Mould Cracking Simulator are very promising. It is expected that this new physical model will help in the study of the thermo-mechanical properties of commercial steels motivated by the continuous trend towards improved casting productivity by increasing casting speed and higher quality, as well as for the development of new steel grades.

7.2 Conclusions

Cracking at the surface of continuously cast steel slabs has been one of the main problems in casting for many years. Additionally, the thermo-mechanical properties of steels are still poorly known at temperatures in the solidification range. Therefore, it becomes important for the improvement of the performance of continuous casters to know more precisely such properties. This thesis contemplates the thermo-mechanical behaviour of steels in relation to the solidification conditions in the continuous casting mould.

The following conclusions can be drawn from this study:

- The LCAK has a high cracking sensitivity because it is very low alloyed steel grade. Its microstructure is coarse and fragile during solidification. In addition, it has a low Mn/S ratio, favouring the formation of MnS low-melting films at the interdendritic spaces and grain boundaries, reducing even more its ductility and broadening the ΔT_B .
- For the LR-HSLA there are components playing a role in its cracking propensity, namely the possibility due to local segregation to solidify with a peritectic susceptibility.
- The HSLA is less hot tearing sensitive because it forms TiN during solidification, as early as in the temperature range involved in the ΔT_B , triggering the coalescence of the dendrites at the last stages of solidification and its microstructure is refined due to the presence of alloying elements playing a role in growth restriction.

Last but not least, this study has been focussed on the hot-cracking sensitivity of three commercial steel grades and not on the shell breakouts propensity. Although the breakouts are related to hot tearing sensitivity and were the primary reason for this study, there are many more aspects in the continuous casting process that will influence the breakout occurrence than only the thermo-mechanical properties of steel.

References

1. Turkdogan, E. T., *Causes and effects of nitride and carbonitride precipitation during continuous casting*, Iron Steelmaker, 16 (5), 1989, 61-
2. Nakagawa, T., Umeda, T., Murata, J., Kamimura, Y., and Niwa, N., *Deformation Behavior during Solidification of Steels*, ISIJ International, 35 (6), 1995, 723-729.
3. Santillana, B., Boom, R., Eskin, D., Mizukami, H., Hanao, M., and Kawamoto, M., *High-Temperature Mechanical Behavior and Fracture Analysis of a Low-Carbon Steel Related to Cracking*, Metallurgical and Materials Transactions A, 2012, 1-10.
4. Lankford, W. T., *Some considerations of strength and ductility in the continuous-casting process*, Metallurgical and Materials Transactions B, 3 (6), 1972, 1331-1357.

Summary

Nowadays a vast majority of the steel produced worldwide is via the continuous casting process route because this is the most low-cost, efficient and high quality method to mass produce metal products in a variety of sizes and shapes. Most of the continuous casters are the initial manufacturing step of a product which is very close to the final shape, reducing the need for further finishing. During continuous casting the liquid steel is solidified under controlled conditions of heat extraction to a semi-finished product that can subsequently be processed until final shape is reached. However, there is no perfect process and cracking during solidification of continuously cast steel slabs has been one of the main problems in casting for many years.

In literature many terms are used for the phenomenon of crack formation at temperatures close to the solidus temperature, e.g. hot tearing, hot shortness, hot cracking or solidification cracking. Regardless of the name, hot tears represent a failure that occurs during casting in the regions of a solidifying slab that are at temperatures between solidus (T_S) and liquidus (T_L) and are subjected to simultaneously acting tensile and compressive stresses.

The three steel grades considered in this study are a Low carbon aluminium killed (LCAK) steel grade, a high strength low alloyed (HSLA) steel grade, micro-alloyed with extra additions of vanadium, nitrogen and niobium, and a low-range HSLA (LR-HSLA), with the same concentration of niobium but a lower concentration of vanadium and nitrogen.

The purpose of this study has been to investigate the differences between these three steel grades, with respect to hot tearing sensitivity upon solidifying in a thin slab caster. This research originates from the industrial demand for defect-free high-speed casting of steels and this thesis focuses on the thermo-mechanical behaviour of steel grades in relation to the solidification conditions in the continuous casting mould.

Although these steel grades are not very different in chemical composition, thermodynamic calculations showed that the two HSLA steel grades have different propensity to the peritectic reaction upon solidification due to the combination of elements in the chemical composition that are either ferrite or austenite stabilisers.

In order to better understand the special behaviour of the HSLA grade, compared with the LR-HSLA and the potential precipitation of TiN, phase field microstructure simulations have been performed, showing that TiN can form already during the latest stage of solidification, even when very low amounts of this element are present. If TiN particles trigger the coalescence of dendrite trunks, then it is possible to understand why, for a given Ti content an increased N content present in the HSLA grade can help to reduce the risk of hot tearing.

Segregating elements in steel can influence the hot tearing susceptibility as they can widen the brittle temperature range (ΔT_B), displacing its lower limit to lower temperatures.

Unique hot tensile tests were carried out in the temperature range involving solidification, where the results suggest that among the studied steel grades, the LCAK steel grade has the lowest strength during solidification and a broader ΔT_B .

Fractographic studies of the samples fractures above the non-equilibrium solidus revealed low melting phases even at temperatures as low as 1360 °C. These low-melting films do have an effect on the hot tearing behaviour of commercial steel grades. The LCAK is particularly prone to develop non-metallic particles at the last stages of solidification.

Whilst the study with the Mould Cracking Simulator did not confirm the increased hot tearing susceptibility of the LCAK and LR-HSLA, it did partially substantiate that the modifications on its design are novel in the way that no other physical model of cracking during continuous casting is able to simulate the process in such a way that it resembles the industrial process.

Despite the alloys tested during the first few experiments were not the same alloy compositions studied in this thesis, the results of the Mould Cracking Simulator are very promising. It is expected that this new physical model will help in the study of the thermo-mechanical properties of commercial steels motivated by the continuous trend towards improved casting productivity by increasing casting speed and higher quality, as well as for the development of new steel grades.

Samenvatting

Tegenwoordig is het meeste van het wereldwijd geproduceerde staal continu gegoten, dit is de meest goedkope, efficiënte en kwalitatief hoogwaardige methode om in grote hoeveelheden metalen producten te produceren in een verscheidenheid van maten en vormen. De meeste continugietmachines zijn de eerste productiestap van een product zeer dicht bij de uiteindelijke vorm, waardoor de behoefte aan verdere afwerking minimaal is. Tijdens continugieten stolt vloeibaar staal onder gecontroleerde omstandigheden van warmteafvoer tot een halfproduct dat vervolgens kan worden bewerkt tot de uiteindelijke vorm. Echter, het is geen perfect proces en scheuren tijdens het stollen van continugegoten staal is een van de belangrijkste onopgeloste problemen.

In de literatuur worden vele termen gebruikt voor het fenomeen van scheurvorming tijdens stolling, bijvoorbeeld *hot tearing*, *hot shortness*, *hot cracking* of *solidification cracking*. Ongeacht de naam, *hot tearing* vertegenwoordigt een fout die optreedt tijdens het gieten in de gebieden tijdens stolling met een temperatuur tussen solidus (T_S) en liquidus (T_L) en zijn onderworpen aan tegelijkertijd optredende trek- en drukspanningen.

De drie staalsoorten hier bestudeerd zijn een *Low carbon aluminium killed* (LCAK) staalkwaliteit, een *hoge sterkte laag gelegeerd* (HSLA) staalkwaliteit, microgelegeerd met extra toevoegingen van vanadium, stikstof en niobium, en een *low-range HSLA* (LR-HSLA), met dezelfde niobiumconcentratie, maar een lagere vanadium- en stikstofconcentratie.

Het doel van deze studie was om de verschillen tussen deze drie staalsoorten te onderzoeken met betrekking tot scheurgevoeligheid tijdens stollen in een dungietmachine. Dit onderzoek vloeit voort uit de industriële vraag naar het foutloos gieten van staal bij hoge gietsnelheden. Dit proefschrift richt zich op het thermo-mechanisch gedrag van staalsoorten tijdens de stolling in de gietvorm.

Hoewel deze staalsoorten niet erg verschillen in chemische samenstelling, laten thermodynamische berekeningen zien dat beide HSLA-staalsoorten een verschillende gevoeligheid hebben voor de peritectische reactie tijdens stolling, door de combinatie van elementen in de chemische samenstelling die ofwel ferriet- of austenietstabilisatoren zijn.

Om het bijzondere gedrag van de HSLA-kwaliteit beter te kunnen begrijpen in vergelijking met de LR-HSLA, en de mogelijke precipitatie van TiN, zijn *phase field* microstructuursimulaties uitgevoerd, die laten zien dat TiN kan worden gevormd tijdens de laatste fase van de stolling, zelfs wanneer er zeer lage hoeveelheden Ti aanwezig zijn. Als TiN-deeltjes brugvorming tussen dendrieten veroorzaken tijdens de stolling, dan is het daarmee te begrijpen waarom bij een gegeven Ti-gehalte een verhoogd-N gehalte in de HSLA-kwaliteit kan helpen om de scheurgevoeligheid te verminderen.

Segregerende elementen in staal kunnen de scheurgevoeligheid beïnvloeden, doordat ze het brosse temperatuurgebied (ΔT_B) kunnen verbreden, door het verplaatsen van de ondergrens naar lagere temperaturen.

Unieke hete trekproeven werden uitgevoerd in het temperatuurgebied tijdens stolling, waarbij de resultaten suggereren dat van de onderzochte staalsoorten de LCAK-kwaliteit de laagste sterkte heeft tijdens het stollen en een bredere ΔT_B .

Fractografisch onderzoek van de gescheurde monsters boven de non-equilibrium solidus heeft aangetoond dat laagsmeltende fasen zelfs bij temperaturen zo laag als 1360°C aanwezig zijn. Deze laagsmeltende films hebben een effect op het hot tearing-gedrag van commerciële staalkwaliteiten. De LCAK is bijzonder gevoelig voor niet-metallische deeltjes die ontwikkelen tijdens de laatste stadia van de stolling.

Het onderzoek met de *Mould Cracking Simulator* heeft de verhoogde scheurgevoeligheid van de LCAK en LR-HSLA niet bevestigd, maar heeft wel gedeeltelijk bewezen dat de wijzigingen van het ontwerp nieuw zijn. Geen enkel andere fysisch model van scheuren tijdens continugieten kan de continugietcondities zodanig simuleren dat het lijkt op het industriële proces.

Ondanks dat de eerste experimenten zijn uitgevoerd met andere staalkwaliteiten dan die in dit proefschrift bestudeerd, zijn de resultaten van de *Mould Cracking Simulator* veelbelovend. Verwacht wordt dat dit nieuwe fysieke model een belangrijke bijdrage zal leveren aan het onderzoek van de thermo-mechanische eigenschappen van staal, gemotiveerd door de continue trend om de productiviteit te verhogen door sneller te gieten met een hogere kwaliteit, en aan de ontwikkeling van nieuwe staalsoorten.

List of Publications

“Minimization of slag entrapment and cold drops” B. Santillana, M.Dziuba, M. Oropeza and E. Frenandez, Ironmaking & Steelmaking, Vol 30 Nr. 6, 2003 Institute of Materials minerals and mining, UK.

“Interlaboratory Inclusions Study Under Standard ASTM E-45, with Commercial Type Steels And High-Clean Steels.” B. Santillana et al. 13th IAS Steelmaking Seminar as a Poster, Buenos Aires, Argentina, November 2001.

“Slag entrapment and macroinclusions” lecture in the “Workshop on defects in long products” by Roberto Coda and the IAS researchers on defects, San Nicolás, Argentina, May 2003.

“Investigating mould heat transfer in thin slab casting with CON1D”, B. Santillana, B. G. Thomas, L. Hibbeler, A. Hamoen, A. Kamperman, AISTech 2007, Indianapolis, USA, May 2007. Published in Iron & Steel Technology, issue July 2008.

“Longitudinal face crack prediction with thermo-mechanical models of thin slabs in funnel moulds”, L.Hibbeler, B. G. Thomas, B. Santillana, A. Hamoen, A. Kamperman, 6th European Continuous Casting Conference (6th ECCC), Riccione, Italy, June 2008.

“Investigating heat transfer in funnel-mould casting with CON1D: Effect of Plate Thickness” L.Hibbeler, B. G. Thomas, B. Santillana, A. Hamoen, A. Kamperman, W. van der Knoop, ISIJ International 2008, Vol.48 (10) 1380-1388.

“A new approach for modelling slag infiltration and solidification in a continuous casting mould”. P.E. Ramirez-Lopez, P.D. Lee, K.C. Mills and B. Santillana.. ISIJ International, 2010. 50(12): p. 1797-1804

“Three Phase Modelling of the Steel-Slag-Mould Interactions in Continuous Casting”, P. E. Ramirez-Lopez, B. Santillana, K. C. Mills and P. D. Lee: Guthrie Honorary Symposium, Montreal West End, Canada, June 6-9, 2011, pp.

“A unified mechanism for oscillation mark formation”, P. E. Ramirez-Lopez, K. C. Mills, P.D. Lee and B. Santillana. 7th European Continuous Casting Conference (7th ECCC), Dusseldorf, Germany, June 2011.

“Towards direct defect prediction on continuous casting”, P.E. Ramirez-Lopez, P.D. Lee, K.C. Mills, C. Puncreobutr, D. Farrugia, B. Santillana and U.Sjöström. 7th European Continuous Casting Conference (7th ECCC), Dusseldorf, Germany, June 2011.

“3D thickness measurement technique for continuous casting breakout shells”, B. Santillana, G. Botman, E.Dekker, B. G. Thomas, 7th European Continuous Casting Conference (7th ECCC), Dusseldorf, Germany, June 2011

“Thermal analysis of commercial steel grades”, B. Santillana, D. G. Eskin, R. Boom, L. Katgerman, F. Grimberg, G. Abbel, 4th International Conference on Modelling and Simulation of Metallurgical Processes in Steelmaking STEELSIM, Dusseldorf, Germany, June 2011

“Effect of V and N on the microstructure evolution during continuous casting of steel”, B. Santillana, D. G. Eskin, R. Boom, L. Katgerman, 3rd International Conference on Advances in Solidification Processes, Rolduc, The Netherlands, June 2011.

“Prediction and verification of initial shell formation and microstructure development in a high speed continuously cast thin slab of a low alloy steel”, B. Santillana, H. Mehrara, R. Boom, D. G. Eskin, L. Katgerman, G. Abbel, 3rd International Conference on Advances in Solidification Processes, Rolduc, The Netherlands, June 2011.

“Review: The “Butterfly” effect in Continuous Casting”, P. D. Lee, P. E. Ramirez Lopez, K. C. Mills and B. Santillana, Iron and Steelmaking, 39 (4), 2012, 244-253.

“A Unified Mechanism for the Formation of Oscillation Marks”, P. E. Ramirez Lopez, Lee, P.D., Mills, K.C., Santillana, B., Metallurgical and Materials Transactions B., Vol. 43B (2012), pp. 107-22.

“Phase Field Modeling of Microstructure Formation during the Solidification of Continuously Cast Low Carbon and HSLA Steels”, B. Santillana, B. Böttger, M. Apel, D. G. Eskin, Modelling of Casting, Welding and Advanced Solidification Processes MCWASP XIII, Shaldming, Austria, June 2012.

“High-Temperature Mechanical Behavior and Fracture Analysis of a Low-Carbon Steel Related to Cracking”, Santillana, B., Boom, R., Eskin, D., Mizukami, H., Hanao, M., and Kawamoto, M., Metallurgical and Materials Transactions A, December 2012, Vol 43A, Issue 13, pp 5048-5057.

“Multi-Phase-Field Modeling of Solidification in Technical Steel Grades”, B. Böttger, G. J. Schmitz, B. Santillana, Transactions of the Indian Institute of Metals: Volume 65, Issue 6 (2012), Page 613-615

“Relationship Between Solidification Microstructure and Hot Cracking Susceptibility for Continuous Casting of Low-Carbon and High-Strength Low-Alloyed Steels: A Phase-Field Study”, B. Böttger, M. Apel, B. Santillana, D. G. Eskin, Metallurgical and Materials Transactions A, Online first April 2013

Acknowledgements

During the last few years a lot of things have positively changed my life, being able to perform this PhD study is one of them.

I would like to thank specially the people who gave me this possibility, first of all my promotor Prof. Rob Boom believed in me and gave me the freedom to prepare a project where I could broaden my knowledge. At that time I asked Prof. Dmitry Eskin to be also my supervisor and to help me with the contents of my idea, I gave him, a too ambitious project, a raw diamond that he had the knowledge and courage to cut it in two. I chose to study the thermo-mechanical properties, and the thermo-physical properties of commercial steels was taken by Hossein Mehrara, whom I trust and believe he will have great results.

My former knowledge group leader and “industrial partner”, Gert Abbel not only supported me daily but also gave me the freedom to perform this study within my workload; I am also thankful to his comments and discussions during these years. I also thanks to Dirk van der Plas to accept and support me with my own expertise within the new PMC group.

A special mention goes to my office-mate and friend Frank Grimberg that gives me every day we share in the office a moment to smile and have fun. Outside office hours Frank and Juanita are personal friends I appreciate and we enjoy the time together.

My Tata Steel “talent development mentor”, Egbert Jansen has given me encouragement and a lot of support “that I was capable to finish this study”, therefore I greatly acknowledge his support.

I want to thank also to all my colleagues at 4H16 begane grond, particularly to Willem van der Knoop, MK Singh, Henk Visser, Ton Spierings and Jelle Agema for the big mugs and cups of tea we serve each other to encourage improving our daily “social index”.

I could not have reached the results I am here publishing without the great help from Sabri Sengo and Tu Phan-Tran, we really have fun and imagination when we look at samples and non metallic inclusions under the microscope.

The “dream-team” to perform the mould cracking simulator tests, Menno Effern, Bastiaan de Bruijn and Nick Ontijt worth also a big thanks in this thesis; and in particular to Marcel Cruijff who designed and made possible the idea I had to test mechanical properties during solidification, resulting in the great design of the Mould Cracking Simulator.

The help with the phase field simulations for this study by Bernd Böttger, Marco Appel and George Schmitz from ACCESS e.V., Aachen has been one of the key cherries on my pie...

The idea to start this study came after the first tensile testing's that Masahito Hanao, Masayuki Kawamoto and Hideo Mizukami performed for me at Sumitomo Metal Industries; therefore their help is also greatly acknowledged.

I also want to specially thank to Prof. Andy Howe for sharing his knowledge with me and his comments and suggestions are a valuable part of this study.

For my friend Roxi Contreras I am out of words to thank her for being my friend and for the design of the cover and the invitations for this thesis, amiga: te quiero y te extraño dia a dia.

A big thanks to my great friend Marimé and my brother-of-the-heart Lucio (and of course for Sol and Eliseo) for being always present for me and my family.

My parents always supported and encouraged me to study and follow my dreams, they are for me in many aspects the role model to follow in my life and I love them and miss them...

Many thanks also for Mieke and Cor for their support and understanding along these times.

And I do not want to forget a big thanks to my "Connect friends" for all those lovely girly talks.

Thank you also to my lovely son Max and our dog Bruno for their unconditional love and cheer and to understand and be patient when I was short in time to play with them because I had to work on my PhD...

Last but not least, not only thanks but also all my love goes to my husband and friend Emiel for being "the great man" next to me with his support, love, encourage and proud.

Begoña Santillana

Curriculum Vitae

Maria Begoña Santillana

Born 28th June 1975 in San Nicolás de los Arroyos, Argentina

- | | |
|--------------|---|
| 1988-1992 | Baccalaureate in Education
Instituto Nstra. Señora de la Misericordia |
| 1992-2002 | Engineer in Metallurgy
Universidad Tecnológica Nacional (UTN), Facultad Regional San Nicolás, Argentina |
| 2000-2004 | Researcher at the Instituto Argentino de Siderurgia (IAS),
Steelmaking and Ironmaking Process Assistance Department. |
| 2004-2005 | Product and customer support at Miguel Abad S.A, Argentina |
| 2006-Present | Principal Researcher at Tata Steel RD&T, Steelmaking and
Casting Department, The Netherlands |

Stellingen behorende bij het proefschrift

Propositions accompanying the thesis

Thermo-mechanical properties and cracking during solidification of thin slab cast steel

1. Contrary to the common assumption, the outer equiaxed chill zone is not formed in continuously cast steel.
In tegenstelling tot wat gemeenschappelijk wordt aangenomen, wordt in continu gegoten staal geen buitenste equiaxed zone gevormd.
2. Although aluminium and steel are two different metallic materials with different solidification paths and properties, the principles of hot tearing developed for aluminium also apply for steel.
Hoewel aluminium en staal twee verschillende materialen zijn met verschillen in eigenschappen en stollingsgedrag kunnen de principes van 'hot tearing' zoals ontwikkeld voor aluminium ook worden toegepast voor staal.
3. The definition of brittleness as a material property should not be confused with the material behaviour
De definitie van brosheid als materiaaleigenschap moet niet worden verward met het materiaalgedrag
4. The presence of very low amounts of some tramp-elements in industrial alloys, otherwise not important, can change the cracking behaviour of an alloy during solidification.
De aanwezigheid van zeer lage hoeveelheden sporenelementen in industriële legeringen, die normaliter niet van belang zijn, kan de scheurgevoeligheid van een legering tijdens het stollen beïnvloeden.
5. A person masters a language when he or she fully understands the jokes.
Een persoon beheerst een taal wanneer hij of zij de grappen in deze taal begrijpt.
6. A meal without wine is like a day without sunshine (Jean Anthelme Brillat-Savarin). Except in some dishes where other alcoholic beverages are more suitable for the meal.
Een maaltijd zonder wijn is als een dag zonder zonneschijn (Jean Anthelme Brillat-Savarin). Behalve in sommige gerechten waar andere alcoholisch dranken meer geschikt zijn voor de maaltijd

7. Ikea furniture is a real-life Lego for adults.
Ikea meubilair is Lego voor volwassenen.
8. Persistence is to the character of man what carbon is to steel (*Napoleon Hill*), unless other elements are added to the composition.
Volharding is voor het karakter van de man, wat koolstof is voor staal (Napoleon Hill), tenzij er andere elementen aan de samenstelling zijn toegevoegd.
9. Women's shoes tell more about the economy than is commonly known.
Vrouwen schoenen vertellen meer over de economie dan algemeen bekend is
10. Contrary to the common Dutch believe, pressing the button of the traffic lights will not speed-up the waiting time.
In tegenstelling tot het gemeenschappelijk Nederlandse geloof, wordt de wachttijd niet verkort door het meermaals drukken van het knopje van het verkeerslicht.

Deze stellingen worden opponeerbaar en verdedigbaar geacht en zijn als zodanig goedgekeurd door de promotoren, Prof. dr. R. Boom en Prof. dr. D. G. Eskin

These propositions are regarded as opposable and defendable, and have been approved as such by the supervisors, Prof. dr. R. Boom en Prof. dr. D. G. Eskin